

INFORMATION TO USERS

This manuscript has been reproduced from the microfilm master. UMI films the text directly from the original or copy submitted. Thus, some thesis and dissertation copies are in typewriter face, while others may be from any type of computer printer.

The quality of this reproduction is dependent upon the quality of the copy submitted. Broken or indistinct print, colored or poor quality illustrations and photographs, print bleedthrough, substandard margins, and improper alignment can adversely affect reproduction.

In the unlikely event that the author did not send UMI a complete manuscript and there are missing pages, these will be noted. Also, if unauthorized copyright material had to be removed, a note will indicate the deletion.

Oversize materials (e.g., maps, drawings, charts) are reproduced by sectioning the original, beginning at the upper left-hand corner and continuing from left to right in equal sections with small overlaps. Each original is also photographed in one exposure and is included in reduced form at the back of the book.

Photographs included in the original manuscript have been reproduced xerographically in this copy. Higher quality 6" x 9" black and white photographic prints are available for any photographs or illustrations appearing in this copy for an additional charge. Contact UMI directly to order.

UMI[®]

Bell & Howell Information and Learning
300 North Zeeb Road, Ann Arbor, MI 48106-1346 USA
800-521-0600

NOTE TO USERS

This reproduction is the best copy available

UMI

**NONDESTRUCTIVE DETERMINATION OF UNKNOWN PILE TIP ELEVATIONS
USING MODAL ANALYSIS**

**A Thesis
Presented to
The Academic Faculty**

By

Mary Leigh Hughes

**In Partial Fulfillment
of the Requirements for the Degree
Doctor of Philosophy in Civil Engineering**

**Georgia Institute of Technology
March 1999**

Copyright © 1999 by Mary Leigh Hughes

UMI Number: 9939866


UMI Microform 9939866
Copyright 1999, by UMI Company. All rights reserved.

**This microform edition is protected against unauthorized
copying under Title 17, United States Code.**

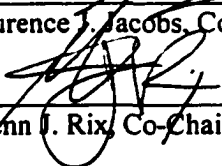
UMI
300 North Zeeb Road
Ann Arbor, MI 48103

NONDESTRUCTIVE DETERMINATION OF UNKNOWN PILE TIP ELEVATIONS
USING MODAL ANALYSIS

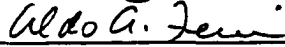
Approved:




Dr. Laurence J. Jacobs, Co-Chairman



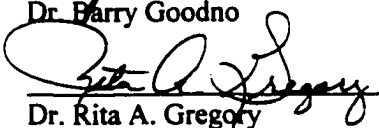
Dr. Glenn J. Rix, Co-Chairman



Dr. Aldo A. Ferri



Dr. Barry Goodno



Dr. Rita A. Gregory

Date Approved by Chairmen 3/3/99

ACKNOWLEDGEMENTS

The author would like to gratefully acknowledge the guidance, support, and encouragement provided by Dr. Laurence Jacobs and Dr. Glenn Rix throughout the pursuit of her doctoral degree. Thanks also are expressed to the remaining members of her reading committee—Drs. Aldo Ferri, Barry Goodno, and Rita Gregory—for their time, comments, and helpful suggestions.

Deep gratitude is extended to the members of the author's family for the ceaseless love and encouragement they have provided throughout the course of her education, as well as for the confidence they showed in her at every point in her life. In particular, thanks are offered to the author's parents, Jack and Maggie, and to her four brothers, John, Mike, Chris, and David.

The author would also like to express her heartfelt appreciation to her fiancé, Carl Hollopeter, for his tireless support and his persistence in urging her to strive for excellence during her degree pursuit.

Special thanks are extended to Dr. Joseph Tedesco, Dr. Allen Ross, and Mrs. Terri Carson for their guidance, encouragement, and friendship, as well as for their willingness to share their considerable knowledge with the author. Sincere appreciation is also expressed for the friendship and professional support provided by Mr. Stan Strickland and Dr. Dave Jerome.

Much appreciation and many kind thoughts are conveyed to the author's friends and classmates, particularly Jim Swanson, Dan Linzell, Jeff Smallidge, Andrea Maleck, and Felipe Acosta. Without their companionship, assistance, and scholarly interaction, the author's doctoral studies would not have been completed.

Finally, gratitude is expressed to the United States Air Force Palace Knight Program for its financial support of the author's doctoral pursuit. Specifically, thanks are extended to members of the Air Force Research Laboratory's Damage Mechanism and Airbase Technology Branches.

TABLE OF CONTENTS

	Page
ACKNOWLEDGEMENTS	iii
LIST OF TABLES	ix
LIST OF FIGURES	xii
SUMMARY	xxi
CHAPTER	
I. INTRODUCTION	1
1.1 Problem Statement	1
1.2 Objective	2
1.3 Background and Previous Work	3
1.3.1 Background	3
1.3.2 Nondestructive Testing Methods for Bridge Piles	5
1.3.3 Recent Studies of Pile Integrity Assessment and Length Determination	20
1.3.4 Modal Analysis for Structural Identification	32
II. TEST CONFIGURATION	35
2.1 Small-Scale Pile Facility	35
2.2 Test Pile Sections	38
2.3 Soil Properties	40

2.3.1	Sand Fill	40
2.3.2	Sand Placement	41
2.4	Equipment and Instrumentation	42
2.4.1	Impact Hammer	42
2.4.2	Piezoelectric Accelerometer	47
2.5	Digital Signal Analyzer	51
III.	MODAL ANALYSIS	53
3.1	Summary of Modal Analysis Theory	53
3.1.1	General Concepts	53
3.1.2	Frequency Response Function Display	63
3.1.3	Modal Parameter Estimation	68
3.2	Current Practice of Modal Analysis for Civil Engineering Applications	78
3.3	Application of Modal Analysis to Pile Length Determination Problem	85
IV.	MODAL ANALYSIS TEST PROCEDURE	88
4.1	Test Method	88
4.1.1	Test Grid	91
4.1.2	Test Procedure	91
4.1.3	Data Windowing	95
4.2	Modal Parameter Estimation	99
4.2.1	Stability Diagram	100
4.2.2	Residue Comparison	104
4.3	Experimental Test Results	106

4.3.1	Results for Tests Along the X Axis	106
4.3.2	Results for Tests Along the Y Axis	120
4.4	Modal Parameter Estimation Results	130
4.4.1	Examples of Estimation Tools	130
4.4.2	Results for Tests Along the X Axis	135
4.4.3	Results for Tests Along the Y Axis	146
4.5	Discussion of Experimental Results	151
V.	NUMERICAL ANALYSES	152
5.1	Analytically Generated Data	152
5.1.1	Results for Tests Along the X Axis	155
5.1.2	Results for Tests Along the Y Axis	170
5.1.3	Discussion of Modal Parameter Estimation Results for Analytically Generated Data	181
5.2	Finite Element Modeling	183
5.2.1	Model for Pile A in Nonembedded Configuration	183
5.2.2	Finite Element Results for Embedded Piles	192
5.2.2.1	Results for Tests Along the X Axis	193
5.2.2.2	Results for Tests Along the Y Axis	199
5.2.3	Discussion of Natural Frequency Results from Finite Element Modeling of Embedded Piles	205
5.3	Theoretical Natural Frequency Calculation for Beam Resting on Elastic Supports	208
5.3.1	Results of Theoretical Natural Frequency Calculations	209
5.3.2	Discussion of Theoretical Natural Frequency Results	213

VI. MODEL PILE WAVE PROPAGATION	215
6.1 Spectrogram Description	216
6.2 Dispersion in Spectrograms	220
6.3 Spectrograms for Steel Flat Stock	223
6.4 Spectrograms for S3x5.7 Model Pile Section	231
VII. CONCLUSIONS AND RECOMMENDATIONS	236
7.1 Conclusions	236
7.1.1 Modal Parameter Estimation of Experimental Frequency Response Function Data	237
7.1.2 Numerical Analyses	238
7.1.3 Wave Propagation Investigation	240
7.2 Recommendations for Future Work	240
7.3 Contributions	243
APPENDIX A: Experimental Frequency Response Functions for Pile C	244
APPENDIX B: Programs for Analytical Generation of Frequency Response Function Data	263
APPENDIX C: Mode Shapes for Pile A in Embedded Configuration Generated by Finite Element Model	273
APPENDIX D: Derivation of Theoretical Solution	282
REFERENCES	290
VITA	296

LIST OF TABLES

	Page
Table 4.1 Details of Group I Test Piles	89
Table 4.2 Pile A Modal Parameter Estimation Results, Nonembedded, Along X Axis	136
Table 4.3 Pile A Modal Parameter Estimation Results, Embedded, Along X Axis	137
Table 4.4 Pile B Modal Parameter Estimation Results, Along X Axis	138
Table 4.5 Pile C Modal Parameter Estimation Results, Along X Axis	139
Table 4.6 Pile D Modal Parameter Estimation Results, Along X Axis	140
Table 4.7 Pile E Modal Parameter Estimation Results, Along X Axis	141
Table 4.8 Pile A Modal Parameter Estimation Results, Embedded, Along Y Axis	146
Table 4.9 Pile B Modal Parameter Estimation Results, Along Y Axis	147
Table 4.10 Pile C Modal Parameter Estimation Results, Along Y Axis	147
Table 4.11 Pile D Modal Parameter Estimation Results, Along Y Axis	148
Table 4.12 Pile E Modal Parameter Estimation Results, Along Y Axis	148
Table 5.1 Pile A, Embedded Configuration Modal Parameter Estimation Results Along X Axis, Analytically Generated Data	162
Table 5.2 Pile B Modal Parameter Estimation Results, Along X Axis, Analytically Generated Data	163

Table 5.3	Pile C Modal Parameter Estimation Results, Along X Axis, Analytically Generated Data	164
Table 5.4	Pile D Modal Parameter Estimation Results, Along X Axis, Analytically Generated Data	165
Table 5.5	Pile E Modal Parameter Estimation Results, Along X Axis, Analytically Generated Data	166
Table 5.6	Pile A, Nonembedded Configuration Modal Parameter Estimation Results, Along X Axis, Analytically Generated Data	167
Table 5.7	Pile A, Embedded Configuration Modal Parameter Estimation Results Along Y Axis, Analytically Generated Data	175
Table 5.8	Pile B Modal Parameter Estimation Results, Along Y Axis, Analytically Generated Data	176
Table 5.9	Pile C Modal Parameter Estimation Results, Along Y Axis, Analytically Generated Data	177
Table 5.10	Pile D Modal Parameter Estimation Results, Along Y Axis, Analytically Generated Data	178
Table 5.11	Pile E Modal Parameter Estimation Results, Along Y Axis, Analytically Generated Data	179
Table 5.12	Comparison of Natural Frequency Values Obtained by Theoretical Solution and by Finite Element Model, Along X Axis	185
Table 5.13	Comparison of Natural Frequency Values Obtained by Theoretical Solution and by Finite Element Model, Along Y Axis	186
Table 5.14	Comparison of Natural Frequency Values Obtained from Experimental Results with Those from Finite Element Model, Along X Axis	187
Table 5.15	Comparison of Natural Frequency Values Obtained from Experimental Results with Those from Finite Element Model, Along X Axis (Modified)	188
Table 5.16	Comparison of Natural Frequency Values Obtained from Experimental Results with Those from Finite Element Model, Along X Axis (Modified Boundary Conditions)	190

Table 5.17	Natural Frequency Results from Finite Element Model for Pile A, Embedded Configuration, Along X Axis	194
Table 5.18	Natural Frequency Results from Finite Element Model for Pile B, Along X Axis	195
Table 5.19	Natural Frequency Results from Finite Element Model for Pile C, Along X Axis	196
Table 5.20	Natural Frequency Results from Finite Element Model for Pile D, Along X Axis	197
Table 5.21	Natural Frequency Results from Finite Element Model for Pile E, Along X Axis	198
Table 5.22	Natural Frequency Results from Finite Element Model for Pile A, Embedded Configuration, Along Y Axis	200
Table 5.23	Natural Frequency Results from Finite Element Model for Pile B, Along Y Axis	201
Table 5.24	Natural Frequency Results from Finite Element Model for Pile C, Along Y Axis	202
Table 5.25	Natural Frequency Results from Finite Element Model for Pile D, Along Y Axis	203
Table 5.26	Natural Frequency Results from Finite Element Model for Pile E, Along Y Axis	204
Table 5.27	Theoretical Natural Frequencies for Pile A, Embedded Configuration	210
Table 5.28	Theoretical Natural Frequencies for Pile B	210
Table 5.29	Theoretical Natural Frequencies for Pile C	211
Table 5.30	Theoretical Natural Frequencies for Pile D	211
Table 5.31	Theoretical Natural Frequencies for Pile E	212

LIST OF FIGURES

	Page
Figure 1.1 Parallel Seismic Test Setup	6
Figure 1.2 Results of Parallel Seismic Test	7
Figure 1.3 Sonic Echo Test Setup	9
Figure 1.4 Acceleration Time History from Sonic Echo Test	10
Figure 1.5 Mobility Curve from Sonic Mobility Test	12
Figure 1.6 Experimental and Theoretical Mobility Curves	18
Figure 1.7 Impedance Log	18
Figure 1.8 Field-Test Setup used by Holt et al.	25
Figure 1.9 Time Records from Two Accelerometers	28
Figure 1.10 SKM Plot Using a 1-cycle 500-Hz Kernel	28
Figure 1.11 Setup for Pile Length Data Collection Used by Pandey et al.	32
Figure 2.1 Experimental Facility for Testing Small-Scale Piles	36
Figure 2.2 End View of Experimental Facility for Testing Small-Scale Piles	37
Figure 2.3 Plan View of Experimental Facility for Testing Small-Scale Piles	38
Figure 2.4 Elevation Views of Small-Scale Pile Test Facility	40
Figure 2.5 Grain Size Distribution for Chattahoochee River Sand	41
Figure 2.6 Schematic of Test Setup and Equipment	43

Figure 2.7	Impact Hammer Details	43
Figure 2.8	Impact Hammer Used for Model Pile Tests	44
Figure 2.9	Force-Time Curves and Frequency Spectra for Various Hammer Tips	46
Figure 2.10	Measured Frequency Spectrum for PCB 068C03 Impact Hammer	46
Figure 2.11	Cutaway of Accelerometer and Corresponding Dynamic Model	47
Figure 2.12	(a) Methods of Accelerometer Attachment (b) Frequency Response Function for Different Attachments	49
Figure 2.13	Frequency Response Functions for Trial Accelerometer Mounting Methods	50
Figure 2.14	Digital Signal Analyzer and Power Amplifiers	51
Figure 3.1	Conceptual Approach Used in Modal Analysis	55
Figure 3.2	Bode Plot of Accelerance for Undamped SDOF System	64
Figure 3.3	Nyquist Plot of Accelerance for Viscously-Damped SDOF System	64
Figure 3.4	Real and Imaginary Parts of Accelerance for Damped SDOF System	65
Figure 3.5	Mobility Plot for MDOF System Showing Individual Modal Contributions	66
Figure 3.6	Decay Rate, σ , of Damped Oscillations	69
Figure 3.7	Illustration of the Peak-Picking Process	71
Figure 3.8	Estimation of Natural Frequency Using Circle Fit Method	73
Figure 3.9	Modal Circle Properties Used to Compute Damping for Circle-Fit Method	75
Figure 3.10	Schematic of Pile Encased in Bridge Superstructure	85
Figure 4.1	Configuration of Pile Group I	89
Figure 4.2	Dimensions for S3x5.7 Section	90

Figure 4.3	Orientation of S3x5.7 Test Specimen with Respect to Supporting W10x45	90
Figure 4.4	Test Grid for Pile A in Nonembedded Configuration	92
Figure 4.5	Test Grid for Piles A-E in Embedded Configuration	93
Figure 4.6	Typical Impact Force Pulse and Force Window	96
Figure 4.7	Illustration of Leakage Phenomenon	97
Figure 4.8	Effect of Applying Exponential Window to Response Signal	100
Figure 4.9	Analytically Generated Driving Point FRF's for Pile A (Nonembedded)	101
Figure 4.10	Stability Diagram for Nonembedded Pile A Data	103
Figure 4.11	Residues for Pile A Data in the Nonembedded Configuration	105
Figure 4.12	Illustration of Accelerometer Orientation for Tests Along the X Axis	107
Figure 4.13	Linearity Validation Plot for Pile A in the Nonembedded Configuration, Tested Along the X Axis	108
Figure 4.14	Linearity Validation Plot for Pile A in the Embedded Configuration, Tested Along the X Axis	109
Figure 4.15	Linearity Validation Plot for Pile B, Tested Along the X Axis	110
Figure 4.16	Linearity Validation Plot for Pile C, Tested Along the X Axis	111
Figure 4.17	Linearity Validation Plot for Pile D, Tested Along the X Axis	112
Figure 4.18	Linearity Validation Plot for Pile E, Tested Along the X Axis	113
Figure 4.19	Driving Point Frequency Response Functions for Pile A, Nonembedded Configuration, Tested Along the X Axis	114
Figure 4.20	Driving Point Frequency Response Functions for Pile A, Embedded Configuration, Tested Along the X Axis	115
Figure 4.21	Driving Point Frequency Response Functions for Pile B, Tested Along X Axis	116

Figure 4.22	Driving Point Frequency Response Functions for Pile C, Tested Along X Axis	117
Figure 4.23	Driving Point Frequency Response Functions for Pile D, Tested Along X Axis	118
Figure 4.24	Driving Point Frequency Response Functions for Pile E, Tested Along X Axis	119
Figure 4.25	Illustration of Accelerometer Orientation for Tests Along the Y Axis	120
Figure 4.26	Linearity Validation Plot for Pile B, Tested Along the Y Axis	121
Figure 4.27	Linearity Validation Plot for Pile C, Tested Along the Y Axis	122
Figure 4.28	Linearity Validation Plot for Pile D, Tested Along the Y Axis	123
Figure 4.29	Linearity Validation Plot for Pile E, Tested Along the Y Axis	124
Figure 4.30	Driving Point Frequency Response Functions for Pile A, Embedded Configuration, Tested Along the Y Axis	125
Figure 4.31	Driving Point Frequency Response Functions for Pile B, Tested Along Y Axis	126
Figure 4.32	Driving Point Frequency Response Functions for Pile C, Tested Along Y Axis	127
Figure 4.33	Driving Point Frequency Response Functions for Pile D, Tested Along Y Axis	128
Figure 4.34	Driving Point Frequency Response Functions for Pile E, Tested Along Y Axis	129
Figure 4.35	Stability Diagram for Pile C FRF Data, Tested Along X Axis, Selected Resonance Locations Circled	131
Figure 4.36	Comparison of Experimental and Resultant Residue Values for Pile C, Tested Along X Axis	132
Figure 4.37	Results of Natural Frequency Estimation for Group I Piles, Along X Axis	142
Figure 4.38	Results of Damping Estimation for Group I Piles, Along X Axis	143

Figure 4.39	Ninth Through Twelfth Mode Shapes Calculated From Pile C Modal Parameter Estimates	144
Figure 4.40	Eighth Through Eleventh Mode Shapes Calculated From Pile E Modal Parameter Estimates	145
Figure 4.41	Results of Natural Frequency Estimation for Group I Piles, Along Y Axis	149
Figure 4.42	Results of Damping Estimation for Group I Piles, Along Y Axis	150
Figure 5.1	Analytically Generated Driving Point Frequency Response Functions for Pile A, Embedded Configuration, Along X Axis	156
Figure 5.2	Analytically Generated Driving Point Frequency Response Functions for Pile B, Along X Axis	157
Figure 5.3	Analytically Generated Driving Point Frequency Response Functions for Pile C, Along X Axis	158
Figure 5.4	Analytically Generated Driving Point Frequency Response Functions for Pile D, Along X Axis	159
Figure 5.5	Analytically Generated Driving Point Frequency Response Functions for Pile E, Along X Axis	160
Figure 5.6	Analytically Generated Driving Point Frequency Response Functions for Pile A, Nonembedded Configuration, Along X Axis	161
Figure 5.7	Natural Frequency vs. Mode Number for Analytically Generated Data, Along X Axis	168
Figure 5.8	Damping vs. Mode Number for Analytically Generated Data, Along X Axis	169
Figure 5.9	Analytically Generated Driving Point Frequency Response Functions for Pile A, Embedded Configuration, Along Y Axis	170
Figure 5.10	Analytically Generated Driving Point Frequency Response Functions for Pile B, Along Y Axis	171
Figure 5.11	Analytically Generated Driving Point Frequency Response Functions For Pile C, Along Y Axis	172

Figure 5.12	Analytically Generated Driving Point Frequency Response Functions For Pile D, Along Y Axis	173
Figure 5.13	Analytically Generated Driving Point Frequency Response Functions For Pile E, Along Y Axis	174
Figure 5.14	Natural Frequency vs. Mode Number for Analytically Generated Data, Along Y Axis	180
Figure 5.15	Damping vs. Natural Frequency for Analytically Generated Data, Along Y Axis	181
Figure 5.16	Preliminary Finite Element Model of Pile A, Nonembedded Configuration, Clamped at Top End, Free at Bottom End	184
Figure 5.17	Connection Arrangement for Model Piles in Test Fixture	189
Figure 5.18	Modified Boundary Condition Arrangement	190
Figure 5.19	Finite Element Model for Pile C in Its Embedded Configuration	193
Figure 5.20	Natural Frequency Results from Finite Element Modeling vs. Mode Number, Along X Axis	199
Figure 5.21	Natural Frequency Results from Finite Element Modeling vs. Mode Number, Along Y Axis	205
Figure 5.22	Beam on Elastic Supports Idealized as Springs	208
Figure 5.23	Theoretical Natural Frequency vs. Mode Number	212
Figure 5.24	Percent Difference from Pile A Theoretical Natural Frequency Results	213
Figure 6.1	Spectrogram of a Force Impulse Applied to a Stretched String	217
Figure 6.2	Spectrograms for a Stretched String with Window Lengths Decreasing from (a) to (d)	219
Figure 6.3	Spectrograms for a Beam Impacted Transversely with Window Lengths Decreasing from (a) to (c)	221
Figure 6.4	Acceleration Time History for Hammer Impact on Flat Stock, Impact Applied at 0.3L, Acceleration Measured at 0.8L	223

Figure 6.5	(a) Spectrogram for Flat Stock Subjected to Transverse Impact (Window Length = 128)	225
Figure 6.5	(b) Spectrogram for Flat Stock Subjected to Transverse Impact (Window Length = 32)	226
Figure 6.6	Dispersion Relationship for Steel Flat Stock	228
Figure 6.7	(a) Spectrogram for S3x5.7 Section Subjected to Transverse Impact in Middle of Web (Window Length = 128)	232
Figure 6.7	(b) Spectrogram for S3x5.7 Section Subjected to Transverse Impact in Middle of Web (Window Length = 64)	233
Figure 6.7	(c) Spectrogram for S3x5.7 Section Subjected to Transverse Impact in Middle of Web (Window Length = 32)	234
Figure A.1	Experimental Frequency Response Functions for Pile C, Tested Along X Axis, Accelerometer at Position 1, Impact at Positions 1-9	245
Figure A.2	Experimental Frequency Response Functions for Pile C, Tested Along X Axis, Accelerometer at Position 2, Impact at Positions 1-9	246
Figure A.3	Experimental Frequency Response Functions for Pile C, Tested Along X Axis, Accelerometer at Position 3, Impact at Positions 1-9	247
Figure A.4	Experimental Frequency Response Functions for Pile C, Tested Along X Axis, Accelerometer at Position 4, Impact at Positions 1-9	248
Figure A.5	Experimental Frequency Response Functions for Pile C, Tested Along X Axis, Accelerometer at Position 5, Impact at Positions 1-9	249
Figure A.6	Experimental Frequency Response Functions for Pile C, Tested Along X Axis, Accelerometer at Position 6, Impact at Positions 1-9	250
Figure A.7	Experimental Frequency Response Functions for Pile C, Tested Along X Axis, Accelerometer at Position 7, Impact at Positions 1-9	251
Figure A.8	Experimental Frequency Response Functions for Pile C, Tested Along X Axis, Accelerometer at Position 8, Impact at Positions 1-9	252
Figure A.9	Experimental Frequency Response Functions for Pile C, Tested Along X Axis, Accelerometer at Position 9, Impact at Positions 1-9	253

Figure A.10	Experimental Frequency Response Functions for Pile C, Tested Along Y Axis, Accelerometer at Position 1, Impact at Positions 1-9	254
Figure A.11	Experimental Frequency Response Functions for Pile C, Tested Along Y Axis, Accelerometer at Position 2, Impact at Positions 1-9	255
Figure A.12	Experimental Frequency Response Functions for Pile C, Tested Along Y Axis, Accelerometer at Position 3, Impact at Positions 1-9	256
Figure A.13	Experimental Frequency Response Functions for Pile C, Tested Along Y Axis, Accelerometer at Position 4, Impact at Positions 1-9	257
Figure A.14	Experimental Frequency Response Functions for Pile C, Tested Along Y Axis, Accelerometer at Position 5, Impact at Positions 1-9	258
Figure A.15	Experimental Frequency Response Functions for Pile C, Tested Along Y Axis, Accelerometer at Position 6, Impact at Positions 1-9	259
Figure A.16	Experimental Frequency Response Functions for Pile C, Tested Along Y Axis, Accelerometer at Position 7, Impact at Positions 1-9	260
Figure A.17	Experimental Frequency Response Functions for Pile C, Tested Along Y Axis, Accelerometer at Position 8, Impact at Positions 1-9	261
Figure A.18	Experimental Frequency Response Functions for Pile C, Tested Along Y Axis, Accelerometer at Position 9, Impact at Positions 1-9	262
Figure C.1	Pile A, Embedded Configuration, Finite Element Mode Shapes 1,2,3,5	274
Figure C.2	Pile A, Embedded Configuration, Finite Element Mode Shapes 5,7,8,10	275
Figure C.3	Pile A, Embedded Configuration, Finite Element Mode Shapes 11,12,13,14	276
Figure C.4	Pile A, Embedded Configuration, Finite Element Mode Shapes 16,17,18,19	277
Figure C.5	Pile A, Embedded Configuration, Finite Element Mode Shapes 20,21,22,25	278
Figure C.6	Pile A, Embedded Configuration, Finite Element Mode Shapes 26,28,29,30	279

Figure C.7	Pile A, Embedded Configuration, Finite Element Mode Shapes 31,33,34,36	280
Figure C.8	Pile A, Embedded Configuration, Finite Element Mode Shapes 37,38,39	281
Figure D.1	Beam on Elastic Supports Idealized as Springs	284

SUMMARY

A comprehensive experimental study was conducted to investigate the suitability of a modal analysis approach for identification of unknown pile embedment lengths. A small-scale pile facility containing partially embedded piles of different lengths, cross section dimensions, and encasement attributes was constructed so that experimental pile response data could be gathered in a controlled laboratory environment. Impact tests were performed at a number of locations on each model pile, and the modal parameters for each were estimated from the resulting frequency response function data.

To supplement the information gathered in the experimental program, three types of numerical analyses were conducted to simulate the frequency response characteristics of the pile-soil systems. Modal parameters corresponding to those computed from the experimental data were produced from each of the three analyses.

Comparison of the modal parameters estimated from model piles with similar cross section dimensions and different buried lengths showed essentially no variation in natural frequency values as the buried length increased, in the frequency range that was practical to measure. Modal damping values showed greater variation with pile embedment depth, but no discernable trends were apparent that would allow identification of the embedded length. Results from the numerical studies indicated the same. It was concluded, then, for reasons

cited in the text, that identification of pile embedment lengths using modal analysis is not a practically feasible task.

CHAPTER I

INTRODUCTION

1.1 Problem Statement

As our nation's infrastructure ages, it becomes increasingly imperative that engineers develop economical and efficient methods for assessing the condition of the large number of existing structures that make up that infrastructure. Several interested agencies, including the Federal Highway Administration (FHWA) and many state transportation departments, have recognized this need and have addressed it by allocating resources for research programs focused on this objective.

One particular area of interest is the nondestructive evaluation of highway bridges. For many years, the primary method of assessing a bridge's condition has consisted of a subjective visual inspection performed by an experienced engineer (Washer, 1998). Although this method has merit, it does not provide a quantitative estimate of the structural condition of a bridge system. Fortunately, new methods have been developed that provide a more objective, comprehensive, and quantitative appraisal of the structural state of various bridge elements. Many of these methods are nondestructive in nature; obviously, this type of testing offers the distinct advantage of allowing inspectors to gather important information without damaging the existing structure and incurring repair costs.

There are still certain aspects of the bridge evaluation process, though, that have yet to be fully refined. One such area is the determination of the tip elevation of piles (or, more simply put, the determination of the length of pile that is buried in the surrounding soil) for bridges whose foundation properties are unknown. According to the FHWA, there are “100,000 bridges [in our country] for which we do not know how deep the foundation piles extend or even, in some cases, whether or not there are piles. Any type of scour or seismic assessment is meaningless without that information.” (Chase and Washer, 1997)

As this statement implies, pile tip elevation is an important parameter—it relates directly to the pile’s capacity, and ultimately to the capacity of the entire bridge. For older bridges whose records no longer exist, for bridges that were not constructed as designed, or for those whose condition has changed over time (perhaps due to scour), there exists a need for the ability to quickly and correctly determine the buried lengths of the existing bridge piles.

1.2 Objective

The objective of this study is to investigate the use of the modal analysis technique (to be described in detail in a later section) to nondestructively determine the embedded lengths of piles for bridges in which that information is not known. Various methods have been developed to accomplish this task for piles whose top surface is exposed and free to be instrumented. However, such piles rarely exist in bridge structures, and the more common case is that the tops of the piles are cast into the bent cap. This lack of access poses a challenging problem, and the research project described herein investigates the use of

flexural waves, induced by striking the piles with a lateral impact, to determine the unknown embedment lengths.

The next section will include an overview of some of the previous research work that has been performed in the area of nondestructive testing, and in the area of pile tip elevation determination in particular. A description of the modal analysis technique as it relates to the objective at hand will be provided in Chapter II, and will be followed by a detailed explanation of the testing procedure, instrumentation, and equipment employed in this investigation in Chapter III. The results of the modal analysis study will be presented and discussed in Chapter IV, and numerical simulations corresponding to the physical testing will be described in Chapter V, along with a theoretical solution that is included for comparison purposes. A study of the wave propagation characteristics of the pile test specimens will be presented in Chapter VI. Chapter VII will contain a discussion of the results and conclusions of the investigation, and will provide suggestions for future research.

1.3 Background and Previous Work

1.3.1 Background

The National Bridge Inventory contains approximately 470,000 bridges (excluding culverts and tunnels), the majority of which are fabricated of steel, followed in number by concrete, prestressed concrete, and timber (Chase and Washer, 1997). Many of the bridges were built shortly following the Great Depression, and another bridge-building “spurt” occurred as the interstate system was being constructed. Unfortunately, approximately

110,000 of those bridges are classified as structurally deficient, meaning that they have “a poor or worse rating for the condition of the deck, superstructure, or substructure” or that their “load-carrying capacity is significantly below minimum standards.” (Chase and Washer, 1997) Of those structurally deficient bridges, 59% are steel bridges, 19% are timber, 18% are concrete, and 3% are prestressed concrete, with the remaining 1% made of other materials such as masonry, iron, and aluminum. It is interesting to note that among deficient steel bridges, less than adequate substructures are more prevalent than poor superstructures or decks. Another alarming fact is that approximately 5000 bridges become deficient each year (Chase and Washer, 1997). It is this growing number of inadequate bridge structures that has prompted the FHWA to sponsor a nondestructive evaluation (NDE) research program, and in fact, they have plans to construct a national center for nondestructive evaluation validation at the Turner Fairbank Highway Research Center.

As stated previously, individual state agencies are also concerned about the condition of their aging bridge structures. For example, according to personnel at the Georgia Department of Transportation, pile tip elevations are unknown for nearly half of Georgia’s 14,500 bridges (Gratton, 1994). Other states have similar statistics, and unfortunately, there are too many instances in which the substandard condition of bridges has led to collapse and loss of life. Some notable examples are the collapse of the Silver Bridge at Point Pleasant, West Virginia in 1967, the snapping of two steel cables on New York’s Brooklyn Bridge in 1982, the 1980 collapse of the Sunshine Skyway Bridge in Tampa after impact by a 609-foot freighter, and the drop of a 100-foot section of the Mianus River Bridge into the water below in 1983 (Hellier, 1995). It becomes more and more obvious that strides must be made

to develop reliable procedures for determining a bridge's structural condition, and subsequently ascertaining it's load-carrying capacity and potential for repair.

1.3.2 Nondestructive Testing Methods for Bridge Piles

The investigation of nondestructive testing methods for metals and for concrete was begun in the 1930's, and by the early 1960's, there was some measure of standardization of the experimental procedures and interpretation of the data (Jones, 1962). By the late 1960's and early 1970's, nondestructive test methods were being readily developed for use in quality control testing of newly-constructed cast-in-place pile foundations (Davis and Dunn, 1974). The great majority of nondestructive testing procedures are based upon the response of the material being tested to the introduction of energy into the specimen in various forms. Some of the most common forms of input are mechanical impacts or electrical pulses that induce stress waves, probes of the material with ultrasonic or electromagnetic waves, penetration of the material with radiation, and magnetic energy infusion (Thomas, 1995). Many excellent references exist in the literature that detail the various methods (Hellier, 1995; Thomas, 1995; Stain, 1982; Olson and Wright, 1989; Rix et al., 1993; Olson and Sack, 1995), and an overview of the nondestructive tests that are most pertinent to pile integrity and length assessment will be presented in the following paragraphs.

Parallel Seismic Method. The parallel seismic test, although nondestructive in nature, is an intrusive evaluation technique. As such, it is more costly and time-consuming than some of the tests that will be described later, but it does have two distinct advantages—it is not affected by soil conditions, and there is no limitation on the depth for which it can gather information (Stain, 1982). The test procedure consists of lowering a hydrophone into a

water-filled, closed-end tube that has been driven into a hole drilled parallel to the pile in question. The hydrophone is lowered to a specified depth, then the pile structure is impacted with an instrumented hammer, as shown in Figure 1.1. A recording is made of the time that it takes the stress wave to reach the hydrophone (both the hydrophone and the hammer are connected to a data acquisition system), then the hydrophone is elevated a specified distance, and the pile structure is again struck with the instrumented hammer. Once again, the travel time for the stress wave to reach the hydrophone is recorded, and the process is repeated incrementally--the results are plotted as a graph of depth against stress wave transit time (Stain, 1982; Davis, 1997). One obvious requirement for the method to work optimally is that the shaft that houses the hydrophone be drilled in very close proximity to the pile specimen, so that the stress wave will have to travel through a minimum thickness of soil to be detected.

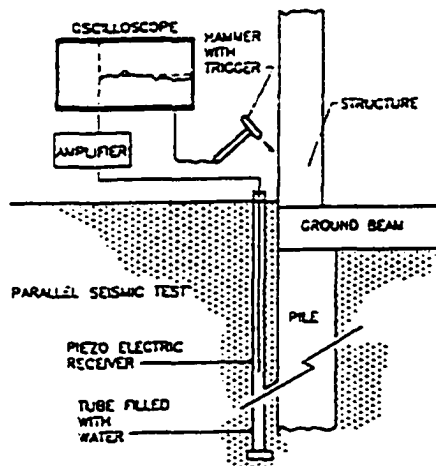


Figure 1.1: Parallel Seismic Test Setup (Davis, 1997)

Figure 1.2 shows the type of plot that is generated in a parallel seismic test. When the hydrophone is raised to a depth above the bottom of the pile, or when it reaches a depth at which there is a defect in the pile, the graph will show a change in the rate of travel time with depth. In Figure 1.2, this is indicated as a change in slope at a depth of approximately 6 meters, indicating the position of the pile toe. One can easily see that this test becomes attractive for its ease of data interpretation. As Stain states, “Although sometimes considered a ‘last resort’ the method is quite sensitive and does have a number of useful applications.” (Stain, 1982)

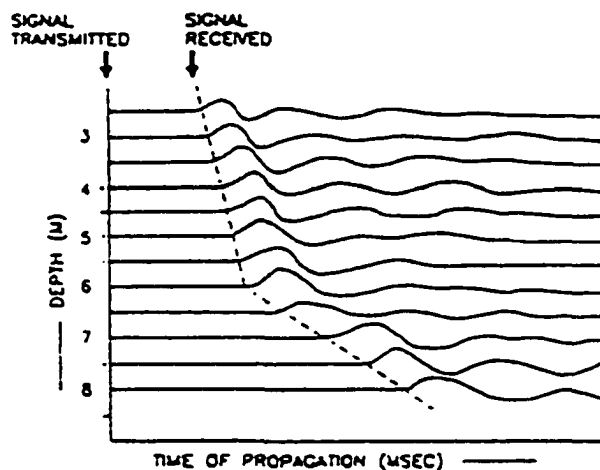


Figure 1.2: Results of Parallel Seismic Test (Davis, 1997)

Sonic Echo Method. The theory behind the sonic echo test method is fairly intuitive, and is based upon measurement of propagation time of longitudinal stress waves in a pile. As

seen in the test setup presented in Figure 1.3, an instrumented hammer is used to strike the top of the pile. This transient force input (measured by the force transducer mounted in the face of the hammer) generates a compressive wave that travels down the length of the pile to a reflector, which could be either the end of the pile, or a defect encountered in the pile material. The wave is then reflected, and it travels back to the top of the pile, where its motion is measured by an accelerometer (displacement and velocity transducers can also be used) mounted to the top surface of the pile. The accelerometer is connected to a data acquisition system, and the acceleration time history is observed to determine the time required for the reflection to return to the top of the shaft. With this information, the depth to the reflector can be calculated according to Equation 1.1:

$$z = \frac{v_c \cdot \Delta t}{2} \quad (1.1)$$

where

z = depth to the reflector,

v_c = compression wave velocity for pile material, and

Δt = travel time of the reflected wave.

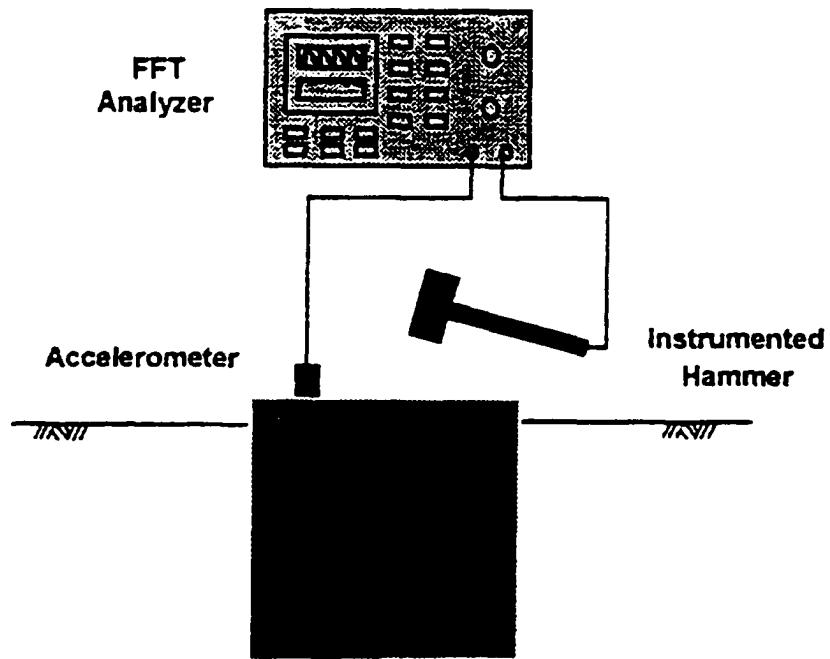


Figure 1.3: Sonic Echo Test Setup

Figure 1.4 shows an acceleration time history recorded at the top of a drilled shaft for the study described by Rix et al. in 1993. Using the reflection observed at 9.47 msec and the compressive wave velocity for the concrete shaft (that had been previously determined), the pile length was easily calculated using Equation 1.1. It is clear that the sonic echo method's simplicity makes it a very attractive nondestructive tool, yet its inherent limitation is also clear—the technique can only be used when the top of the pile under investigation is accessible for testing. Further descriptions of the procedure can be found in the works by Stain, 1982, Olson and Wright, 1989, and Rix et al., 1993, and a description of an early pile

length determination study using the sonic echo method is presented in Alexander's 1980 paper.

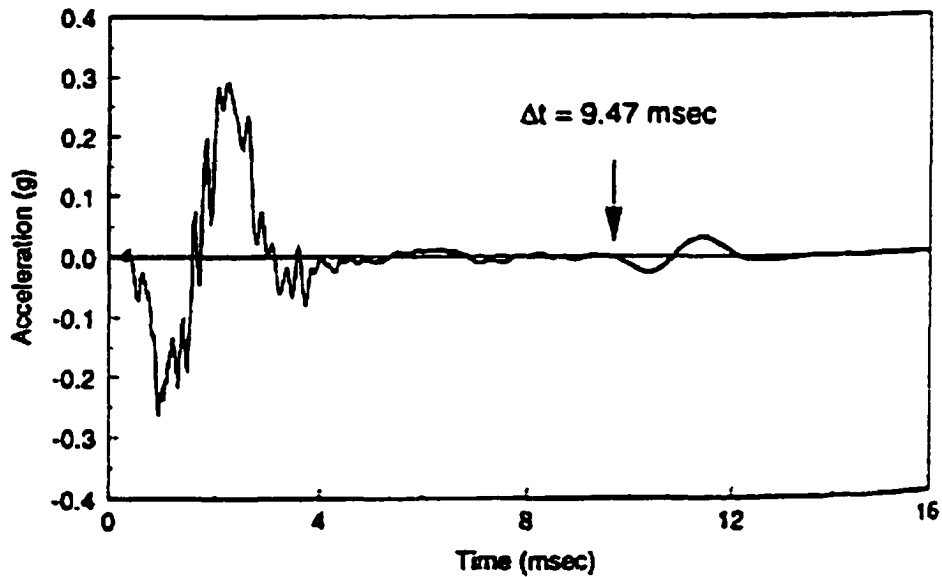


Figure 1.4: Acceleration Time History from Sonic Echo Test (Rix et al., 1993)

Sonic Mobility Method. The testing procedure for the sonic mobility method (sometimes referred to as the transient dynamic response method or the impulse response method) is exactly the same as that for the sonic echo method, but the data is processed in a very different manner. For the sonic mobility test, both the force and acceleration data are transformed into the frequency domain using a Fast Fourier Transform (FFT) analyzer. The results of these transformations are the force spectrum and the acceleration spectrum; the inertance frequency response function (FRF) is defined as the acceleration spectrum divided by the force spectrum. Integration of the acceleration spectrum produces the velocity

spectrum. Dividing this quantity by the force spectrum produces the mobility frequency response function, which is the quantity of interest for the sonic mobility test. Equation 1.2 presents these relationships in mathematical format:

$$\text{Inertance FRF} \equiv \frac{A(f)}{P(f)} \quad (1.2a)$$

$$\text{Mobility FRF} \equiv \frac{V(f)}{P(f)} = \frac{A(f)}{i\omega P(f)} \quad (1.2b)$$

where

$A(f)$ = particle acceleration spectrum,

$P(f)$ = force spectrum of hammer,

$V(f)$ = particle velocity spectrum,

$i = \sqrt{-1}$, and

$\omega = 2\pi f$ = the circular frequency.

The frequency response functions are complex-valued quantities, but usually only the magnitudes are plotted for use in the sonic mobility method.

Figure 1.5 gives a mobility curve for the same shaft investigated in the sonic echo study above, described in Rix et al., 1993. A wealth of information is contained in a plot such as this.

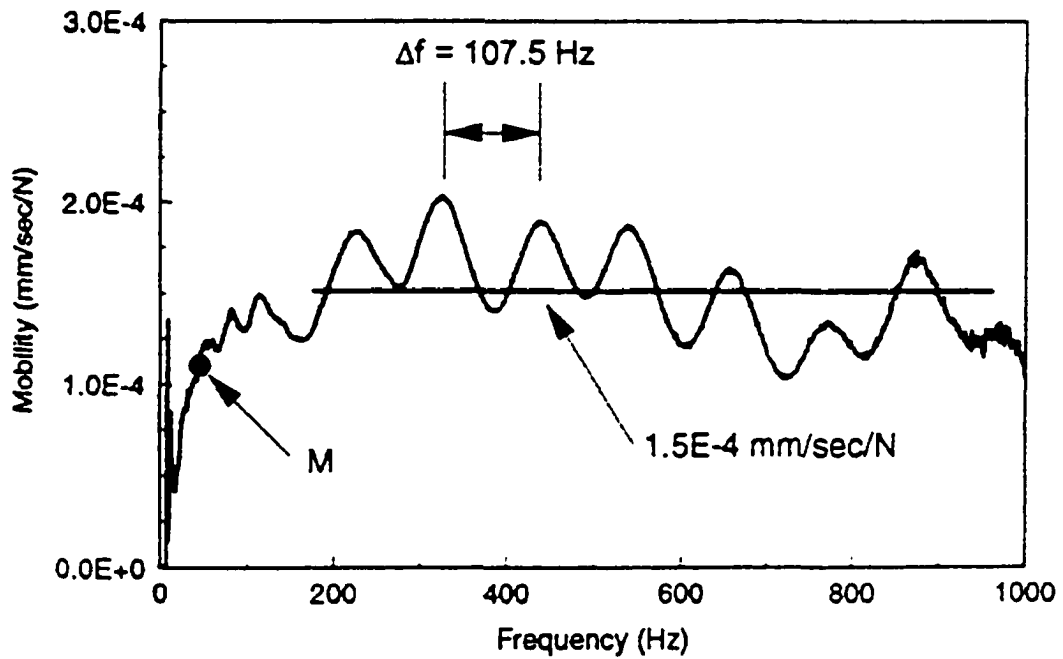


Figure 1.5: Mobility Curve from Sonic Mobility Test (Rix et al., 1993)

One should notice a series of peaks with fairly regular spacing at frequencies above about 200 Hz. These are resonance peaks, and the distance between them, Δf , can be used to determine the length of the shaft (or the depth to any defects) using Equation 1.3:

$$z = \frac{v_c}{2 \cdot \Delta f} \quad (1.3)$$

When the Δf value of 107.5 Hz was used to calculate the shaft length, the result agreed very well with the length calculated using the sonic echo method. However, transformation of the data into the frequency domain made the plotted data much easier to interpret, as is often the case. The same information is present in both plots; it is merely presented in a different, more easily discernable format in the mobility plot. Additionally, as mentioned above, there is more information that can be gathered from the frequency domain data, even though the physical testing procedure is exactly the same as that for the sonic echo method. Of course, this cost-efficient trait makes the sonic mobility method quite appealing.

The horizontal line superimposed on Figure 1.5 indicates the average value of the mobility at higher frequencies, which corresponds inversely to the average impedance of the shaft, as seen in Equation 1.4 below (Stain, 1982; Rix et al., 1993). This value can be used to calculate the average cross-sectional area of the shaft, providing the mass density and compressive wave velocity can be measured or assumed.

$$N = \frac{1}{\rho_c \cdot A_c \cdot v_c} \quad (1.4)$$

where

N = average mobility value at higher frequencies,

ρ_c = mass density of the shaft material, and

A_c = average cross-sectional area of the shaft material.

Another useful parameter that can be determined from the mobility plot is the low-strain stiffness of the pile, taken from the slope of the initial portion of the trace (Stain, 1982; Olson and Wright, 1989; Rix et al., 1993). A convenient point, M, from the low-frequency part of the trace is chosen, and its coordinates are used to calculate the low-strain stiffness as follows:

$$K_{mob} = \frac{2\pi f_M}{\left| \frac{V(f)}{P(f)} \right|_M} \quad (1.5)$$

where

K_{mob} = low-strain stiffness calculated from mobility plot,

f_M = frequency of chosen point on initial portion of curve, and

$\left| \frac{V(f)}{P(f)} \right|_M$ = mobility magnitude at f_M .

The point “M” indicated on Figure 1.5 was used to calculate the low-strain stiffness in the 1993 study by Rix et al. Although the low-strain stiffness is sometimes much greater than the “working load” stiffness because of its low strain level, it can be used as a relative measurement. As noted by the authors, “Once a typical value is established for the shafts at a site, shafts that have stiffnesses that differ significantly from the typical value can be identified as suspect.” (Rix et al., 1993)

In the early days of sonic mobility testing, rather than using an instrumented hammer to produce an impact force on a pile, a mechanical vibrator was often employed to apply a sinusoidal force to the pile. In fact, the testing method used to be called simply “vibration testing” (Davis and Dunn, 1974; Stain, 1982). The vibrator was driven by a sine wave generator capable of delivering sinusoidal signals over a wide range of frequencies. A starting frequency would be chosen, the pile would be vibrated and its response monitored, then the frequency would be changed and the pile vibrated again at the new frequency. This process would be repeated throughout the frequency range of interest until a mobility plot could be produced similar to that shown in Figure 1.5. This method worked well and was especially useful since modern, portable FFT analyzers were not available at the time. The equipment used was quite cumbersome, however, and the time and labor required to perform the test made it a somewhat costly venture. The advent of the portable FFT analyzer, and the realization that a hammer impact would impart a signal containing energy at a wide range of frequencies greatly increased the appeal of the sonic mobility method. Detailed descriptions of the “vibration test method” and its underlying principles can be found in Davis and Dunn, 1974, and Stain, 1982.

Impedance Log Tests. The impedance log method is another nondestructive procedure that makes use of the same physical data gathered in sonic echo and sonic mobility tests. Once again, it is only the data processing technique that differs. Impedance log plots are quite interesting in that they create a “picture” of the pile in question by mathematically manipulating the velocity time data collected at the top of the pile. The basic principle employed is that changes in mechanical impedance along the length of the pile will produce

“reflection coefficients” that can be observed when the velocity time history is processed in a certain manner (Rix et al., 1993). First, a theoretical mobility plot is calculated and plotted for an unflawed, infinitely long pile of the same diameter and subjected to the same surrounding soil conditions as the pile under investigation. Resonance peaks that are apparent in the experimental mobility plot will not appear in the theoretical plot since there are no reflection points present in an infinitely long pile that is free of defects. The lack of reflective surfaces also influences the shape of the theoretical plot, causing it to depend only on the initial impact and the response of the surrounding soil. Next, this theoretical curve is subtracted from the curve produced using the experimental data. The shape of the experimental curve includes the effects of the initial impact, the soil response, and the reflective surfaces, so after subtracting one from the other, what remains is a curve containing only the effect of the reflective surfaces (any defects and the end of the pile). This association is represented by Equation 1.6 (Rix et al., 1993):

$$\left(\frac{V(f)}{P(f)}\right)_{\text{reflected}} = \left(\frac{V(f)}{P(f)}\right)_{\text{experimental}} - \left(\frac{V(f)}{P(f)}\right)_{\text{theoretical}} \quad (1.6)$$

In the next step, the inverse FFT of the reflected curve is calculated, producing the impulse response, or time-domain velocity response of the reflected signal. This represents a time history of the reflections that return to the top of the pile, and is called a “relative reflectogram” (Rix et al., 1993). Reflection coefficients corresponding to changes in the pile impedance along its length are then determined by scaling the relative reflectogram.

Equation 1.7 is subsequently used to backcalculate the impedance as a function of time (Rix et al., 1993):

$$Z(t) = Z(0) \cdot \exp\left[2 \cdot \int R(t) dt\right] \quad (1.7)$$

where

$Z(t)$ = impedance as a function of time,

$Z(0)$ = nominal impedance at the top of the shaft, and

$R(t)$ = reflection coefficients from the scaled relative reflectogram.

Lastly, $Z(t)$ is converted from a function of time to a function of depth, using the compressive wave velocity, to create the impedance log, which is a “map” of the impedance along the depth of the pile. Assuming as before that the mass density and the compressive wave velocity are known, impedance changes that are observed indicate changes in the cross-sectional area of the pile.

Figure 1.6 shows the theoretical and experimental mobility curves for the investigation described by Rix et al. in 1993. Notice the absence of resonance peaks in the theoretical curve. The corresponding impedance log is presented in Figure 1.7. As stated previously, the impedance log takes a sort of “mathematical picture” of a cross section of the pile. One can observe from the figure that the actual diameter of the shaft was larger than the reported nominal diameter. After discovering this situation, field notes taken during construction were checked, and it was discovered that the actual diameter shown in the impedance log was consistent with the volume of concrete poured.

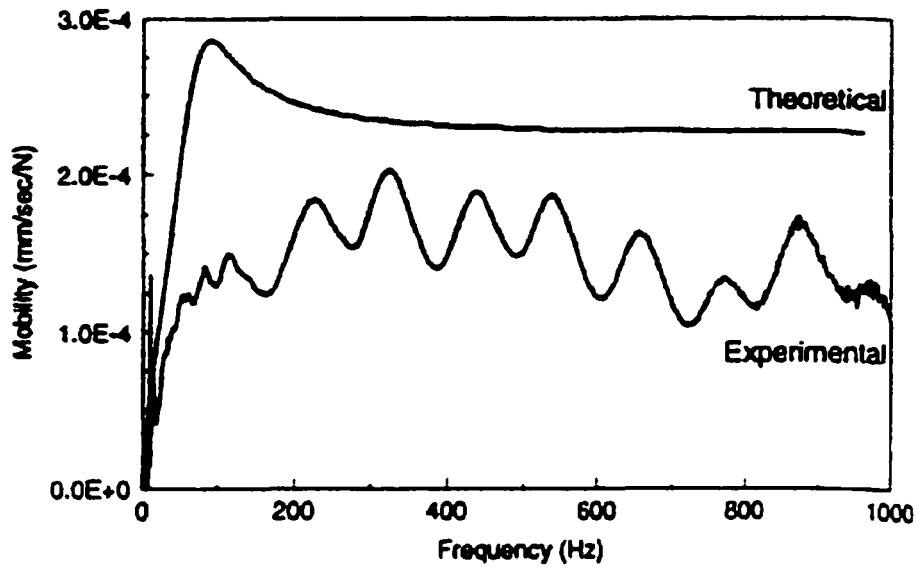


Figure 1.6: Experimental and Theoretical Mobility Curves (Rix et al., 1993)

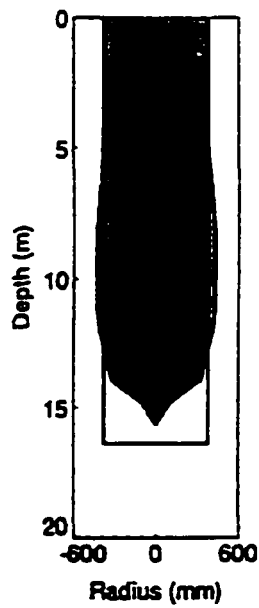


Figure 1.7: Impedance Log (Rix et al., 1993)

The impedance log is very useful for indicating the presence of bulbs or reductions in diameter along the length of a pile, and perhaps its greatest value stems from the fact that it can be produced from the data that has already been collected for a sonic mobility test. A thorough explanation of this method is detailed in Rix et al., 1993, from which this summary was assembled. Another example of the use of impedance logs as a nondestructive tool is given in Davis's 1997 paper.

Velocity Reflector Method. One nondestructive method that has received scant mention in the literature, but that seems worthy of further investigation, is the velocity reflector method. The actual testing procedure for this method is the same as for the sonic echo and sonic mobility tests, but a different data-processing operation is employed. Raw velocity-time data is subjected to the FFT routine two times in succession "to produce a plot of the most significant stress wave velocity reflectors encountered down the pile shaft." (Davis, 1997) The one plot that Davis shows to illustrate this method contains a single strong peak corresponding to the pile toe depth-- he claims that this was the most successful method of several that he tried to determine pile tip elevations.

Considering the various advantages and disadvantages of each of the tests described above makes it clear that Stain's remarks of 1982 are still very appropriate today: "The old saying 'there are horses for courses' applies equally to integrity tests and the engineer with an appreciation of the different techniques will be able to select an appropriate programme (sic) which might well include more than one type of test." (Stain, 1982)

1.3.3 Recent Studies of Pile Integrity Assessment and Length Determination

Each of the last four nondestructive test methods described above was initially developed for piles whose top surfaces are exposed and free to be impacted and instrumented. The parallel seismic method does not bear this limitation, but it is intrusive and costly as mentioned before. Three relatively recent studies have been performed concerning nonintrusive pile integrity assessment and length determination for those piles with inaccessible top surfaces. These three studies, two of which deal with timber piles, and one that deals with concrete drilled shafts, will be briefly summarized below.

Finno described a study on a test section at the National Geotechnical Experimentation Site at Northwestern University containing five drilled shafts of varying lengths and diameters (Finno, 1997). He evaluated the capabilities of using the sonic mobility method (referred to in Finno's work as the impulse response method) to determine integrity of piles both without pile caps (accessible-head condition), and with pile caps (inaccessible-head condition). For the accessible-head condition, he impacted the top of the shaft with an instrumented hammer and measured particle velocity with a geophone on the same surface. After completion of the accessible-head tests, reinforced concrete pile caps were poured, and similar tests were conducted from the tops of the pile caps.

In his discussion of the sonic mobility method, Finno stated, "Because of a shaft's cylindrical shape, elastic theory indicates that a prismatic deep foundation has a constant frequency spacing between resonant peaks that is a function of the shaft length and propagating wave velocity, if the induced wave lengths are greater than the diameter of the shaft [i.e. Equation 1.3]." He went on to say that resolution of sonic mobility signals can be

defined in terms of the relative heights of the resonance peaks and valleys in the mobility plot, mentioning that “[h]igher signal resolution makes the resonant peaks easier to distinguish, and thus makes it easier to interpret pile length and location of apparent anomalies.”

The presence of the pile cap for the inaccessible-head tests created two notable effects on the mobility plots. First, the average mobility and the resolution both decreased, which Finno attributed to the increased mass of the pile cap, which forms an impedance change at the juncture of the shaft and the pile cap. He stated that this impedance difference “causes an incident wave to reflect, resulting in less energy being transmitted down the shaft.”

The second observable effect of the pile cap was a marked change in shape of the mobility plot. Rather than the constant magnitude of resonance peaks and valleys that appear in the accessible-head plots, the inaccessible-head plots contained “peaks which follow an exponentially decreasing trend in the lower frequency region.” Finno suggested that this discrepancy should be attributed to the fact that the pile caps transform the one-dimensional wave propagation response of an isolated drilled shaft to a more three-dimensional wave propagation response for the shaft/pile cap system. He noted that at higher frequencies, the wavelengths might not be greater than the dimensions of the pile cap, thus invalidating the use of one-dimensional wave theory.

This notion led Finno to determine a “cutoff” frequency for the inaccessible-head tests, above which no reliable information could be ascertained concerning an underlying drilled shaft. From a comparison of experimentally-derived mobility curves to mobility curves obtained from numerical simulation of the inaccessible-head tests, Finno was able to

identify cutoff frequencies by observing “where the *trends* of an experimental mobility curve diverge from the corresponding simulated curve, since the simulation is based on one-dimensional wave propagation which does not consider surface wave or three dimensional effects.” He then used the cutoff frequencies observed for the various shaft and pile cap dimensions to develop empirical relationships for the cutoff frequency “based on geometric relations and the idea that one-dimensional conditions are satisfied when the wavelength is greater than or equal to the diameter of the shaft.” His proposed relation is given below:

$$f_c = \frac{v_c}{\lambda_c} \approx \frac{v_c}{D_{eff}} = \frac{v_c}{D(\alpha_s + \alpha_t)} \quad (1.8)$$

where

f_c = cutoff frequency,

v_c = compressive wave velocity,

λ_c = wavelength at which wave propagation in a cylindrical rod is no longer one dimensional,

D_{eff} = effective diameter of pile cap/shaft system,

D = diameter of the shaft,

α_s = factor to account for the plan area of the pile cap relative to the area of the shaft,

and

α_t = factor to account for the relative thickness of the pile cap.

α_s and α_t are defined as follows:

$$\alpha_s = \frac{A_{eff}}{\left(\frac{\pi D^2}{4}\right)} \quad (1.9)$$

where

A_{eff} = effective area of the pile cap.

$$\alpha_t = \left(1 + \frac{B}{D}\right) \quad (1.10)$$

where

B = thickness of the pile cap.

It can be observed from the above relations that as the ratio of the pile cap tributary area to the shaft area increases, the effective diameter of the shaft increases because of the increase in α_s . This, in turn, causes the cutoff frequency to approach zero. Finno pointed out that as the cutoff frequency becomes small, three-dimensional effects begin to mask resonances from the toe of the shaft. He stated that α_s is usually larger than α_t and therefore has a greater effect on the cutoff frequency.

Finno concluded that the sonic mobility method can indeed be used to assess the integrity of drilled shafts with inaccessible heads if the geometry of the shaft/pile cap

system does not violate one-dimensional wave propagation conditions. He did recognize, however, that certain factors could limit the overall applicability of the method, including the length-to-diameter ratio of the shaft, the soil stratigraphy, and the shear wave velocity of the soil.

Holt et al. (1994) examined the properties of dispersive stress wave propagation to determine the lengths of in-service timber piles. Dispersion is a wave phenomenon that occurs when different frequencies in a signal travel at different velocities, and flexural waves created by a transverse impact on a bounded medium (such as a bridge pile) are dispersive in nature. The authors used a mathematical technique called the Short Kernel Method (SKM) (developed by Douglas in a previous study of layered media (Douglas and Eller, 1986; Eddy, 1988; Douglas et al., 1989) to process the dispersive flexural waves induced on timber piles to determine their overall length.

Holt et al. stated that the Fourier transform technique has traditionally been employed in the signal analysis of dispersive waves, but they contend that it is not well suited for this purpose because of its inability to distinguish between multiples of the period corresponding to a particular frequency. In the Fourier transform method, relative phase angles are computed for individual frequencies between two measurement points and used to calculate the time required for the frequencies to traverse the measured distance. Velocity can be determined from this information, but according to Holt et al., "it is not possible to tell whether the computed phase is the actual value or whether the actual value is the computed value plus some integer multiple of the frequency's period." (Holt et al., 1994) The authors reported that the Short Kernel Method overcomes this limitation successfully.

Figure 1.8 is an illustration of the test setup Holt et al. used in their investigation. As shown in the figure, timber piles were impacted transversely, rather than longitudinally, and accelerometers were spaced at pre-defined points along the exposed length of the pile. The transverse impact created flexural waves, in contrast to all of the methods described earlier, which made use of axial waves.

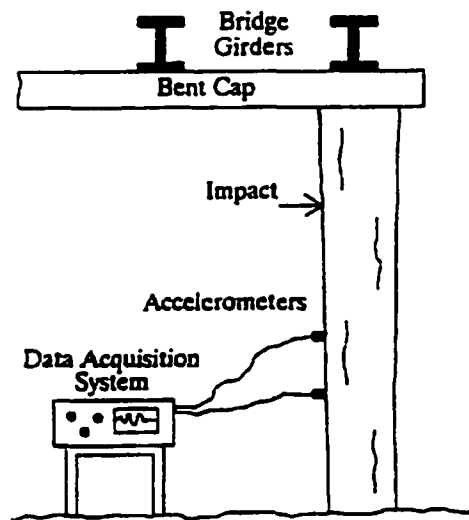


Figure 1.8: Field-Test Setup used by Holt et al. (Holt et al., 1994)

The authors mention that if bending waves were not dispersive, the data processing required would be similar to that of the sonic echo or sonic mobility methods, where wave speeds could be calculated simply from observation of the times at which the waves passed by the two accelerometers. However, dispersive waves continually change form as they travel, and tracking an individual dispersive wave becomes a daunting process considering the many reflections that are present after the pile is impacted. Holt et al. state that a

dispersive wave must be separated into its harmonic components to correctly distinguish the phase velocities of its different frequencies, and that there are two methods to do so: the Fourier phase method and the Short Kernel Method. The authors chose to use the SKM for their investigation.

The Short Kernel Method is based on the cross-correlation procedure detailed by Bendat and Piersol (1980). Equation 1.11 gives the mathematical expression for a single value of the SKM at a particular frequency:

$$\text{SKM}(j, k) = \sum_{i=1}^{N_2-N_1} f(\tau_i) \cdot g[(\tau_i + j \cdot \Delta t), k] \cdot \Delta t \quad (1.11)$$

where

$\text{SKM}(j, k) = j^{\text{th}}$ term of the cross-correlation currently being performed at the k^{th} frequency,

f = time record from one accelerometer,

g = fragment of kernel used to perform the cross-correlation,

N_2 = number of data points in f ,

N_1 = number of data points in g , and

Δt = time step between data points.

Olson et al. (1995) summarized the principles of the SKM in the following manner:

The method is similar to narrow band cross-correlation procedures between the input (the hammer blow) and the output (receiver response(s)). However, instead of measuring the hammer blow, a periodic function of 1 or more cycles

is used as the “Kernel Seed,” and a number of seeds for frequencies ranging from 500 to 4000 Hz may be cross-correlated with the receiver responses. The SKM correlation procedure amplifies bending wave energy responses with the selected seed frequency and in a way bandpass filters the response data since frequencies higher and lower than the seed frequency are filtered out. Two receivers are used in order to measure the bending wave velocity (distance divided by elapsed time between the bending wave arrival peaks) between them as determined from the peak responses in the cross-correlated data of the two receivers. The use of two receivers also allows one to determine whether the reflections of the bending wave energy are traveling back up the pile after reflection from the pile bottom, or if the bending wave energy is traveling back down the pile after reflection from the pile top or beam. This is identical to the procedures used in Sonic Echo tests when two receivers are used. The dispersion of the bending wave velocity is thus accounted for by calculating the bending wave velocity for each kernel seed frequency.

Figures 1.9 and 1.10, taken from the study by Holt et al., give a visual description of the use of the SKM. Figure 1.9 shows the acceleration time histories of the two accelerometers before application of the SKM (the top trace is from the accelerometer closest to the pile head, while the bottom trace is from the accelerometer closest to the ground surface). The authors state that regions A and A' record the first passage of the wave that travels downward from the impact location, regions B and B' record the wave that first traveled upward from the impact, was reflected from the pile head/bent cap juncture, then traveled downward through the accelerometer locations, and regions C and C' are the reflection from the pile toe of the wave that was first recorded in regions A and A'.

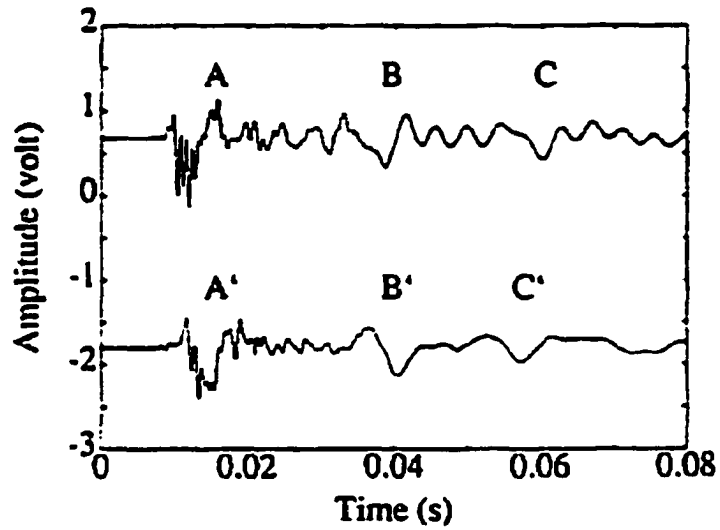


Figure 1.9: Time Records from Two Accelerometers (Holt et al., 1994)

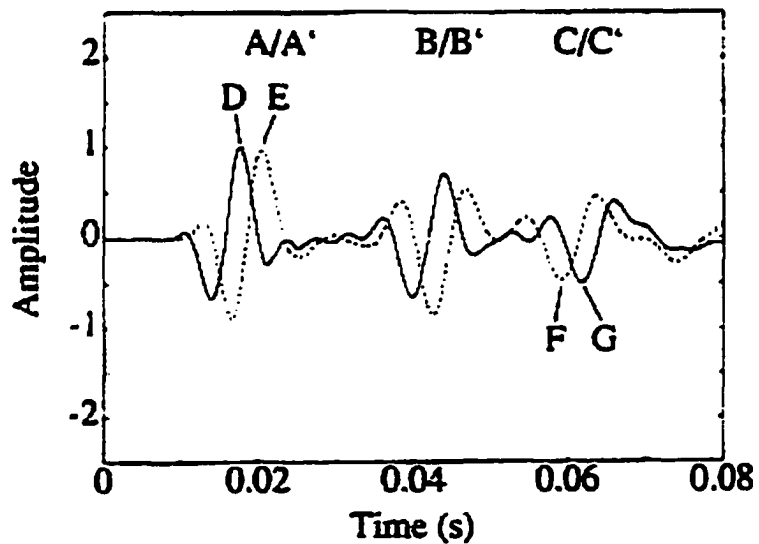


Figure 1.10: SKM Plot Using a 1-cycle 500-Hz Kernel (Holt et al., 1994)

In Figure 1.10, the signals have been processed by the SKM, assuming a 1-cycle 500 Hz kernel; the solid line represents the top accelerometer and the dotted line represents the

bottom accelerometer. Holt et al. stated that “the SKM has acted as a ‘sieve,’ in that it extracted the 500-Hz component from the signals and displayed its approximate location inside both time records.” (Holt et al., 1994)

The time difference between Points D and E of Figure 1.10 is divided into the accelerometer spacing to calculate the phase velocity. This quantity is then used to determine the pile length using Point F or G, which represent “the return of the 500-Hz frequency from the pile toe,” identified by noticing that the trace from the bottom accelerometer (dotted line) leads the trace of the top accelerometer (solid line) at these points. The pile length can be determined using the time difference between Points D and G (or E and F) and the velocity that was computed previously. Equation 1.12 details the calculation:

$$OL = T_b + \frac{C_p \cdot Npts \cdot \Delta t}{2} \quad (1.12)$$

where

OL = overall pile length,

T_b = distance from pile head to accelerometer being used for calculation,

C_p = computed phase velocity,

$Npts$ = number of data points between Points D and G (or E and F), and

Δt = acceleration trace time step.

The authors were careful to note that:

In choosing the negative peaks F and G in Figure [1.10], the assumption was made that the 500-Hz component reverses its algebraic sign once it is reflected from the pile toe. This may not always be the case; sign reversal is possibly dependent upon the degree of confinement of the embedded portion of the pile. Both assumptions were made during the analysis and a range of lengths [was] reported.

In all, Holt et al. tested 40 piles, 14 of which could not be analyzed “either because of bad signals, because no return wave was found in their time records, or the pile’s records were not clear enough for identification.” For the remaining 26 piles, the percent difference obtained between lengths computed with the SKM and those obtained from installation records or from direct measurement of piles that were pulled ranged from -11.8 percent to $+8.5$ percent. Although these results indicate that the SKM was a relatively successful tool for determining in-place timber pile lengths, it does have some notable limitations. The fact that it is based on observation of peaks and valleys in time-domain waveforms makes it somewhat subjective and imprecise in nature, especially for situations in which the waveforms are visually complex. Olson et al. (1995) expressed this shortcoming by commenting that it can be very difficult to identify propagation paths of flexural waves, especially if there are several reflecting boundaries such as the pile top, the groundline, pile defects, etc. Also, it is sometimes difficult to impact the piles in such a way as to produce recognizable signals, as evidenced by the 14 piles in this study that could not be analyzed. As stated, though, the method was somewhat successful for length determination in timber piles.

Pandey et al. (1998) described the use of a longitudinal stress wave technique to determine the length of in-place timber piles, with the ultimate goal of calculating the scour resistance of timber bridges. The authors reported that longitudinal stress waves, produced by a hammer impact, travel along the length of a timber pile at a velocity that depends on pile density, moisture content, and material quality. They further stated that, “[t]o adapt the NDE [nondestructive evaluation] technique for pile length determination, modifications to existing impact methods and sensor attachments were necessary, coupled with further testing on piles of known lengths.”

Figure 1.11 shows the test setup used in the study; the impacting modification is clear from the figure. Instead of striking the pile directly, a lag bolt was inserted into the pile at a 45 degree angle, and the lag bolt was struck with the instrumented hammer. According to the authors, this impact arrangement induced a wave in the pile that had enough energy in the longitudinal direction to be considered a longitudinal wave. The length determination was then evaluated by measuring the time required for the wave to travel to the base of the pile and be reflected back along the pile length. This time, coupled with the stress wave velocity, was used to calculate the length of the piles. The authors report that the accuracy of their length determinations was ± 15 percent. This method, then, seems to work reasonably well for timber piles, but its applicability to piles of other types is unknown.

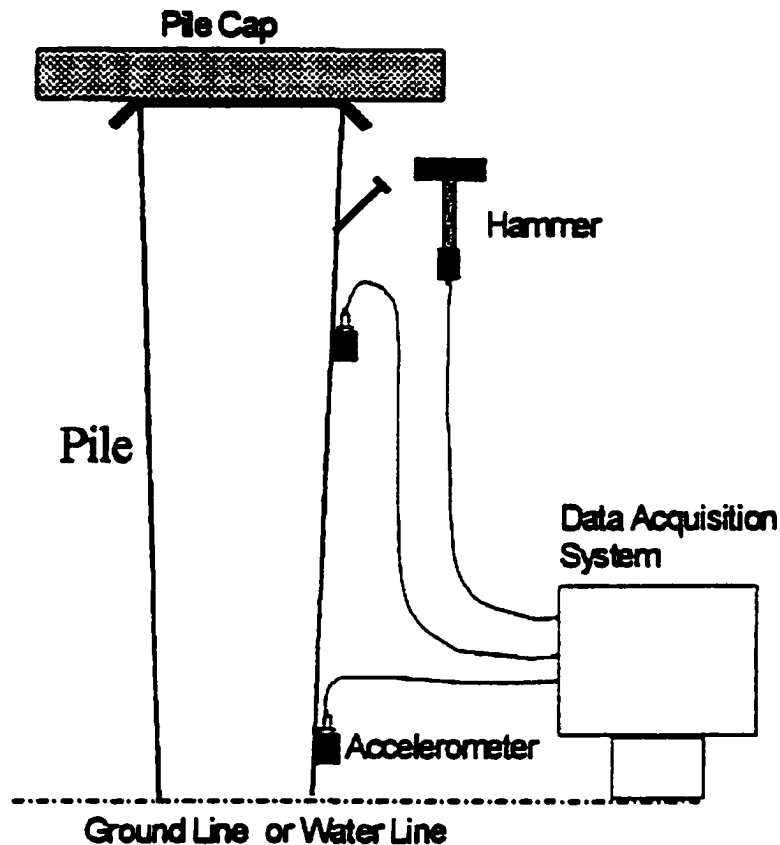


Figure 1.11: Setup for Pile Length Data Collection Used by Pandey et al. (Pandey et al., 1998)

1.3.4 Modal Analysis for Structural Identification

Modal analysis is a technique that employs results from the measurement of the vibration behavior of a structural system to aid in identification of the system characteristics that govern that behavior. This approach possesses several advantages over its predecessors for the pile length determination problem, making it attractive for use in this arena. First, it is well-suited to the systematic examination of impact data, which is easily measured,

recorded, and stored, even in typical field conditions. Also, the analysis process is easily implemented for flexural data, collected as a result of a transverse impact on the pile, so that access to the top of the pile is not required. Additionally, and most importantly, the unknown embedment length problem seems a prime candidate for solution via modal analysis techniques because all of the properties of the pile-soil system are known or can be well-characterized, except for one—the embedded length of the pile. The modal parameters (natural frequency, damping, and mode shapes) of a structural system can be expressed as a mathematical combination of its physical traits, so that if one of the properties (such as the embedded length of a pile) changes, the modal parameters should change accordingly. The modal analysis approach, whose hallmark is the identification of the modal parameters of a system, lends itself well to isolation of the unknown property, since once the modal parameters are known, the unknown trait can be backcalculated from them. Finally, an additional advantage of the use of modal analysis for the pile length determination study is that it relies not on the subjective visual identification of graphical trends (as is the case for many of the techniques previously employed to address this problem), but on an objective analysis of the measured data. A much more detailed discussion of modal analysis and the theories governing its development, as well as its suitability for the pile length determination problem will be presented in Chapter III.

Although no previous studies have been performed on the use of the modal analysis technique with flexural waves for length determination of in-place piles (to the author's knowledge), several papers do exist in the literature that describe the use of this technique for other types of structural identification purposes. Summaries of a selected few of these

publications will be outlined in Chapter III; as stated above, it will also contain a detailed description of the modal analysis technique as it relates to the objectives of the study described in this report.

CHAPTER II

TEST CONFIGURATION

2.1 Small-Scale Pile Facility

A small-scale pile facility was constructed in the Civil Engineering Laboratories Building on the Georgia Institute of Technology campus so that experimental pile response data could be gathered in a controlled laboratory environment. A concrete pit measuring 12 ft long by 9 ft wide by 5 ft deep comprised the “embedment” portion of the facility; the lower 4.5 ft of the pit was located beneath the surface of the floor, while the remaining 6 in. extended above the floor and formed a “rim” surrounding the test fixture. Figure 2.1 shows a photograph of the test fixture, while end and plan views of the apparatus are illustrated in Figures 2.2 and 2.3.

As seen in the figures, two vertical steel channel sections (C9x13.4) were bolted to the rim of the pit on both of the 9-ft sides. Two horizontal W10x45 sections, having plates welded to each end, ran parallel to the 12-ft sides, and the plates were bolted to the top portion of the channel sections at either end of the pit. The horizontal W10x45 sections were positioned such that the web assumed a vertical orientation, and the bottom flange of each section was suspended 5 ft above the rim of the pit. Two 3 ft x 2 ft x 1 in thick plates were bolted to the bottom flanges of both W10x45 members, spanning the gap between

them. To further stiffen the test frame, two 2.5 in. thick plates were welded along the length of the top flange of the W10x45 members, then four S3x5.7 sections were welded at angles above the plates, as shown in Figure 2.3. Additional angled bracing was provided near the bottom of the fixture as shown in Figures 2.1 and 2.2. Once the frame was fully assembled, the flanges of five vertical model pile sections were welded to the outside flange edges of each of the two W10x45 horizontal sections, resulting in a total of ten test specimens. One pile was tested in this condition (without soil; details of the test procedure will be outlined in Chapter IV), then the pit was filled with Chattahoochee River Sand (to be fully described later in this chapter) and all the piles were tested in the embedded configuration.

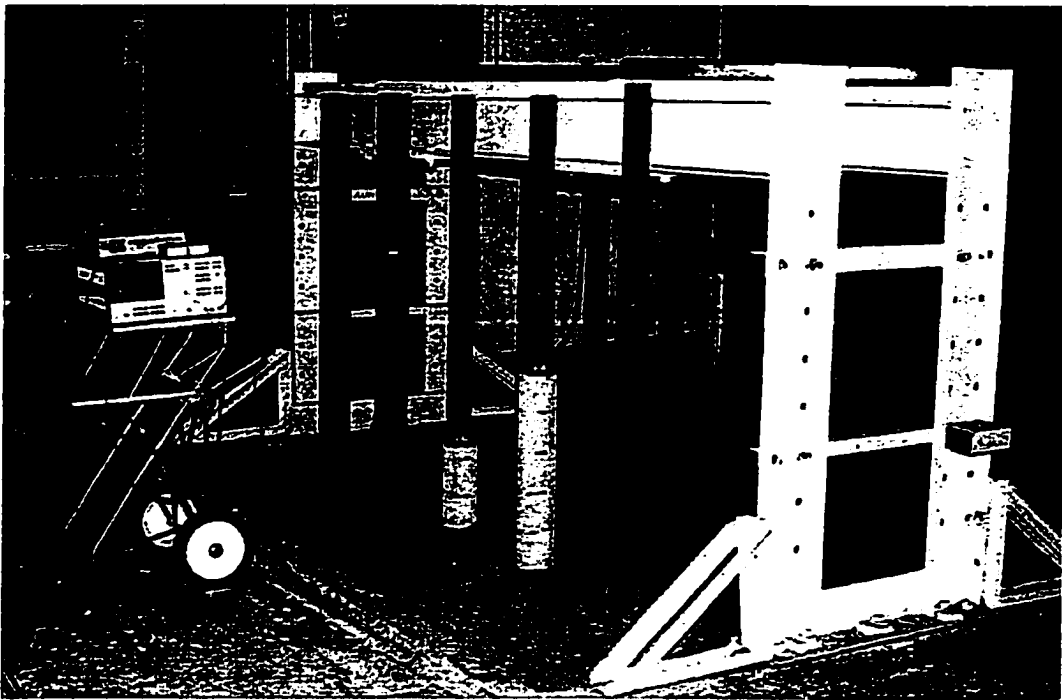


Figure 2.1 Experimental Facility for Testing Small-Scale Piles

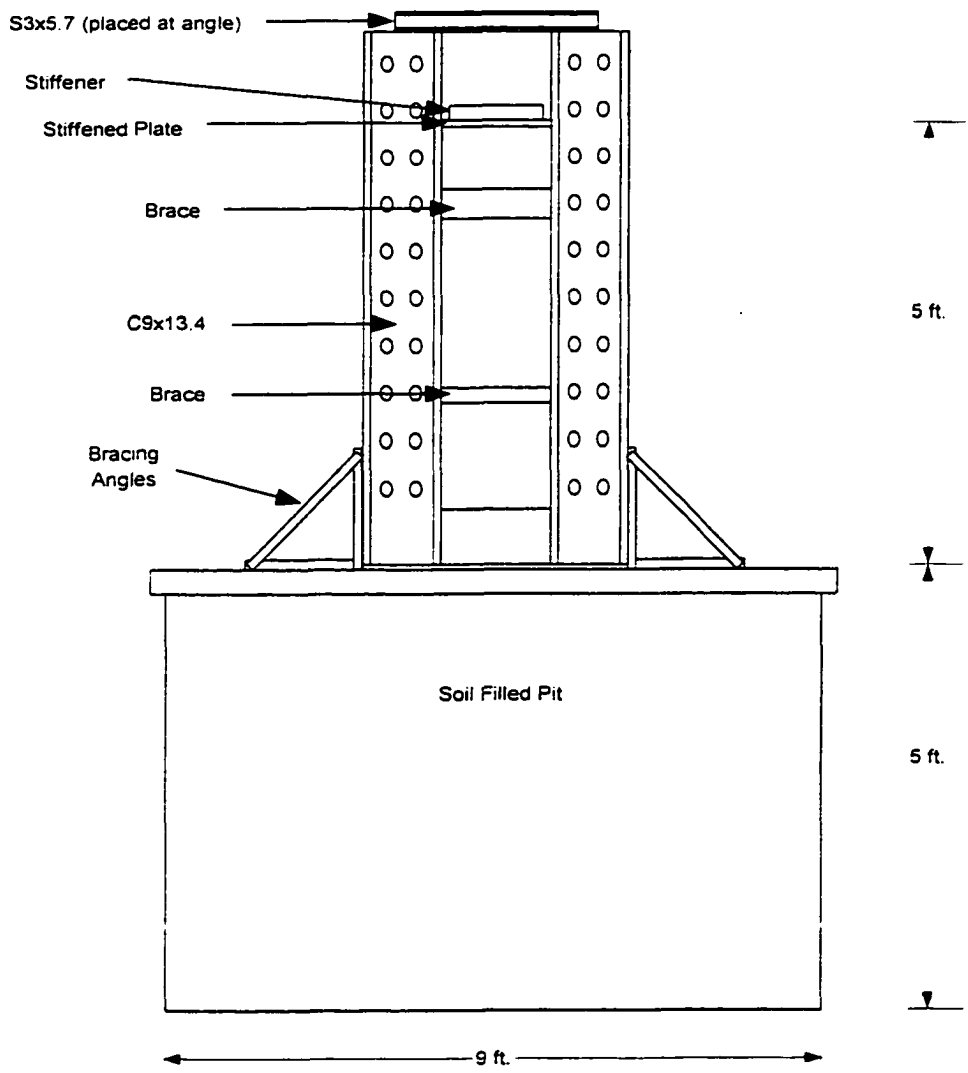


Figure 2.2 End View of Experimental Facility for Testing Small-Scale Piles

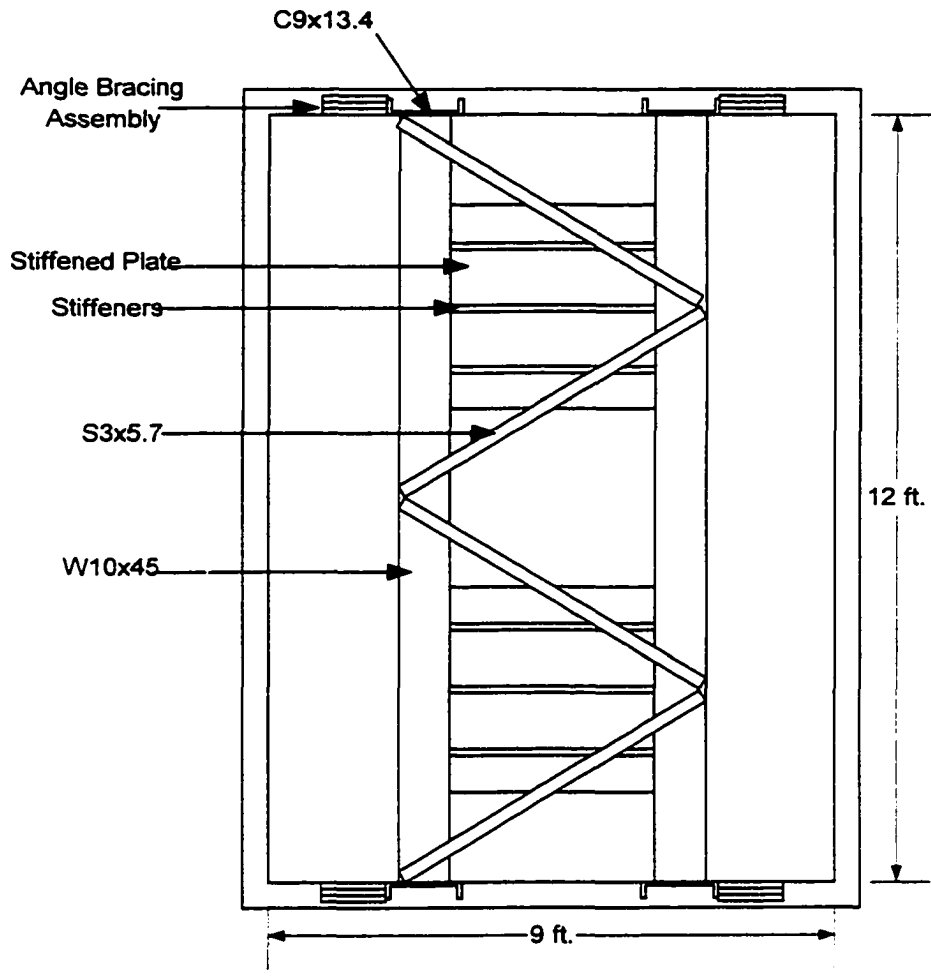


Figure 2.3 Plan View of Experimental Facility for Testing Small-Scale Piles

2.2 Test Pile Sections

Pile sections chosen for laboratory testing were selected based on bridge design information provided by personnel at the Georgia Department of Transportation (DOT) (Gratton, 1994). They indicated that a typical steel H pile section is an HP12x53 measuring

15 to 60 ft in length, with a concrete casement from the groundline to 2 ft above the waterline. These dimensions yield an average ratio of length to section depth (L/D) of 37.5. The test piles ranged in length from 6 ft to 10 ft, with an average of 8 ft. To determine the optimum model pile section depth, this 8-ft average length was divided by the L/D ratio of 37.5, yielding an ideal value of 2.6 in. Based on that dimension, S3x5.7 sections were chosen for the representative test pile sections. Two W4x13.0 sections were also included to determine the effect of section size on the pile length evaluation method being developed.

Figure 2.4 shows right and left elevations of the test facility and the arrangement of the test piles within the pit. As stated previously, all piles were welded to the outer flange edges of the W10x45 sections, and all had exposed lengths of 5 ft. Piles A through E, as designated in the figure, were S3x5.7 sections with embedment lengths of 1 ft for Pile A to 5 ft for Pile E, increasing in 1 ft increments. Pile F, an S3x5.7 section that rested on the concrete pit bottom to simulate an end-bearing pile, was included to examine the influence of a “fixed” end condition on pile response, as opposed to the response of the floating end condition of Piles A through E. Piles G and H were S3x5.7 sections of length 9 ft and 7 ft, respectively, and each had a 6-in diameter concrete casing surrounding the portion of the pile just above the groundline, as shown in the figure. Casings such as these are sometimes used on bridges to protect steel sections from corrosion, and they were included in the test series to investigate their effects on pile response. As mentioned before, two W4x13 sections, Piles I and J, were included to distinguish their response from that of the smaller S3x5.7 piles of the same lengths (Piles B and D).

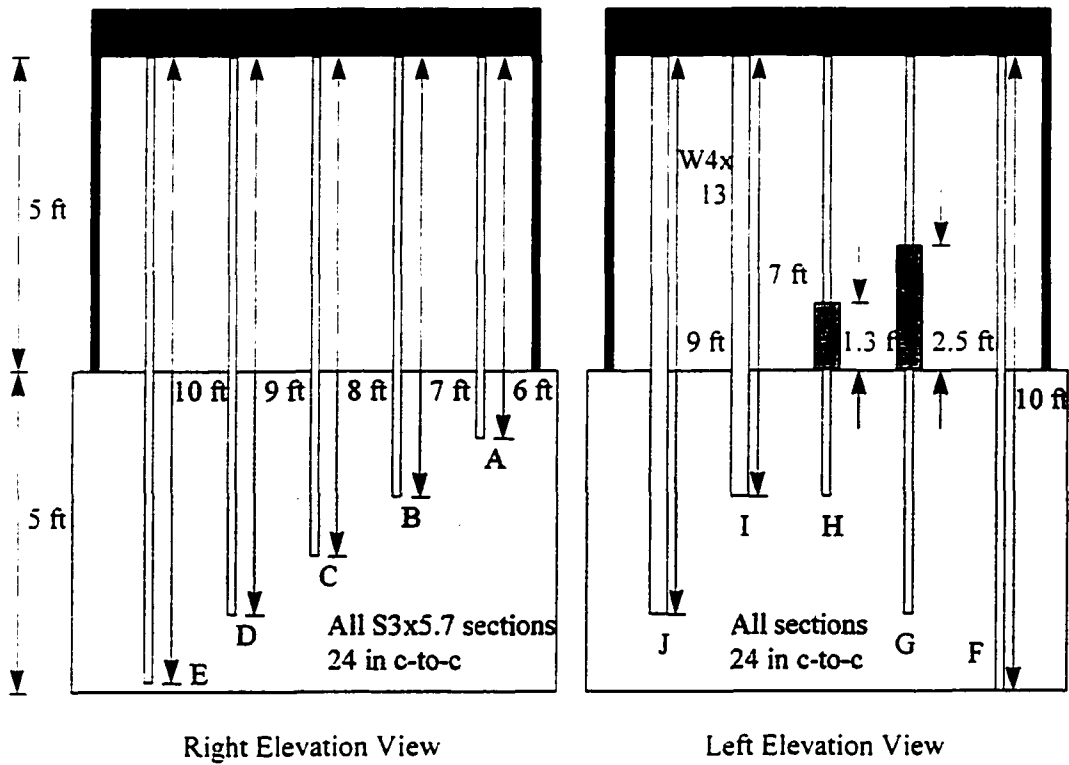


Figure 2.4 Elevation Views of Small-Scale Pile Test Facility

2.3 Soil Properties

2.3.1 Sand Fill

The soil used for embedment of the model pile sections was a Chattahoochee River Sand which was visually classified as a white-tan, medium to fine, poorly graded, micaceous sand (SP). Figure 2.5 shows the grain size distribution for the sand.

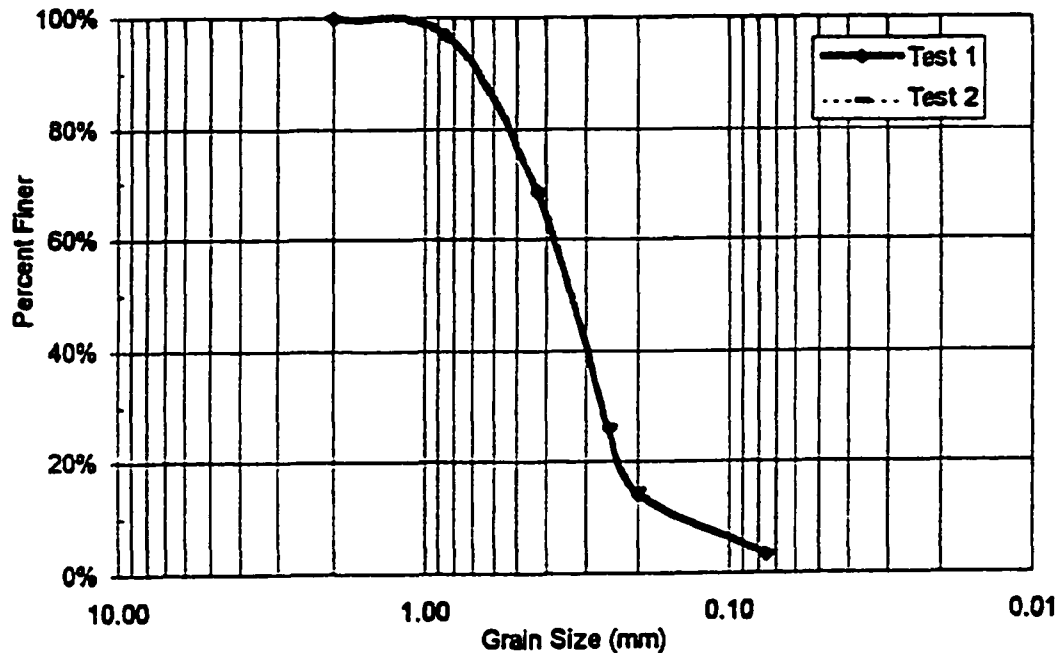


Figure 2.5 Grain Size Distribution for Chattahoochee River Sand

The sand's maximum dry density was obtained according to ASTM D 4253-93 (ASTM, 1993), with the average value of six tests computed as 98.6 pcf. ASTM D 4254-91 (ASTM, 1991) was used to determine the minimum dry density; its average value was found to be 80.8 pcf (three tests were performed using Method A and three using Method B of this standard).

2.3.2 Sand Placement

The sand was placed into the pit in 6-in. lifts, and compacted with a Wacker Corporation vibratory plate compactor having a plate size of approximately 18 inches square. This small plate size allowed the operator to carefully maneuver around the test piles to ensure uniform

compaction. Lifts were compacted to greater than 95 percent of the maximum dry density; density control tests were performed with a nuclear moisture-density gauge. It should be noted that rather than driving the piles, as would normally be done in the field, the sand was compacted around pre-placed piles for the embedded tests, so that “perfect insertion” was the method used to embed the piles.

2.4 Equipment and Instrumentation

2.4.1 Impact Hammer

Figure 2.6 shows a schematic of the general test setup used to collect experimental pile response data on the small-scale model piles. The hammer used to impart a lateral impact to the piles was a PCB Piezotronics, Inc. Model 086C03 modally tuned impact hammer with a built-in force transducer. Force transducers detect the magnitude of the force felt by the hammer, which is assumed to be equal and opposite to that felt by the test specimen (Ewins, 1985). Figure 2.7 is an illustration showing the significant parts of a typical impact hammer.

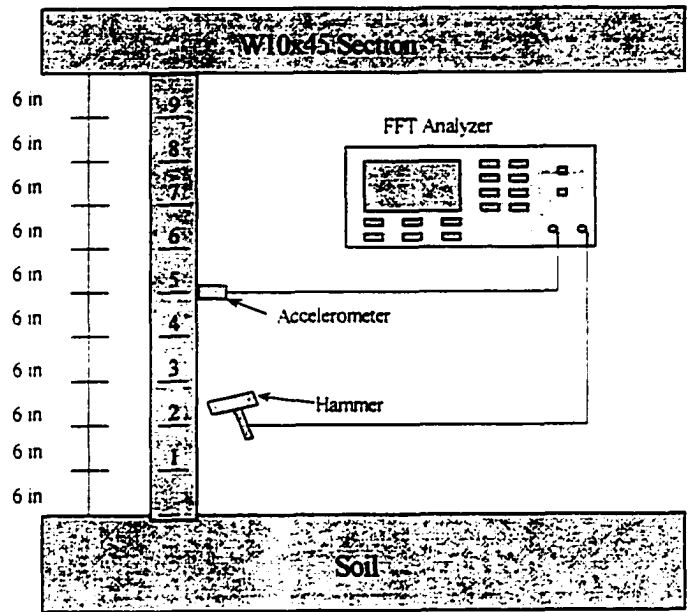


Figure 2.6 Schematic of Test Setup and Equipment

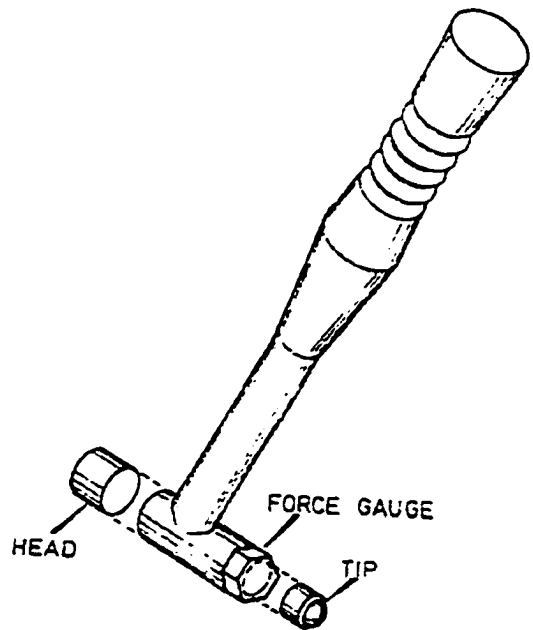


Figure 2.7 Impact Hammer Details (Ewins, 1985)

The PCB hammer used for the present tests measured 8 inches in length, with a head diameter of 0.6 in and a tip diameter of 0.25 in, and its nominal sensitivity was 10 mV/lbf.

A photograph of the hammer is presented in Figure 2.8.

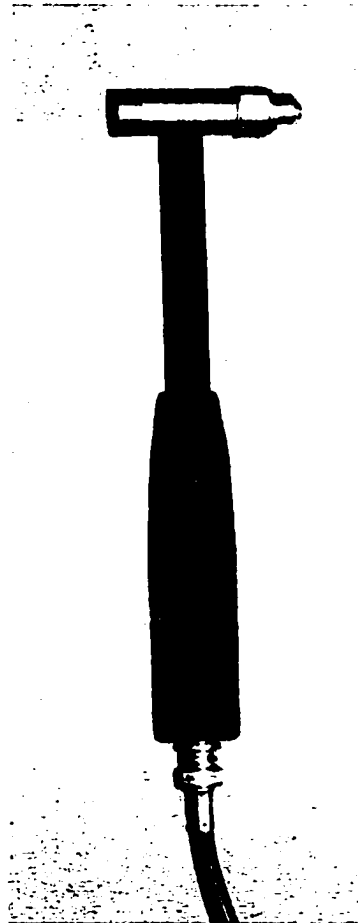


Figure 2.8 Impact Hammer Used for Model Pile Tests

Three interchangeable hammer tips were included with the hammer: one rubber tip, one hard plastic tip, and one metal tip were available. Each tip excites a different frequency range on impact; for the model pile tests the metal tip was used because of its ability to excite higher frequencies than the others. Figure 2.9 shows the general shape of the impact force vs. time curves and the frequency spectra for the three available hammer tips (this figure was taken from Døssing's 1988 publication for explanation purposes, therefore the magnitudes do not correspond to the actual hammer used for the model pile tests). It can be seen from the figure that the frequency spectrum for the steel tip drops off much more gradually than do those for the other tips, therefore the steel tip is useful up to much higher frequencies. In general, the upper end of the usable frequency range is indicated as the frequency at which the spectrum magnitude has decayed by 10 to 20 dB (Ewins, 1985). The measured frequency spectrum of the PCB 086C03 hammer used for the present tests is given in Figure 2.10, and close inspection reveals that the upper limit of the usable frequency range is approximately 4 kHz, since the curve decays 20 dB (from the relatively flat portion) only slightly after that value.

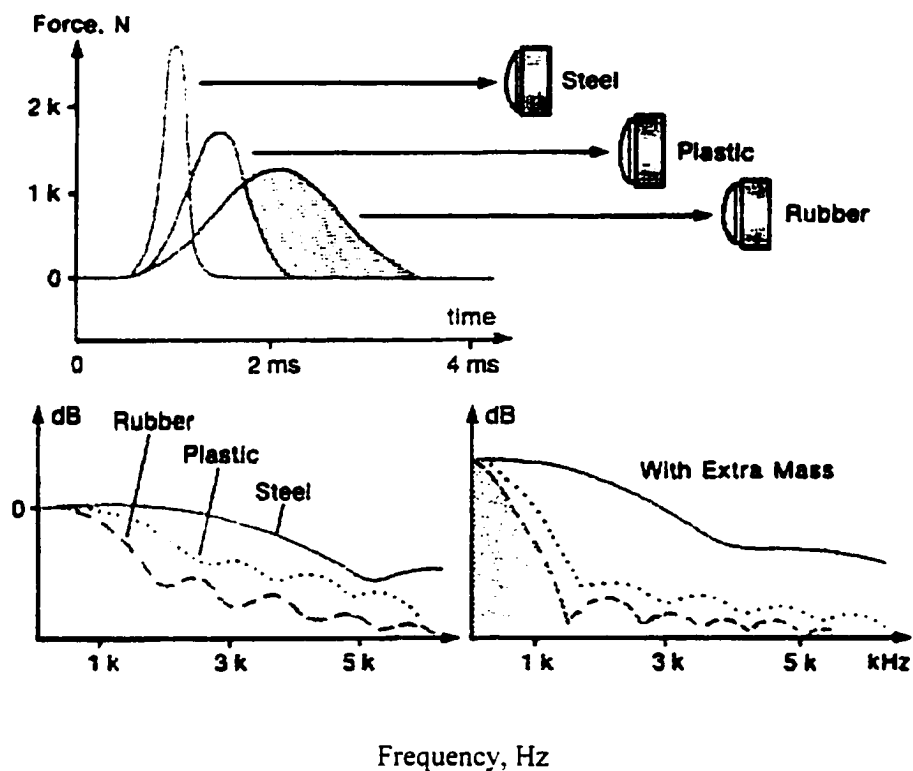


Figure 2.9 Force-Time Curves and Frequency Spectra for Various Hammer Tips (Døssing, 1988)

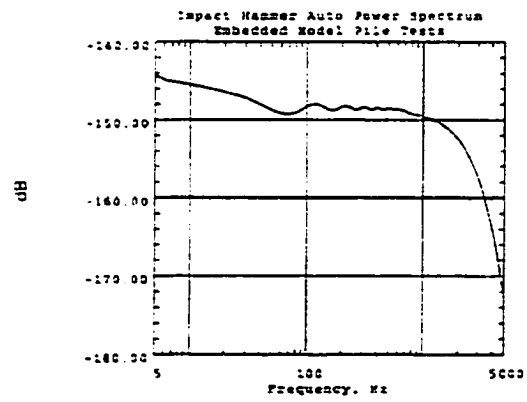


Figure 2.10 Measured Frequency Spectrum for PCB 068C03 Impact Hammer

2.4.2 Piezoelectric Accelerometer

A piezoelectric material is one that generates an electrical charge across its end faces when exposed to a mechanical stress. These materials are usually either natural or synthetic crystals, and accelerometers containing them can be designed such that the stress induced (and thus the electrical charge) is proportional to the acceleration of the test specimen. To achieve this design, a seismic mass is placed above the crystals as shown in Figure 2.11.

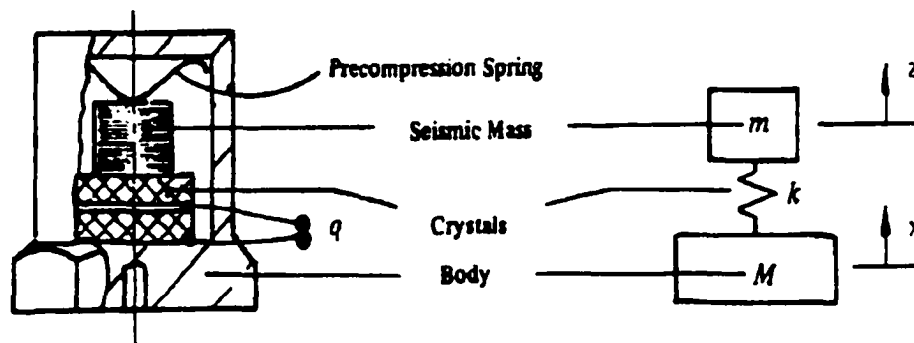


Figure 2.11 Cutaway of Accelerometer and Corresponding Dynamic Model (Ewins, 1985)

The force exerted on the crystals is the seismic mass's inertia force, $m\ddot{z}$, and as long as the body of the accelerometer and the seismic mass move together ($\ddot{x} = \ddot{z}$) the transducer output will be proportional to \ddot{x} (the acceleration of the accelerometer body) (Ewins, 1985). These two accelerations are essentially equal up to approximately 33 percent of the accelerometer's resonant frequency (Ewins, 1985); it is important to remember this when noting the manufacturer's recorded resonant frequency. In general, the resonant frequency depends on the test specimen's material characteristics and on the method used to mount the

accelerometer to the specimen. Usually, the manufacturer's recorded resonant frequency is the lowest natural frequency reported when the accelerometer is attached to a rigid base. Thus it is wise to make the accelerometer attachment to the test specimen as rigid as possible to utilize the largest valid frequency range.

For the tests described herein, a Wilcoxon Research Model 732A piezoelectric accelerometer was chosen to measure pile response. This accelerometer had a recorded resonant frequency of 60 kHz, its usable frequency range was 2 Hz to 15 kHz, and its nominal sensitivity was 10 mV/g. Several options were available for fixing the accelerometer to the test structure, each having unique advantages and disadvantages. Figure 2.12(a) shows some of the techniques that have been used in the past, and it is easy to see from Figure 2.12(b) that the mounting method has a measurable effect on structural response. The positions of the resonance peaks for the various curves in the figure give a relative indication of the usable frequency range, and it is clear from the figure that, in general, stud-mounting provides the highest range. However, it is not always convenient to drill holes into the test specimen at each accelerometer location, especially if there are many measurement points. Also, as stated by Ewins (Ewins, 1985):

The particularly high-frequency capability of the screwed stud attachment can only be attained if the transducer is affixed exactly normal to the structure surface so that there is a high stiffness contact between the two components. If, for example, the axis of the tapped hole is not normal to the surface, then the misalignment which results will cause a poor contact region with a corresponding loss of stiffness and of high-frequency range.

Achieving this high degree of accuracy when drilling and tapping stud holes is sometimes a difficult task, therefore, more convenient mounting methods usually warrant consideration.

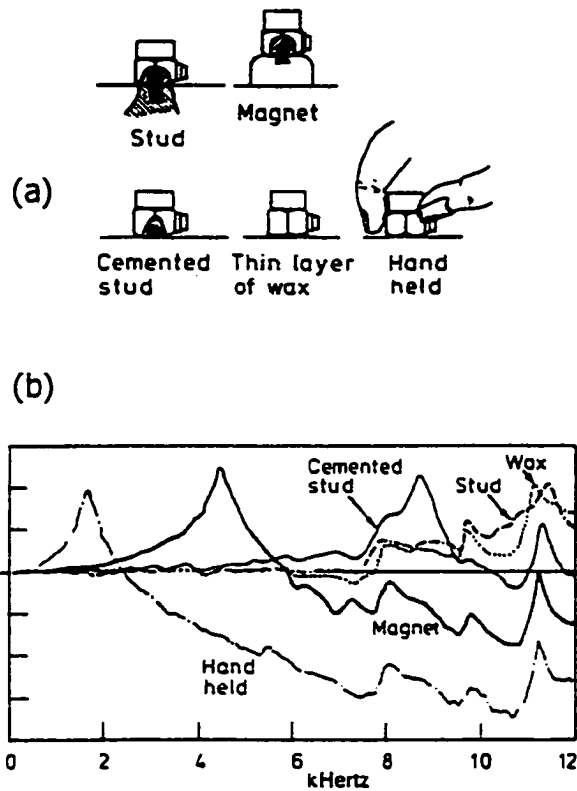


Figure 2.12 (a) Methods of Accelerometer Attachment
 (b) Frequency Response Function for Different Attachments
 (Ewins, 1985)

With the aforementioned limitations in mind, various mounting methods were investigated for the model pile tests, and the results of these tests are given in Figure 2.13. It was decided to use the mounting adhesive Loctite 422[®] since it was easily applied and removed, and its usable frequency range was very close to that observed with the stud-mounting technique.

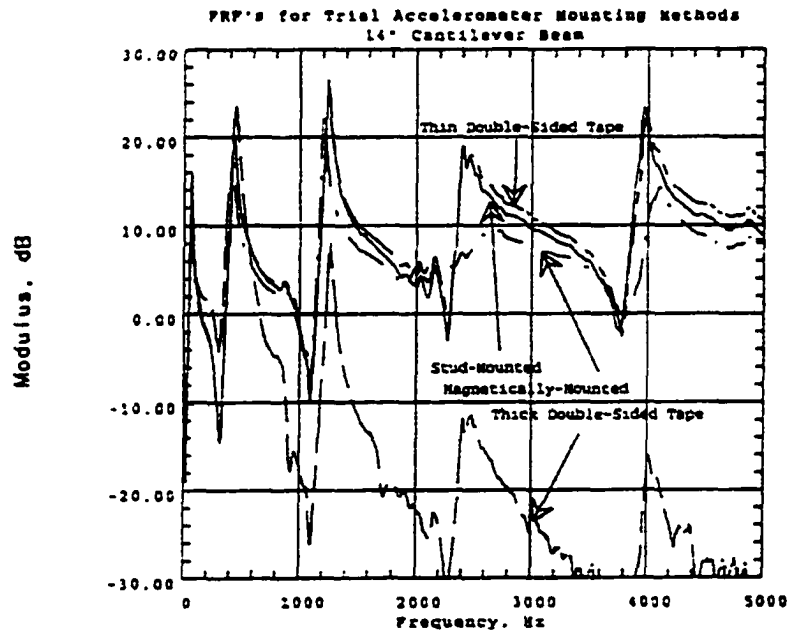
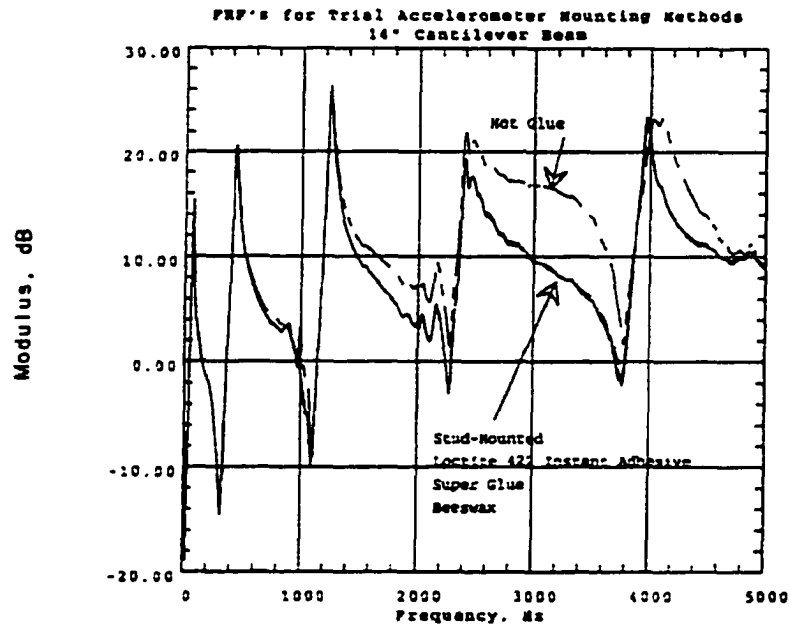


Figure 2.13 Frequency Response Functions for Trial Accelerometer Mounting Methods

2.5 Digital Signal Analyzer

A Hewlett-Packard Model 3562A dual-channel dynamic signal analyzer was used to process the data collected by the force transducer and accelerometer. A photograph of the analyzer (along with the power amplifiers for the piezoelectric accelerometers, the impact hammer, and the disk drive used to store data for later analysis) is presented in Figure 2.14.

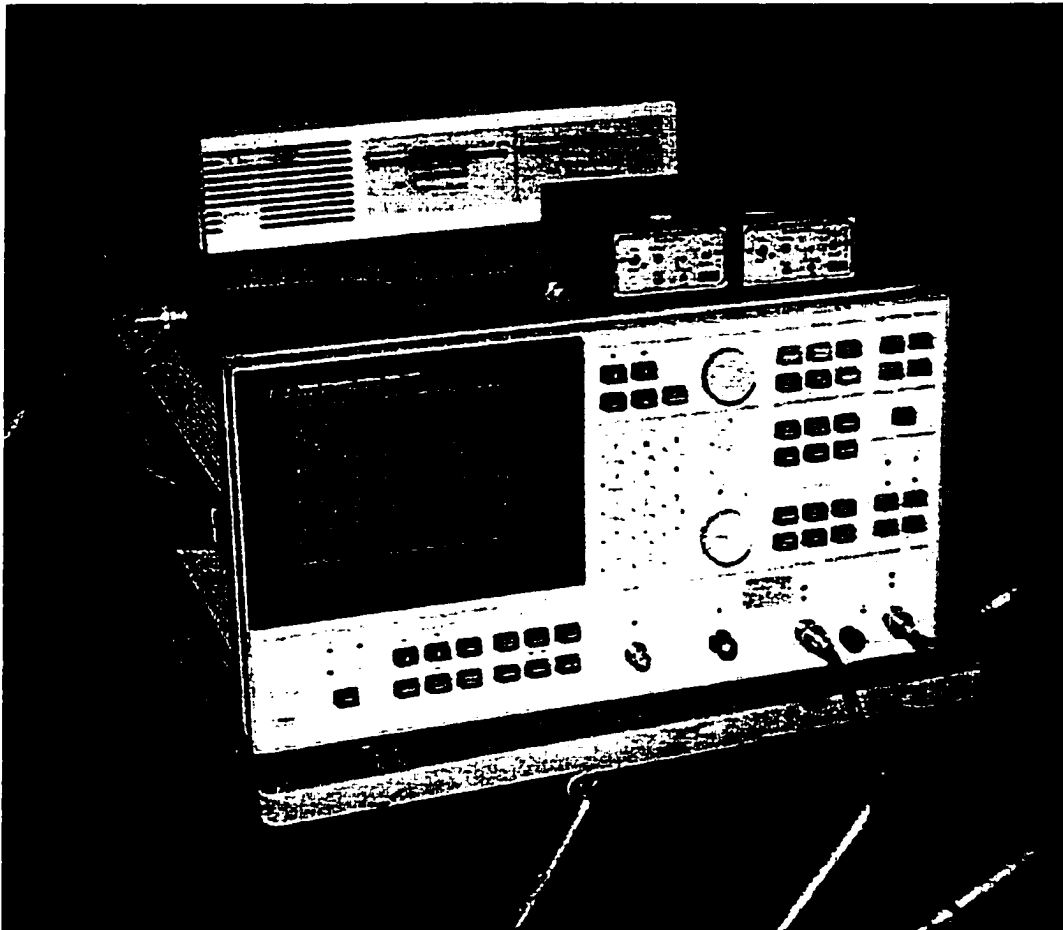


Figure 2.14 Digital Signal Analyzer and Power Amplifiers

Analog time history signals (force vs. time and acceleration vs. time) were sampled and digitized by the analyzer, where the record lengths and the sampling rate governed the frequency range and resolution of the analysis. Each time record was multiplied by a “window” function; specifically, a uniform (rectangular) window spanning the short duration of the impact was used to multiply the force record, while the acceleration record was multiplied by an exponentially decaying window. The windowing functions served to taper the data, which makes it more amenable to processing with the Fast Fourier Transform (FFT), which is the next step in the analysis process. Time signals were converted to the frequency domain using the FFT since data in the frequency domain is often more readily interpreted than in the time domain. The particulars of the windowing functions and the FFT process as they relate to modal analysis will be discussed in greater detail in the next chapter. Suffice it to say that there are numerous books and papers to which the interested reader can refer for detailed information on digital signal processing techniques; three excellent references are the works by Bendat and Piersol, 1980, Bendat and Piersol, 1986, and Halvorsen and Brown, 1977.

CHAPTER III

MODAL ANALYSIS

3.1 Summary of Modal Analysis Theory

3.1.1 General Concepts

Modal analysis can be broadly described as the process of examining the vibration response of a system to a prescribed dynamic input, using this response to identify the modal characteristics of the system (natural frequencies, damping, and mode shapes), then creating a spatial model of the system from the modal information. The applications of modal testing are widespread, though perhaps its main use has been in the vibration control arena, where excessive machinery and structural vibrations have been prevented and eliminated by proper identification (and subsequent manipulation) of the system modal model. In many instances, modal analyses are undertaken to validate (or invalidate) the predicted responses of a finite element or other theoretical model. Once the response to simple forms of excitation are correlated between the finite element and experimental modal studies, the finite element model can be used to predict a structure's response to more complicated loading patterns. Results of modal tests can also be used to generate models

that predict the vibration response to a structural modification, before the original structure is actually altered. It is obvious that modal analysis is a powerful engineering tool.

Figure 3.1 illustrates the three major steps involved in the modal analysis process. As seen in the figure, the first step is to form the response model; this is done using results from a series of vibration tests performed on the structure under investigation. For modal testing, the vibration response is most commonly expressed in the form of a frequency response function (FRF) measurement, denoted as H_{jk} , and defined as follows:

$$H_{jk}(\omega) = \frac{\text{Response at Position } j}{\text{Excitation at Position } k} = \frac{\ddot{u}_j(\omega)}{P_k(\omega)} \quad (3.1)$$

where

$\ddot{u}_j(\omega)$ = acceleration at designated response position j (as a function of circular frequency, ω), and

$P_k(\omega)$ = force at a designated source position k (as a function of circular frequency, ω).

Here, acceleration is designated as the response parameter, but displacement or velocity data can be used with equal validity if it is more conveniently measured.

Response Model

$$H = \begin{bmatrix} H_{11}(\Omega) & H_{12}(\Omega) & \dots & H_{1m}(\Omega) \\ H_{21}(\Omega) & H_{22}(\Omega) & & \\ \vdots & & \ddots & \\ H_{n1}(\Omega) & & & H_{nm}(\Omega) \end{bmatrix}$$

Modal Model

Natural Frequency
 Modal Damping
 Mode Shape } for each mode

Spatial Model

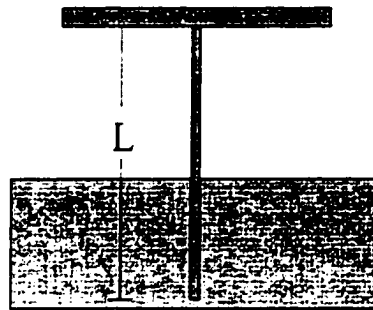


Figure 3.1 Conceptual Approach Used in Modal Analysis (Rix et al., 1996)

A more detailed expression for the frequency response functions of a structural system can be derived from its equations of motion. Details of the derivation will not be presented here, but the general steps in the process will be discussed. Equation 3.2 gives the mathematical expression for the equations of motion:

$$[M]\{\ddot{u}(t)\} + [C]\{\dot{u}(t)\} + [K]\{u(t)\} = \{P(t)\} \quad (3.2)$$

where

$[M]$ = the mass matrix for the structural system,

$[C]$ = the system's viscous damping matrix,

$[K]$ = the system stiffness matrix,

$\{P(t)\}$ = vector of time-varying system forces, and

$\{\ddot{u}(t)\}$, $\{\dot{u}(t)\}$, $\{u(t)\}$ = the time-varying acceleration, velocity, and displacement vectors, respectively, for all degrees of freedom being considered.

Of course, these equations are for a multi-degree-of-freedom (MDOF) system; those for a single-degree-of-freedom (SDOF) system would have single values for the various quantities rather than matrices and vectors. Also, the system damping may be of some form other than viscous, (e.g. hysteretic), but viscous damping is included here for generality.

A free-vibration analysis of these equations (one for which the forcing function, $\{P(t)\}$, equals zero) leads to a diagonal matrix of eigenvalues, $[\lambda]$, containing information about both natural frequencies and damping, and an eigenvector matrix, $[\Psi]$, the columns of which represent the system mode shapes. A forced-vibration analysis may then be performed to produce expressions for the displacement quantities u , \dot{u} , and \ddot{u} in terms of ω , and these results may be used to form the frequency response function (FRF) matrix, $[H_{jk}(\omega)]$, in the manner described in Equation 3.1. It should be noted that the members of the FRF matrix

are not constant, but are functions of frequency, ω . If m is equal to the number of source positions on the test structure, and n is the number of response positions, then the structure's FRF matrix contains $m \times n$ individual frequency response functions, each of which is complex-valued, possessing both magnitude and phase information. In a sense, then, the FRF matrix is three-dimensional since each of the member FRF's is a vector whose length depends on the frequency resolution of the vibration measurement. As a matter of notation, if the response is considered in terms of acceleration, the FRF matrix is known as the inertance, or accelerance matrix. Velocity-based FRF matrices are referred to as mobility matrices, while those FRF matrices containing displacement information are called receptance, or admittance matrices.

The following equation, which can be obtained from the operations described above, shows the relationship between a system's accelerance frequency response characteristics and its modal properties:

$$H_{jk}(\omega) = \frac{\ddot{u}_j}{P_k} = -\omega^2 \sum_{r=1}^N \frac{(\Psi_j)_r (\Psi_k)_r}{m_r (\lambda_r^2 - \omega^2)} \quad (3.3)$$

where

$H_{jk}(\omega)$ = the accelerance frequency response function at frequency ω ,

$(\Psi_j)_r$ = the j^{th} element of the r^{th} eigenvector $\{\psi\}_r$ (relative displacement at point j during vibration in mode r),

m_r = the r^{th} modal mass,

λ_r^2 = the eigenvalue of the r^{th} mode, and

N = the number of modes (or number of degrees of freedom being considered).

Equation 3.3 forms the basis for all (accelerance) modal analysis studies, since it details directly the connection between the frequency response function, which can be easily measured, and the modal properties (λ, ψ) needed to “backcalculate” unknown spatial properties (e.g. length, modulus of elasticity, etc.). Ewins states it this way: “From a purely theoretical viewpoint [Equation 3.3] provides an efficient means of predicting response (by performing a free vibration analysis first) while from a more practical standpoint, it suggests that there may be means of determining modal properties from [accelerances] which are amenable to direct measurement.” (Ewins, 1985)

It should be noted that, as Ewins suggests, it is more practical to measure a forcing function and the resulting acceleration it produces on a test specimen than it is to measure the quantities necessary to form the specimen’s mass, stiffness, and damping matrices. Thus, the former values are usually measured and used to compute an accelerance FRF. Common practice is to monitor force and acceleration signals for a specific length of time, then to employ a dynamic signal analyzer of the type described in Chapter II to convert the time-domain signals into the frequency domain using the Fast Fourier Transform (FFT) technique. These frequency-domain values are then substituted into Equation 3.1 to form the FRF.

In reality, however, the process is slightly more complicated, due to the fact that measurement noise will likely be present in the force and acceleration signals. Halvorsen

and Brown (Halvorsen and Brown, 1977) present a concise explanation of this concept, and their work is summarized here.

As stated previously, the frequency response function is a measure of the acceleration (output from a given excitation) divided by the input excitation (forcing function). To minimize the effect of noise on the measurement, the frequency response function is formed in practice by dividing the cross-spectrum between the input and the output by the power spectrum of the input. These quantities are frequency-based, and are computed by multiplying the numerator and denominator of the “theoretical” FRF by the complex conjugate of the Fourier transform of the input signal. The details of this formulation are shown mathematically in the following equation:

$$H(\omega) = \frac{G_{io}(\omega)}{G_i(\omega)} = \frac{I^*(\omega) O(\omega)}{I^*(\omega) I(\omega)} \quad (3.4)$$

where

$H(\omega)$ = frequency response function,

$G_{io}(\omega)$ = cross-spectrum between $i(t)$ and $o(t)$,

$i(t)$ = system input as a function of time,

$o(t)$ = system output as a function of time,

$G_i(\omega)$ = power-spectrum of $i(t)$,

$I(\omega)$ = Fourier transform of $i(t)$,

$O(\omega)$ = Fourier transform of $o(t)$, and

$I^*(\omega)$ = complex conjugate of the Fourier transform of $i(t)$.

The usefulness of this form of the equation can be realized by considering that the actual, measured input and output signals will contain noise, and may be expressed as follows:

$$H'(\omega) = \frac{O(\omega) + N(\omega)}{I(\omega) + M(\omega)} = \frac{Y(\omega)}{X(\omega)} \quad (3.5)$$

where

$H'(\omega)$ = *measured* FRF,

$O(\omega)$ = Fourier transform of output signal, $o(t)$,

$N(\omega)$ = Fourier transform of output noise, $n(t)$,

$I(\omega)$ = Fourier transform of input signal, $i(t)$, and

$M(\omega)$ = Fourier transform of input noise, $m(t)$,

$Y(\omega)$ = Fourier transform of output plus output noise, and

$X(\omega)$ = Fourier transform of input plus input noise.

Multiplying the numerator and denominator of the middle section of the above equation by the complex conjugate of the denominator (the input plus input noise) gives:

$$H'(\omega) = \frac{G_{io}(\omega) + G_m(\omega) + G_{mo}(\omega) + G_{mn}(\omega)}{G_i(\omega) + G_{im}(\omega) + G_{mi}(\omega) + G_m(\omega)} \quad (3.6)$$

where the quantities with double subscripts represent cross-spectra between the specified signals and those with a single subscript represent power spectra. If the measurement noise signals are noncoherent with each other and with the input signal, then the expected value of the cross-spectrum terms containing m and n will equal zero (43) and Equation 3.6 reduces to:

$$H'(\omega) = \frac{G_{io}(\omega)}{G_i(\omega) + G_m(\omega)} = \frac{H(\omega)}{1 + \frac{G_m(\omega)}{G_i(\omega)}} \quad (3.7)$$

where $H(\omega)$ is the true frequency response function that is desired. Therefore, if the noise-to-signal ratio of the input signal is very small (much less than 1), the measured FRF will approximately equal the true FRF.

The cross-spectrum value between the input and output signals is also a part of another important quantity called the coherence function. Qualitatively speaking, the coherence is a measure of how much the output is due to the input, rather than due to noise or other spurious sources that are not meant to be a part of the test. The coherence function is defined as:

$$\gamma_{xy}^2(\omega) = \frac{|G_{xy}(\omega)|^2}{G_x(\omega) + G_y(\omega)} \quad (3.8)$$

where

$\gamma_{xy}^2(\omega)$ = coherence function between input with noise and output with noise,

$G_{xy}(\omega)$ = cross-spectrum between input signal with noise and output signal with noise,

$G_x(\omega)$ = power spectrum of input signal with noise, and

$G_y(\omega)$ = power spectrum of output signal with noise.

The coherence value ranges between 0 and 1; if the system is completely linear and there is no measurement noise, the coherence value will be 1 for all frequencies. If the input and output signals are totally uncorrelated, the value will be zero; the measured value is generally somewhere in between. A low coherence value serves as a good indicator that signal contamination is occurring and the test setup should be examined carefully.

When performing modal tests, it is common to average several FRF measurements for each particular source/receiver combination to reduce the bias error that is inherent in the cross-spectrum calculation. Halvorsen and Brown (Halvorsen and Brown, 1977) explain this practice, emphasizing its importance for the impulse technique, which relies on an impulsive force (an impact) for excitation of the structure:

It should be pointed out...that there is an inherent bias error associated with the computation of the cross-spectrum and the magnitude of this bias error is inversely proportional to the number of averages in the computation. Thus, the greater the measurement noise, the greater the number of averages required to approach the expected value of the cross-spectrum between the input and output measurement signals. With measurement techniques employing many averages, the bias error can usually be reduced to an insignificant level so that it is only necessary to minimize the noise in the measurement of the input signal. However, if there is significant measurement noise and only a few averages are used, then the computed values of the cross-spectrum terms involving the noise signals in Equation [3.6] can be large relative to the true cross-spectrum, with resulting large errors in the measured frequency response function. In general, only a few averages are used in the impulse technique; otherwise, one of its major advantages

– its speed – is lost. Therefore, it is important to minimize measurement noise in both the input and output signals when using the impulse technique.

3.1.2 Frequency Response Function Display

Because frequency response functions have complex values, a simple two-dimensional plot cannot clearly show all three quantities of interest (magnitude, phase, and frequency) simultaneously. Consequently, three types of graphical output are commonly used for display—the first is a Bode plot, in which the magnitude and the phase of the FRF are plotted separately but shown together. The second type of plot is known as a Nyquist plot, in which the real part of the FRF is plotted as the abscissa and the imaginary part is plotted as the ordinate. This plot is quite interesting in that as the frequency increases, a circular shape is produced. The third common type of data presentation has no unique name, but it consists of two plots, one of the real part of the FRF vs. frequency and one of the imaginary part vs. frequency. Figures 3.2, 3.3, and 3.4 show examples of each type of plot for a single-degree-of-freedom system.

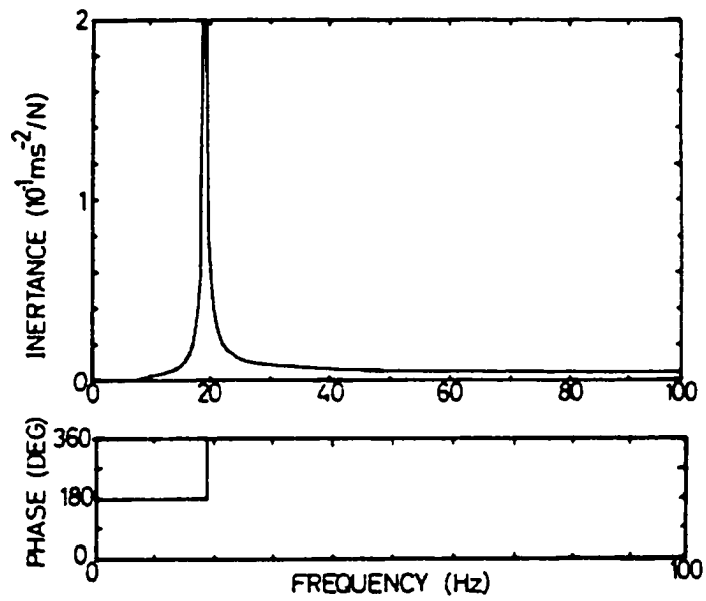


Figure 3.2 Bode Plot of Accelerance for Undamped SDOF System (Ewins, 1985)

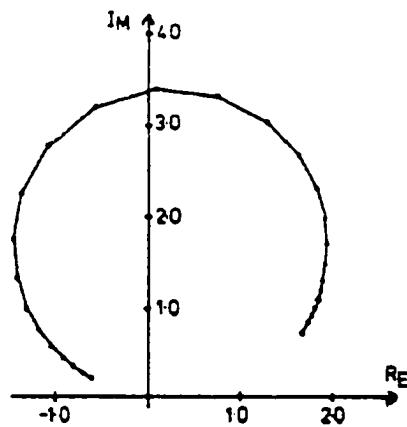


Figure 3.3 Nyquist Plot of Accelerance for Viscously-Damped SDOF System (Ewins, 1985)

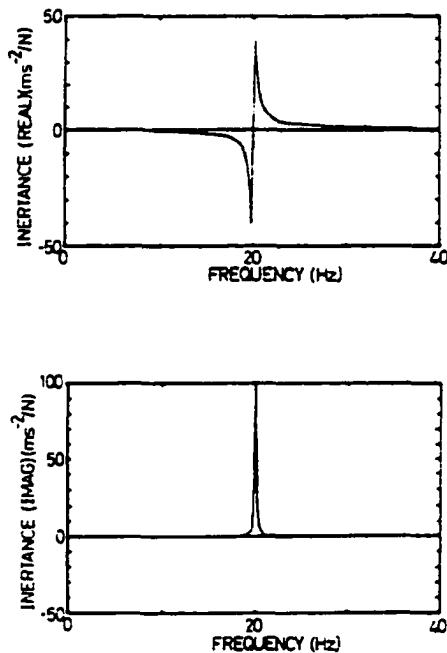


Figure 3.4 Real and Imaginary Parts of Accelerance for Damped SDOF System (Ewins, 1985)

Each of the plots shown above has distinctive properties worth noting. Perhaps the most important are those present in the Bode plot, since this is the type of graphical presentation that was chosen for the present study. Obviously the main feature of Figure 3.2 is the peak in the magnitude occurring at 19 Hz, and the corresponding 180° shift in phase at the same frequency. These characteristics indicate that a resonance, or natural frequency, of the system occurs at this point. All Bode plots will exhibit these attributes at resonance locations, but not all will be as “clean” as the undamped SDOF plot of Figure 3.2. If damping is present, the peak will be rounded to some degree, and phase angles will deviate

from exactly 0° or 180° , but a 180° phase shift should occur at every resonance location nonetheless. Bode plots for multi-degree-of-freedom systems can become quite intricate, especially when there are several closely-spaced modes. In general, though, plots of MDOF systems may be interpreted as the superposition of several SDOF system plots, as illustrated in Figure 3.5.

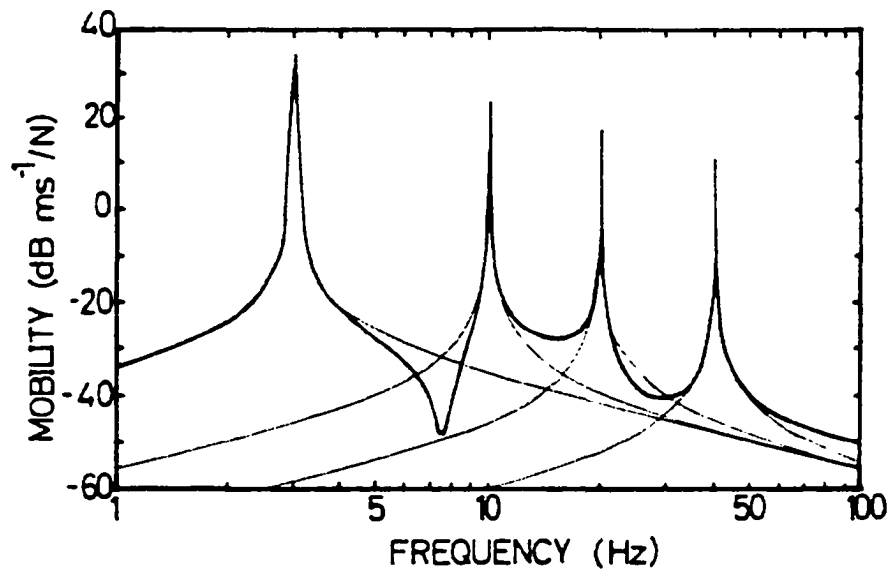


Figure 3.5 Mobility Plot for MDOF System Showing Individual Modal Contributions (Ewins, 1985)

Figure 3.5 illustrates another common practice in creating Bode plots. Often, the frequency and magnitude values that must be included in a plot span quite a large range, so either one or both of the axes will be plotted using a logarithmic scale. In Figure 3.5 the frequency axis is plotted on a log scale, while the magnitude is plotted using a decibel scale.

Figure 3.3 shows the Nyquist plot for a viscously-damped SDOF system. Points appearing on the curve correspond to individual frequencies (increasing in the clockwise direction). As evidenced in the figure, the progression of points traces out a near-circular arc, with the greatest frequency spacing occurring around the resonance frequency. This characteristic distortion aids in identification of the resonance frequency, since it makes those frequencies around the resonance much more distinct than the closely-spaced values that occur far from a resonance. It can be shown mathematically that only two cases theoretically produce an exact circle—a mobility plot for a viscously-damped system, and a receptance plot for a hysteretically-damped system (Ewins, 1985). The other cases (receptance or inertance plots for viscously-damped systems and mobility or inertance plots for hysteretically-damped systems) only trace approximately circular shapes for which the amount of distortion depends on the damping level.

Graphs of the real and imaginary parts of the frequency response function corresponding to Figure 3.3 are presented in Figure 3.4. It is obvious from the figure that for inertance FRF's, the real part changes sign when passing through a resonance, whereas the imaginary part experiences a peak at that location. Such sharp peaks and distinct sign changes seem quite useful for identifying resonances, however, since both positive and negative values must be displayed, this type of graphical output does not lend itself well to logarithmic scaling. For this reason, and because of the intricacy associated with multi-degree-of-freedom systems, the previous display options are much more widely utilized.

3.1.3. Modal Parameter Estimation

A key element in the modal analysis process is the estimation of modal parameters from the measured frequency response functions. Several methods have been developed to accurately and efficiently perform this task, but the experience and best engineering judgment of the researcher are still called upon a great deal in this operation.

Peak-Picking Method. For very simple structures, such as a cantilevered beam, the resonance peaks are likely to be well-spaced and quite distinct from one another; this condition is referred to as having “lightly coupled” modes. For such structures, each mode acts virtually independently of the others, and modal frequencies and damping can be determined from any measured FRF. Modal frequencies (damped natural frequencies) are determined simply by noting the frequency corresponding to the peaks of the FRF curve. The modal damping is somewhat more difficult to determine, which is not surprising, since damping is the most “elusive” of all the modal parameters. The amount of damping is related to the width of FRF peaks—the lighter the damping, the narrower the peak. For very lightly-damped structures, the peak may be so narrow that an accurate measurement of the bandwidth is impossible, making it necessary to perform a “zoom” analysis in the vicinity of the peak. Once this operation has been performed, one can determine the frequency span required for the FRF to drop 3 dB in both directions from the peak value. This value, denoted as σ , is the rate at which free vibrations of the system die out (at a particular damped natural frequency) (Rix et al., 1996). Figure 3.6 illustrates the concept of the decay rate σ . (An alternate criterion that is sometimes used for determining the damping value is to note the frequency bandwidth required for the FRF to drop to a level that is the magnitude

at resonance divided by $\sqrt{2}$ on either side of the resonance peak. The corresponding frequencies are known as the “half-power” points, and the modal damping constant, ζ_r , is approximately equal to two times the identified bandwidth divided by the resonance frequency. (Ewins, 1985))

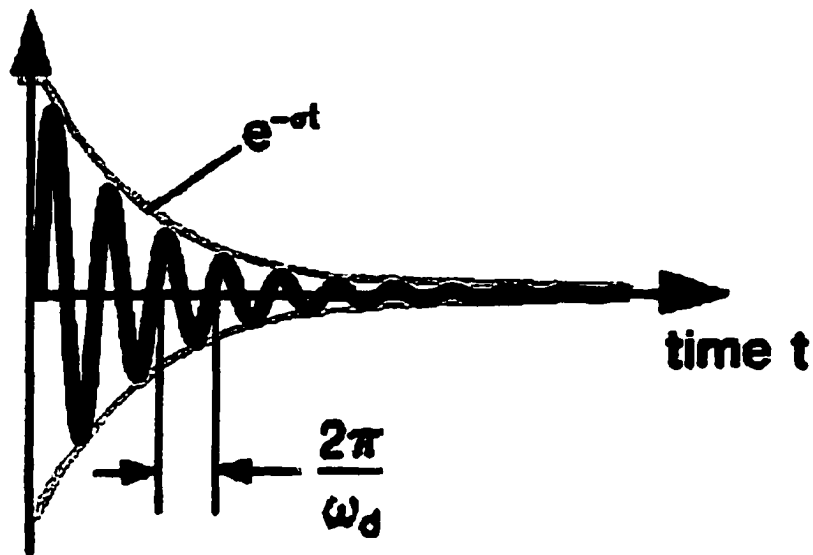


Figure 3.6 Decay Rate, σ , of Damped Oscillations (Døssing, 1988)

Mode shapes for the simple structure discussed above can be determined using a procedure known as “peak-picking.” It can be shown that at a modal frequency, the complex accelerance value becomes a purely imaginary number, according to the following equation (Rix et al., 1996):

$$A(\omega)_{dr} \approx i \frac{(\phi_r \Phi_j)(\phi_r \Phi_k)}{2\sigma} \omega_{dr} \quad (3.9)$$

where

$A(\omega)_{dr}$ = accelerance FRF magnitude at the r^{th} damped natural frequency, ω_{dr} , and
 $\phi_r \Phi =$ the mass-normalized r^{th} mode shape (remembering that mode shape values are
relative displacement quantities, and are therefore often scaled for consistency).

This equation is closely related to Equation 3.3, but the damping now has been included in a more specific sense and the expression has been evaluated for one mode corresponding to one damped natural frequency. Equation 3.9 shows that the FRF magnitude is proportional to the modal displacement, and it is this fact that leads to the following procedure for determining mode shapes from peak-picking. First, an accelerometer is fixed to a predetermined “reference” location on the structure. Next the structure is excited at several locations, including the reference point. FRF’s are measured for each excitation event, then the imaginary parts are “picked” at the natural frequencies for each FRF, and the resulting shape formed from the value at each excitation point for a certain natural frequency is its associated mode shape. Figure 3.7 illustrates the process, with Point #2 shown as the reference degree of freedom (DOF). It should be noted that while this is the simplest of the modal parameter estimation techniques, it does have limited applicability; one significant limitation is that it can only be used on structures possessing proportional damping (i.e. the damping matrix is proportional to the mass and stiffness matrices) (Ewins, 1985).

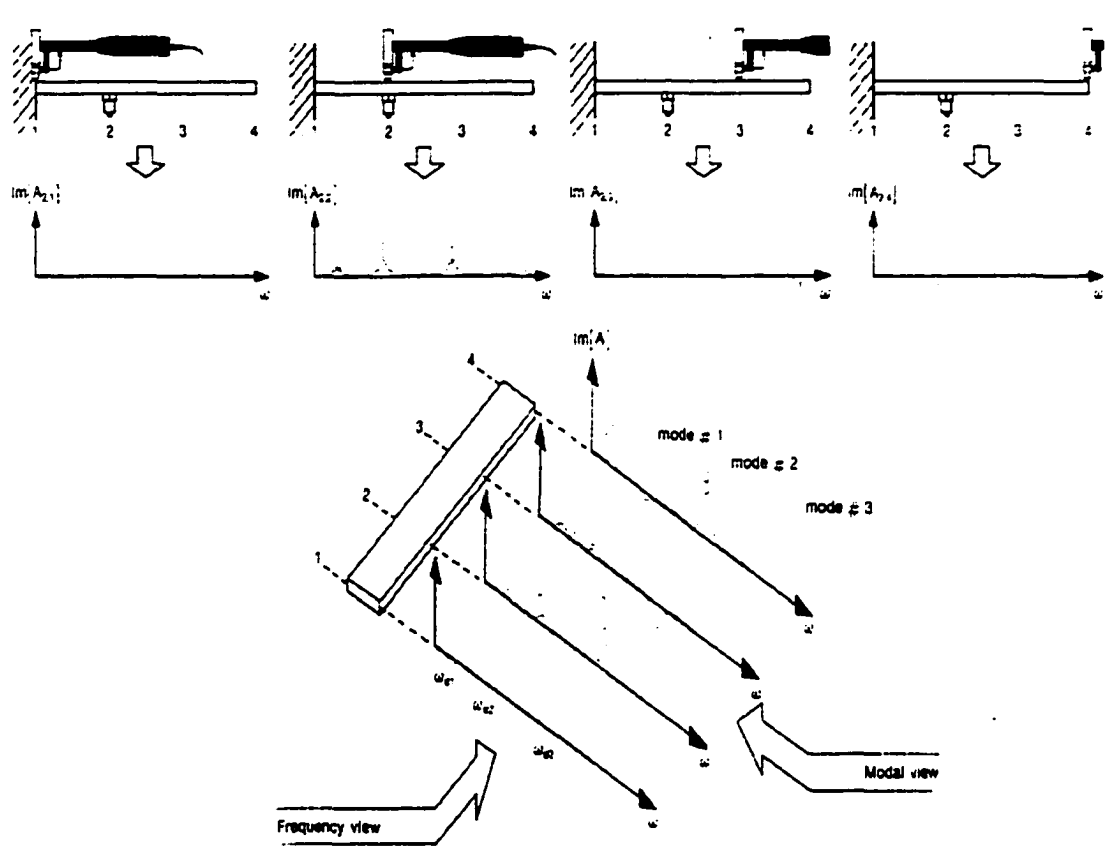


Figure 3.7 Illustration of the Peak-Picking Process (Døssing, 1988)

Unfortunately, not all structures have FRF's that are as simple and easily interpreted as those of the type described above so more sophisticated methods of modal parameter extraction are usually necessary to obtain accurate results. For structures whose FRF's contain many closely-spaced (highly coupled) modes or significant noise contamination, or for analyses which demand a high degree of accuracy, the more rigorous parameter estimation techniques are normally recommended. The great majority, if not all, of these

methods involve some type of curve-fitting algorithm that seeks to minimize the difference between the measured FRF and a mathematical, computer-generated FRF designed to match it. Døssing (1988) describes the curve-fitting technique in this manner, “Curve-fitting is where the mathematical theory and practical measurements meet. The theory provides us with a mathematical parametric model for the theoretical FRF of a structure, and our measurements give the real FRF. Curve-fitting is the analytical process to determine the mathematical parameters which give the closest possible fit to the measured data.”

SDOF curve-fitters are used for fairly simple structures whose modes are lightly-coupled, meaning that each modal frequency behaves as if it were that for a SDOF structure, and the surrounding modes exert little, if any, influence over the mode of interest. The analyst must choose the frequency span over which each individual mode of each individual frequency response function has dominance. As Døssing states, “This is always a compromise between including as many data points as possible, to maximize the statistical estimation, and moving so far away from the resonance that other modes become dominant and the SDOF assumption becomes invalid.” (Døssing, 1988)

Circle-Fit Method. The most widely used SDOF curve-fitting algorithm is the circle-fit method, and it makes use of the Nyquist type plot described earlier in Section 3.1.2. First the analyst examines the measured FRF and chooses the frequency span surrounding the mode of interest. Next, any one of many curve-fitting routines is used to produce a circle that is “closest” to the arc traced by the FRF in the Nyquist plot. Ewins points out that either of two philosophies could be followed to calculate the deviation between the “model” circle and the FRF arc. In the first, the distance between the FRF points and the nearest

point on the circle is minimized, and for the second, the distance between the FRF points and the location that they should occupy on the circle is minimized. Although the second philosophy is more accurate, the first is more easily implemented and is therefore more commonly employed (Ewins, 1985).

The next step in the circle-fit procedure is to obtain the natural frequency and damping estimates using the calculated circle. The natural frequency is determined by constructing radial lines from the center to several points surrounding the apparent peak frequency, and noting the angles they subtend with each other. The frequency corresponding to the maximum sweep rate around the circle is the natural frequency. An example of this process is pictured in Figure 3.8.

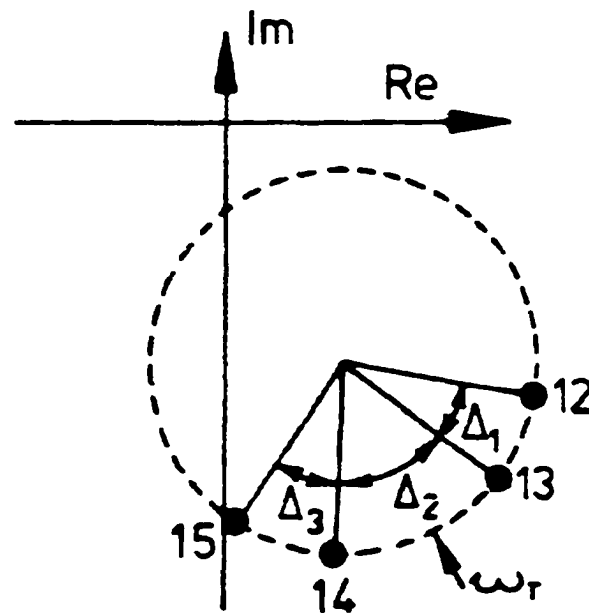


Figure 3.8 Estimation of Natural Frequency Using Circle Fit Method (Ewins, 1985)

From the properties of the modal circle, it can be shown that the damping of the mode may be computed using Equation 3.10 below, whose quantities are illustrated graphically in Figure 3.9:

$$\zeta_r = \frac{2(\omega_a^2 - \omega_b^2)}{\omega_r^2 \left(\tan\left(\frac{\theta_a}{2}\right) + \tan\left(\frac{\theta_b}{2}\right) \right)} \quad (3.10)$$

where

ζ_r = damping constant for the r^{th} mode,

ω_a = frequency corresponding to the half-power point following the resonance frequency, ω_r ,

ω_b = frequency corresponding to the half-power point preceding the resonance frequency,

θ_a = angle subtended between ω_b and ω_r , and

θ_b = angle subtended between ω_r and ω_a .

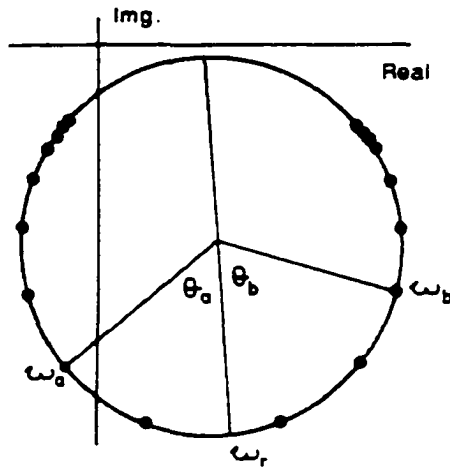


Figure 3.9 Modal Circle Properties Used to Compute Damping for Circle-Fit Method (Ewins, 1985)

It is often helpful to calculate a number of damping estimates from different combinations of points around the resonance frequency, using Equation 3.10. Each estimate should give virtually the same value, so a calculation of the mean and standard deviation of the values should give an indication of whether the analysis is satisfactory. Ewins suggests that a deviation of less than 4-5% is highly acceptable, but if the deviation is near 20% or 30%, a problem exists; likely candidates include poor experimental measurement techniques or interference from surrounding modes.

For many structural systems, a SDOF curve-fit is not appropriate or effective, and a more elaborate MDOF curve-fit algorithm must be employed. Examples of such structures are those that exhibit many closely-spaced modes, those that are so lightly damped that accurate estimates of the half-power bandwidth are unattainable, and those that are so heavily damped that resonance peaks are not clearly defined. Numerous MDOF curve-fitters are

available for modal parameter estimation; some operate on data in the frequency domain, while others make use of time-domain data to extract the necessary quantities. Only one method, the frequency polyreference technique will be discussed here, since it was chosen for the pile length determination tests.

Frequency Polyreference Technique. It has already been mentioned that the first step in the modal analysis process is the collection of vibration response data in the form of frequency response functions, using equipment such as that described in Chapter II. The amount of data acquired depends on the analyst's judgment regarding the number of degrees of freedom necessary to represent the true dynamics of the structural system. Often, this decision is based upon the expected geometrical intricacy of the mode shapes—more DOF's are required to adequately depict geometrically complex mode shapes than to model simpler, less complicated shapes. Once again, the researcher's engineering judgment is called upon to weigh the time and cost of including a great number of data points to ensure the system dynamics are sufficiently represented against the certain, possibly dangerous, errors that will result if too few DOF's are included.

Once that important decision has been made, it is usually the practice in modal analysis to choose a reference (or source) DOF where the excitation will be applied, and to monitor the response at each of the other response (or receiver) DOF's. Depending on the equipment available, all of the response data can be collected at once following a single reference excitation, or each response can be measured separately after successive excitations of the reference DOF. Often, then, another reference DOF will be chosen from the set, and the response will again be measured at each of the response locations. The

resulting FRF's can be organized into a response model such as that depicted in Figure 3.1. Each reference-response combination leads to a single FRF, so it can be seen that a great deal of data can be easily and quickly amassed when using the modal analysis test procedure.

As noted in the previous section, SDOF curve-fitters seek to fit data surrounding one peak in one FRF at a time. Obviously, it would take an enormous amount of time to process data for large structural systems, even if the SDOF curve-fit technique were applicable for the analysis. Many MDOF curve-fitters provide a fit for a complete FRF measurement in one step, and the frequency polyreference method, as its name implies, is able to produce a fit for many FRF's from multiple references all at one time. This is advantageous not only because it reduces the analysis time, but also, since the method operates in the frequency domain, the residual effects of modes outside the frequency range of interest are able to be included (Døssing, 1988). Also, since data from several references is fit simultaneously, the chances are lessened that some resonances may be missed due to application of the excitation at a node (point of zero displacement) of a certain mode. For these reasons, the frequency polyreference approach was selected as the appropriate curve-fitting scheme for the pile length determination tests.

The basis of the method involves a curve-fit of the following analytical frequency response function expression:

$$H_{jk}(\omega) = \sum_{r=1}^N \left(\frac{A_{jk_r}}{i\omega - \lambda_r} + \frac{A_{jk_r}^*}{i\omega - \lambda_r^*} \right) \quad (3.11)$$

where

A_{jk_r} = the residue term for mode r , which is proportional to the product of modal displacements at the multiple reference and receiver locations, i.e. $A_{jk_r} \propto \Psi_{j_r} \Psi_{k_r}$,

$A_{jk_r}^*$ = the complex conjugate of A_{jk_r} ,

λ_r^* = the complex conjugate of λ_r ,

and the remaining terms are the same as those defined for Equations 3.2 and 3.3. This expression is essentially equivalent to Equation 3.3, only written in a different format, except that in this case, $H_{jk}(\omega)$ represents a receptance FRF rather than an acceleration FRF. The equation can, of course, be transformed into that for acceleration (remembering that acceleration is simply the second derivative of the displacement with respect to time), but it is presented here in the receptance format because that is the more general of the two. As in the circle-fit method, the modal parameters are determined from the measured frequency response functions via a least squares curve-fit of the analytical expression above. Several mathematical tools exist that aid in the frequency polyreference parameter estimation process; details of these will be discussed in the next chapter.

3.2 Current Practice of Modal Analysis for Civil Engineering Applications

It was mentioned earlier in this chapter that until fairly recently, modal analysis was used predominately for vibration control studies of mechanical and aerospace engineering systems. Its use in the civil engineering community has spread, however, and it is now accepted as an extremely useful tool in the area of nondestructive testing of large structural

systems. Condition and damage assessment of existing structures is the pervading nondestructive application, due to the underlying principle that since a structure's vibration behavior is governed by its mass, stiffness, damping properties, and boundary conditions, any changes in these properties over time should produce changes in the vibration characteristics. Several papers will be briefly summarized below to give the reader a sense of the state of current modal analysis practice for condition assessment of civil engineering structures.

In a relatively early account of structural integrity evaluation, Wojnarowski et al. (1977) described a parametric study they performed to assess the structural state of a large offshore light station tower. They began by creating an analytical model of the existing structure, then determined the variation in natural frequencies produced by changing one physical attribute at a time. Examples of the parameters they varied were soil foundation properties and tower leg heights, entrained water content of the concrete piles, amount of marine growth and corrosion, and inclusion of failed structural members. After the analytical study was completed, they gathered experimental vibration data from the actual tower, performed a modal analysis of the results, and compared the corresponding measured and calculated natural frequencies. The results were used to "provid[e] a calibration basis for later measurements, on a regular or contingency basis, to ascertain whether the structure deviates from its original design characteristics." Wojnarowski et al. noted that this scheme was intended to replace the "long, expensive and depth-limited system of diver inspection with vibration calculations and measurements that can predict the failure of structural members at a fraction of the cost."

In a 1981 study of what he called the “resonance frequency technique,” (but that is now called modal analysis) Alexander “evaluate[d] the feasibility of using the resonance frequency technique with impact excitation for in situ evaluation of the degree of deterioration, hence integrity, of large concrete Civil Works structures.” He performed a series of impact tests on large (3 ft. x 6 ft. x 10 ft.) concrete block lab specimens, after noticing that he could obtain reliable resonance frequency values from impact tests of small (3.5 in. x 4.5 in. x 16 in.) freezing-and-thawing specimens. He used the resonance results of the subsequent modal analysis to determine the dynamic modulus of elasticity for the blocks, then conducted a similar analysis on eight in-place concrete piers of a dam across the St. Mary’s River. Alexander praised the powerful mathematical advantages afforded by the newly-developed digital signal analyzers and noted that the use of impact excitation was indeed a feasible, as well as economical, tool for performing tests to evaluate the vibrational properties of massive concrete structures. He pointed out that measuring the modal characteristics of a system at regular intervals, then noting any significant changes that occur between intervals and investigating their causes, is an effective means of monitoring a structure’s integrity throughout its lifetime. This concept of continual structural health monitoring is echoed in numerous other papers.

Morgan and Oesterle (1985) presented a brief summary of the many terms and concepts involved in modal analysis, then went on to describe some of the information that could be inferred from modal test results as they pertain to the evaluation, inspection, and maintenance of bridge structures. For instance, the authors noted that if two modes whose mode shapes differed only slightly were identified at relatively close frequencies, a local

distressed area might be indicated. They stated that the distressed area should be evident from comparison of the mode shapes. Additionally, the authors suggested that if two modes were found to have quite different frequencies, but very similar mode shapes, two active load mechanisms might be present. They stated that a soft foundation under one support would be evidenced by, “an unusual characteristic shape with only a single support or portion of a support participating excessively in the motion.” Morgan and Oesterle then described the field tests that were performed to assess the condition of two aging structures.

Richardson and Mannan (1993) detailed a procedure for identifying structural damage through a comparison of the modal analysis results of an “ideal” structure (recorded from a priori modal testing or from finite element modeling) with those of the corresponding damaged structure. They examined “measurement techniques, changes in the modal parameters caused by physical changes, fault location and quantification, and the use of a neural network to recognize changes in the modal parameters.” The results of two experiments in which they induced damage and measured the resulting changes in modal parameters were also included.

Aktan et al. (1994) provided specific definitions for the condition assessment of a structure and for structural damage. They then used those definitions to establish objectives and recommend assessment techniques based on modal testing. After describing the results of two integrity evaluations of existing bridges, they concluded that “[i]t is possible to design, execute and post-process modal tests of bridges by impact and/or force excitation, such that an accurate measure of their flexibility may be obtained with a fine spatial resolution.” The authors brought forth an important point, that due to the inevitable

experimental errors inherent in the modal testing of large in-place structures, “the reliability associated with individual mode shapes or frequencies of complex constructed facilities cannot exceed 90%.” They went on to say, however, that this reliability level is acceptable for damage evaluation, according to the definitions they provided.

In his discussion of the merits of modal testing for structural condition assessment, Salawu (1994) pointed out that unlike most conventional nondestructive testing methods, modal testing is a global procedure rather than a location-dependent one. Hence, “the measurement points can be chosen to suit the test situation.” He noted that though enough measurement points must be included to accurately represent the structure’s mode shapes, an advantage still exists in that damage can be detected at points not directly monitored by a response transducer. Salawu declared that another attractive feature of vibration testing is the fact that it does not require large force inputs, since dynamic amplification naturally occurs, ensuring a measurable response. He continued by detailing specific aspects of a structure’s condition that can be indicated by modal testing results. The author made the following noteworthy point: “Despite the sensitivity of damping values to damage, it is probably the least appropriate damage identification parameter because of the large scatter in reported experimentally-determined values. During procedures to extract modal parameters from measured dynamic response, estimates of damping values usually have the greatest degree of uncertainty.” Once again, it is evident that damping is the least well understood of the modal properties.

Samman and Biswas, in Part I of a two-part paper (Samman and Biswas, 1994a), outlined the theory behind the use of waveform-recognition techniques for damage detection

in bridge structures. After choosing the accelerance frequency response function as the appropriate bridge signature for condition monitoring, the authors defined, then detailed the three stages of signature recognition. They defined the first stage as the preprocessing step, in which signatures are smoothed and noise is eliminated prior to application of signature-recognition tools. Stage two, the processing stage, involves the use of pattern-recognition tools to emphasize certain features in the signature. The third stage is the interpretation phase, in which heuristic or experience-based criteria are used to determine if two signatures are significantly different, based on the features highlighted in the second stage. In the remainder of Part I, the authors presented the details of the various methods that can be used to complete the three stages. In Part II of the paper, Samman and Biswas (1994b) described an application of the theory given in Part I, involving the identification of the presence of simulated cracks in the girders of a laboratory bridge specimen and in an existing highway bridge.

Lenett et al. (1997) discussed many of the quality control issues that should be addressed when using modal analysis for integrity assessment of bridges. Most of the guidelines they mentioned are applicable to other modal testing applications as well. Two “behavioral assumptions which are fundamental requirements of modal analysis” were specified to be linearity and time-invariance. The authors explained that linearity is usually verified (or denied) using Maxwell-Betti’s principle of reciprocity. Typically, FRF’s from two reciprocal locations (e.g. H_{23} and H_{32}) are overlaid; for linear systems, the plots will be nearly identical, while there will be noticeable differences between the two for systems containing nonlinearities. An alternate linearity check involves the comparison of FRF’s

collected from the same source/receiver pair with different levels of excitation. Linear systems should reveal that increasing the excitation level increases the response level proportionally, so that the division of the response by the excitation (i.e. the FRF) should produce the same results for each force level.

Time-invariance, the second requirement enumerated by Lennett et al., is somewhat of a concern for bridge structures due to the fact that steel, concrete, and asphalt have temperature-dependent stiffnesses. After conducting tests at various times of the day for several days and comparing results, the authors concluded that, “testing at a particular time of day and the use of an optimum [test DOF] grid will permit the investigated bridge to be modelled as a time-invariant system.” The authors also addressed the various quality control measures that can be taken to ensure that linearity and time-invariance are satisfied, and that the data is not corrupted with bias-type errors. Measures they discussed included temperature control, proper data acquisition settings, maximization of signal-to-noise ratios, optimum hammer characteristics, and checks of raw time data and FRF’s to eliminate obviously flawed results.

There are numerous other publications that provide excellent descriptions of and commentary about condition assessment and damage detection of structural systems using modal analysis. Doebling et al. have compiled and given summaries of a comprehensive list of such works, and the interested reader is encouraged to consult their paper, available on the World Wide Web at http://esaea-www.esa.lanl.gov/damage_id/.

3.3 Application of Modal Analysis to the Pile Length Determination Problem

Now that the basic concepts and some structural applications of the modal analysis procedure have been explored, it can be seen that this process seemed particularly well suited to the unknown pile length problem. Figure 3.10 shows an idealization of a typical pile encased in a bent cap. For the present project, it was assumed that all of the labeled parameters were either known or could be measured, except for L_2 , the length of pile embedded in the surrounding soil.

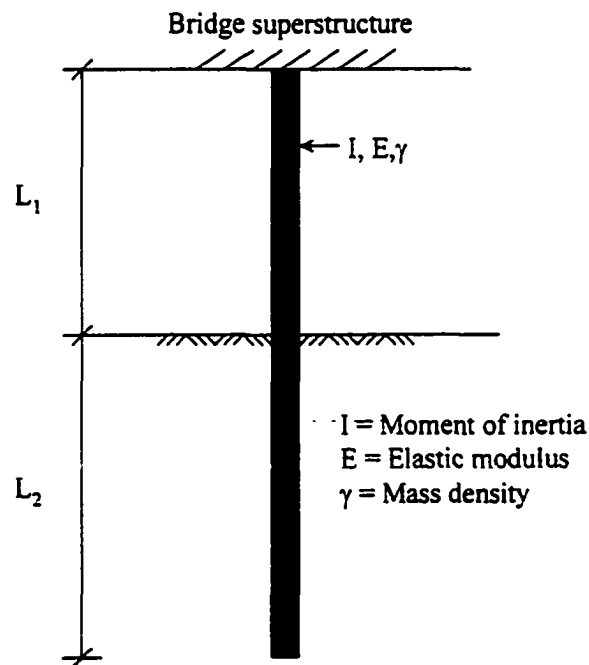


Figure 3.10 Schematic of Pile Encased in Bridge Superstructure

Since the ratio of a pile's length to its section depth is quite large, it was considered to be a long, slender member. From simple beam theory, one may recall that the natural

frequencies of undamped transverse vibrations are a function of a beam's physical properties and end conditions, according to the following equation:

$$\omega_r = \frac{k^2}{L^2} \sqrt{\frac{EI}{\gamma}} \quad (3.12)$$

where

ω_r = the r^{th} mode natural frequency,

k = dimensionless constant based on end restraint conditions,

L = beam length = $L_1 + L_2$,

E = modulus of elasticity,

I = moment of inertia, and

γ = mass per unit length of the beam.

Examination of the above equation revealed two points related to the present study. The first was quite obvious, that as the beam length is varied (in this case due to a variation in length of the embedded portion, L_2), the natural frequency values change accordingly. Secondly, for a given end condition, the length term should dominate the frequency computation since it is squared while the remaining terms are raised to the $\frac{1}{2}$ power. Although Equation 3.12 is based on simple beam theory, expressions for more complex beams are similar in form. In all cases, the natural frequencies are functions of the quantities pictured in Figure 3.10, all of which are known except one. It was believed, then,

that if the frequency response to a known flexural excitation could be obtained (through modal analysis), the unknown length could be “backcalculated” from Equation 3.12.

It was clear from the beginning of the project that the two primary complexities present in the pile length determination problem were the effect that the embedment soil had on the modal parameters, and the proper determination of the true boundary conditions. Chapter IV contains a description of the testing procedure used to quantify these effects, and the corresponding analytical models are presented in Chapter V.

CHAPTER IV

MODAL ANALYSIS TEST PROCEDURE

4.1 Test Method

The small-scale pile facility constructed for the present study was described in detail and pictured in Chapter II. In the following paragraphs, the modal analysis testing procedure used to characterize the small-scale piles' modal properties is summarized, and the test results are discussed. As stated previously, the primary objective of the testing series was to quantify the variation in modal parameters determined for piles with different embedment lengths. Once the modal parameters for each pile were identified, they would be used to backcalculate the length of the embedded portion, remembering that all other properties were known or were easily measured.

The first pile group studied consisted of five steel S3x5.7 piles, designated as A through E, having identical exposed lengths and different embedded lengths, which ranged from one foot for Pile A to five feet for Pile E. Table 4.1 gives details of the Group I pile configuration, and Figure 4.1 illustrates their placement within the test facility. Figure 4.2 shows the dimensions for a typical S3x5.7 steel section, while the orientation of the test piles with respect to the supporting W10x45 section is presented in Figure 4.3.

Table 4.1 Details of Group I Test Piles

Pile	Total Length	Exposed Length	Embedded Length
A	6 ft.	5 ft.	1 ft.
B	7 ft.	5 ft.	2 ft.
C	8 ft.	5 ft.	3 ft.
D	9 ft.	5 ft.	4 ft.
E	10 ft.	5 ft.	5 ft.

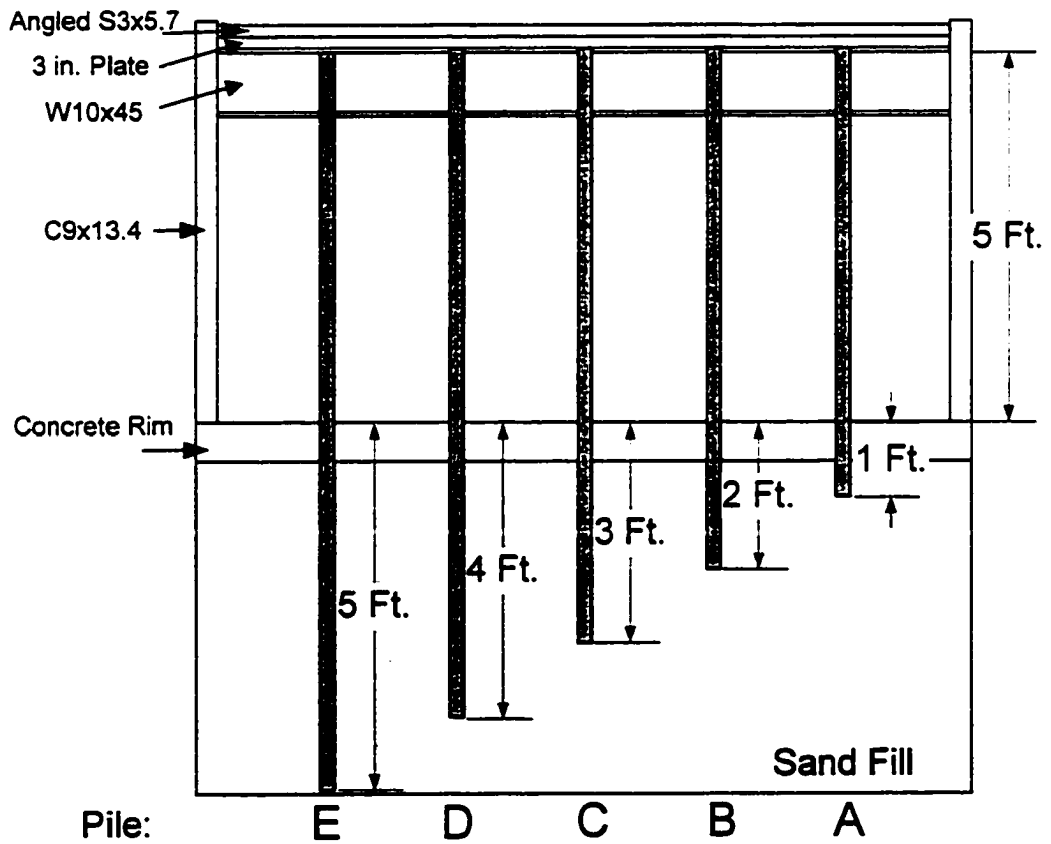


Figure 4.1 Configuration of Pile Group I

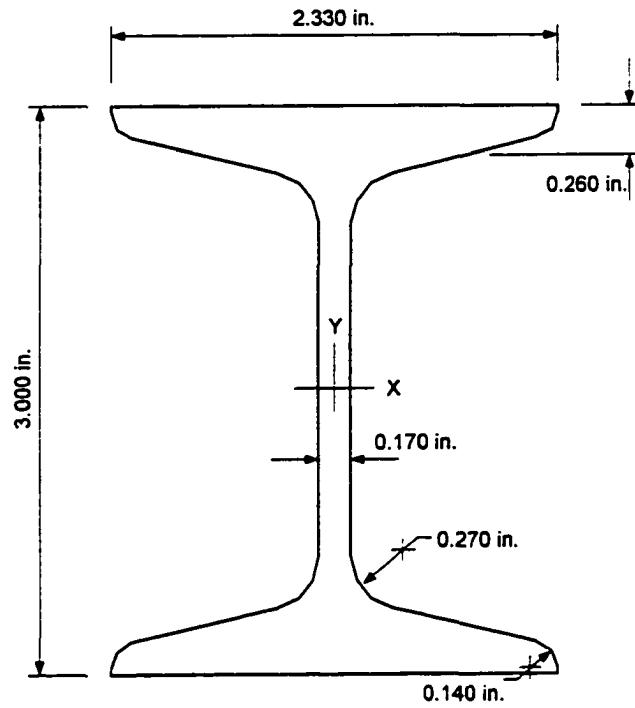


Figure 4.2 Dimensions for S3x5.7 Section

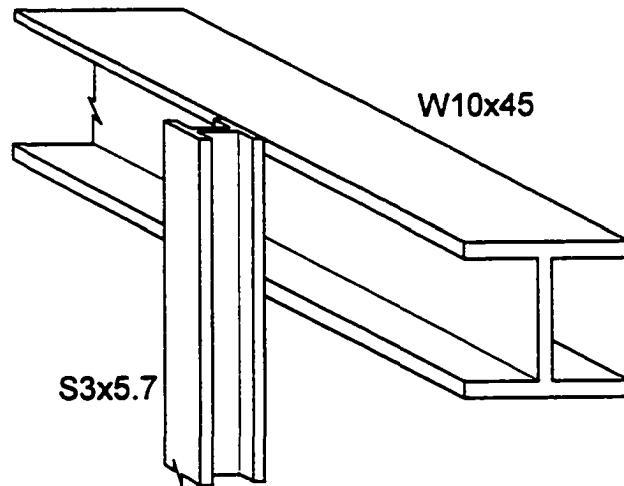


Figure 4.3 Orientation of S3x5.7 Test Specimen with Respect to Supporting W10x45

4.1.1 Test Grid

Nonembedded Tests. To obtain data for the simplest available boundary conditions, Pile A was tested before the sand fill was placed in the pit. Without the embedment sand present, each pile was essentially a cantilevered beam, and the intent was to collect modal data that could be compared to that generated from a closed-form solution, as well as a finite element analysis for a fixed-free beam.

The test grid for Pile A in the nonembedded configuration is shown in Figure 4.4. The numbered positions are locations at which the pile was either impacted or at which the accelerometer was attached to record the wave motion resulting from an impact; the test procedure will be described in detail in the next section.

Embedded Tests. After the tests for Pile A in the nonembedded configuration were completed, the sand fill was placed in the pit in the manner described in Chapter II. Since each of the piles A through E then had an exposed length of 5 ft., the test grid for each was identical, and is pictured in Figure 4.5.

4.1.2 Test Procedure

For each test, an accelerometer was placed at one of the numbered positions, and the impact hammer described in Chapter II was used to strike the pile at that or another of the designated locations. The resulting force and acceleration data were collected, converted from analog to digital format, transformed into the frequency domain, and used to compute a frequency response function, which was then displayed on the signal analyzer's screen. The coherence function (described in Chapter III) was displayed concurrently with the FRF, so

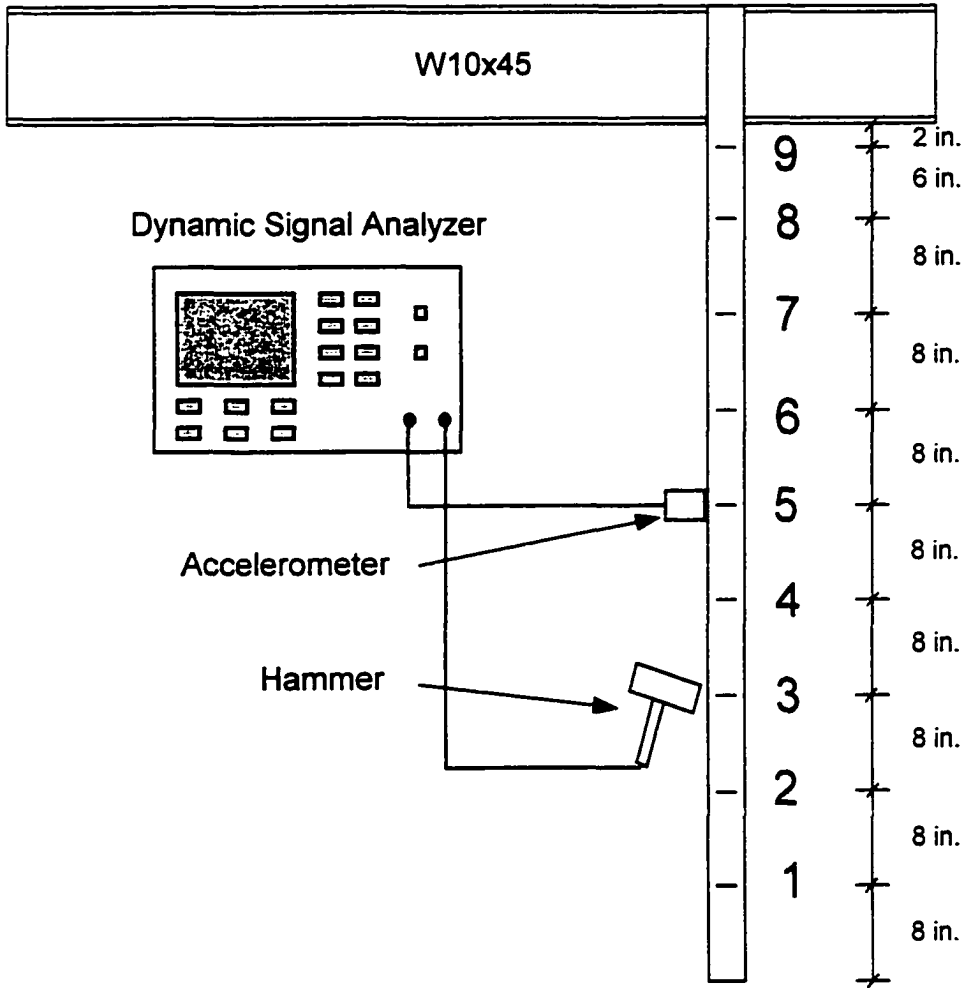


Figure 4.4 Test Grid for Pile A in Nonembedded Configuration

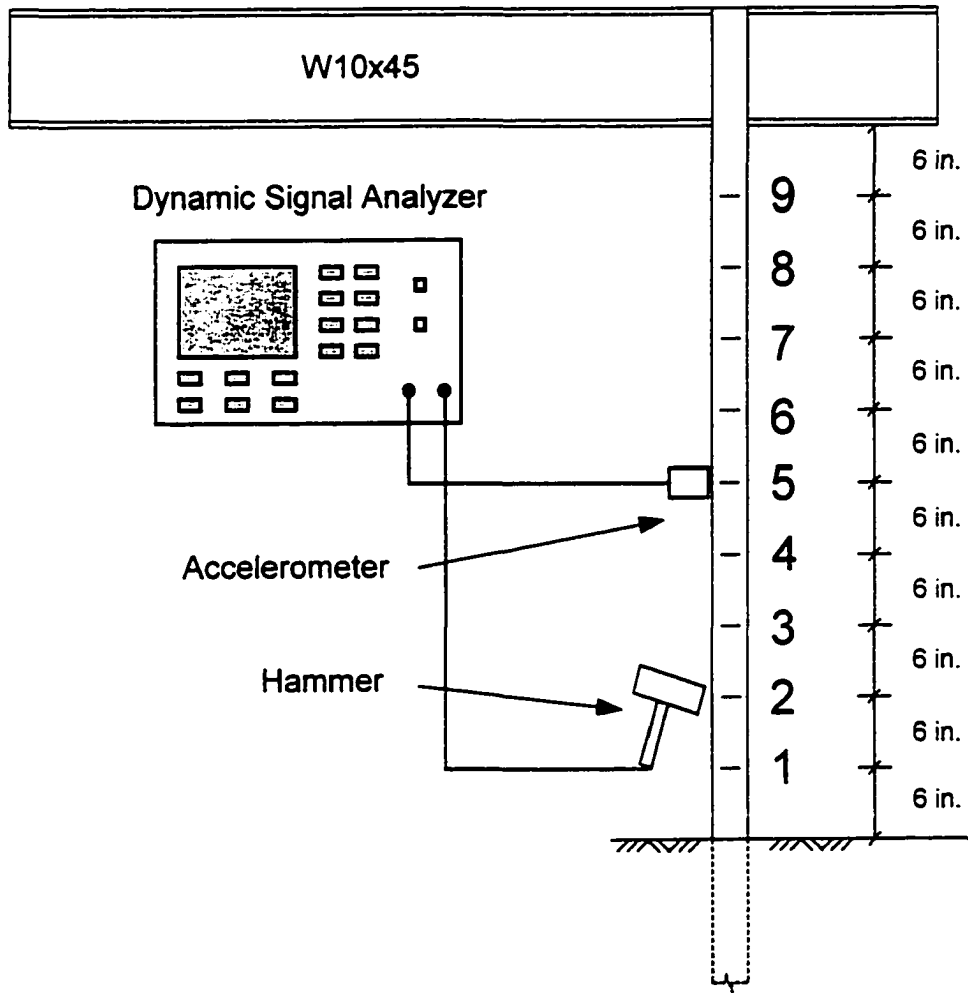


Figure 4.5 Test Grid for Piles A-E in Embedded Configuration

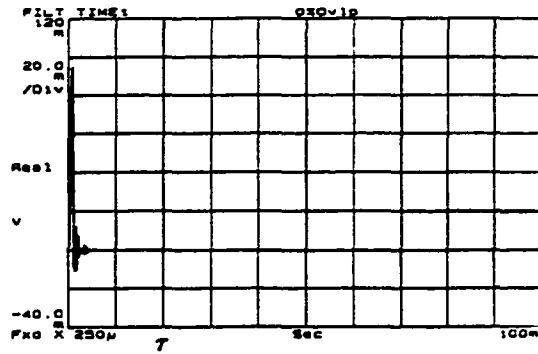
that aberrant signals could be identified and their cause investigated. If all of the displays were found to be acceptable, the test was repeated until five FRF's had been recorded and averaged for that particular source/receiver location combination. Five averages were used to reduce the bias error associated with the frequency response computation, as discussed in Chapter III. This was in accordance with the international standard (ISO 7626-5:1994) that deals with tests of this type, which states that “[i]n a low-noise environment, averaging three to five impacts is usually sufficient to verify data quality.”

The hammer was then moved to a different position, and the entire process was repeated for the new source/receiver combination. In order to perform the tests in an organized manner, the first impact was applied at the topmost position (Position 9 of Figures 4.4 and 4.5), then the impact position was moved systematically down the pile to successively lower-numbered locations. After FRF's had been collected for each of the required impact positions, the accelerometer was relocated, and the impact process repeated. Due to the principle of dynamic reciprocity, mentioned briefly in Chapter III, only the upper (or lower) triangular portion of the complete FRF matrix was required, but several additional measurements were performed to verify the linearity of the system, as recommended in the international standard quoted in the preceding paragraph. Frequency response functions were designated using the letter of the specific pile being examined, along with the numbers of the source and receiver locations for a particular test. For instance, C58 refers to the FRF measured on Pile C, with the accelerometer located at Position 5, and the impact applied at Position 8.

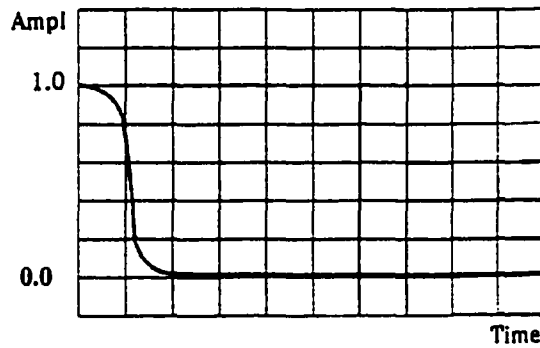
Measurements of the type described above were performed along both the X and Y axes of the S3x5.7 sections, since the different stiffnesses exhibited along each axis resulted in unique responses to dynamic impacts for each direction. Care was taken when testing along the Y axis to impact as near to the center of the flange as possible (the impact position was marked on the flange), so that the impulse would travel directly through the web (which was only 0.17 inches thick) to the accelerometer on the other side.

4.1.3 Data Windowing

Since the time duration of an impact is usually much shorter than the total time sample length, the energy of the noise present in the portion of the signal following the impact may be significant compared to that of the impact itself, even for traces with high signal-to-noise ratios (Halvorsen and Brown, 1977). Since the impact event is the only real area of interest, a mathematical “window” has been developed that greatly reduces the noise in the remaining segment of the force signal. The force window is a function that begins with a flat portion of amplitude 1.0 (corresponding to the time that the impact is occurring), followed by a cosine taper leading to another flat section of amplitude zero that lasts for the duration of the sample length. Elimination of the noisy segment of the signal significantly improves the quality of frequency response functions that utilize impact excitation (Halvorsen and Brown, 1977). Figure 4.6 shows a typical impact force pulse and the associated force window.



Force Pulse



Force Window

Figure 4.6 Typical Impact Force Pulse and Force Window (HP App. Note 243-3)

Undesirable noise may also comprise a large part of the response signal if the test structure is heavily damped and the signal decays quickly relative to the total time sampled. For lightly damped structures, though, the response signal may not have substantially decayed by the end of the time record. If this is the case, the signal will be abruptly truncated at the end of the sample time, leading to the phenomenon known as “leakage,” in which the resonance peaks in the signal’s frequency spectrum are broader than those

without truncation, have lower amplitude values, and are accompanied by smaller secondary lobes on either side of the peak (Døssing, 1988). Leakage is a result of the nature of Fourier transformation, since it is only ideally suited to perfectly periodic signals. Figure 4.7 shows the relation between truncated and nontruncated displacement time histories, $x(t)$, and their corresponding Fourier transforms, denoted as $|\hat{X}(\omega)|$, where the scripted F's above the curved arrows represent Fourier transformation into the frequency domain.

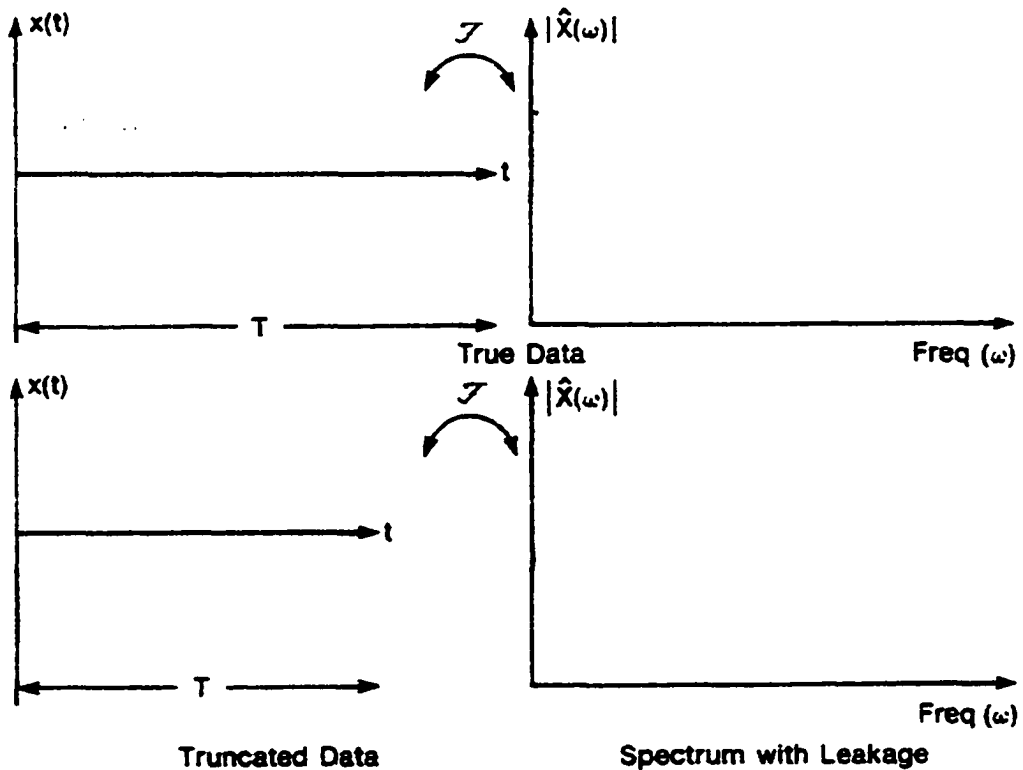


Figure 4.7 Illustration of Leakage Phenomenon (Døssing, 1988)

An exponential window can deal effectively with both of the situations discussed above. The window consists of an exponentially decaying function of the form given in Equation 4.1 below.

$$w(t) = e^{-\frac{t}{\tau}} \quad (4.1)$$

where

$w(t)$ = window function (function of time, t), and

τ = selected time delay constant.

As is evident from Equation 4.1, the exponential window has an initial value of 1.0 at time $t = 0$, after which it decays at a rate dependent on the value chosen for τ (which corresponds to the time it takes to decrease in amplitude by an amount $1/e$). Various guidelines exist for choosing the proper time constant; one recommendation is to select it so that the amplitude of the response signal will decrease to 1-5% of its initial value by the end of the time record (Halvorsen and Brown, 1977; ISO 7626-5:1994), while another is to set the value of τ to be $\frac{1}{4}$ of the total time record (Hewlett-Packard, 1986). In any case, multiplication of the exponential window by the time-domain response record serves to significantly decrease errors due to excessive noise for highly damped structures, and due to truncation errors for lightly damped structures.

Figure 4.8 illustrates the effect an exponential window has on a test specimen's displacement response to an impact. Once again, the scripted F 's above the arrows refer to

Fourier transformation into the frequency domain, and the autospectrums of the time signal before and after windowing are computed and denoted as $G_{xx}(\omega)$. The figure shows that although the measured resonance peak in the windowed autospectrum is slightly broader and lower in amplitude than the true peak, the resulting trace is much cleaner than that for the unwindowed data. Halvorsen and Brown (1977) stated the following concerning the exponential window:

...the exponential window does change the resulting measured frequency response function; but its only effect is to increase the apparent damping in the resonances. It does not change the resonance frequencies and, because the effect of the exponential window is the same on all frequency response measurements, it will not alter the measured mode shapes if applied to all measured frequency response functions. In addition to reducing noise and truncation errors, the exponential window will also reduce errors which often occur when testing lightly damped systems in which the damping varies with the measurement position on the structure.

Force and exponential windows were applied to all data collected for the modal analysis work described in this chapter.

4.2 Modal Parameter Estimation

As discussed in Chapter III, the frequency polyreference modal parameter estimation technique was employed to extract the modal characteristics of Piles A through E. It was also mentioned that several tools were available to facilitate the estimation process; those used in the present study will be described in the following paragraphs.

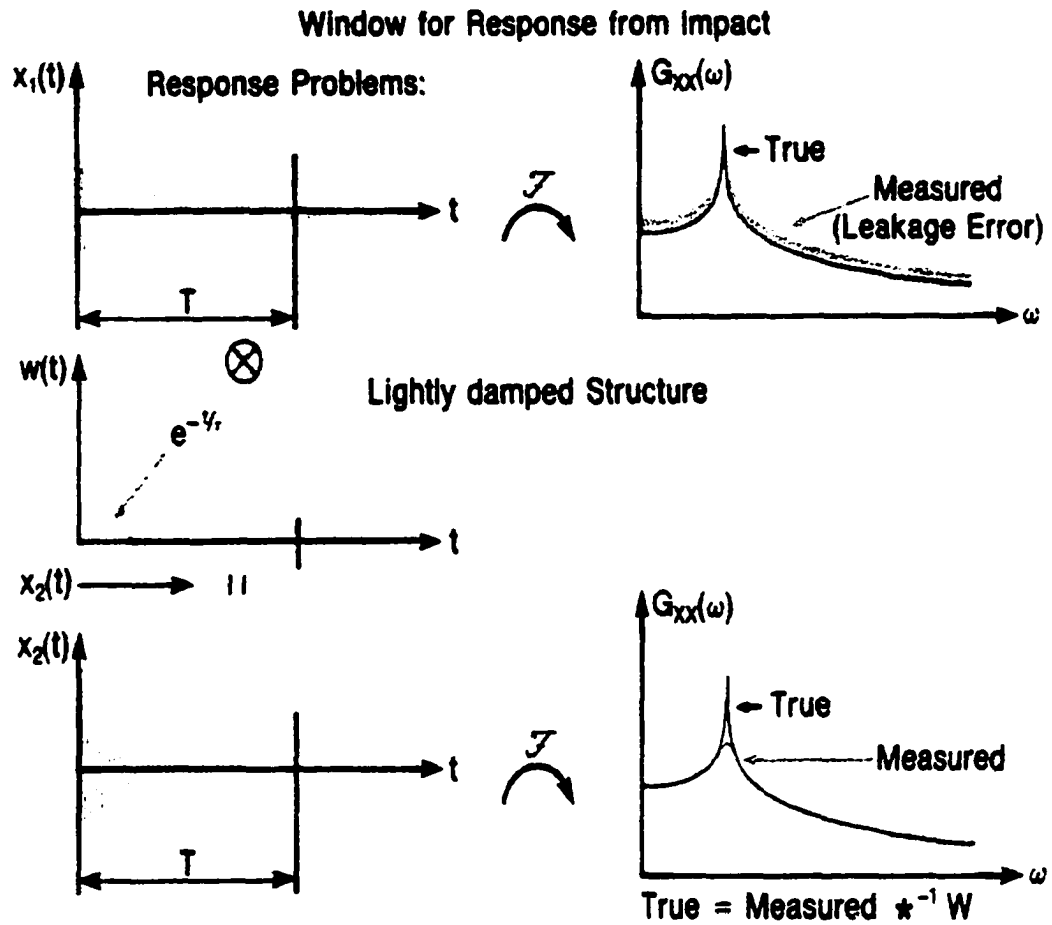


Figure 4.8 Effect of Applying Exponential Window to Response Signal (Døssing, 1988)

4.2.1 Stability Diagram

Figure 4.9 shows a set of typical driving point (impact applied at the same location as the accelerometer) frequency response functions for Pile A in the nonembedded configuration.

The data shown here has been analytically generated; it is used for illustration purposes

because it is "ideal" data and its trends are somewhat more easily identifiable than those of the experimental data are.

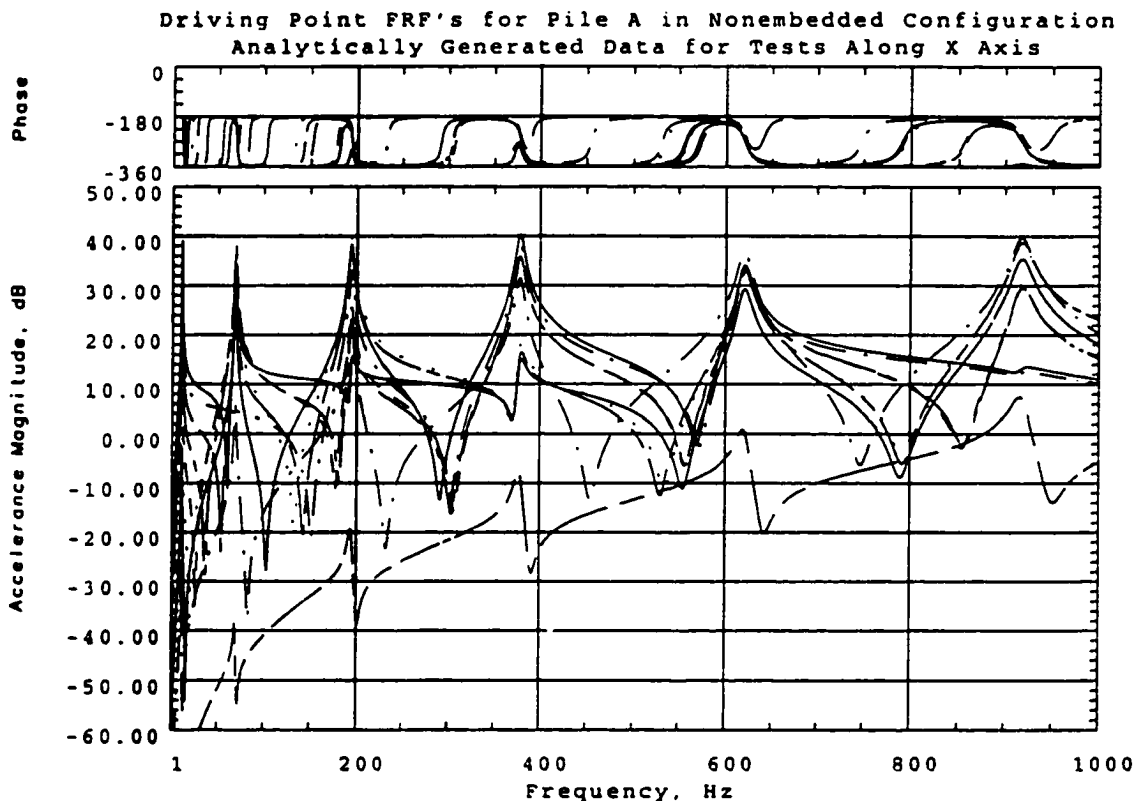


Figure 4.9 Analytically Generated Driving Point FRF's for Pile A (Nonembedded)

From the figure, one can observe that it would be a relatively simple task to estimate by eye the natural frequencies of the pile (frequencies where peaks exist). In fact, the

nonembedded configuration is essentially that of a cantilevered beam of the type described in Chapter II, whose modal parameters could indeed be identified without any type of curve-fitting scheme. However, experimental data is rarely as well behaved as analytical data, and natural frequencies are not always readily identifiable from plots of experimental FRF's.

Various tools exist in commercially available modal parameter identification packages (such as the frequency polyreference scheme found in I-DEAS Modal™) that allow for a more objective identification of the natural frequencies. One such tool that is commonly used to “pinpoint” the natural frequencies, and specifically, to establish the number of resonances that exist in the frequency range of interest, is the stability diagram. The stability diagram corresponding to the nonembedded Pile A data is presented in Figure 4.10. As is evident from the figure, the diagram is a plot of the number of poles (natural frequencies), or model order, versus frequency, and various symbols are employed to indicate the changing stability of the poles as the curve-fit model order increases. Allemang et al. (1994) described the stability diagram as follows:

The stability diagram...involves tracking the estimates of frequency, damping, and possibly modal participation factor as a function of model order. As the model order is increased, more and more modal frequencies are estimated but, hopefully, the estimates of the physical modal parameters will stabilize as the correct model order is found. For modes that are very active in the measured data, the modal parameters will stabilize at a very low model order. For modes that were poorly excited in the measured data, the modal parameters may not stabilize until a very high model order is chosen. Nevertheless, the nonphysical (computational) modes will not stabilize during this process and can be sorted out of the modal parameter data set...easily.

It is often helpful to overlay a plot of one of the measured frequency response functions onto the stability diagram to further aid in selection of the resonance locations. In Figure 4.10, the primary curve of the multivariate mode indicator function (MvMIF) has been

overlaid onto the stability diagram, and the selected natural frequencies have been circled for emphasis. Simply put, the MvMIF is a mathematical manipulation of the frequency response data obtained from multiple references; it is formed to identify normal modes (those for which the response is purely imaginary and lags the excitation force by exactly 90 degrees), and its graphical results appear as a series of sharp inverted peaks at resonance locations (Døssing, 1995).

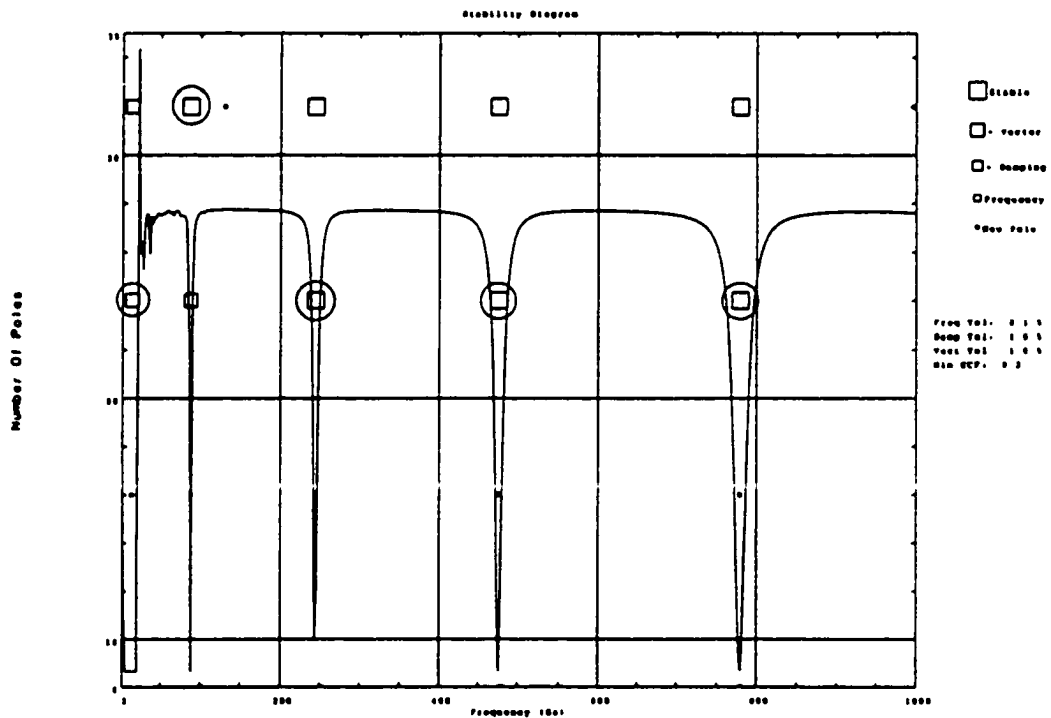


Figure 4.10 Stability Diagram for Nonembedded Pile A Data

4.2.2 Residue Comparison

Once the resonance locations have been determined, and the model order has been verified using the stability diagram, the natural frequencies and damping factors (which represent the percentage of critical damping for the pile-soil structural system) of the measured FRF's are calculated for each mode using the frequency polyreference curve-fitting scheme described previously. To make certain, then, that the curve-fit numerical estimation of the FRF's is in good accord with the measured data, residues are computed for each of the test specimen locations. In essence, this means that frequency response amplitude values are calculated and compared to those that were measured at each of the predetermined points. Figure 4.11 shows the residues that were determined for Position 4 of Pile A. In the figure, the plots (from top to bottom) show the accelerance FRF's at Position 4 due to impact at Positions 3 (top plot), 4 (second plot), and so on, through Position 7. The solid lines represent the Pile A data, while the broken lines represent the numerical estimates calculated by the software. It is evident from the figure that a good fit has been achieved (in fact, it is somewhat difficult to distinguish the solid lines from the broken lines, since the data lie so close together), and confidence can be placed in the modal parameter estimates, as would be expected for a simple case such as the one described here.

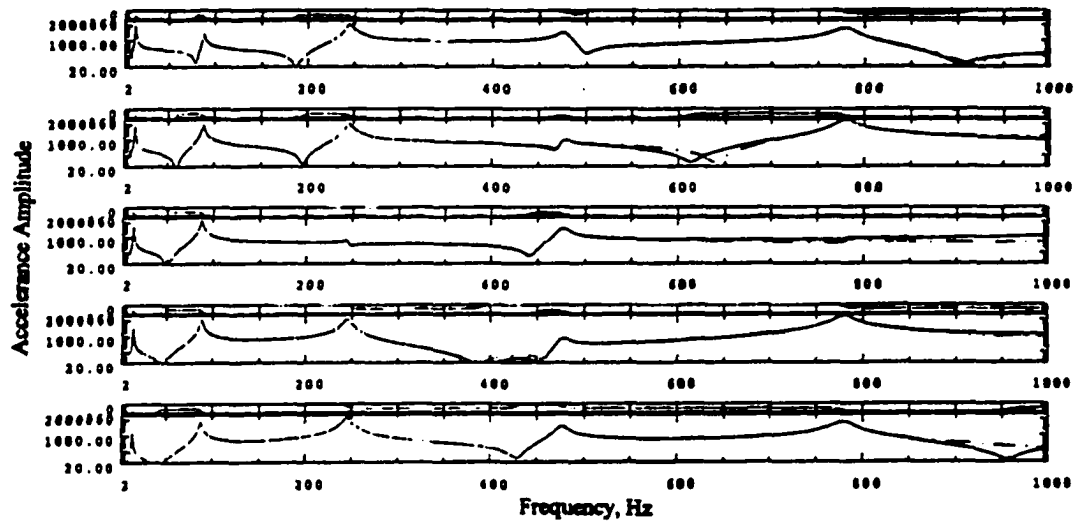


Figure 4.11 Residues for Pile A Data in the Nonembedded Configuration

Each of the procedures described above was applied to the data collected for the piles in Group I, and the measured FRF's and parameter estimation results will be presented in the next section. All of the estimations for the measured data were performed using the I-DEAS Modal™ software, produced by the Structural Dynamics Research Corporation (SDRC).

4.3 Experimental Test Results

4.3.1 Results for Tests Along the X Axis

For tests conducted along the X coordinate axis (as designated in Figure 4.2), the accelerometer was attached to the web of the S3x5.7 test specimen so that its axis was perpendicular to the length of the pile, as pictured in Figure 4.12. The impacts were applied with the same orientation, but were applied to the opposite side of the web for testing convenience. Plots validating the linearity of the Group I pile systems for tests along their X axes are presented in Figures 4.13 through 4.18. In the figures, frequency response functions measured for various reciprocal positions are overlaid; the close agreement between the two FRF's shown for every pile indicates that each of the pile-soil systems was indeed linear in nature.

It should be noted that all measurements for Pile A in the nonembedded configuration were performed for a frequency span of 0-1000 Hz. Preliminary numerical analyses (of the type that will be described in the next chapter) indicated that if significant differences existed in the frequency responses of the embedded piles, they would be exhibited at relatively high frequencies. Therefore, a frequency span of 0-5000 Hz was measured for the embedded piles.

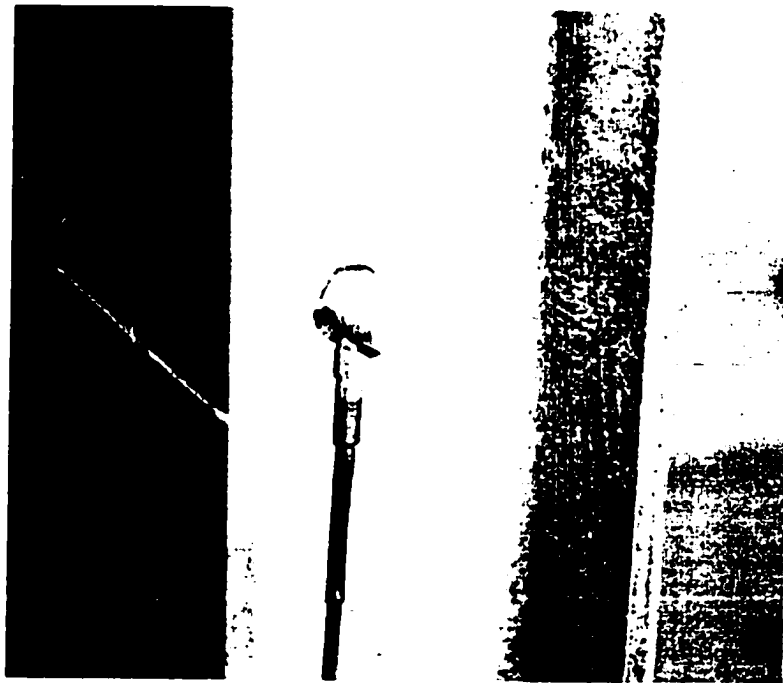


Figure 4.12 Illustration of Accelerometer Orientation for Tests Along the X Axis

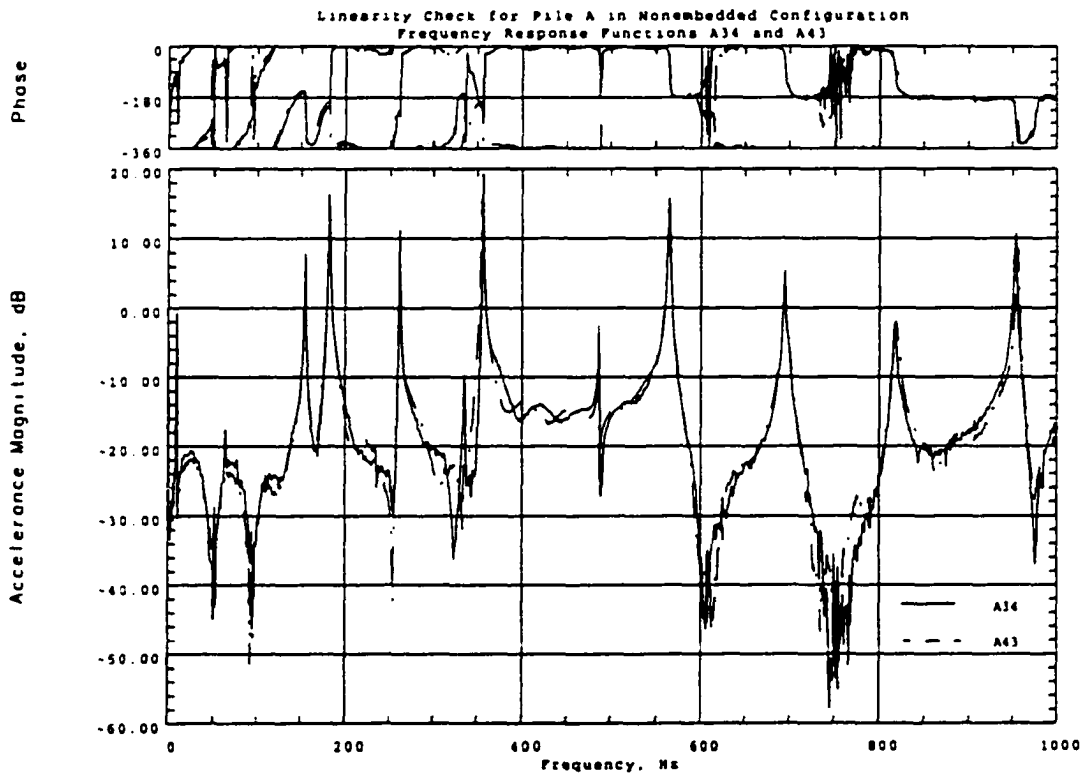


Figure 4.13 Linearity Validation Plot for Pile A in the Nonembedded Configuration, Tested Along the X Axis

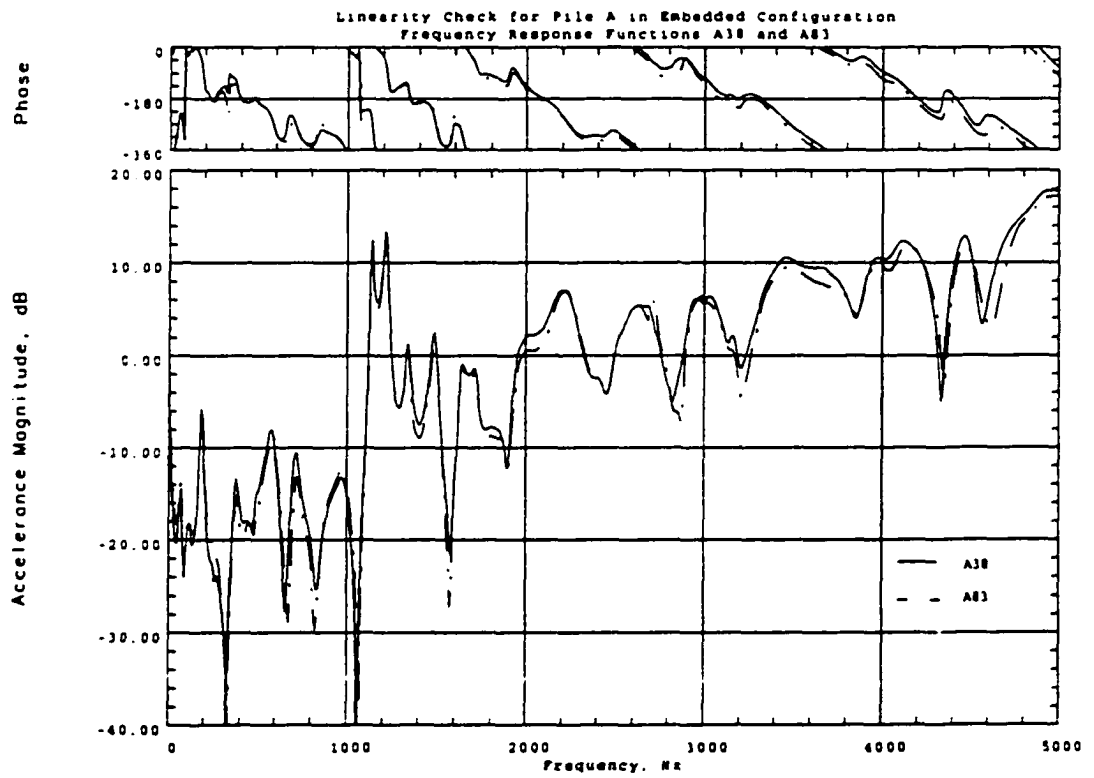


Figure 4.14 Linearity Validation Plot for Pile A in the Embedded Configuration, Tested Along the X Axis

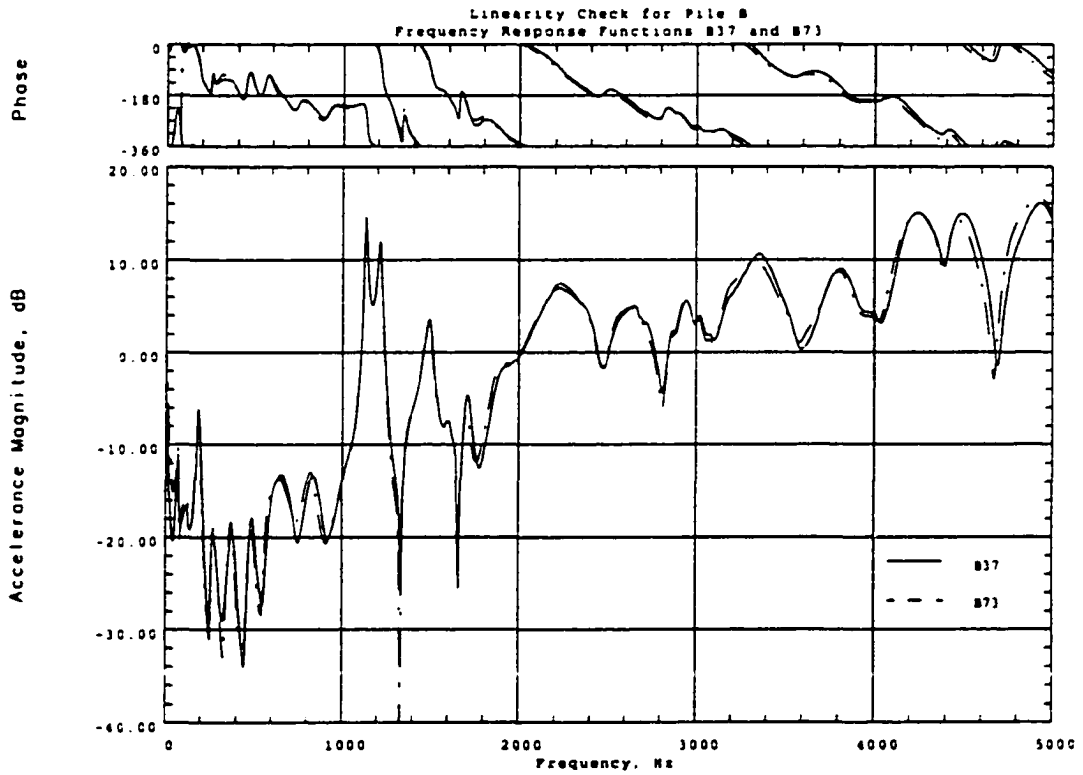


Figure 4.15 Linearity Validation Plot for Pile B, Tested Along the X Axis

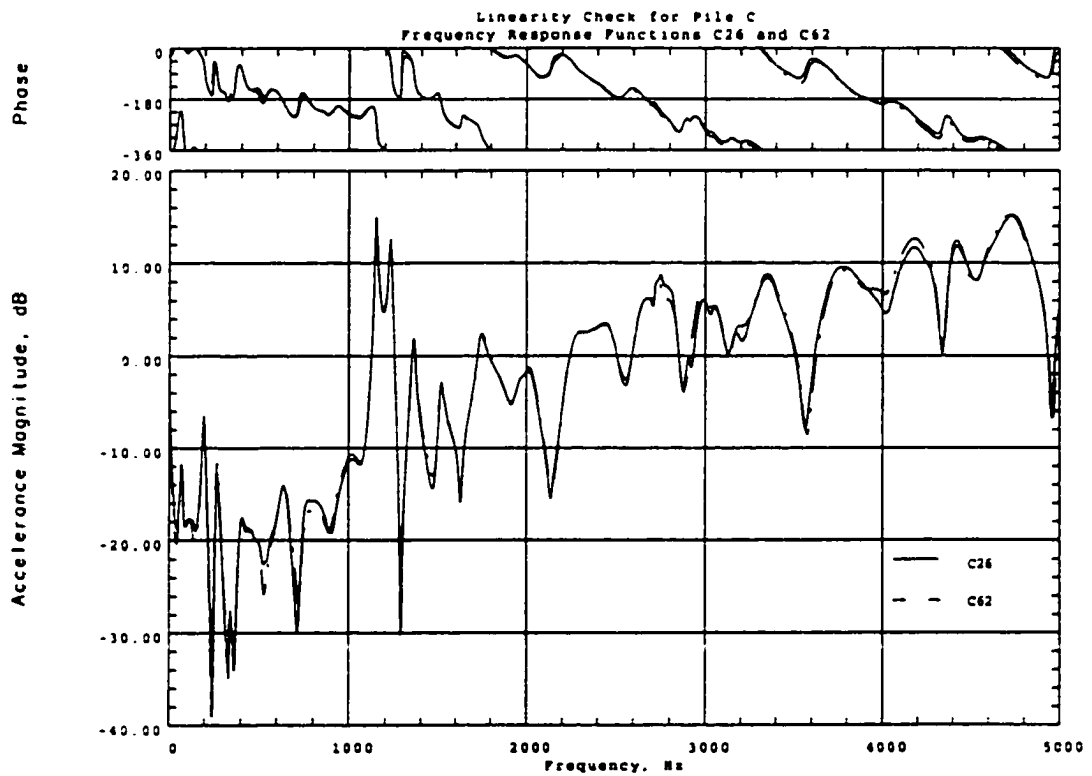


Figure 4.16 Linearity Validation Plot for Pile C, Tested Along the X Axis

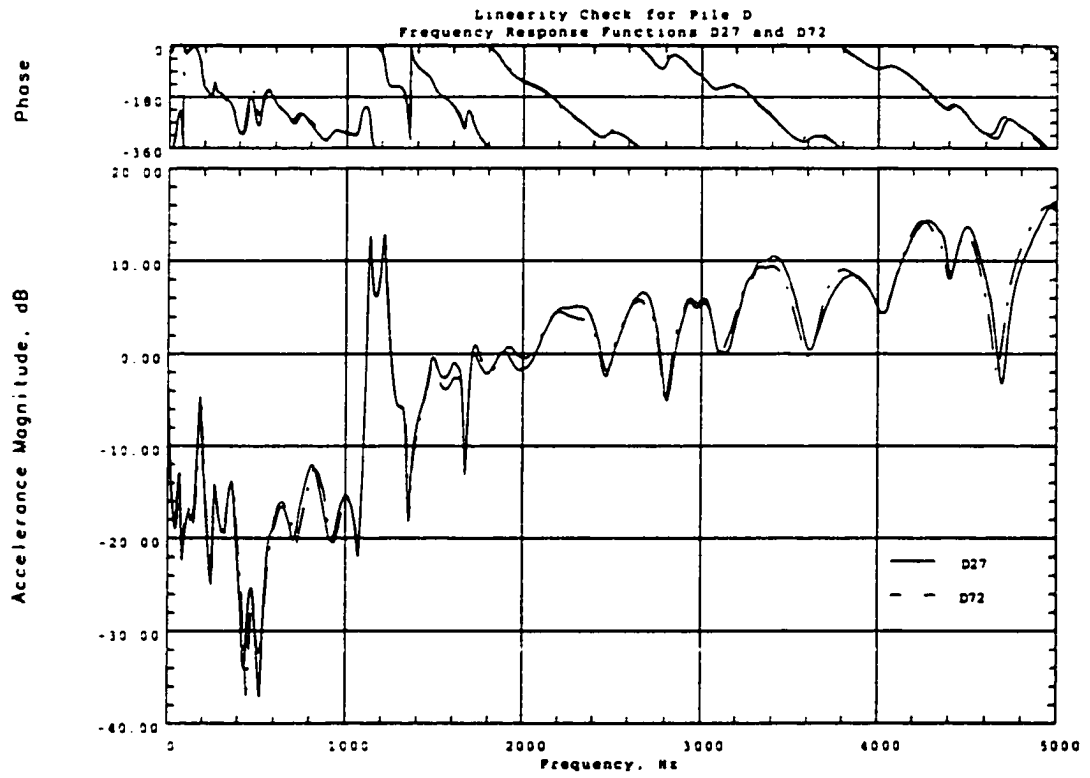


Figure 4.17 Linearity Validation Plot for Pile D, Tested Along the X Axis

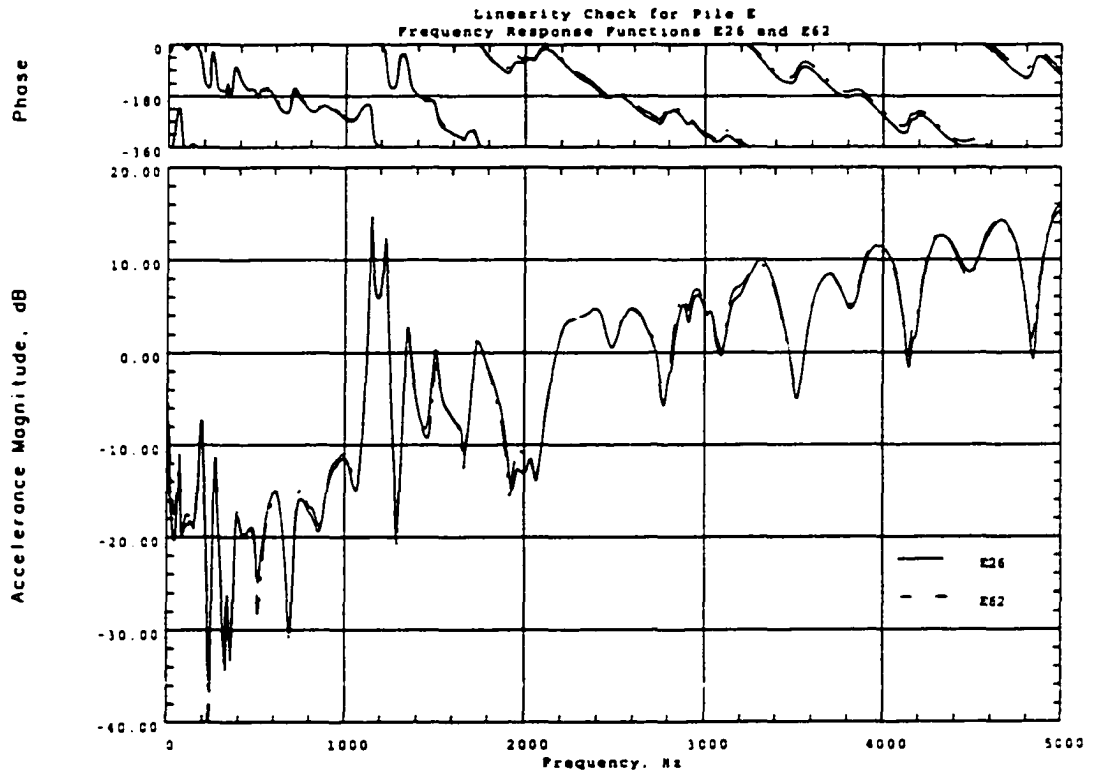


Figure 4.18 Linearity Validation Plot for Pile E, Tested Along the X Axis

Driving point frequency response functions are those for which the impact force and acceleration are measured at the same location, while cross-point FRF's are those for which the two are measured at different locations. To illustrate the general shapes and trends of the FRF's for each test pile, the nine driving point response functions for Piles A through E are overlaid and presented in Figures 4.19 through 4.24. It is important to note that for the modal parameter estimation process, driving point and cross-point measurements were included, but for clarity of illustration, only the driving point FRF's are presented in the following figures. Figures containing the remaining FRF's for Pile C (as a representative case) are included as Appendix A.

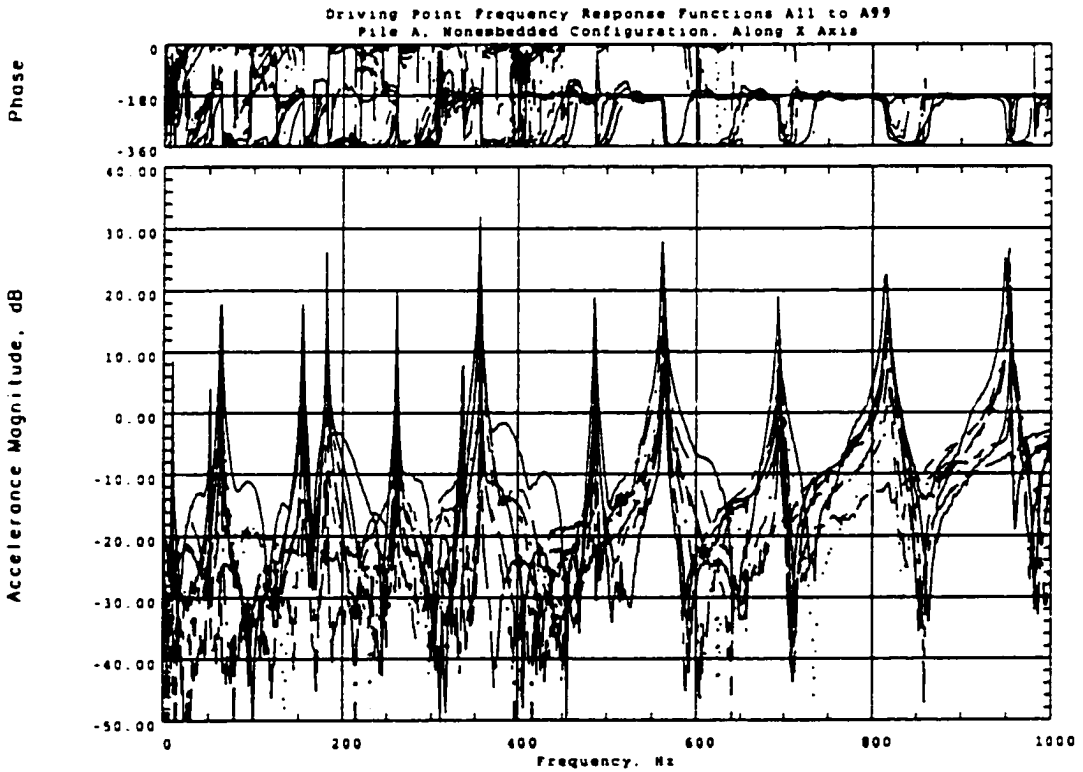


Figure 4.19 Driving Point Frequency Response Functions for Pile A, Nonembedded Configuration, Tested Along the X Axis

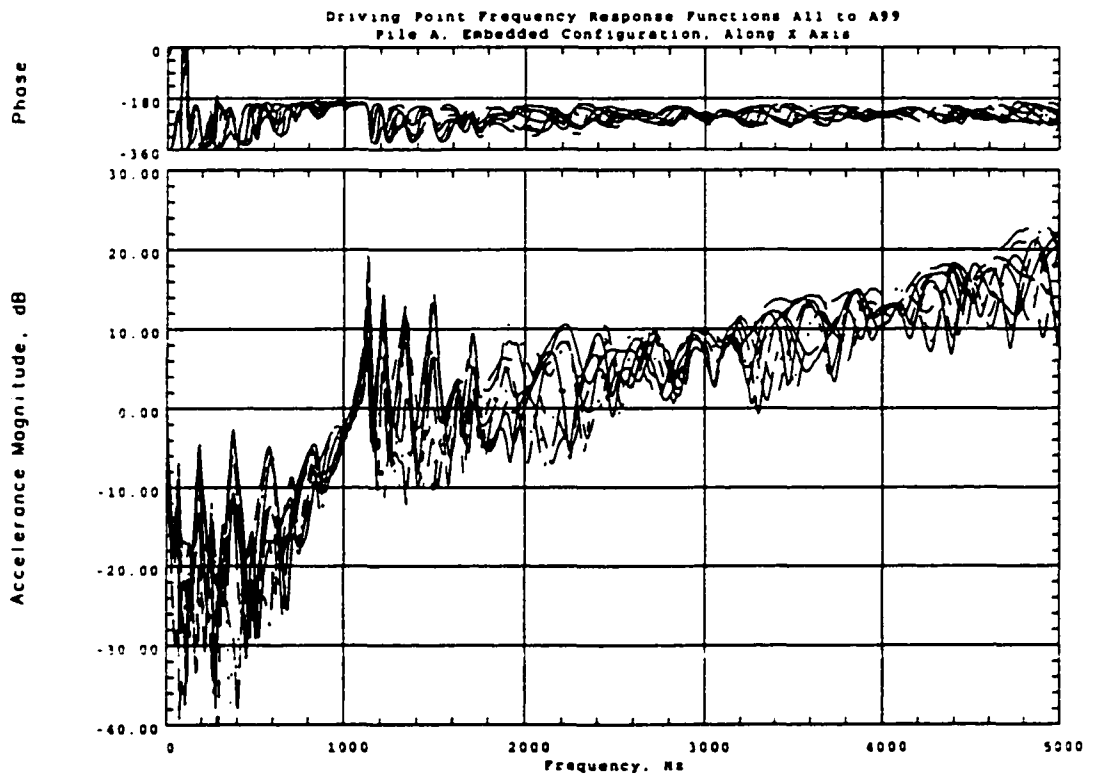


Figure 4.20 Driving Point Frequency Response Functions for Pile A, Embedded Configuration, Tested Along the X Axis

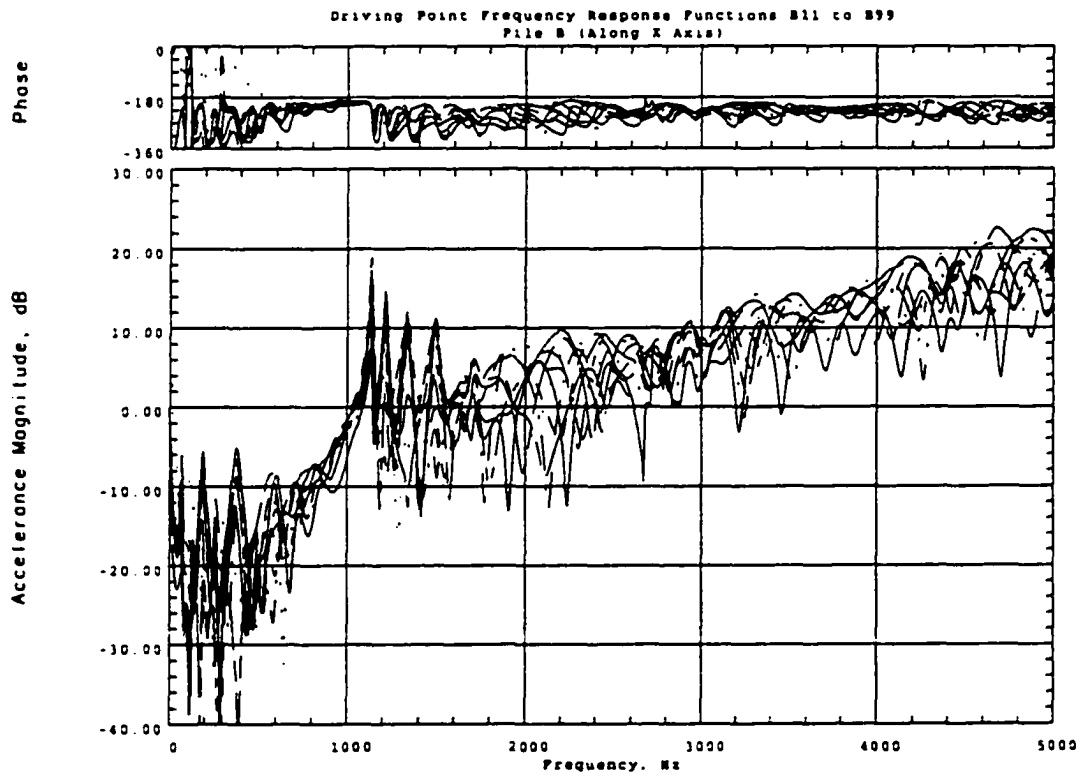


Figure 4.21 Driving Point Frequency Response Functions for Pile B, Tested Along X Axis

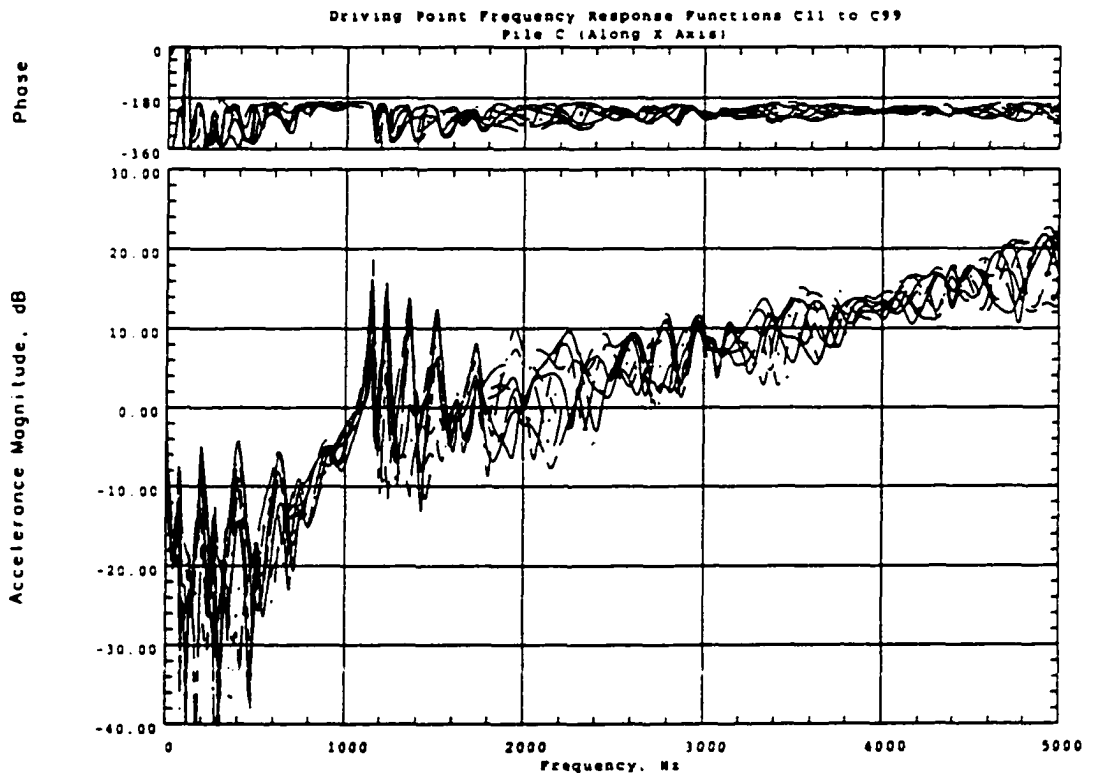


Figure 4.22 Driving Point Frequency Response Functions for Pile C, Tested Along X Axis

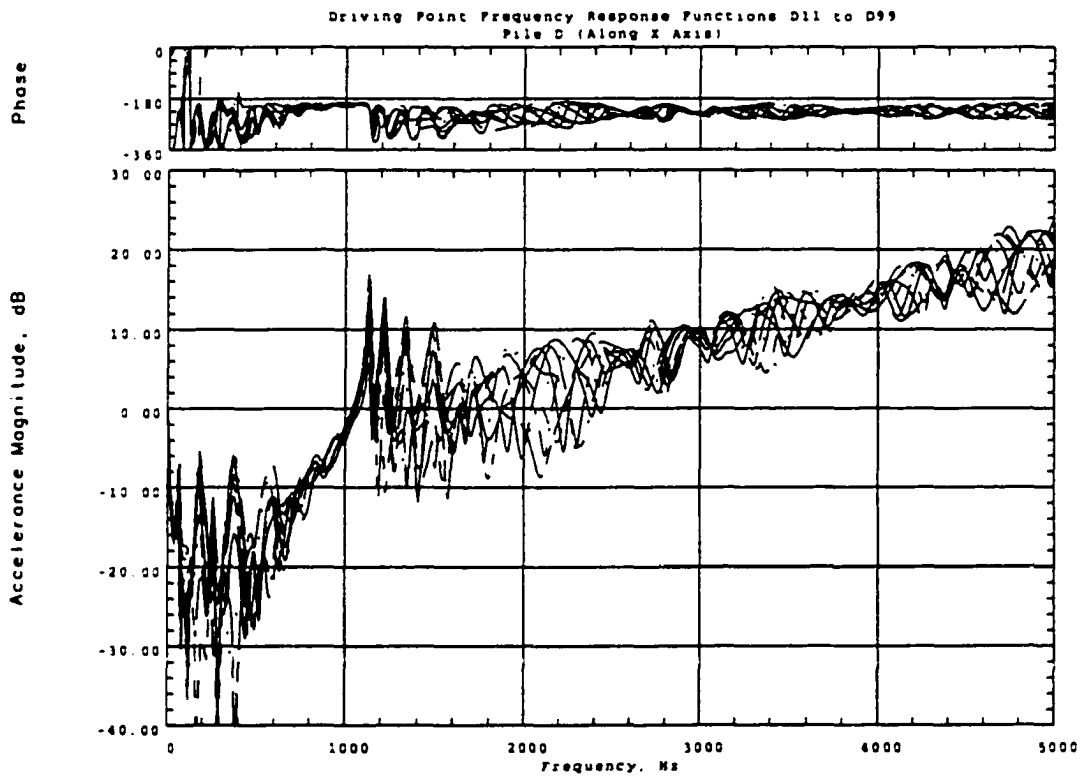


Figure 4.23 Driving Point Frequency Response Functions for Pile D, Tested Along X Axis

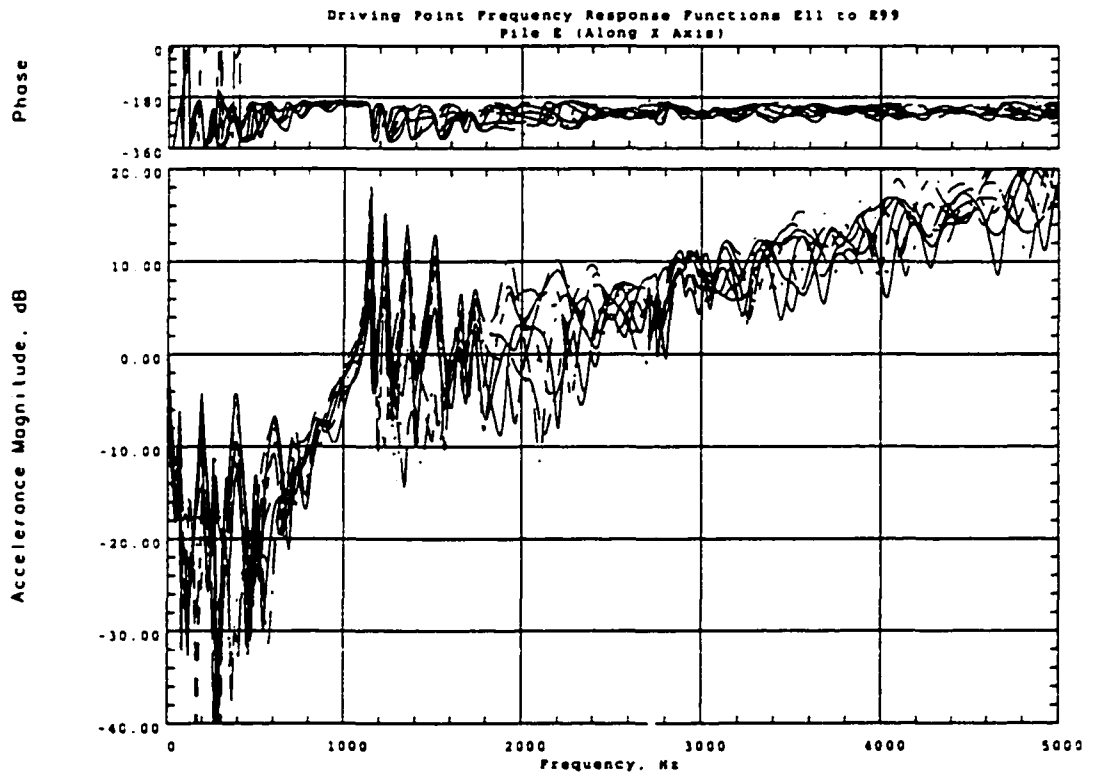


Figure 4.24 Driving Point Frequency Response Functions for Pile E, Tested Along X Axis

4.3.2 Results for Tests Along the Y Axis

For tests conducted along the Y coordinate axis (as designated in Figure 4.2), the accelerometer was attached to the outside flange of the S3x5.7 test specimen so that its axis was perpendicular to the length of the pile, as illustrated in Figure 4.25. The impacts were applied with the same orientation, but were applied to the opposite flange for testing convenience. Plots validating the linearity of the Group I pile systems for tests along their Y axes are presented in Figures 4.26 through 4.29. Once again, the close agreement between the two overlaid FRF's for each pile shown indicates the linear nature of the soil-pile systems. It should be noted that linearity validation tests along the Y axis were not performed for Pile A, but it is reasonable to assume that the results would be similar to those for Piles B through E.

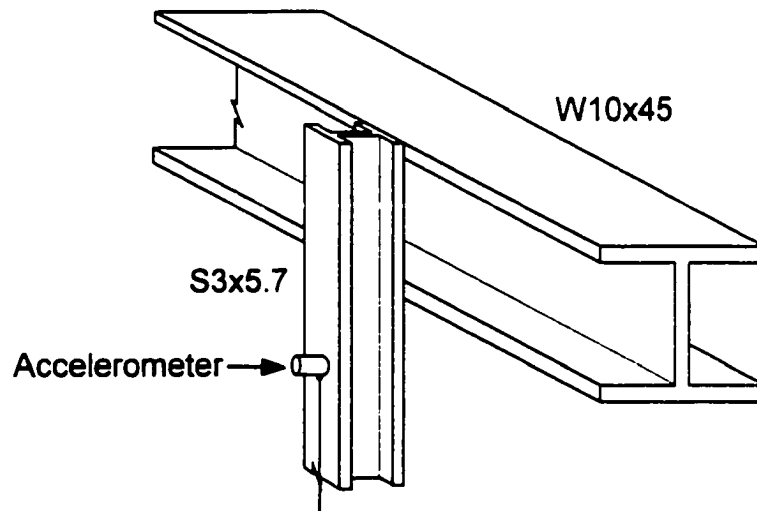


Figure 4.25 Illustration of Accelerometer Orientation for Tests Along the Y Axis

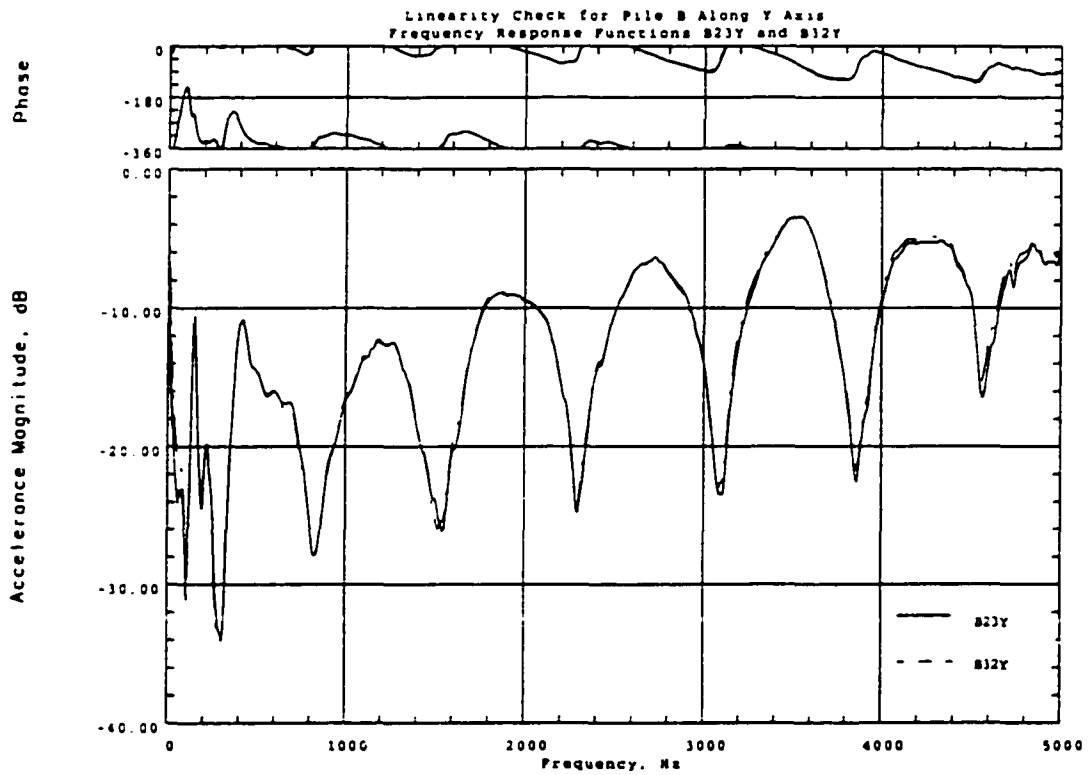


Figure 4.26 Linearity Validation Plot for Pile B, Tested Along the Y Axis

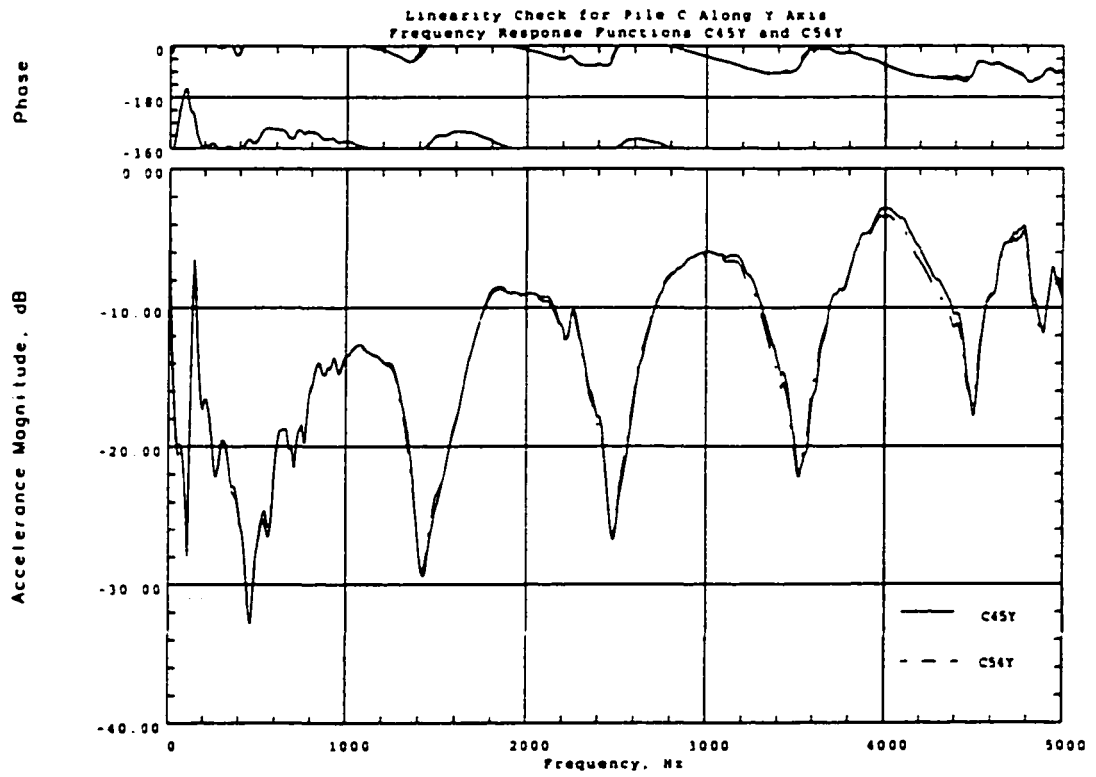


Figure 4.27 Linearity Validation Plot for Pile C, Tested Along the Y Axis

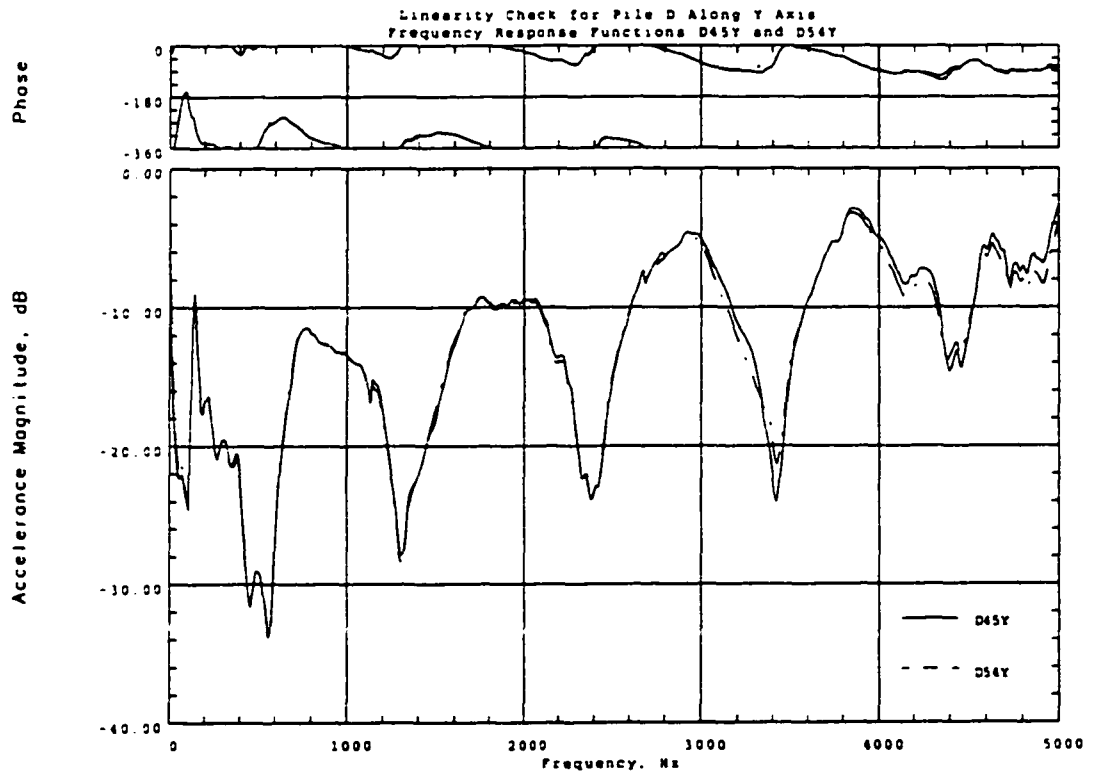


Figure 4.28 Linearity Validation Plot for Pile D. Tested Along the Y Axis

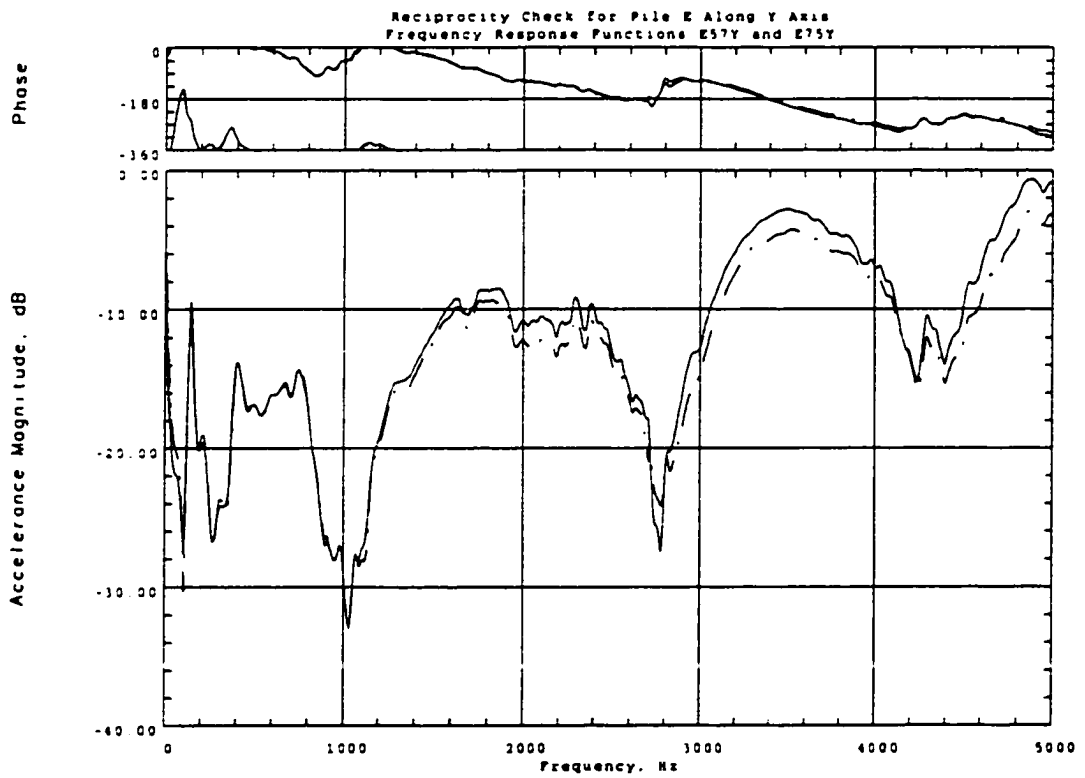


Figure 4.29 Linearity Validation Plot for Pile E, Tested Along the Y Axis

Driving point measurements conducted along the Y axis for Piles A through E, respectively, are presented in Figures 4.30 through 4.34. Once again, it should be noted that driving point and cross-point measurements were included in the modal parameter estimation process, but for clarity of illustration, only driving point FRF's are presented in the following figures.

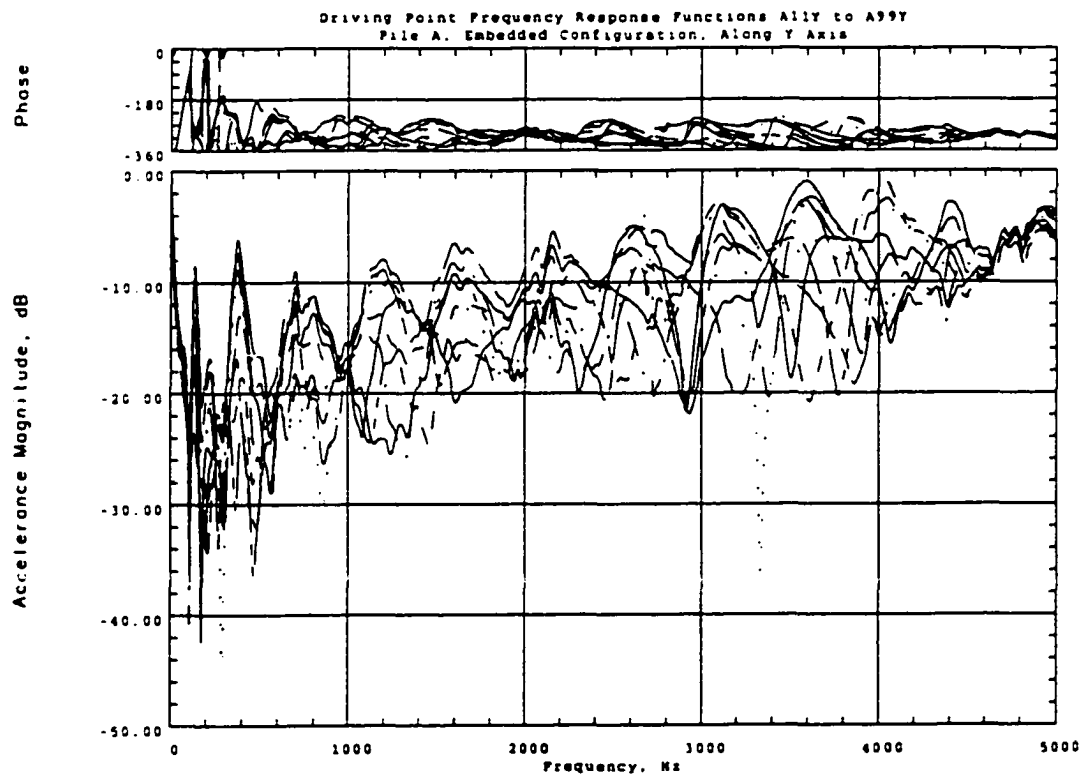


Figure 4.30 Driving Point Frequency Response Functions for Pile A, Embedded Configuration, Tested Along the Y Axis

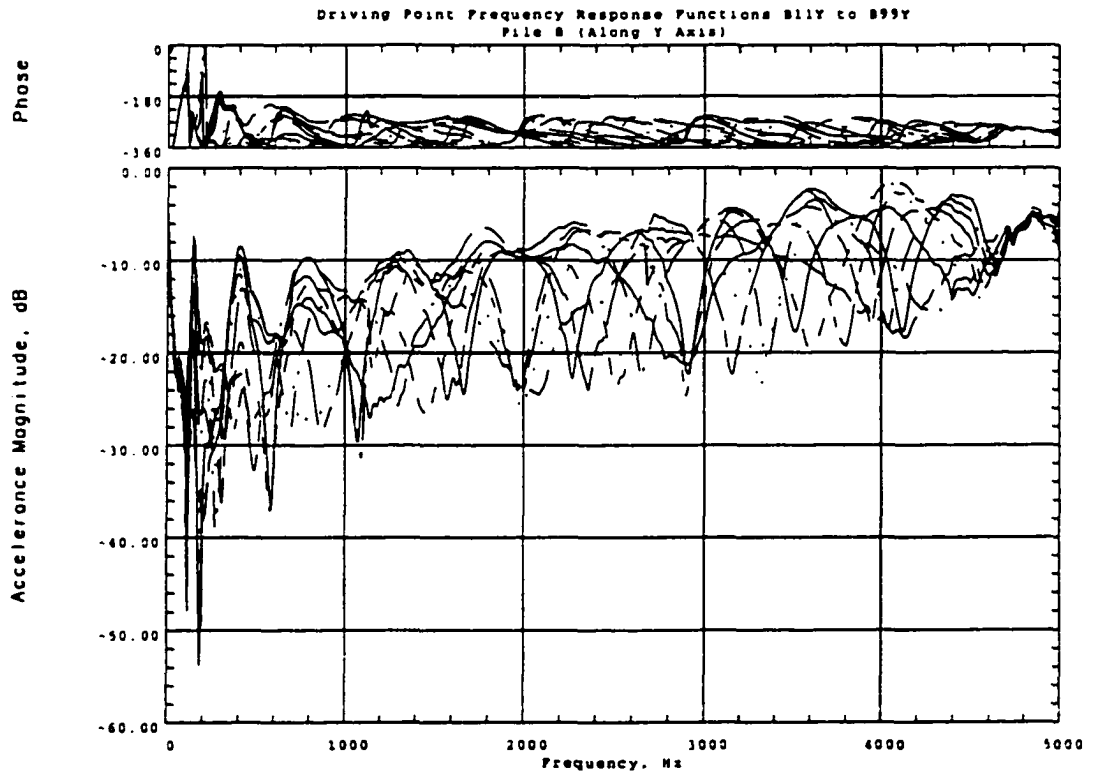


Figure 4.31 Driving Point Frequency Response Functions for Pile B, Tested Along Y Axis

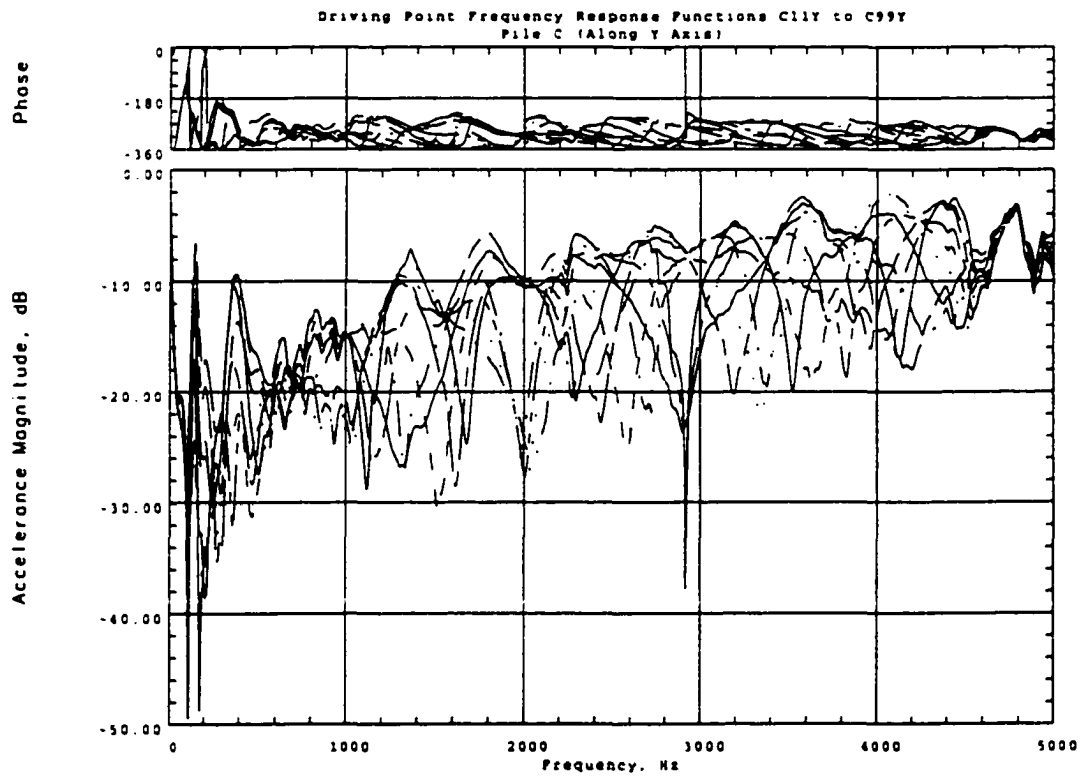


Figure 4.32 Driving Point Frequency Response Functions for Pile C, Tested Along Y Axis

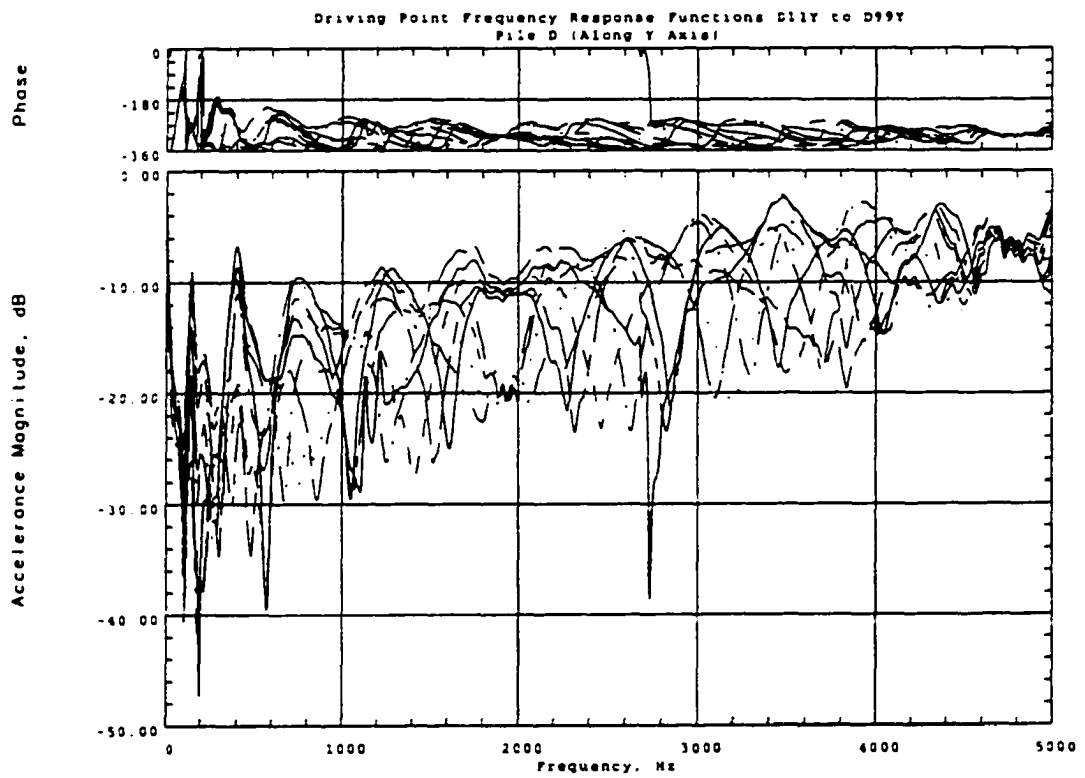


Figure 4.33 Driving Point Frequency Response Functions for Pile D, Tested Along Y Axis

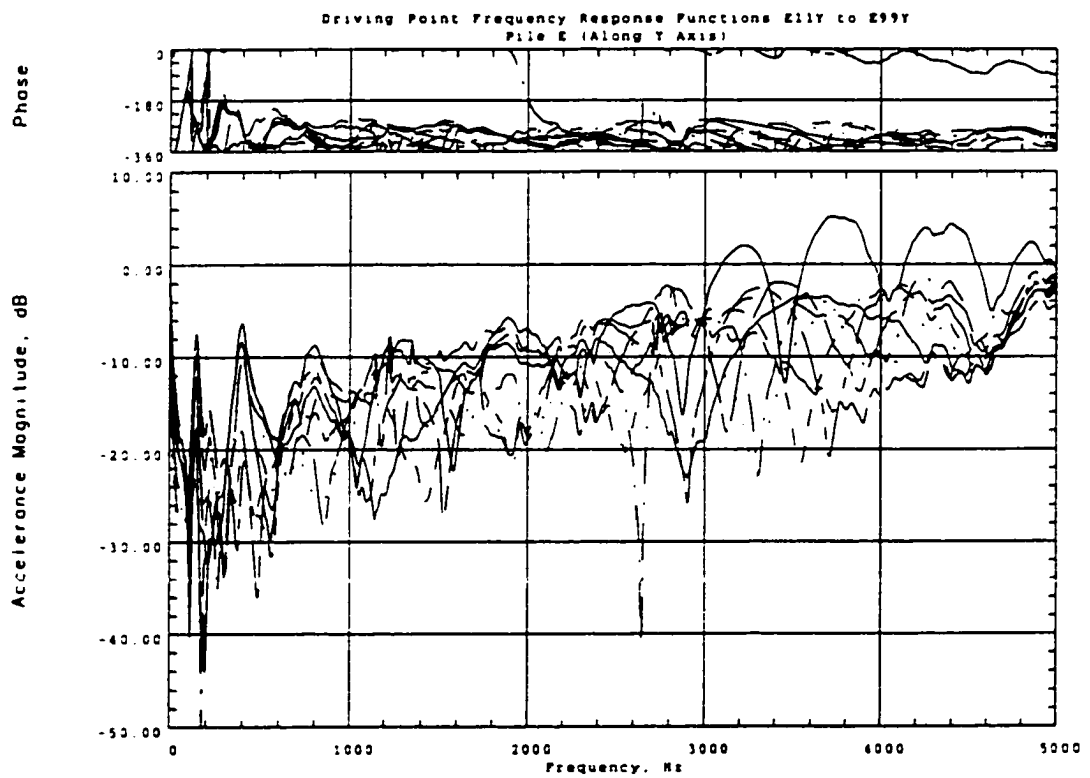
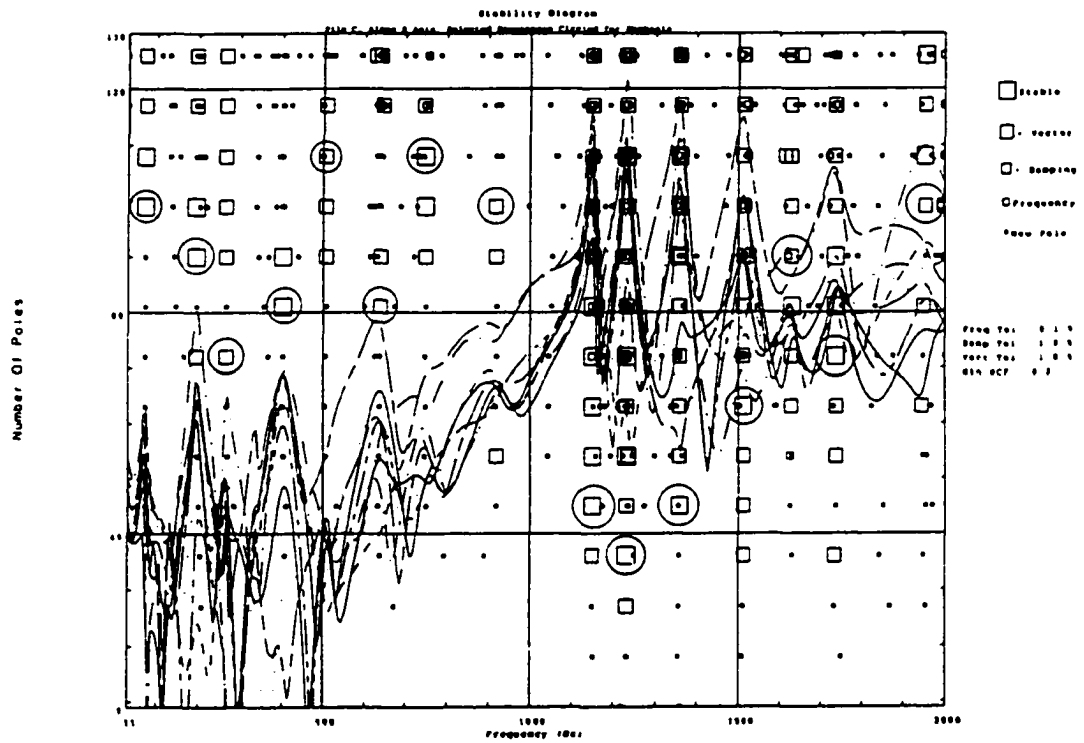


Figure 4.34 Driving Point Frequency Response Functions for Pile E, Tested Along Y Axis

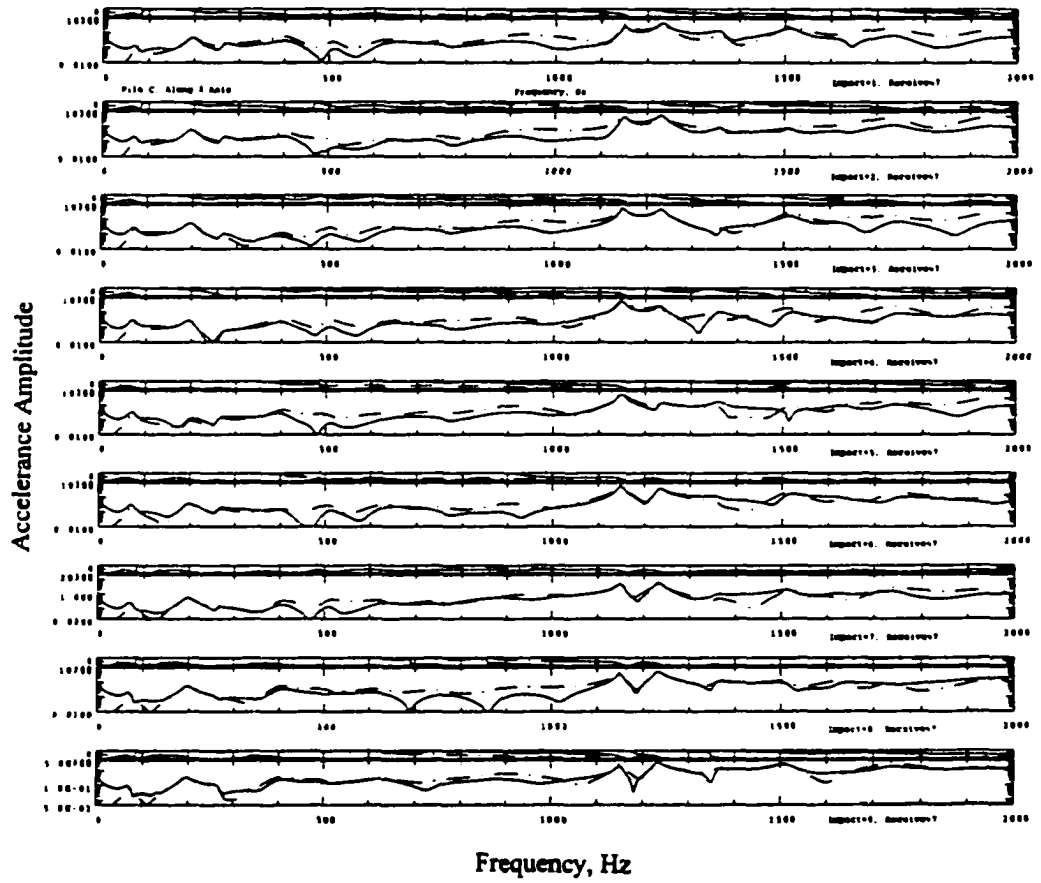
4.4 Modal Parameter Estimation Results

4.4.1 Examples of Estimation Tools

A sampling of the many tools available to aid in the modal parameter estimation curve-fitting process were discussed in Section 4.2, including the stability diagram, the multivariate mode indicator function, and the comparison of residues calculated from the estimation results. Examples of the stability diagram and of the residue comparison, computed for Pile C, are presented in Figures 4.35 and 4.36 to illustrate their appearance for experimental data. One can easily see that the proper selection of resonance frequency locations and model order requires much greater consideration and judgement by the analyst for experimental data than for the analytically generated data of Figures 4.9 through 4.11.



4.35 Stability Diagram for Pile C FRF Data, Tested Along X Axis, Selected Resonance Locations Circled



4.36 Comparison of Experimental and Resultant Residue Values for Pile C, Tested Along X Axis

In Figure 4.35, the driving point FRF's for Pile C have been overlaid onto the stability diagram to aid in the proper selection of natural frequency locations, and the resonances that were chosen have been circled for emphasis. The stability diagram shown only includes frequencies up to 2000 Hz since experimental data above that frequency level was not included in the parameter estimation routine. The decision to decrease the frequency range of interest from the 5000 Hz that was measured to 2000 Hz was made after examination of the experimental FRF's revealed that the data quality appeared to decrease significantly in the range from 3000 to 5000 Hz. The data peaks in this region were quite indistinct, and appeared to "drift" upward with increasing frequency. Examples of this trend can be seen in Figures 4.20 through 4.24. Ewins (1985) makes the following comments regarding data of this type:

A...check can be made towards the upper end of the frequency range where it is sometimes found, especially on point mobility [i.e. driving point] measurements, that the curve becomes asymptotic to a mass line or, more usually, to a stiffness line. Such a tendency can result in considerable difficulties for the modal analysis process and reflects a situation where the excitation is being applied at a point of very high mass or flexibility. Although not incorrect, the data thus obtained will often prove difficult to analyse (sic) because the various modal parameters to be extracted are overwhelmed by the dominant local effects. Such a situation suggests the use of a different excitation point.

Since this trend was present in the FRF's recorded at all the excitation points (and therefore a different excitation point did not eliminate the effect), it was decided that only the data in the lower 2000 Hz could be successfully subjected to the modal parameter estimation process.

Although there is only scant evidence of it in the figure, another tool known as the Modal Confidence Factor (MCF) was considered in determining the appropriate number of poles

(curve-fit model order) to select at each resonance location. The MCF value is an indication of the likelihood that a mode identified by the curve-fit routine at a certain frequency and pole number is a physical, rather than computational, mode. (The I-DEAS™ Test Modal Analysis User's Guide describes a computational mode as "one that corresponds to no physical mode of vibration, but which is generated by the modal extraction algorithm to account for unwanted effects [including] noise, filter characteristics, leakage...and nonlinearities.") The MCF "exploits redundant phase relationships that are satisfied by physical modes, but which are meaningless for computational modes" (I-DEAS™, 1995) to produce a value between 1.0 and zero; an MCF value near 1.0 indicates that the mode is most likely physical, whereas a value close to zero suggests a computational mode. Although Figure 4.35 shows that the minimum MCF considered by the curve-fitter was 0.2, the minimum MCF for the resonances selected was much higher--usually modes were not selected that had MCF's below 0.85, and most had values of 0.95 or higher.

The residues shown in Figure 4.36 are presented in the same format as those of Figure 4.11. The plots (from top to bottom) show the accelerance FRF's at Position 7 due to impact at Positions 1 (top plot), 2 (second plot), and so on, through Position 9. The solid lines represent the measured Pile C data, while the broken lines represent the residues generated numerically from the modal parameter estimation results. One can see from the figure that a relatively good fit was achieved for frequencies from zero to 2000 Hz, which is the frequency range included in the estimation process. This fit was deemed sufficient to consider that the modal parameters identified (which will be presented for all Group I piles

in the next section) were indeed those of the pile system under consideration (Pile C for the figures shown).

Plots of the type shown in the two previous figures were produced for each of the Group I piles, and modal parameters were identified for each. The results of the parameter estimation process will be presented in the next section, and the conclusions drawn from them will be discussed in Chapter VII.

4.4.2 Results for Tests Along the X Axis

The natural frequency and damping factor estimates determined using the frequency polyreference modal parameter estimation technique are presented in Tables 4.2 to 4.7 for Piles A through E, respectively, for tests along the X Axis. The results are presented graphically in Figures 4.37 and 4.38 as plots of natural frequency and damping versus mode number. Mode shapes were also generated from the estimated parameters, and a comparison of the shapes for each pile revealed that every pile did not exhibit all of the modes present in every other pile. Thus, the natural frequency and damping values have been separated in the tables and figures such that values corresponding to like modes are given the same mode number. For example, the ninth through twelfth mode shapes calculated for Pile C are presented in Figure 4.39, and those calculated for the eighth through eleventh modes of Pile E are given in Figure 4.40. It is clear from the figures that the mode shapes shown correspond to like modes, even though the mode numbers are different. These modes, then, were assigned like mode numbers in Tables 4.5 and 4.7. This “matching” of modes for each pile accounts for the gaps that are present in Tables 4.2 to 4.7

and in Figures 4.37 and 4.38. Additionally, the modes identified for Pile A in the nonembedded configuration do not correspond with those identified for the embedded piles, because of the dissimilar boundary conditions encountered at the “bottom” end of the pile, but its values are included for completeness and comparison purposes.

Table 4.2 Pile A Modal Parameter Estimation Results

Pile A, Nonembedded Configuration Experimental Data, Tests Along X Axis		
Mode Number	Natural Frequency, Hz	Damping, %
1	9.1	19.1
2	63.3	0.3
3	154.5	0.1
4	181.6	0.1
5	261.3	0.1
6	335.7	0.2
7	355.5	0.1
8	485.6	0.1
9	563.5	0.1
10	692.7	0.2
11	817.0	0.3
12	950.7	0.2

Table 4.3 Pile A Modal Parameter Estimation Results

Pile A, Embedded Configuration Experimental Data, Tests Along X Axis		
Mode Number	Natural Frequency, Hz	Damping, %
1	68.5	9.9
2	183.9	4.5
3	255.1	3.1
4	375.3	4.3
5	488.0	2.9
6	586.0	4.6
7	710.8	3.3
8	837.6	5.0
9		
10	1134.1	0.5
11	1216.1	0.8
12	1337.9	1.2
13	1491.0	1.1
14	1635.2	1.2
15	1714.9	1.2
16	1909.2	1.9

Table 4.4 Pile B Modal Parameter Estimation Results

Experimental Data, Tests Along X Axis		
Mode Number	Natural Frequency, Hz	Damping, %
1	70.5	9.7
2	187.0	5.7
3	260.0	3.7
4	379.9	6.0
5		
6	587.4	6.4
7		
8		
9		
10	1131.7	0.6
11	1215.3	0.8
12	1338.1	1.4
13	1493.8	1.4
14	1629.6	2.4
15	1707.4	1.6
16		

Table 4.5 Pile C Modal Parameter Estimation Results

Experimental Data, Tests Along X Axis		
Mode Number	Natural Frequency, Hz	Damping, %
1	72.8	8.3
2	195.4	4.6
3	266.8	3.5
4	401.6	5.4
5	507.2	3.1
6	639.4	5.4
7	748.6	5.2
8		
9	917.6	6.0
10	1149.6	0.5
11	1232.4	0.7
12	1358.8	0.9
13	1512.2	1.2
14	1629.3	1.3
15	1737.6	1.6
16	1952.9	2.1

Table 4.6 Pile D Modal Parameter Estimation Results

Experimental Data, Tests Along X Axis		
Mode Number	Natural Frequency, Hz	Damping, %
1	69.4	9.4
2	186.2	5.6
3	258.6	4.2
4	375.9	6.0
5		
6	589.7	5.3
7	701.9	6.9
8		
9		
10	1134.9	0.6
11	1217.0	1.0
12	1337.4	1.3
13	1495.3	1.5
14	1652.5	1.3
15		
16	1922.7	4.4

Table 4.7 Pile E Modal Parameter Estimation Results

Experimental Data, Tests Along X Axis		
Mode	Natural	
Number	Frequency, Hz	Damping, %
1	70.6	9.0
2	191.4	4.3
3	264.3	3.2
4	388.8	4.7
5	495.2	2.4
6	605.8	6.4
7		
8	875.7	5.7
9		
10	1147.3	0.6
11	1228.8	0.7
12	1351.0	1.0
13	1506.3	1.2
14	1656.1	1.3
15	1732.1	1.4
16	1926.8	2.3

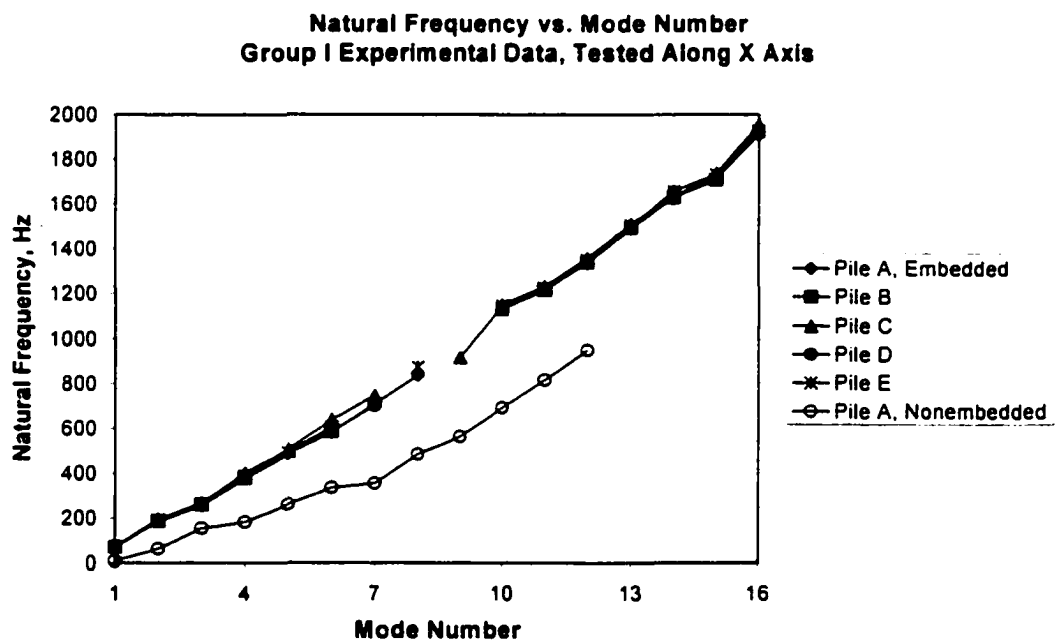


Figure 4.37 Results of Natural Frequency Estimation for Group I Piles

Damping vs. Mode Number
Group I Experimental Data, Tested Along X Axis

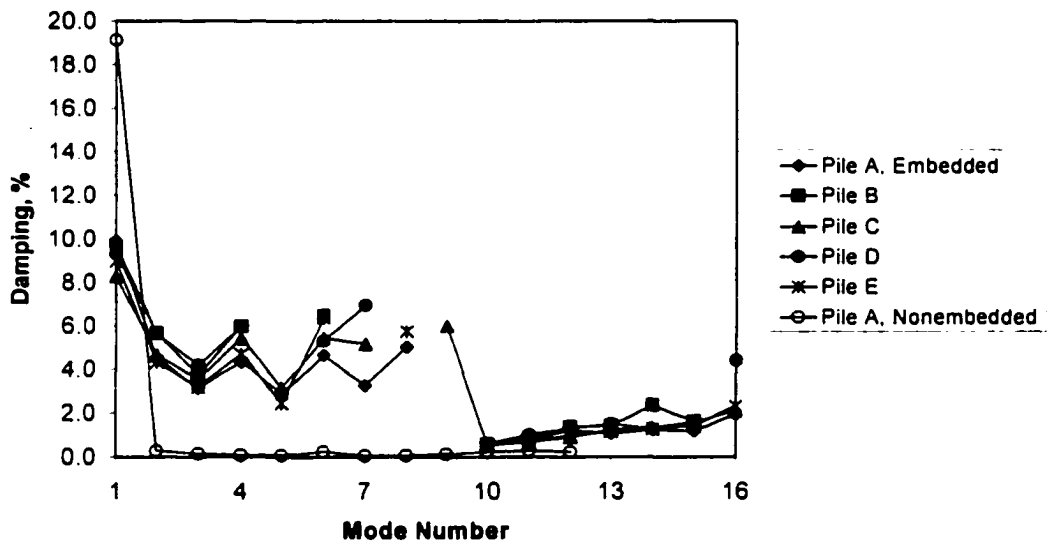


Figure 4.38 Results of Damping Estimation for Group I Piles

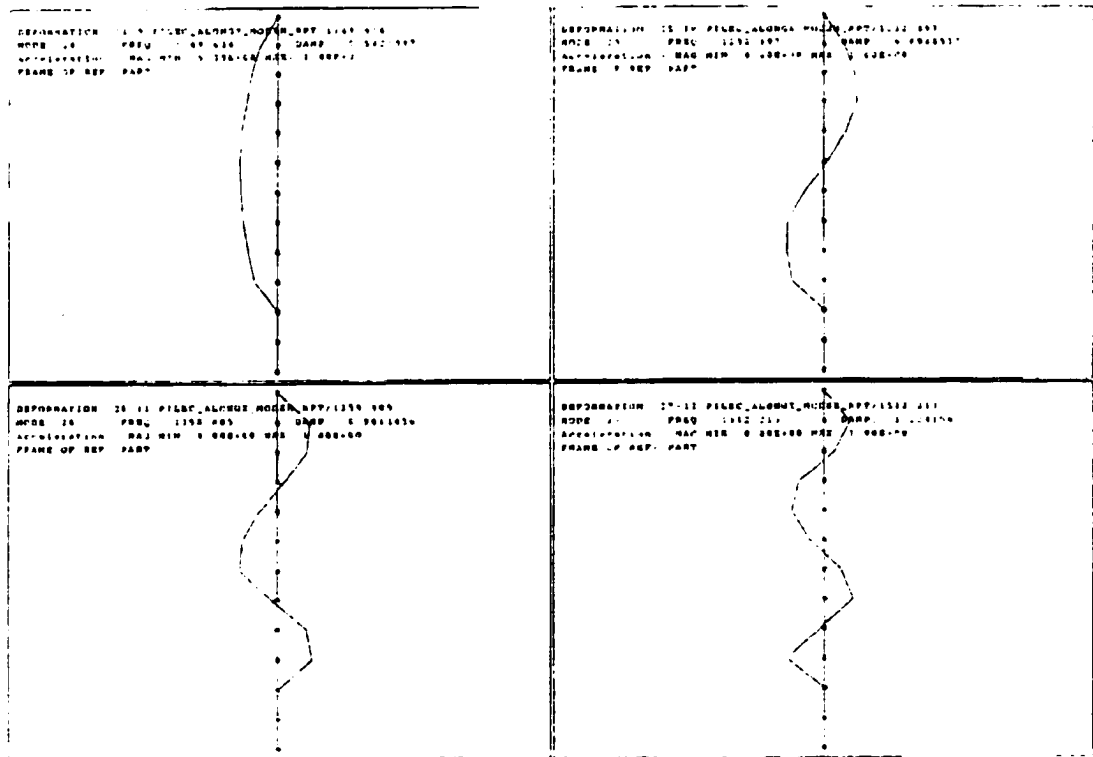


Figure 4.39 Ninth Through Twelfth Mode Shapes Calculated from Pile C Modal Parameter Estimates

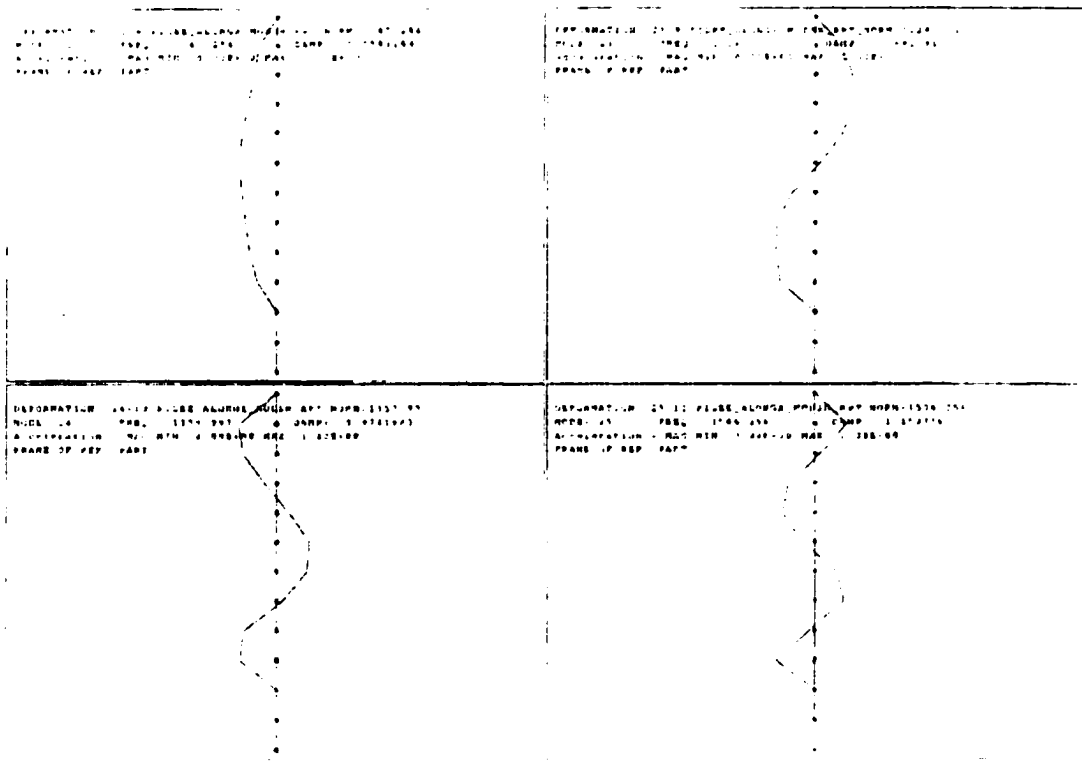


Figure 4.40 Eighth Through Eleventh Mode Shapes Calculated from Pile E Modal Parameter Estimates

4.4.3 Results for Tests Along the Y Axis

The natural frequency and damping factor estimates determined using the frequency polyreference modal parameter estimation technique are presented in Tables 4.8 to 4.12 for Piles A through E, respectively, for tests along the Y Axis. The results are presented graphically in Figures 4.41 and 4.42 as plots of natural frequency and damping versus mode number. In a manner similar to that described in Section 4.4.2 above, mode shapes calculated from the parameter estimates were examined and compared, revealing that every pile did not exhibit all of the modes present in every other pile. Once again, then, the natural frequency and associated damping values have been separated in the tables and figures so that those values corresponding to like modes are given the same mode number. Tests were not performed along the Y axis for Pile A in the nonembedded configuration.

Table 4.8 Pile A Modal Parameter Estimation Results

Pile A, Embedded Configuration Experimental Data, Tests Along Y Axis		
Mode Number	Natural Frequency, Hz	Damping, %
1	132.9	11.4
2	376.0	4.2
3	708.1	2.7
4	987.5	2.2
5	1132.9	0.7
6	1214.1	1.1
7	1336.9	1.5
8		
9	1620.4	2.3
10		
11	1946.7	1.8
12	1998.8	0.7

Table 4.9 Pile B Modal Parameter Estimation Results

Experimental Data, Tests Along Y Axis		
Mode Number	Natural	
	Frequency, Hz	Damping, %
1	146.8	7.3
2	396.0	8.8
3	752.3	12.9
4		
5	1131.1	0.6
6	1217.4	0.8
7	1344.5	1.0
8	1505.2	1.2
9		
10	1716.8	1.4
11		
12		

Table 4.10 Pile C Modal Parameter Estimation Results

Experimental Data, Tests Along Y Axis		
Mode Number	Natural	
	Frequency, Hz	Damping, %
1	145.8	7.7
2	377.0	8.8
3		
4		
5	1153.5	2.5
6	1231.9	1.0
7	1308.4	6.8
8		
9		
10	1773.6	1.2
11		
12		

Table 4.11 Pile D Modal Parameter Estimation Results

Experimental Data, Tests Along Y Axis		
Mode Number	Natural	
	Frequency, Hz	Damping, %
1	150.5	11.5
2	403.0	4.6
3	754.4	6.8
4		
5	1132.7	0.5
6	1215.0	1.0
7		
8		
9		
10		
11		
12	1996.6	0.8

Table 4.12 Pile E Modal Parameter Estimation Results

Experimental Data, Tests Along Y Axis		
Mode Number	Natural	
	Frequency, Hz	Damping, %
1	144.7	9.1
2	391.7	6.4
3	719.1	3.7
4		
5	1145.2	0.8
6	1226.3	0.8
7	1354.5	1.0
8		
9		
10	1738.6	1.4
11	1949.0	2.2
12		

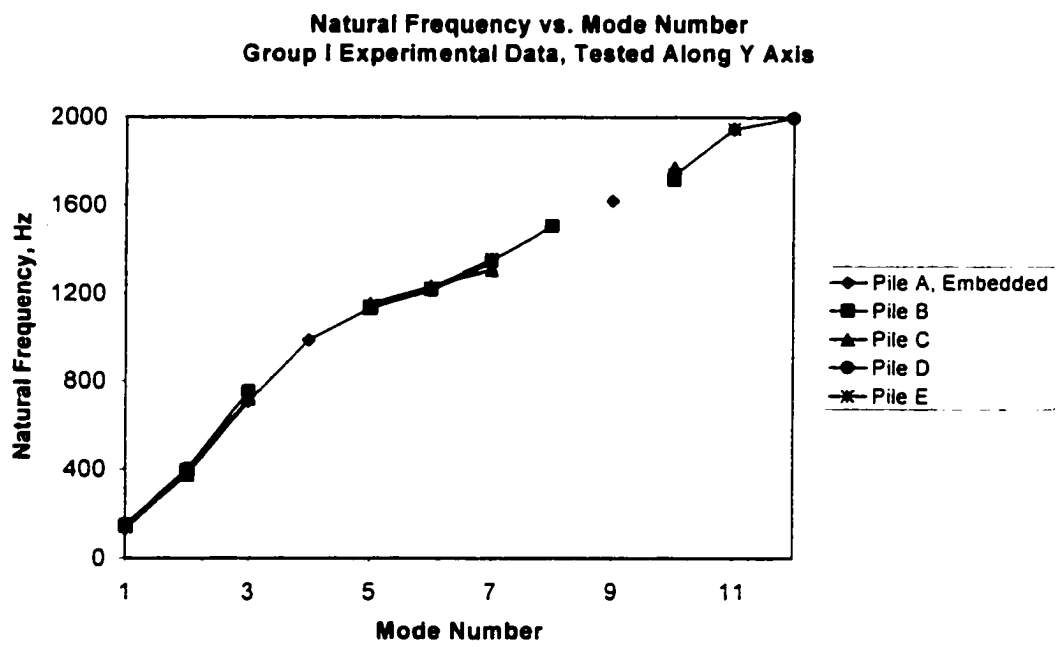


Figure 4.41 Results of Natural Frequency Estimation for Group I Piles

Damping vs. Mode Number
Group I Experimental Data, Tested Along the Y Axis

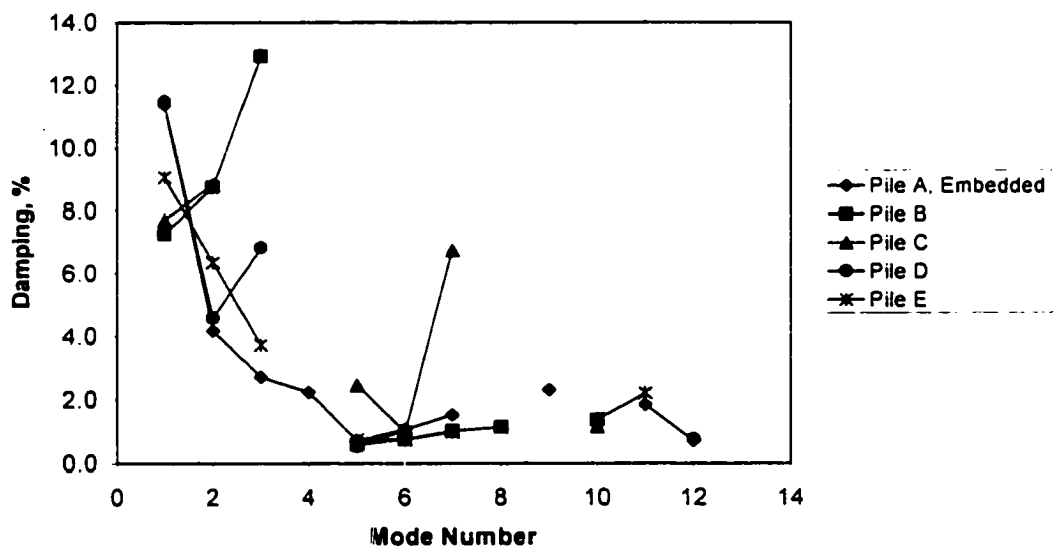


Figure 4.42 Results of Damping Estimation for Group I Piles

4.5 Discussion of Experimental Results

It is apparent from Figures 4.37 and 4.41 that the natural frequencies of the Group I model piles are quite similar, and in fact, are virtually indistinguishable from each other in the frequency range considered valid for the modal parameter estimation process. The largest percentage difference from the Pile A results is for Pile C, along the X Axis, with a difference of 9.1%. For most of the frequencies, though, for tests along both axes, the difference from the corresponding Pile A frequencies is less than 3%.

Differences in damping values between the piles, though their magnitude is somewhat greater than that for the natural frequencies, do not follow a distinctive pattern. It can be seen in Figure 4.38 that damping quantities along the X axis for each of the embedded piles follow similar trends as the mode number increases. However, there is no clear pattern established for one pile to have the highest damping value at each mode, then another to have the next highest value for each mode, etc. The quantities presented in Figure 4.42 for damping values along the Y axis exhibit even less distinguishable trends, although the values do seem to generally decrease in magnitude as the mode number increases. This lack of distinction based on the damping values is not altogether surprising, since, as stated earlier in this work, damping is the most “elusive” of the modal characteristics, and the most difficult to measure experimentally.

Three types of numerical analyses were performed to further investigate the modal differences (or lack thereof) of the Group I pile systems; these analyses will be discussed at length in the next chapter, as will their relevance to the experimental results described above.

CHAPTER V

NUMERICAL ANALYSES

Three types of numerical analyses were performed to simulate the frequency response characteristics of the Group I pile-soil systems. In the first, a series of MATLAB® programs were written to analytically generate frequency response functions analogous to those collected in the experimental portion of the study. For the second, finite element models were created to simulate each of the Group I piles, and the natural frequencies of the simulated piles were calculated and recorded. A theoretical solution for a beam resting on elastic supports, developed in the text by Weaver, Timoshenko, and Young (Weaver et al., 1990), was investigated in the third numerical study.

5.1 Analytically Generated Data

Theories presented in Novak et al., 1978, Novak and Aboul-Ella, 1978a, and Novak and Aboul-Ella, 1978b were combined to produce a series of MATLAB® programs which were used to calculate frequency response functions corresponding to those measured in the experimental study. In the first of the aforementioned papers, an analytical approach was used to “defin[e] the soil reactions to the harmonic motion of an embedded cylindrical body in terms of linear viscoelasticity limited to cases that can be viewed as plane strain.” The

authors pointed out that “such a situation arises, e.g., when a rigid cylinder extending to infinity in an infinite medium undergoes uniform lateral displacements or rotates around its axis. Then, no strain develops on the plane perpendicular to the axis and only a unit thickness of the medium needs to be considered in the analysis.” The approach developed in the first paper expanded on earlier studies of a similar nature by including frequency independent material damping (hysteretic damping). The soil reactions were formulated in terms of complex stiffnesses associated with vertical, horizontal, antisymmetric (also referred to as “rocking”), and torsional displacements of the embedded cylinder. As stated in the paper, the real part of the complex stiffness represents the “true” stiffness, while the imaginary part represents damping.

The results of the first paper were extended in the second to include variation of pile and soil properties with depth. The pile-soil system was divided into layers, and the portion of pile contained in one layer was considered an element. Element stiffness matrices were formulated and combined appropriately to form the structural stiffness matrix $[K]$, which was recognized as the “link” between the nodal forces $\{X\}$ and nodal displacements $\{\Delta\}$, according to the relationship $\{X\} = [K] \{\Delta\}$. The authors noted that “in this approach, explicit mass and stiffness matrices need not be formulated as is the case with the standard finite element method. The mass and damping of both the pile and soil are contained in the stiffness matrix, $[K]$, which is, therefore, complex and frequency variable.” (Energy dissipation in the soil is responsible for the complexity of the stiffness terms.)

In the third paper, the authors stated that the approach developed in the previous paper produced an approximate solution, since it was essential to assume that “the soil reaction

associated with a certain displacement within a particular layer is equal to that of an infinite pile undergoing a uniform displacement of the same magnitude in a homogeneous medium with the properties of that layer.” They then examined the “acceptability” of the assumption by comparing the approximate solution with more a more rigorous analytical solution, a solution produced using the finite element method, and a set of experimental data. The results of the approximate solution were found to agree quite well with those of the other solutions investigated, and the authors mentioned that the primary advantages of the approximate approach were its versatility and relative simplicity.

In the programs that were written (included as Appendix B), the Group I piles were discretized into segments whose lengths corresponded to the spacing dictated by the measurement locations defined in the experimental studies (shown in Figures 4.4 and 4.5). Element lengths used for the exposed portion of the piles were continued into the buried portion, and soil properties were set equal to zero for elements falling within the exposed length. Analytical frequency response function data was generated for Piles A through E for tests along the X and Y axes. Data was produced for Pile A in the nonembedded configuration only for tests along the X axis.

After the FRF data was produced, a procedure similar to that used to analyze the experimental data was performed; first, the data was imported into the I-DEAS Modal™ software package, then the frequency polyreference modal parameter estimation technique was used to identify the modal characteristics for each of the piles. As in the experimental program, stability diagrams and residues were produced to aid in the parameter estimation process.

5.1.1 Results for Tests Along the X Axis

Figures 5.1 through 5.6 show the driving point frequency response functions generated by the programs described above for tests along the X Axis. It should be noted that, as for the experimental tests, acceleration data for all 81 source/receiver combinations was generated and used in the parameter estimation process, but, for illustration purposes, only the driving point FRF's are shown. In Figure 5.6 (which shows the driving point FRF's for Pile A in its nonembedded configuration), the one FRF that does not "fit" well with the others is that for Position 9, located only two inches below the supporting W10x45 section. It is not surprising that the FRF for a position so close to the support (assumed to be fixed in the analytical model) is shaped somewhat differently those measured at other locations, since the motion of Pile A in its nonembedded configuration is essentially that of a cantilevered beam. For such a beam, the acceleration experienced by points very near the support is much less than that experienced at locations farther along the beam's length.

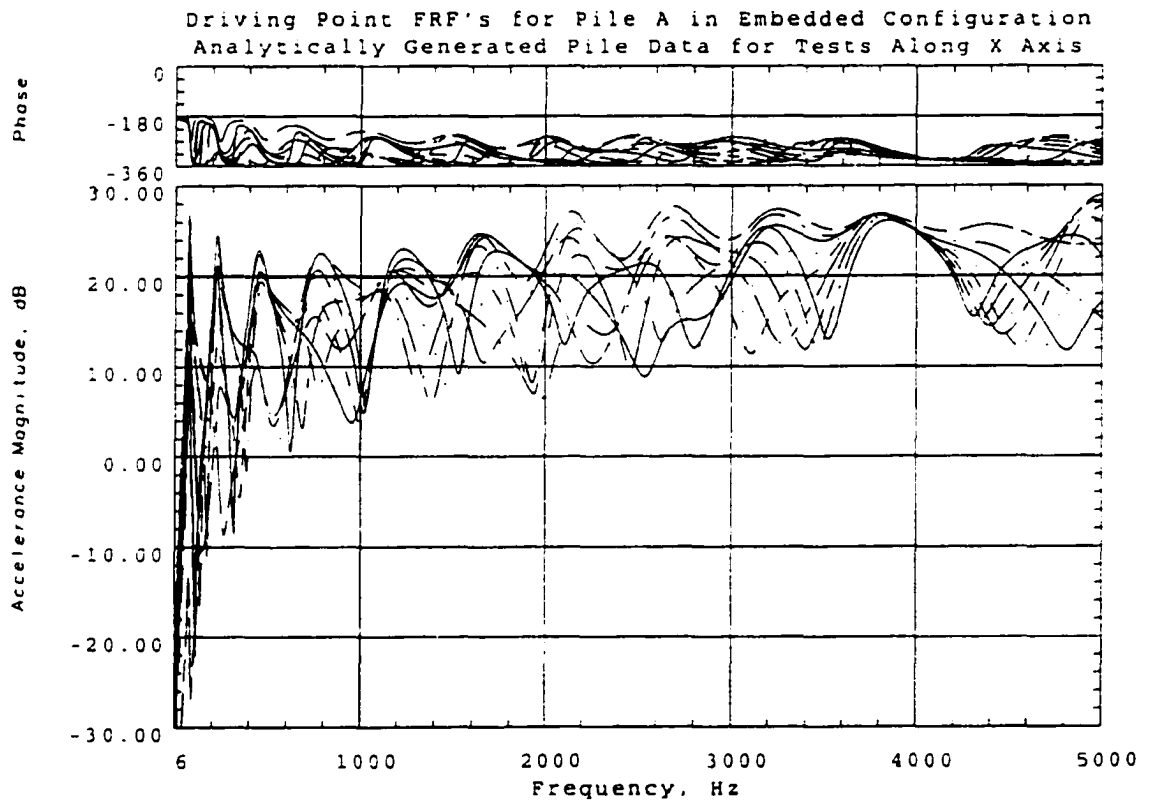


Figure 5.1 Analytically Generated Driving Point Frequency Response Functions for Pile A, Embedded Configuration, Along X Axis

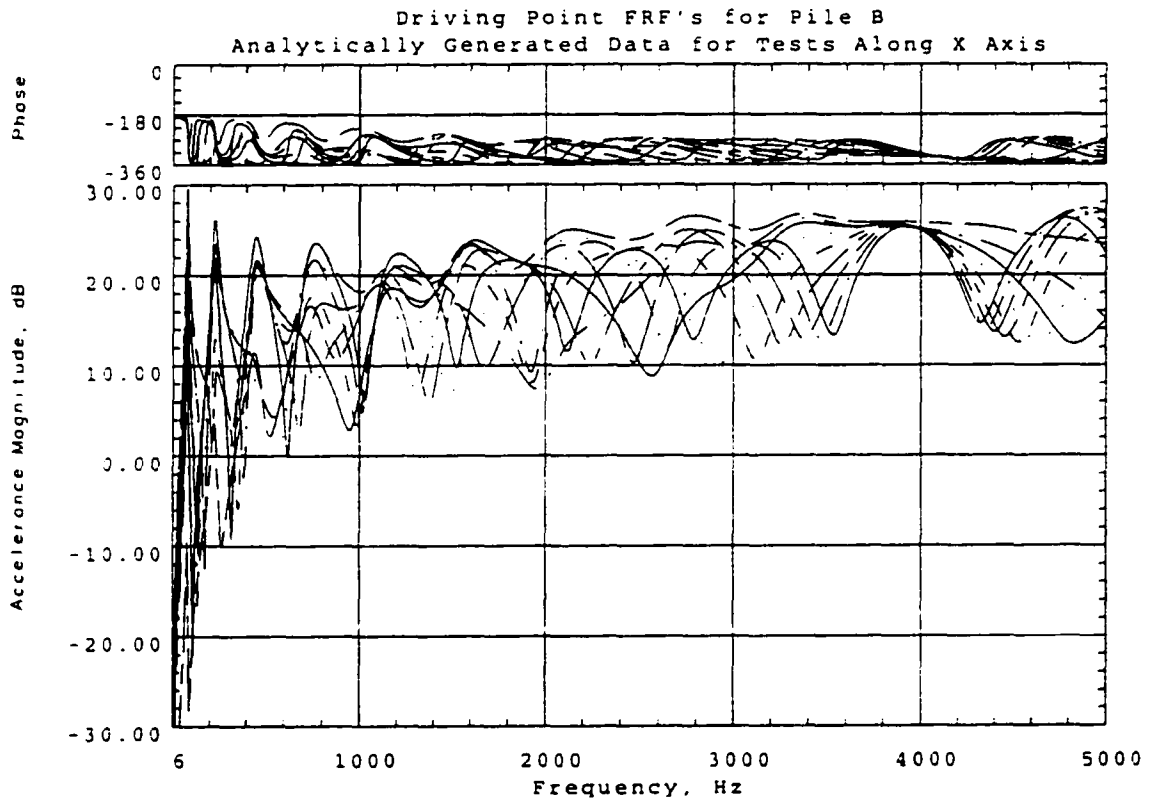


Figure 5.2 Analytically Generated Driving Point Frequency Response Functions for Pile B, Along X Axis

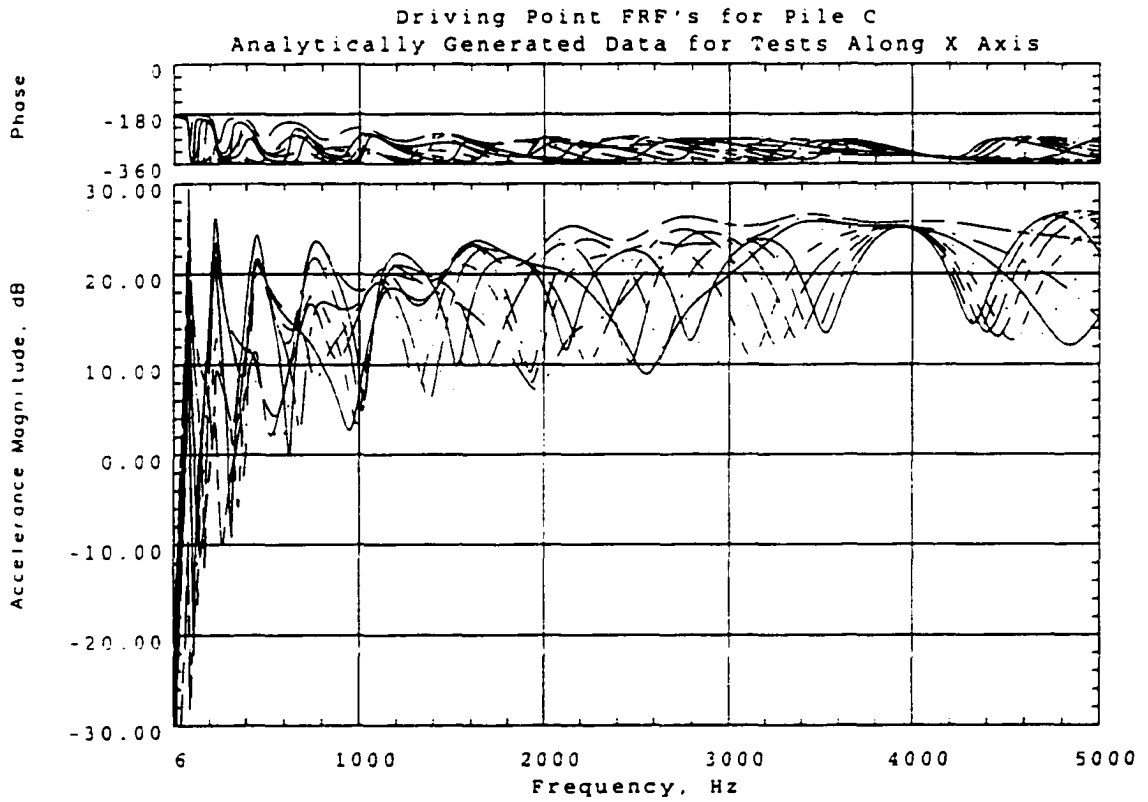


Figure 5.3 Analytically Generated Driving Point Frequency Response Functions for Pile C, Along X Axis

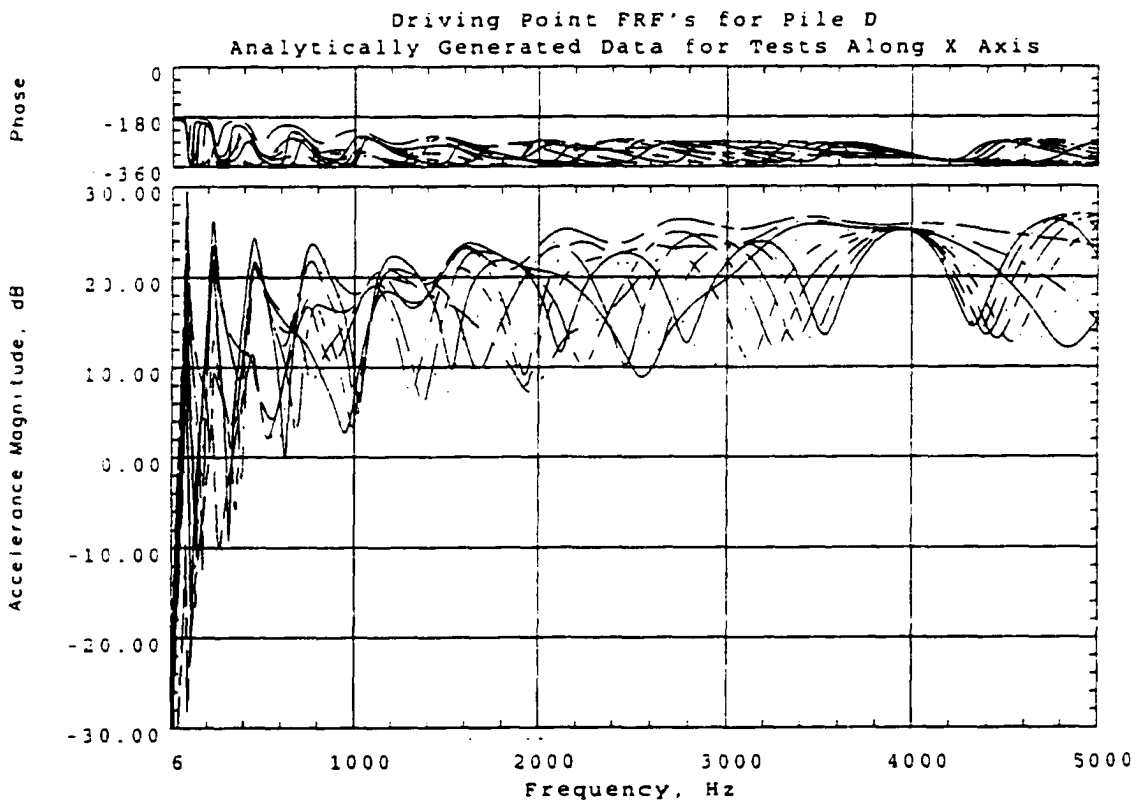


Figure 5.4 Analytically Generated Driving Point Frequency Response Functions for Pile D, Along X Axis

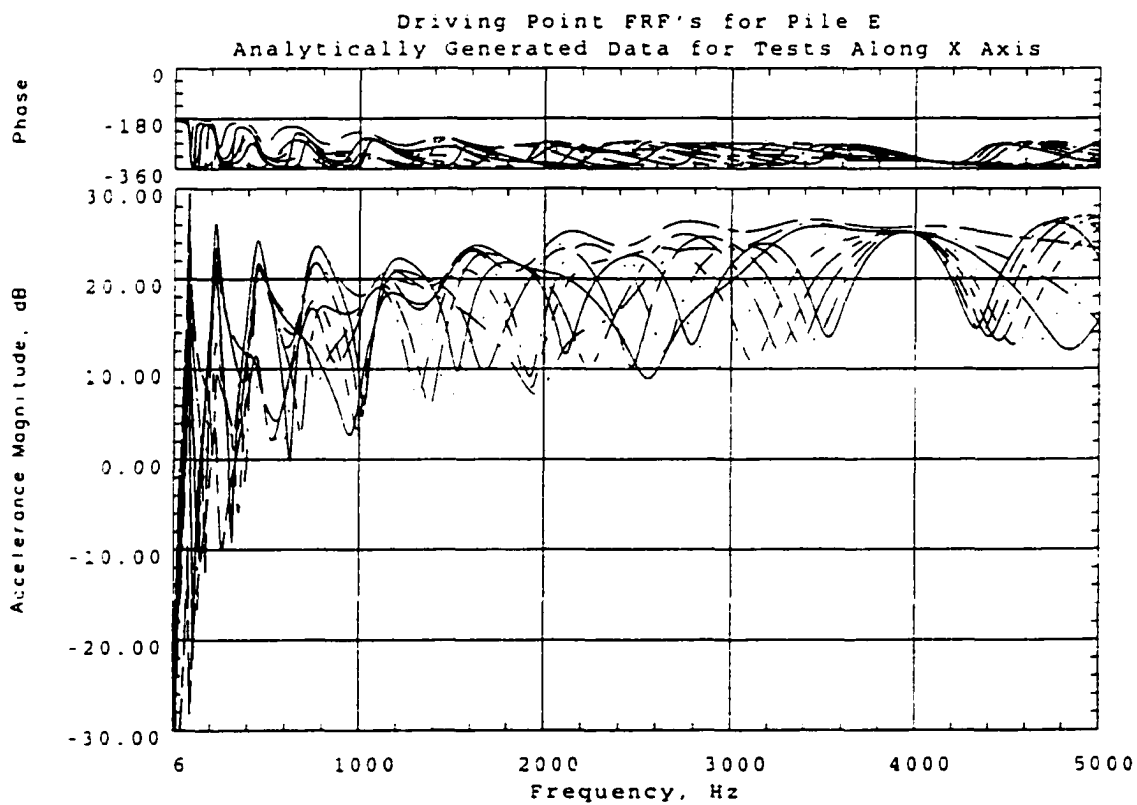


Figure 5.5 Analytically Generated Driving Point Frequency Response Functions for Pile E, Along X Axis

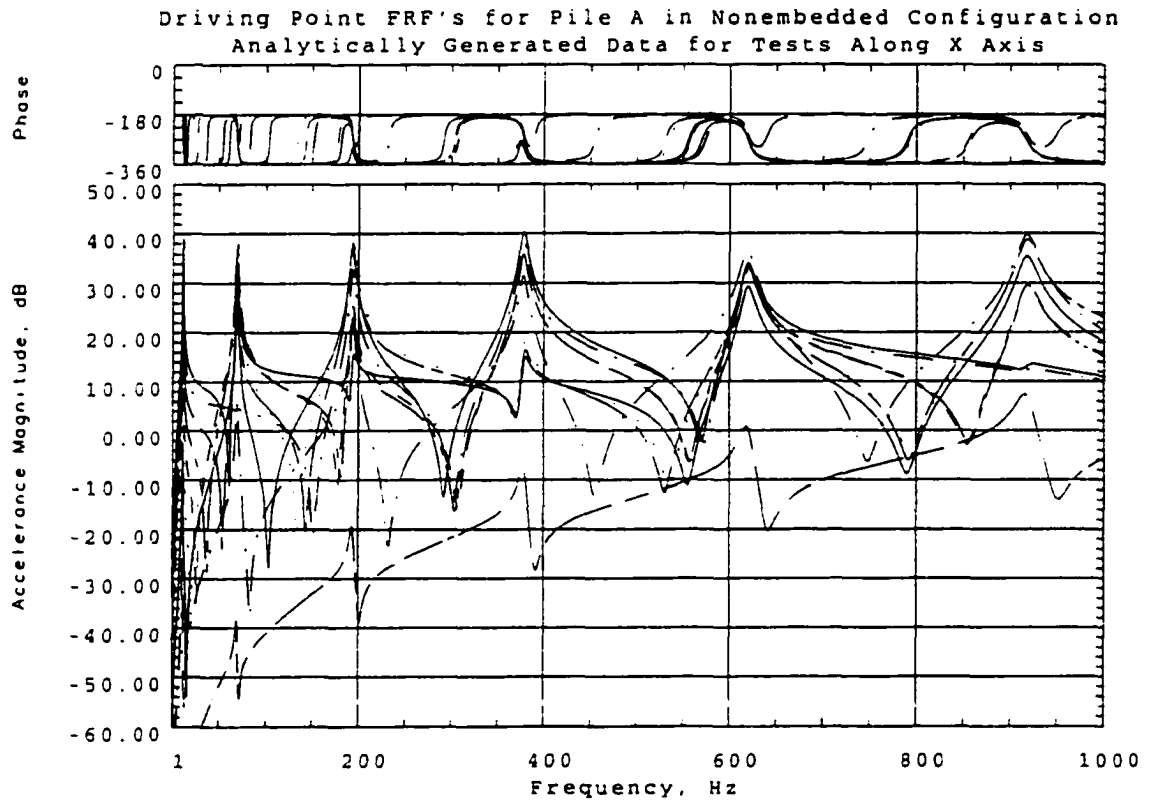


Figure 5.6 Analytically Generated Driving Point Frequency Response Functions for Pile A, Nonembedded Configuration, Along X Axis

The natural frequency and damping factor estimates determined for the analytically generated data using the frequency polyreference modal parameter estimation technique are presented in Tables 5.1 to 5.6 for Piles A through E and for Pile A in the nonembedded configuration, respectively, for tests along the X Axis. The results are presented graphically in Figures 5.12 and 5.13 as plots of natural frequency and damping versus mode number. In a manner similar to that described in Section 4.4.2, mode shapes calculated from the parameter estimates were examined and compared, revealing that every pile did not exhibit all of the modes present in every other pile. As such, the natural frequency values and associated damping values have been separated in the tables and figures so that those values corresponding to like modes are given the same mode number.

Table 5.1 Pile A, Embedded Configuration Modal Parameter Estimation Results Along X Axis, Analytically Generated Data

Pile A, Embedded Configuration Analytically Generated Data, Along X Axis		
Mode Number	Natural Frequency, Hz	Damping, %
1	80.5	5.5
2	225.2	7.2
3	446.6	9.3
4	752.0	11.7
5	1068.5	43.8
6	1172.2	11.3
7	1631.6	7.8
8	2119.1	6.3
9		
10	2639.7	5.9
11	3184.1	5.9
12	3742.0	5.8
13	4327.4	5.1
14		
15	4987.5	0.2

**Table 5.2 Pile B Modal Parameter Estimation Results, Along X Axis
Analytically Generated Data**

Pile B		
Analytically Generated Data, Along X Axis		
Mode	Natural	
Number	Frequency, Hz	Damping, %
1	82.3	3.8
2	228.0	5.6
3	449.3	7.5
4	748.2	9.2
5		
6	1131.4	10.0
7	1579.4	9.5
8	2067.3	11.1
9	2377.9	17.3
10	2755.6	9.0
11	3305.2	7.6
12	3821.4	8.7
13	4267.1	7.8
14	4816.7	6.0
15	4991.1	2.1

**Table 5.3 Pile C Modal Parameter Estimation Results, Along X Axis
Analytically Generated Data**

Pile C		
Analytically Generated Data, Along X Axis		
Mode Number	Natural Frequency, Hz	Damping, %
1	82.3	3.9
2	228.1	5.7
3	449.6	7.5
4	748.6	9.0
5		
6	1127.3	9.9
7	1578.5	10.3
8	1977.6	31.0
9	2113.2	10.2
10	2671.3	10.5
11	3356.3	8.8
12	3902.8	10.4
13	4204.7	9.8
14	4757.1	7.1
15	4987.5	0.2

**Table 5.4 Pile D Modal Parameter Estimation Results, Along X Axis
Analytically Generated Data**

Pile D		
Analytically Generated Data, Along X Axis		
Mode Number	Natural Frequency, Hz	Damping, %
1	82.4	3.9
2	228.1	5.7
3	449.6	7.5
4	748.7	9.0
5		
6	1126.8	9.9
7	1580.8	10.4
8	2105.6	10.3
9	2696.6	10.0
10	3208.1	18.1
11	3361.8	9.9
12	3992.7	11.2
13	4132.7	11.5
14	4728.9	8.6
15	4987.5	0.2

Table 5.5 Pile E Modal Parameter Estimation Results, Along X Axis
Analytically Generated Data

Pile E		
Analytically Generated Data, Along X Axis		
Mode Number	Natural Frequency, Hz	Damping, %
1	82.3	3.9
2	228.1	5.7
3	449.6	7.5
4	748.7	9.0
5		
6	1126.8	9.9
7	1580.9	10.3
8	2105.9	10.4
9	2695.6	10.2
10		
11	3343.9	10.1
12	4042.5	10.1
13		
14	4746.3	9.4
15	4987.5	0.2

**Table 5.6 Pile A, Nonembedded Configuration Modal Parameter Estimation Results
Along X Axis, Analytically Generated Data**

Pile A, Nonembedded Configuration*		
Analytically Generated Data, Along X Axis		
Mode	Natural	
Number	Frequency, Hz	Damping, %
1	11.1	1.0
2	69.6	1.0
3	193.9	1.0
4	377.8	1.0
5	619.9	1.0
6	917.6	1.0
7		
8		
9		
10		
11		
12		
13		
14		
15		

* Experimental data collected in 0-1000 Hz range.

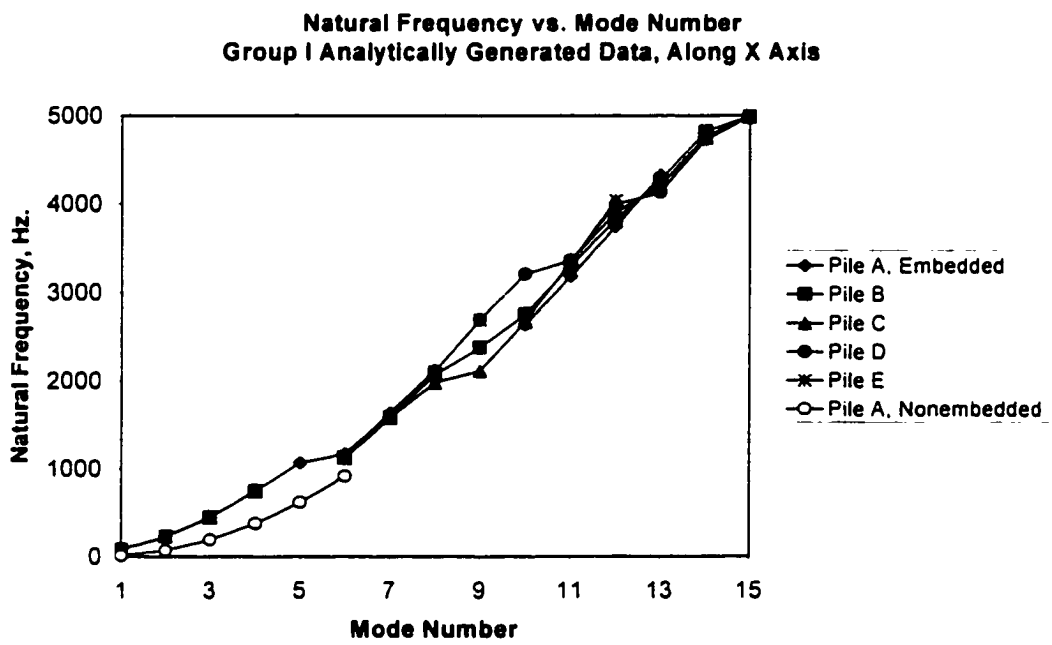


Figure 5.7 Natural Frequency vs. Mode Number for Analytically Generated Data, Along X Axis

Damping vs. Mode Number
Group I Analytically Generated Data, Along X Axis

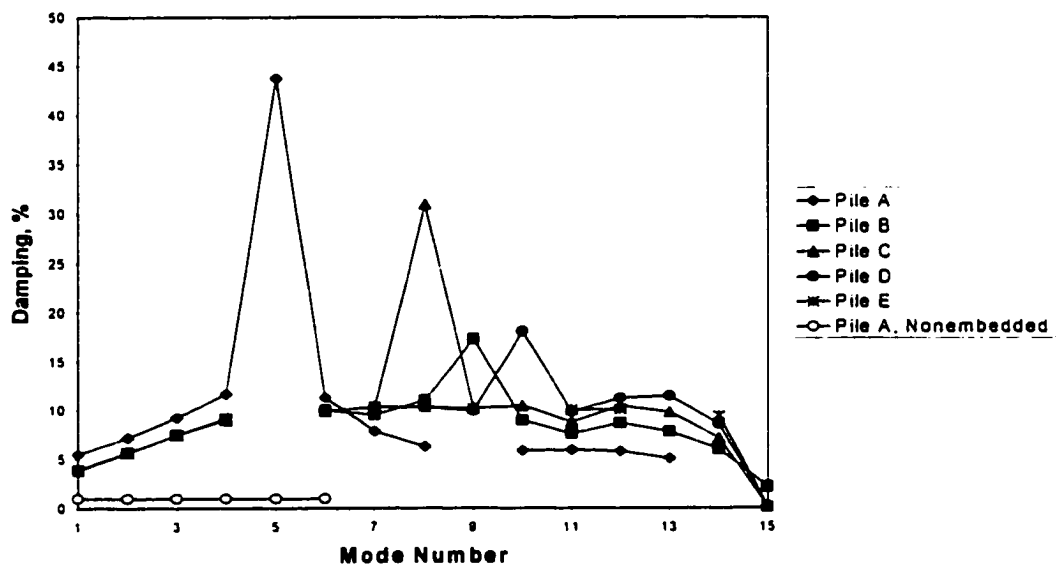


Figure 5.8 Damping vs. Mode Number for Analytically Generated Data, Along X Axis

5.1.2 Results for Tests Along the Y Axis

Figures 5.9 through 5.13 show the driving point frequency response functions that were generated by the programs described above for tests along the Y Axis. Again, it should be noted that data for all 81 source/receiver combinations were used in the parameter estimation process, but, for illustration purposes, only the driving point FRF's are shown.

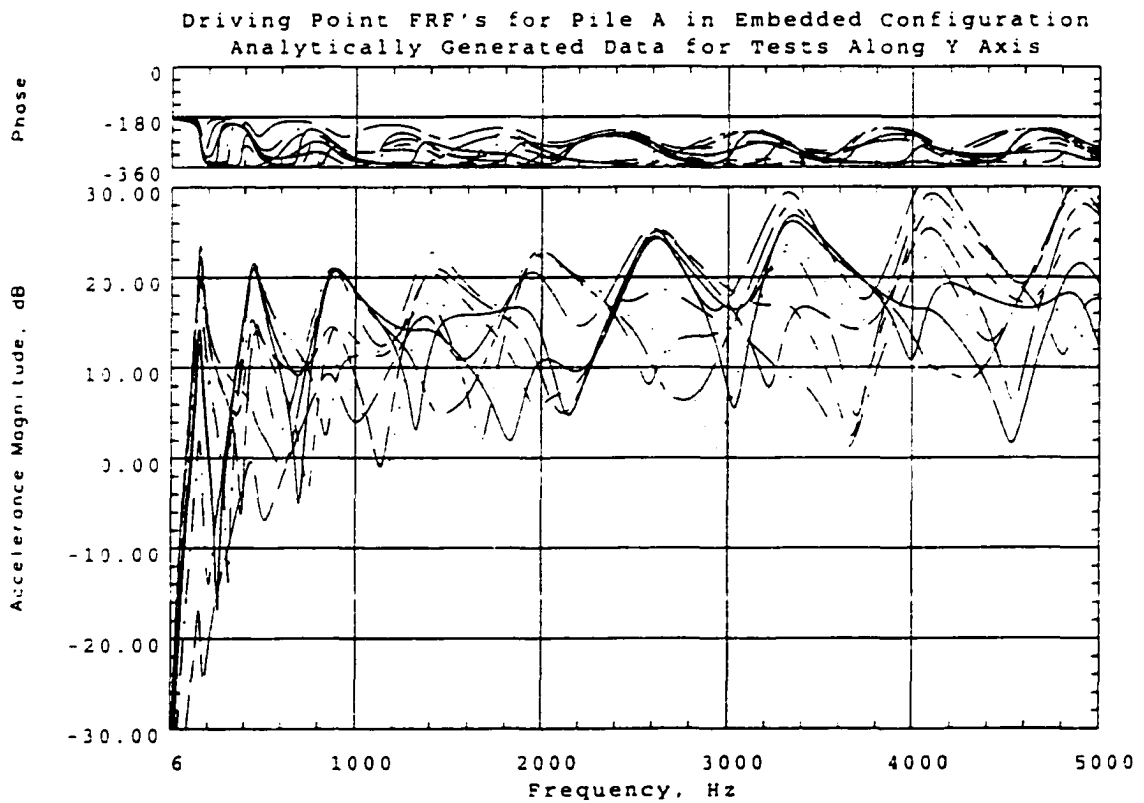


Figure 5.9 Analytically Generated Driving Point Frequency Response Functions for Pile A, Embedded Configuration, Along Y Axis

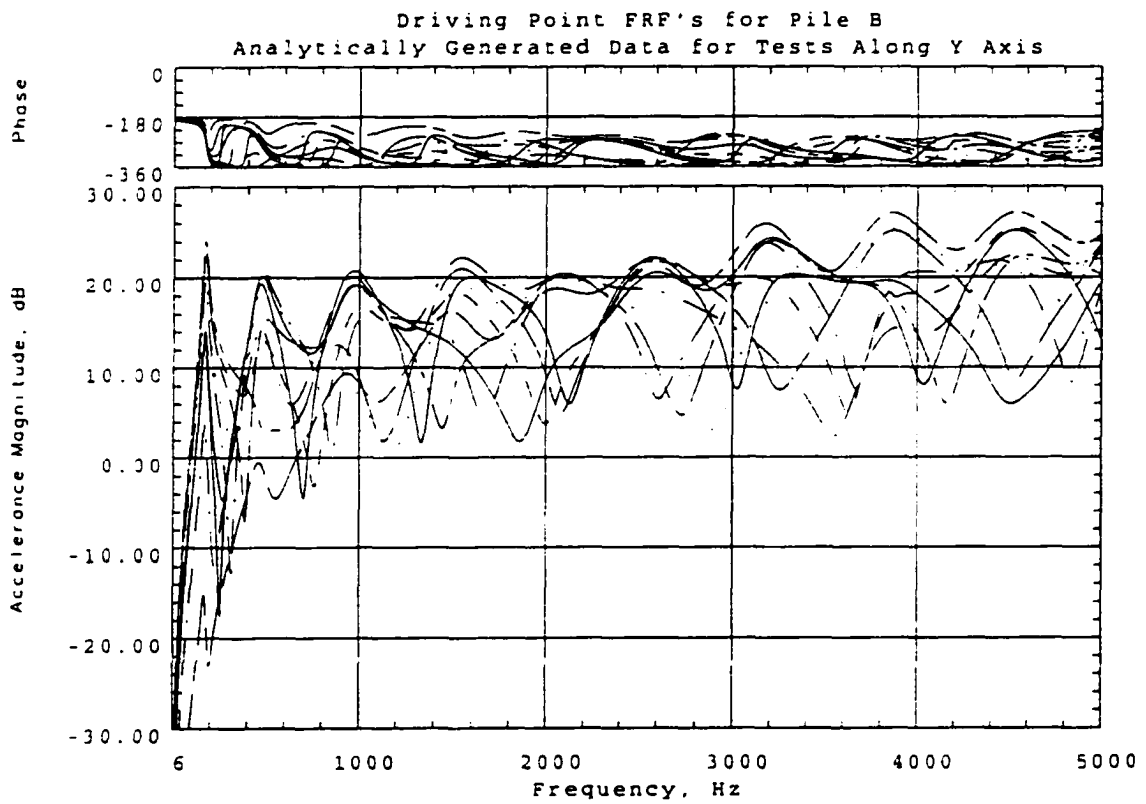


Figure 5.10 Analytically Generated Driving Point Frequency Response Functions for Pile B, Along Y Axis

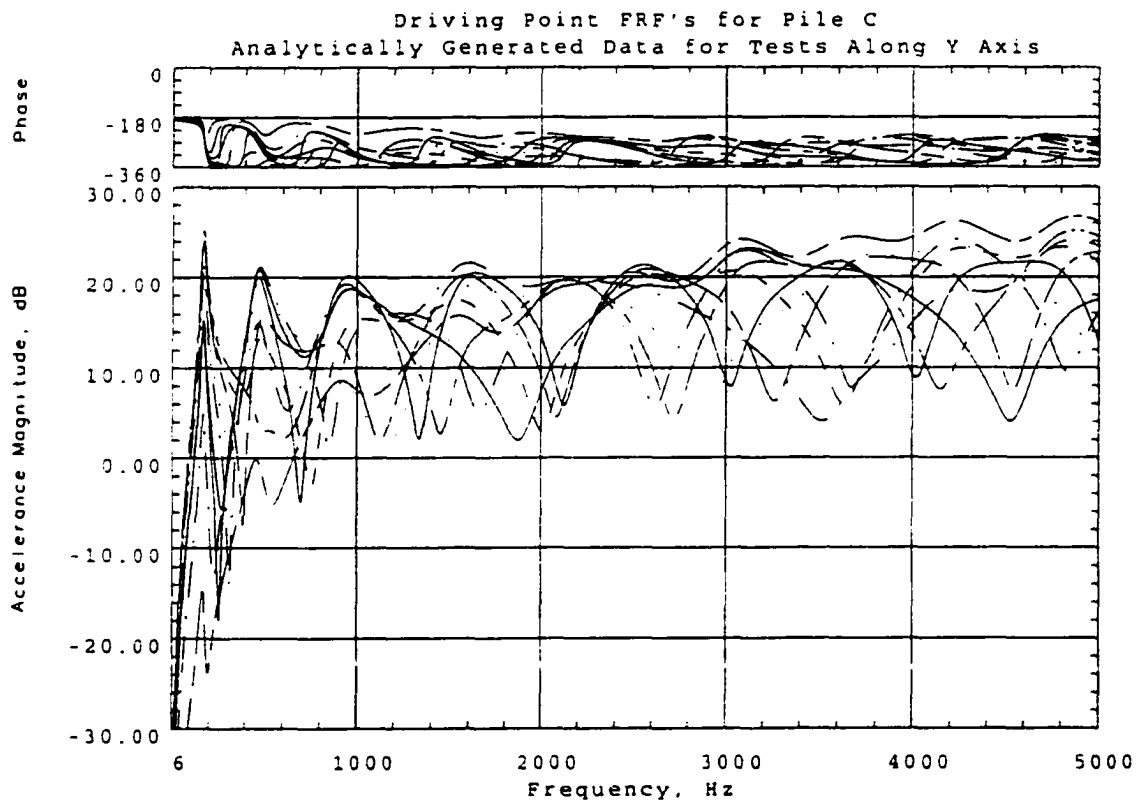


Figure 5.11 Analytically Generated Driving Point Frequency Response Functions for Pile C, Along Y Axis

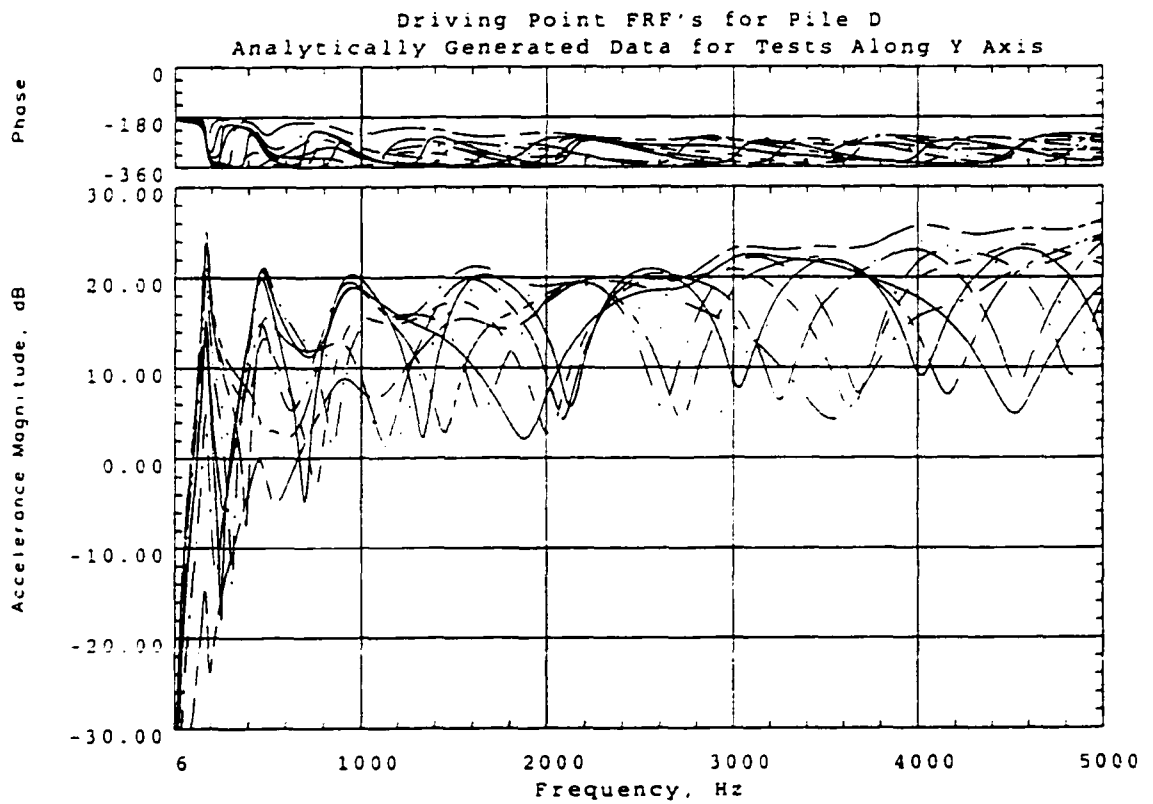


Figure 5.12 Analytically Generated Driving Point Frequency Response Functions for Pile D, Along Y Axis

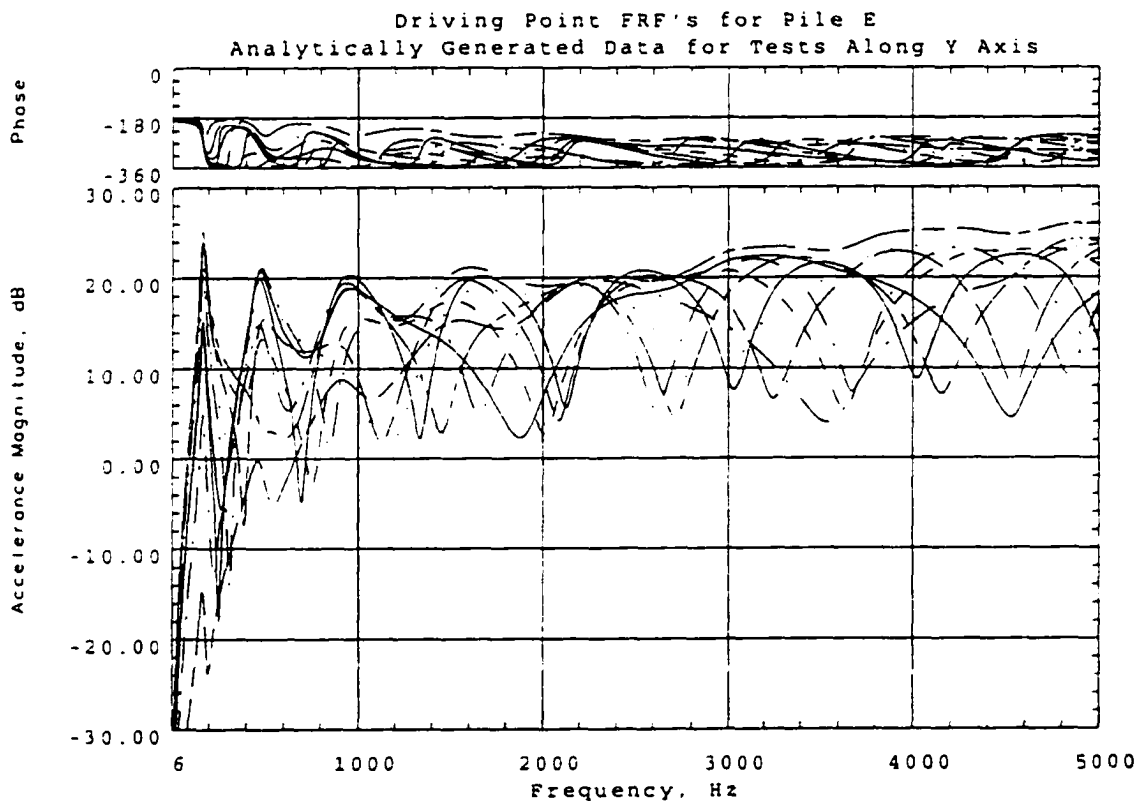


Figure 5.13 Analytically Generated Driving Point Frequency Response Functions for Pile E, Along Y Axis

The natural frequency and damping factor estimates determined for the analytically generated data using the frequency polyreference modal parameter estimation technique are presented in Tables 5.7 to 5.11 for Piles A through E, respectively, for tests along the Y Axis. The results are presented graphically in Figures 5.14 and 5.15 as plots of natural frequency and damping versus mode number. In a manner similar to that described in Section 4.4.2, mode shapes calculated from the parameter estimated were examined and compared, revealing that every pile did not exhibit all of the modes present in every other pile. As such, the natural frequency and associated damping values have been separated in the tables and figures so that those values corresponding to like modes are given the same mode number.

Table 5.7 Pile A, Embedded Configuration Modal Parameter Estimation Results Along Y Axis, Analytically Generated Data

Pile A, Embedded Configuration Analytically Generated Data, Along Y Axis		
Mode Number	Natural Frequency, Hz	Damping, %
1	154.0	8.0
2	444.8	9.0
3	871.9	9.5
4	1387.6	8.8
5		
6	1962.1	7.4
7		
8	2604.1	5.4
9		
10		
11		
12	3316.1	3.8
13		
14	4080.4	3.0
15		
16	4879.9	2.6
17	4999.9	0.0

**Table 5.8 Pile B Modal Parameter Estimation Results, Along Y Axis
Analytically Generated Data**

Pile B		
Analytically Generated Data, Along Y Axis		
Mode Number	Natural Frequency, Hz	Damping, %
1	170.1	7.7
2	470.8	11.4
3	951.0	12.9
4	1504.9	9.7
5		
6	2043.9	10.5
7		
8	2558.0	8.5
9		
10		
11		
12	3171.6	5.8
13	3836.8	5.2
14	4495.9	5.0
15		
16		
17	4987.5	0.2

Table 5.9 Pile C Modal Parameter Estimation Results, Along Y Axis
Analytically Generated Data

Pile C		
Analytically Generated Data, Along Y Axis		
Mode Number	Natural Frequency, Hz	Damping, %
1	170.5	6.6
2	467.9	10.2
3	913.9	14.3
4	1248.0	33.1
5	1559.4	12.1
6	2103.8	12.2
7		
8	2521.3	10.9
9	3079.1	7.4
10		
11		
12	3646.7	7.6
13		
14		
15		
16		
17		

**Table 5.10 Pile D Modal Parameter Estimation Results, Along Y Axis
Analytically Generated Data**

Pile D		
Analytically Generated Data, Along Y Axis		
Mode Number	Natural Frequency, Hz	Damping, %
1	170.5	6.7
2	468.3	10.3
3	921.2	13.5
4	1463.9	26.5
5		
6	1575.9	15.6
7		
8	2149.4	13.3
9	2491.8	12.8
10	3016.8	9.0
11		
12	3477.3	9.4
13	3991.3	7.0
14	4524.1	7.2
15		
16	4987.5	0.2
17		

Table 5.11 Pile E Modal Parameter Estimation Results, Along Y Axis
Analytically Generated Data

Pile E		
Analytically Generated Data, Along Y Axis		
Mode Number	Natural Frequency, Hz	Damping, %
1	170.5	6.7
2	468.2	10.3
3	921.2	13.8
4	1521.0	15.9
5		
6		
7	1679.5	24.8
8	2184.5	14.0
9	2468.5	14.4
10	2970.6	10.7
11	3339.3	10.4
12		
13	3846.1	8.5
14	4266.0	8.2
15	4785.8	6.9
16	4987.5	0.2
17		

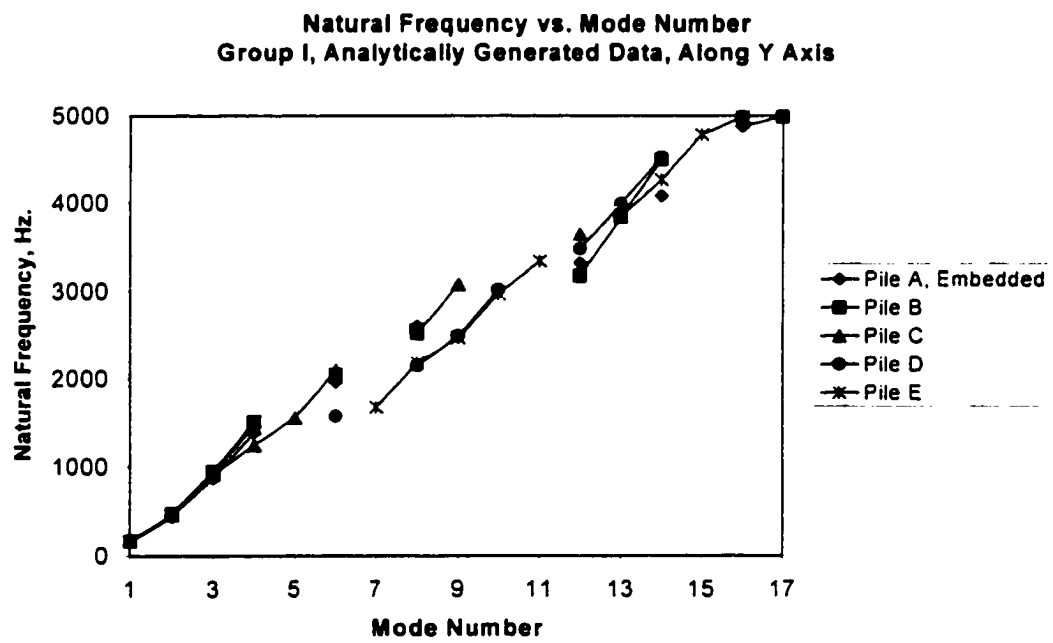


Figure 5.14 Natural Frequency vs. Mode Number for Analytically Generated Data, Along Y Axis

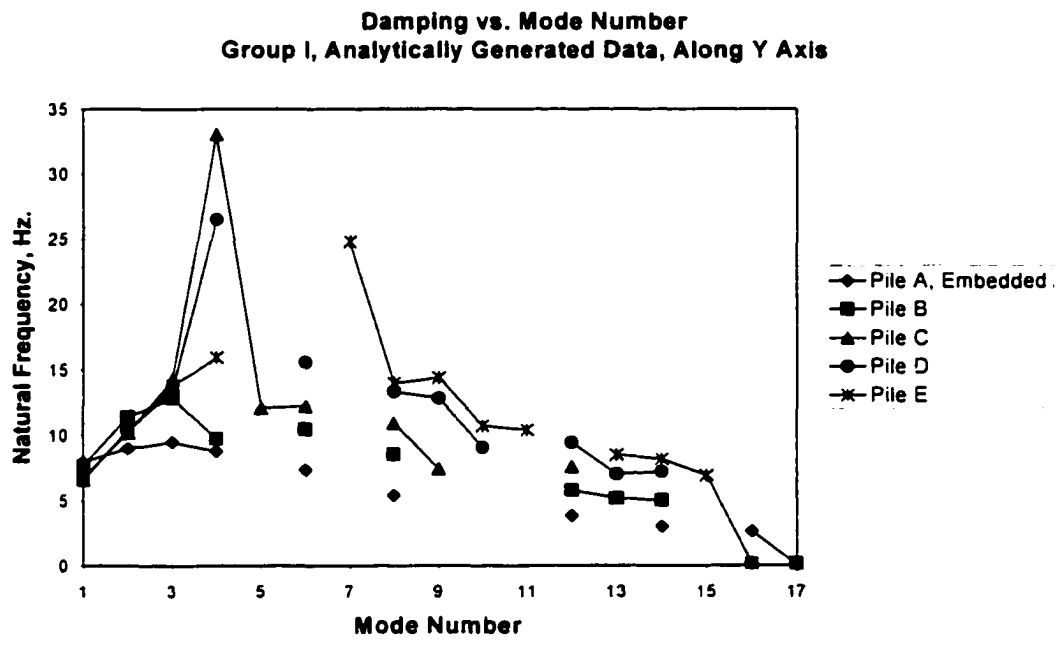


Figure 5.15 Damping vs. Natural Frequency for Analytically Generated Data, Along Y Axis

5.1.3 Discussion of Modal Parameter Estimation Results for Analytically Generated Data

As was the case with the experimental data, there do not appear to be any significant differences discernable in natural frequency values for the five embedded piles in the 0-5000 Hz frequency range for which the analytically generated data was produced. Although there is some "spread" of the frequency values observed in Figure 5.7 for the sixth through fourteenth modes (in the 1125-4800 Hz range), the variation is relatively slight and is without a clearly defined pattern from which identification of a particular embedded pile

length could be made. Values presented in Figure 5.14 for tests along the Y axis show a greater degree of diversity, but once again, no trend is developed that would make one pile distinguishable from another. It should also be noted that in the 0-2000 Hz range (which corresponds to the range considered valid for the experimental modal parameter estimation process), there is essentially no variation at all in the frequency values of the embedded piles, for tests along both axes.

The damping plots shown in Figures 5.8 and 5.15 are somewhat more interesting, though not much more useful for the embedment length identification process. It is interesting to note the damping peak progression in Figure 5.8; as indicated in the figure, a local maximum occurs for each of Piles A through D, though not in progressive order (not for Pile A, then for Pile B, then C, etc.). Since the progression does not follow any logical trend, no clear deduction can be made as to embedded pile length identification from the curves shown.

The curves shown in Figure 5.15 for tests along the Y axis hint at a similar local maximum progression, and the damping values are more decidedly different for each pile than those for tests along the X axis, but once again, a distinct pattern is not identifiable for the various piles. Also, for tests along both axes (i.e., for data in Figures 5.8 and 5.15), the peak progression is only partially completed in the range of modes corresponding to the 0-2000 Hz frequency range valid for modal parameter identification of the experimental results (modes 1 through 8 for both figures). So even if the location of the peaks could ideally be used to identify piles with certain embedment lengths, that scheme would not be feasible in the frequency range that was found to be valid for the experimental results.

5.2 Finite Element Modeling

To further investigate the difference in modal characteristics of the Group I model piles, finite element models were created of each pile (and of Pile A in the nonembedded configuration), and the first forty natural frequencies and mode shapes of each were calculated from an eigenvalue analysis. A series of springs was used to represent the restraint provided by the soil surrounding the piles; the spring stiffnesses were derived from the magnitude of the complex stiffnesses calculated in the programs discussed above.

5.2.1 Model for Pile A in Nonembedded Configuration

As has been stated previously, if any one of the model piles is considered in its nonembedded configuration (i.e., without any surrounding embedment soil), the resulting arrangement is essentially that of a cantilevered beam. In the case of the model piles attached to the test facility described in Chapter II, the upper end is the fixed (or nearly fixed, as will be discussed shortly) end, while the lower end is free. As a preliminary model, then, a 6-foot long cantilevered beam (analogous to Pile A in its nonembedded configuration) was created using 72 1-inch long beam elements whose section properties were those of an S3x5.7 wide flange section. (The I-DEAS software package was used for finite element modeling throughout the study; an S3x5.7 section was one of those available in the I-DEAS section catalog.) To model the fixity of the top end, a clamped restraint (allowing no translation or rotation in any direction) was placed at the uppermost node. Figure 5.16 shows the model and its orientation with respect to the coordinate axes.

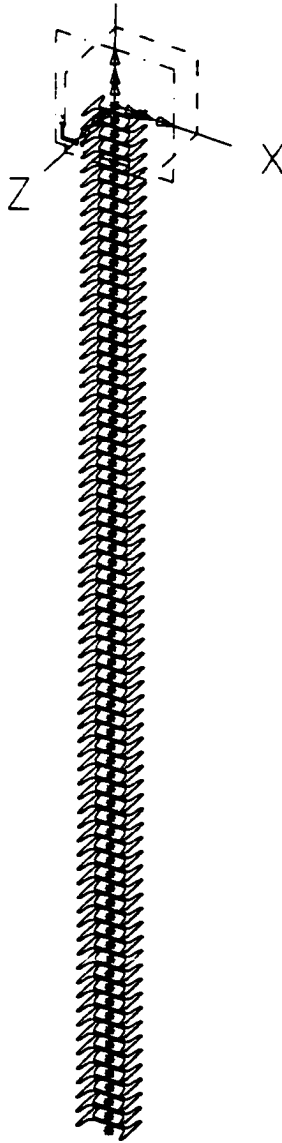


Figure 5.16 Preliminary Finite Element Model of Pile A, Nonembedded Configuration, Clamped at Top End, Free at Bottom End

Natural frequency values obtained from the finite element model are shown in Tables 5.12 and 5.13 for the first ten vibration modes along the X and Y axes, alongside values

obtained from the well-known closed-form solution for calculating the natural frequencies of cantilevered beams. The analytical solution, derived from simple beam theory, is of the form shown in Equation 3.12 (presented on page 85).

Table 5.12 Comparison of Natural Frequency Values Obtained by Theoretical Solution and by Finite Element Model, Along X Axis

Pile A, Nonembedded Configuration Along X Axis			
Mode Number	Natural Frequency, Hz		
	Theoretical Solution	Finite Element Model	Error, %
1	11.2	11.2	0.6
2	70.0	70.3	0.5
3	196.0	196.7	0.4
4	384.1	384.8	0.2
5	634.9	634.7	0.0
6	948.6	945.5	0.3
7	1324.6	1316.3	0.6
8	1763.3	1746.1	1.0
9	2264.2	2233.4	1.4
10	2830.5	2777.0	1.9

Table 5.13 Comparison of Natural Frequency Values Obtained by Theoretical Solution and by Finite Element Model, Along Y Axis

Pile A, Nonembedded Configuration Along Y Axis			
Mode Number	Natural Frequency, Hz		
	Theoretical Solution	Finite Element Model	Error, %
1	26.3	26.4	0.5
2	164.7	164.9	0.1
3	461.2	458.7	0.6
4	903.9	890.6	1.5
5	1494.1	1455.0	2.6
6	2232.3	2143.0	4.0
7	3117.3	2944.8	5.5
8	4149.7	3850.0	7.2
9	5329.6	4847.7	9.0
10	6661.3	5927.5	11.0

As expected for the relatively simple case of a cantilevered beam, the natural frequency values calculated with the finite element model agreed quite well with the values obtained using simple beam theory, especially for the lower modes. It should be noted that for the comparison detailed above, shear effects were not included in the formulation of the finite elements, since the solution derived from simple beam theory does not take them into account. For those subsequent comparisons in which it was appropriate, shear effects were introduced into the beam finite elements included in the model.

Quantities obtained from the finite element model were next compared to those determined from the experimental modal parameter estimation process (for tests along the X axis only since experimental results for tests along the Y axis were not available for this configuration). Since shear effects were present in the actual piles tested in the

experimental program, they were added to the finite element model as well. As before, a clamped restraint was placed at the uppermost node. The results of this comparison are summarized below in Table 5.14.

Table 5.14 Comparison of Natural Frequency Values Obtained from Experimental Results with Those from Finite Element Model, Along X Axis

Pile A, Nonembedded Configuration Along X Axis			
Mode Number	Natural Frequency, Hz		
	Experimental Results	Finite Element Model*	Error, %
1	9.1	11.2	19.2
2	63.3	70.1	9.8
3	154.5	195.3	20.9
4	181.6	379.9	52.2
5	261.3	622.0	58.0
6	335.7	918.7	63.5
7	355.5	1266.4	71.9
8	485.6	1661.7	70.8
9	563.5	2100.7	73.2
10	692.7	2580.0	73.2

* Shear effects included, clamped at top node.

As is obvious from Table 5.14, the results do not compare very favorably, especially those for modes higher than the second. However, if the third, fifth, sixth, eighth, and tenth modes obtained experimentally are considered to be spurious modes that do not represent purely flexural vibration along the X axis, and are removed from the list, there is a marked improvement in agreement between the two sets of results. Table 5.15 shows the modified

values and their associated percentage errors. (A brief discussion of the disregard of nonflexural modes is given below.)

Table 5.15 Comparison of Natural Frequency Values Obtained from Experimental Results with Those from Finite Element Model, Along X Axis (Modified)

Pile A, Nonembedded Configuration Along X Axis			
Mode Number	Natural Frequency, Hz		
	Experimental Results*	Finite Element Model**	Error, %
1	9.1	11.2	19.2
2	63.3	70.1	9.8
3	181.6	195.3	7.0
4	355.5	379.9	6.4
5	563.5	622.0	9.4
6	817.0	918.7	11.1
7		1266.4	
8		1661.7	
9		2100.7	
10		2580.0	

* Non-flexural modes removed, 0-1000 Hz range tested.

** Shear effects included, clamped at top node.

As shown in the table, this procedure greatly improves the correlation between the experimental and finite element results. Further improvement can be realized with a modification of the clamped boundary condition at the top of the pile. One may recall that in the test fixture employed for the experimental test program, the model piles were attached to the supporting W10x45 via welds located along the lines of intersection between the W10x45 flange edges and the outer surfaces of the model pile flanges, as illustrated in Figure 5.17 below.

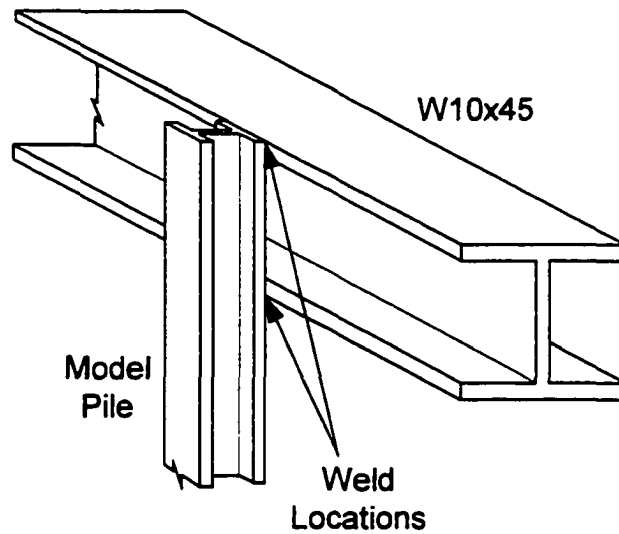


Figure 5.17 Connection Arrangement for Model Piles in Test Fixture

Such a connection arrangement does not actually constitute a built-in condition, as is implied by placing a clamped restraint at the uppermost node. Rather, if the model is modified by adding a group of elements representing the section of pile connected to the supporting W10x45, and by placing pinned restraints at the nodes corresponding to the weld locations, rotation is allowed about the X axis (as oriented in Figure 5.16) at the location of the welds, and the pile is free to translate in the Z direction between the welds. This restraint condition, shown in Figure 5.18, is a more realistic simulation of the actual connection detail, as evidenced by the improved agreement between the modified finite element model results and the experimental results, summarized below in Table 5.16.

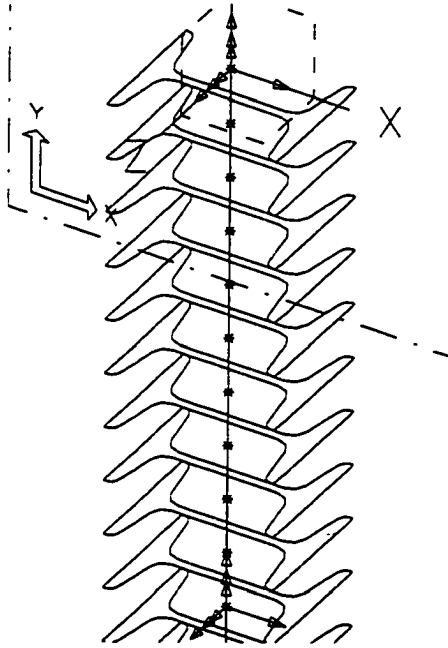


Figure 5.18 Modified Boundary Condition Arrangement

Table 5.16 Comparison of Natural Frequency Values Obtained from Experimental Results with Those from Finite Element Model, Along X Axis (Modified Boundary Conditions)

Pile A, Nonembedded Configuration Along X Axis			
Mode Number	Natural Frequency, Hz		
	Experimental Results*	Finite Element Model**	Error, %
1	9.1	10.3	11.8
2	63.3	65.0	2.7
3	181.6	182.8	0.6
4	355.5	358.1	0.7
5	563.5	589.7	4.4
6	817.0	873.8	6.5
7		1204.6	
8		1563.9	
9		1859.1	
10		2125.8	

* Non-flexural modes removed, 0-1000 Hz range tested.

** Pins allowing rotation about X axis at weld locations.

Though the error between results for the first mode is still relatively high, that for each successive mode is greatly reduced, and it can be concluded that the modified boundary condition arrangement more accurately simulates the physical reality of the model pile test fixture than the clamped configuration. Confident, then, that the modified finite element model is an accurate representation of the piles in their nonembedded state, this model was used as a basis for the finite element study of the Group I embedded piles.

Regarding the presence of nonflexural modes in the experimental results, the following comments can be made. Because of the difficulty encountered in impacting the piles so that only purely flexural modes are excited, it is not unreasonable to expect that some coupled torsional and axial modes (as well as flexural modes in the “off-axis” direction) would be apparent in the experimental frequency response function data, and would therefore be included in estimations of natural frequency. (This difficulty is especially pronounced when testing piles with rather “complex” shapes, such as the S-shaped section used in this study.) For the nonembedded situation, the “expected” natural frequency values for flexural modes are known well enough that it was relatively easy to distinguish the nonflexural modes identified from the modal parameter identification process (as was done to produce Table 5.15). Unfortunately, since there are no theoretical, closed-form solutions available for the more complex embedded pile systems, this “culling” procedure was not easily performed for the embedded model pile experimental results. However, since the purpose of the present study was to identify the embedded lengths of piles from the differences in their modal characteristics, only a comparison of the modal values between piles was necessary, as

opposed to an absolute correlation of their values with theoretical solutions. With this in mind, the numerical analyses described in this chapter were performed to examine the relationship between numerical modal results for each pile, rather than to “match” them exactly to the experimental results.

5.2.2 Finite Element Results for Embedded Piles

Finite element models for each of the Group I piles were created by adding beam elements to the basic model described above, in lengths corresponding to the embedded portion of each pile. To represent the restraint imposed on the piles by the surrounding soil, translational and rotational springs (resisting motion in the models' X and Z directions) were attached to each of the nodes within the embedded portion. As mentioned in the introduction to Section 5.2, the spring stiffnesses were derived from the magnitude of the complex stiffnesses calculated in the programs discussed in Section 5.1; their values were adjusted to correlate with the tributary area between nodes. The model for Pile C is depicted below in Figure 5.19; models for the remaining piles are similar in appearance, differing only in the length of the spring-restrained embedded portion.

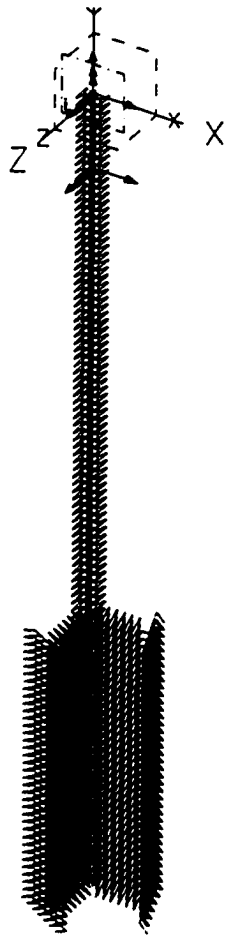


Figure 5.19 Finite Element Model for Pile C in Its Embedded Configuration

5.2.2.1 Results for Tests Along the X Axis

Results of the finite element frequency analyses for the Group I embedded piles are presented in Tables 5.17 through 5.21 for tests along the X axis, and are summarized for the same in graphical format in Figure 5.20.

Table 5.17 Natural Frequency Results from Finite Element Model for Pile A, Embedded Configuration, Along X Axis

Pile A, Embedded Configuration Finite Element Results, Along X Axis	
Mode Number	Natural Frequency, Hz
1	85.6
2	236.3
3	461.0
4	753.4
5	1104.7
6	1494.0
7	1827.6
8	2086.8
9	2476.3
10	2590.2
11	2913.5
12	3302.1
13	3794.3
14	4344.5
15	4913.7
16	5479.9
17	5860.7

Table 5.18 Natural Frequency Results from Finite Element Model for Pile B, Along X Axis

Pile B	
Finite Element Results, Along X Axis	
Mode Number	Natural Frequency, Hz
1	85.6
2	236.3
3	461.0
4	753.5
5	1104.7
6	1494.2
7	1828.0
8	2087.6
9	2479.0
10	2546.9
11	2644.9
12	2887.4
13	3166.9
14	3560.4
15	3957.8
16	4414.8
17	4894.8

Table 5.19 Natural Frequency Results from Finite Element Model for Pile C, Along X Axis

Pile C	
Finite Element Results, Along X Axis	
Mode Number	Natural Frequency, Hz
1	85.6
2	236.3
3	461.0
4	753.5
5	1104.7
6	1494.2
7	1828.0
8	2087.6
9	2479.1
10	2540.8
11	2575.7
12	2680.7
13	2872.0
14	3093.8
15	3389.4
16	3718.2
17	4080.9
18	4466.0

Table 5.20 Natural Frequency Results from Finite Element Model for Pile D, Along X Axis

Pile D	
Finite Element Results, Along X Axis	
Mode Number	Natural Frequency, Hz
1	85.8
2	236.3
3	461.0
4	753.5
5	1104.7
6	1494.2
7	1828.0
8	2087.6
9	2479.1
10	2539.1
11	2555.5
12	2603.7
13	2704.1
14	2862.0
15	3046.6
16	3273.1
17	3556.2
18	3839.2

Table 5.21 Natural Frequency Results from Finite Element Model for Pile E, Along X Axis

Pile E	
Finite Element Results, Along X Axis	
Mode Number	Natural Frequency, Hz
1	85.6
2	236.3
3	461.0
4	753.5
5	1104.7
6	1494.2
7	1828.0
8	2087.6
9	2479.1
10	2538.5
11	2547.6
12	2573.4
13	2627.4
14	2720.6
15	2855.0
16	3012.8
17	3195.6
18	3429.8

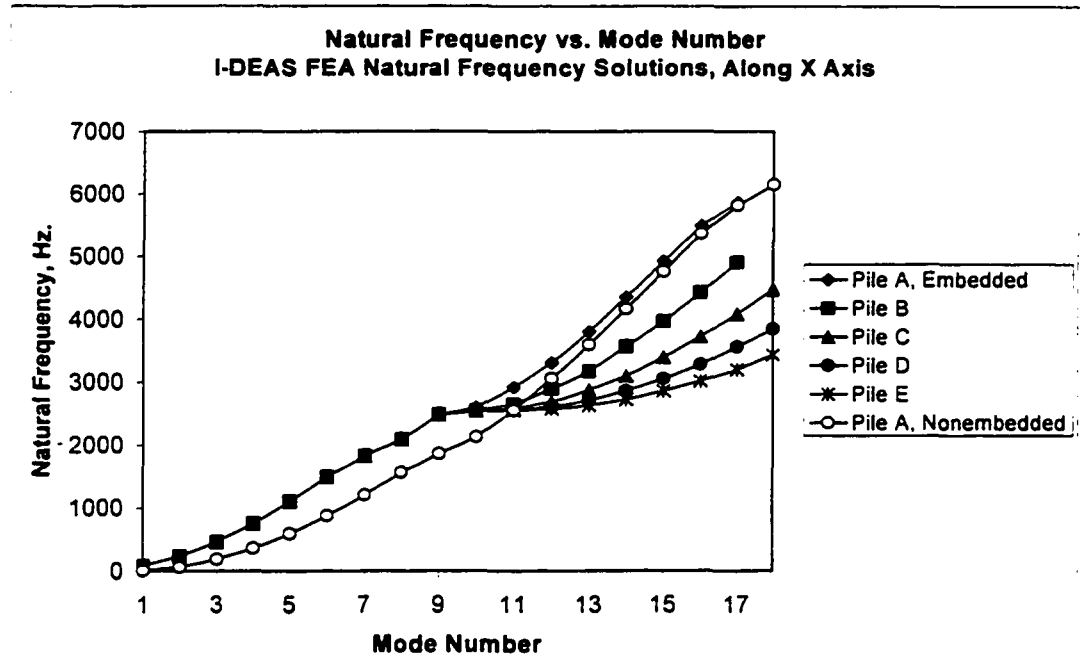


Figure 5.20 Natural Frequency Results from Finite Element Modeling vs. Mode Number, Along X Axis

5.2.2.2 Results for Tests Along the Y Axis

Results of the finite element frequency analyses for the Group I embedded piles are presented in Tables 5.22 through 5.26 for tests along the X axis, and are summarized for the same in graphical format in Figure 5.21.

Table 5.22 Natural Frequency Results from Finite Element Model for Pile A, Embedded Configuration, Along Y Axis

Pile A, Embedded Configuration Finite Element Results, Along Y Axis	
Mode Number	Natural Frequency, Hz
1	192.3
2	497.9
3	905.2
4	1377.2
5	1886.9
6	2410.7
7	2851.3
8	2969.9
9	3421.5
10	3863.0
11	4339.7
12	4856.6
13	5382.9
14	5900.8

Table 5.23 Natural Frequency Results from Finite Element Model for Pile B, Along Y Axis

Pile B	
Finite Element Results, Along Y Axis	
Mode Number	Natural Frequency, Hz
1	193.0
2	499.4
3	907.5
4	1380.3
5	1890.9
6	2414.6
7	2865.7
8	2879.4
9	3050.9
10	3426.8
11	3765.7
12	4178.1
13	4603.5
14	5006.7

Table 5.24 Natural Frequency Results from Finite Element Model for Pile C, Along Y Axis

Pile C	
Finite Element Results, Along Y Axis	
Mode Number	Natural Frequency, Hz
1	193.0
2	499.4
3	907.5
4	1380.3
5	1890.9
6	2414.8
7	2863.1
8	2870.9
9	2930.3
10	3128.9
11	3429.0
12	3704.0
13	4065.8
14	4392.2

Table 5.25 Natural Frequency Results from Finite Element Model for Pile D, Along Y Axis

Pile D Finite Element Results, Along Y Axis	
Mode Number	Natural Frequency, Hz
1	193.0
2	499.4
3	907.5
4	1380.3
5	1890.9
6	2414.8
7	2863.0
8	2872.0
9	2889.8
10	2987.2
11	3179.8
12	3430.8
13	3664.2
14	3972.7

Table 5.26 Natural Frequency Results from Finite Element Model for Pile E, Along Y Axis

Pile E	
Finite Element Results, Along Y Axis	
Mode Number	Natural Frequency, Hz
1	193.0
2	499.4
3	907.5
4	1380.3
5	1890.9
6	2414.8
7	2864.8
8	2871.3
9	2875.9
10	2926.7
11	3036.3
12	3216.5
13	3432.1
14	3635.7

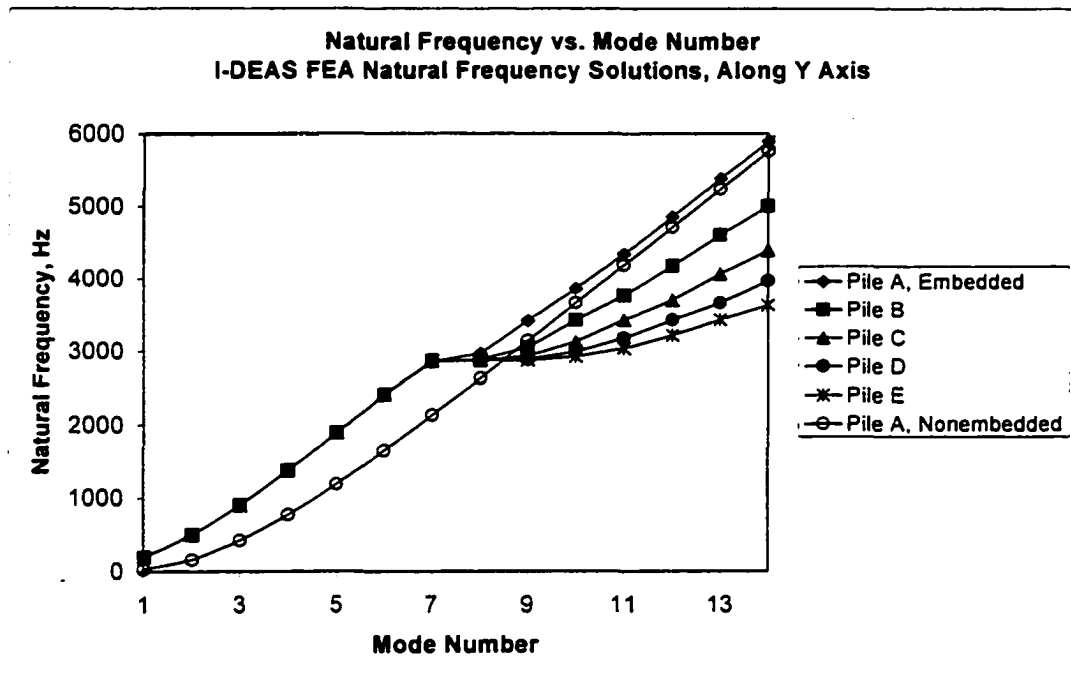


Figure 5.21 Natural Frequency Results from Finite Element Modeling vs. Mode Number, Along Y Axis

5.2.3 Discussion of Natural Frequency Results from Finite Element Modeling of Embedded Piles

Figures 5.20 and 5.21 exhibit two dominant features when viewed in terms of the goals of the present study. The first is that the natural frequencies for the first nine modes (up to approximately 2500 Hz) for tests along the X axis, and for the first seven modes (up to approximately 2800 Hz) for tests along the Y axis, are virtually identical in magnitude. Secondly, above those “threshold” frequencies, there is a gradual “spreading” of the natural frequency values as the mode number increases; this spreading is distinctive in that it

progresses from Pile A to Pile E in successive order. This frequency behavior with increasing mode number suggests that the restraint provided by the soil surrounding the piles (or by the springs in the case of the finite element model) does not appreciably affect the vibrational behavior of each pile differently until the threshold frequency is reached. Once the critical frequency value is attained, however, the natural frequencies progressively decrease (for a constant mode number) as the percentage of pile that is embedded (and therefore heavily restrained) becomes larger.

The trends described above become visibly apparent when viewing the mode shapes for each pile with increasing mode number. From a qualitative standpoint, three “stages” are apparent in the mode shape progression. (The first forty mode shapes for Pile A in its embedded configuration are presented in Appendix C. Those modes that do not appear in the figures are axial and torsional modes.) In the first stage, which consists of approximately modes one through nine for modes along the X axis, and one through seven for modes along the Y axis, the mode shapes are similar to those of a beam supported at both ends. The majority of the deformation takes place in the exposed portion of the pile (in the classical sine wave oscillation pattern), especially for the first two to three modes in each direction. In the later modes of the first stage, there is some deformation in the spring region, but the bottom tip of the pile for each of these modes remains stationary.

In the second stage of mode shape progression, deformation in the exposed portion is similar to that in the first stage, but more excessive deformation is noticed in the embedded portion, and the bottom tip no longer exhibits zero displacement. In fact, for some modes in the second stage, the magnitude of deformation is much greater in the embedded portion

than in the exposed portion. The second stage proceeds somewhat gradually into the third, in which the mode shapes consist of continuous sine wave oscillations throughout the exposed portion and into the embedded portion.

Also shown in Figures 5.20 and 5.21 are the natural frequency vs. mode number curves for Pile A in its nonembedded configuration. As would be expected intuitively, frequency values calculated for the nonembedded pile are lower than those determined for the same pile in its embedded configuration, and lower than those for each of the embedded piles at frequencies below the threshold described above. This feature seems reasonable in view of the fact that the cantilevered pile is not stiffened by the surrounding soil and its tip is free to vibrate, so it should exhibit lower frequencies than the stiffened, embedded piles. At frequencies higher than the threshold, however, the restraining effect of the soil becomes dominant, and the frequencies are reduced accordingly. It is interesting to note, incidentally, that for very high mode numbers (not shown in Figures 5.20 and 5.21), the frequencies for the nonembedded pile become essentially identical to those for Pile A in its embedded configuration.

One last, but quite important, comment should be made concerning the results summarized in Figures 5.20 and 5.21. Since the threshold frequency below which there is no variation in natural frequency with embedment length (for a constant mode number) is above that for which the experimental data could reasonably be analyzed, it appears that identification of pile embedment length using the method investigated in this study may not be feasible in its present state. Additional comments regarding this conclusion will be provided in Chapter VII.

5.3 Theoretical Natural Frequency Calculation for Beam Resting on Elastic Supports

To continue the investigation of the variation in natural frequency with pile embedment length, a theoretical solution based on the work by Weaver, Timoshenko, and Young (Weaver et al., 1990) for beams on elastic supports or elastic foundations was formulated for the Group I embedded piles. The derivation is provided in Appendix D of this paper; it is based on the fact that most in-service beams have end restraints falling into an intermediate state of fixity ranging between the extremes of full restraint (fixed) and zero restraint (free). As stated by the authors, if the restraints can be considered to be linearly elastic in nature, they may be idealized as springs, in the manner shown in Figure 5.22 below.

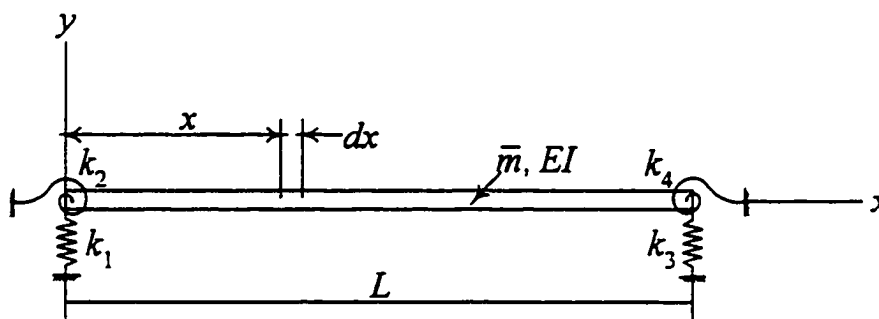


Figure 5.22 Beam on Elastic Supports Idealized as Springs

For the purposes of this theoretical development, the left end was considered to be fully fixed (though it was determined in the previous section that the connection of the model piles to the supporting W10x45 section does not constitute a truly fixed condition). In the

fully fixed condition, k_1 and k_2 (which represent the translational and rotational stiffnesses, respectively, of the springs at the left end) are equal to infinity. The stiffnesses contributed by the embedded portions of the piles were derived once again from the analytical programs described in Section 5.1, and were “lumped” mathematically into the two springs at the right end, k_3 and k_4 . The procedure by which this “lumping” was accomplished is described in Appendix D. The theoretical solution was derived only for the case corresponding to tests along the X axis, since it was apparent from the investigations previously described that tests along the Y axis produced quite similar results in terms of the variation of natural frequency with embedded pile length. For the orientation pictured in Figure 5.22, then, the translational spring, k_3 , resisted motion in the y direction, while the rotational spring, k_4 , resisted rotation about the z axis. (The S3x5.7 section was oriented such that its X axis, as pictured in Figure 4.2, shown on page 90, corresponded to the y axis shown in Figure 5.22.)

5.3.1 Results of Theoretical Natural Frequency Calculations

Results of the calculations for the first ten natural frequencies of the Group I embedded piles, calculated according to the procedure described in Appendix D, are presented in Tables 5.27 through 5.31. To determine the fixity range of the Group I piles in relation to the fixed-free condition and the fixed-fixed condition, the first ten natural frequencies for these cases were computed as well. For the fixed-free condition, springs k_3 and k_4 were given stiffnesses equal to zero; for the fixed-fixed condition, k_3 was assigned a value of 1×10^{30} lb/ft and k_4 was set equal to 1×10^{30} ft-lb/rad. Although the results for the latter two

cases are not presented in tabular format, they do appear on the graph summarizing the natural frequency information, which is presented in Figure 5.23.

Table 5.27 Theoretical Natural Frequencies for Pile A, Embedded Configuration

Pile A, Embedded Configuration Theoretical Solution (Weaver et al.)	
Mode Number	Natural Frequency, Hz
1	94.3
2	262.8
3	519.0
4	862.8
5	1293.7
6	1811.2
7	2414.3
8	3101.3
9	3870.0
10	4717.8

Table 5.28 Theoretical Natural Frequencies for Pile B

Pile B Theoretical Solution (Weaver et al.)	
Mode Number	Natural Frequency, Hz
1	98.0
2	270.9
3	532.3
4	881.5
5	1318.8
6	1843.4
7	2455.3
8	3153.8
9	3937.8
10	4805.9

Table 5.29 Theoretical Natural Frequencies for Pile C

Pile C	
Theoretical Solution (Weaver et al.)	
Mode Number	Natural Frequency, Hz
1	99.4
2	274.4
3	538.5
4	890.9
5	1331.6
6	1860.4
7	2477.1
8	3181.1
9	3972.0
10	4848.5

Table 5.30 Theoretical Natural Frequencies for Pile D

Pile D	
Theoretical Solution (Weaver et al.)	
Mode Number	Natural Frequency, Hz
1	100.2
2	276.3
3	542.0
4	896.5
5	1339.4
6	1871.0
7	2490.7
8	3198.3
9	3993.4
10	4875.4

Table 5.31 Theoretical Natural Frequencies for Pile E

Pile E	
Theoretical Solution (Weaver et al.)	
Mode Number	Natural Frequency, Hz
1	100.7
2	277.6
3	544.3
4	900.1
5	1344.7
6	1878.2
7	2500.2
8	3210.2
9	4008.3
10	4894.0

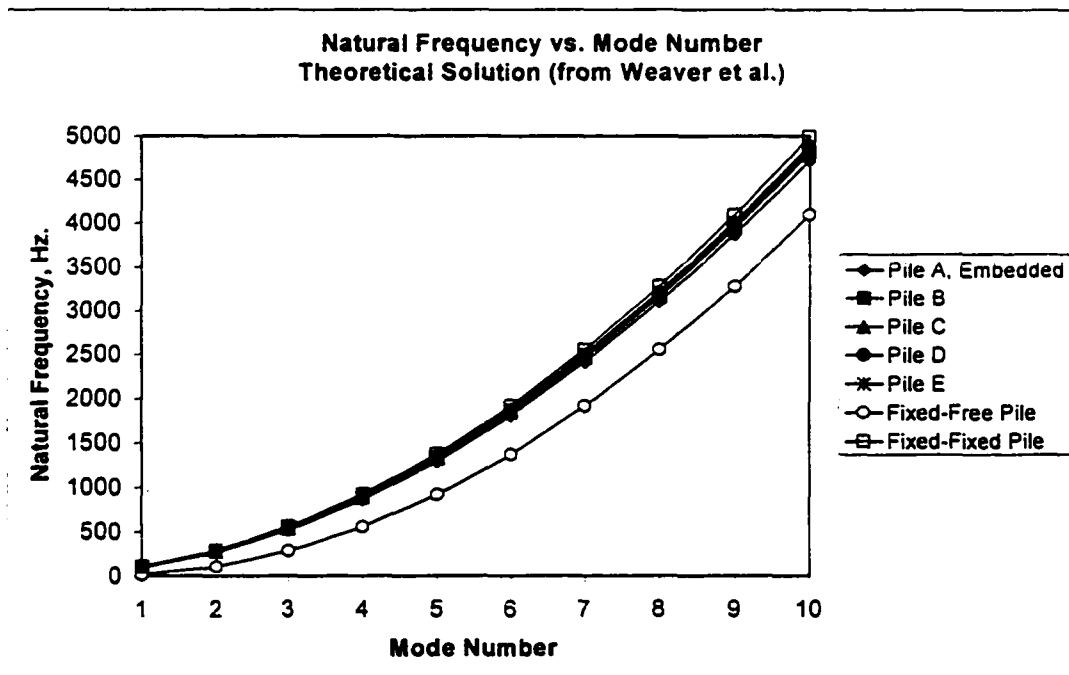


Figure 5.23 Theoretical Natural Frequency vs. Mode Number

5.3.2 Discussion of Theoretical Natural Frequency Results

Examination of Figure 5.23 reveals that, for the embedded piles, there is only a slight variation in the natural frequencies with embedment depth, for a given mode number. In fact, the maximum percentage difference for Piles B-E from the Pile A values is just less than 7%, as shown in Figure 5.24 below.

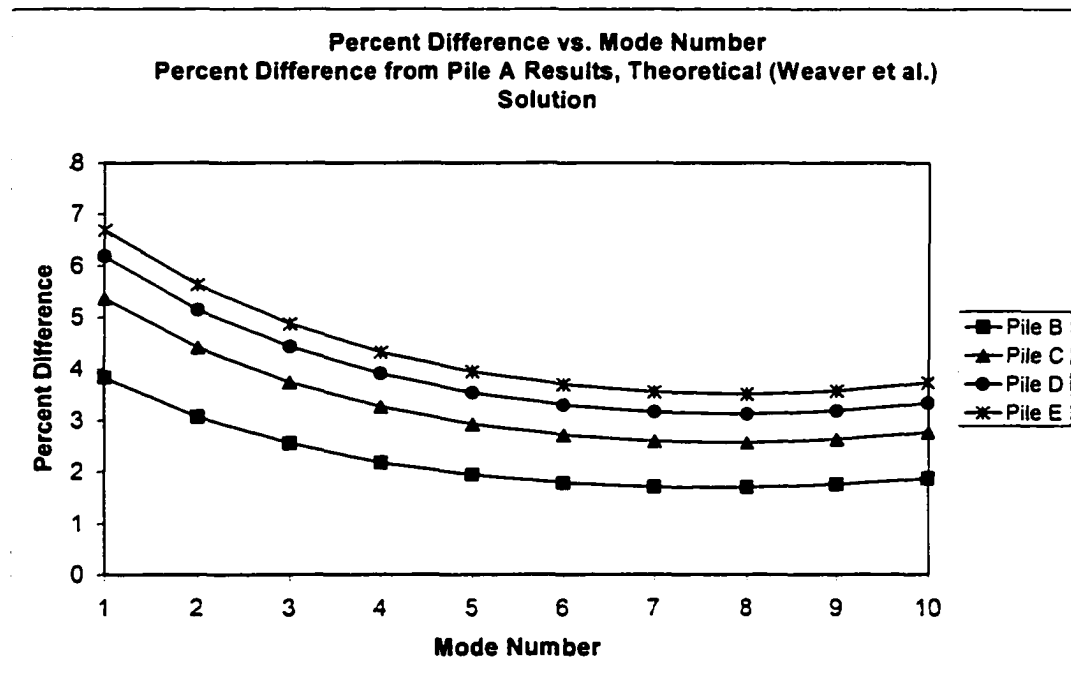


Figure 5.24 Percent Difference from Pile A Theoretical Natural Frequency Results

It is also evident from Figure 5.23 that the natural frequencies for each of the Group I embedded piles are much closer in magnitude to those for the fixed-fixed beam than to those for the fixed-free beam. This characteristic indicates that the soil surrounding the base of

the piles provides a significant degree of fixity, even for Pile A, whose embedded length is only one foot (out of its six foot total length). Once again, as was the case with the experimental results and with the other two types of numerical analyses described earlier in this chapter, it appears that identification of pile embedment length using modal attributes is not practically feasible.

CHAPTER VI

MODEL PILE WAVE PROPAGATION

To supplement the information gathered in the experimental and numerical modal analyses described in Chapters IV and V, several experiments were conducted to investigate the wave propagation characteristics of the S3x5.7 model pile section. This portion of the study was performed to determine the feasibility of the nondestructive identification of pile embedment depths using the “traveling wave” approach, rather than the modal analysis approach. Although the data interpretation procedures for these two philosophies vary somewhat, the knowledge they provide is similar in nature. The wave propagation approach has been used successfully with tests involving longitudinal impacts (as described in Chapter I), though one notable drawback is that it has traditionally relied upon the rather subjective visual identification of graphical data trends. In the present study, a preliminary attempt was made to identify and manipulate the propagation characteristics of flexural waves, rather than longitudinal waves, since access to the top of a pile (which is usually required to impart a longitudinal impact) is typically not conveniently achieved, as noted in Chapter I.

For analyses involving the wave propagation approach, the shape of the cross section through which waves are travelling becomes a noteworthy topic for consideration. For

example, when an impact is applied to the center of the web of an S3x5.7 model pile section, reflections of the resultant wave occur not only at the flange-web intersections, but also at the four “free” flange edges. Consequently, the potential exists for quite a complex wave pattern to be created as the reflected waves interact. With this realization in mind, a freely-suspended steel beam having a rectangular cross section (a length of flat stock) was tested prior to the S3x5.7 model pile section so that comparisons could be made between results for this relatively simple shape and for the somewhat more complex model pile shape. Also, for the preliminary analyses conducted here, the S3x5.7 section was tested in its nonembedded configuration—the specific boundary conditions utilized for the tests will be described in more detail in succeeding sections of this chapter.

6.1 Spectrogram Description

Hodges et al., in their 1985 paper, “investigate[d] the use of a familiar tool in an unfamiliar context.” The authors described a method by which wave propagation in structures could be examined using simple acceleration measurements, along with a mathematical tool typically used in acoustical studies called a spectrogram (referred to as a sonogram in the paper by Hodges et al., also referred to elsewhere as a short-time Fourier transform (STFT)). A spectrogram is a three-dimensional representation of the time-varying power spectrum of a signal that has been measured in the time domain. Typically, the signal is divided in time into overlapping segments, an appropriate mathematical window is applied to each segment, and the Fourier transform of each is computed. A three-dimensional array is then formed whose amplitude represents the power spectrum of the

signal, plotted against time and frequency. An example of a spectrogram is presented in Figure 4.1; what is shown is a surface plot of the spectrogram for a stretched string subjected to a force impulse at $3/10$ of its length and measured at a location $4/5$ along its length. Although not indicated in the figure, the vertical axis represents the power-spectral amplitude of the signal plotted on a linear scale.

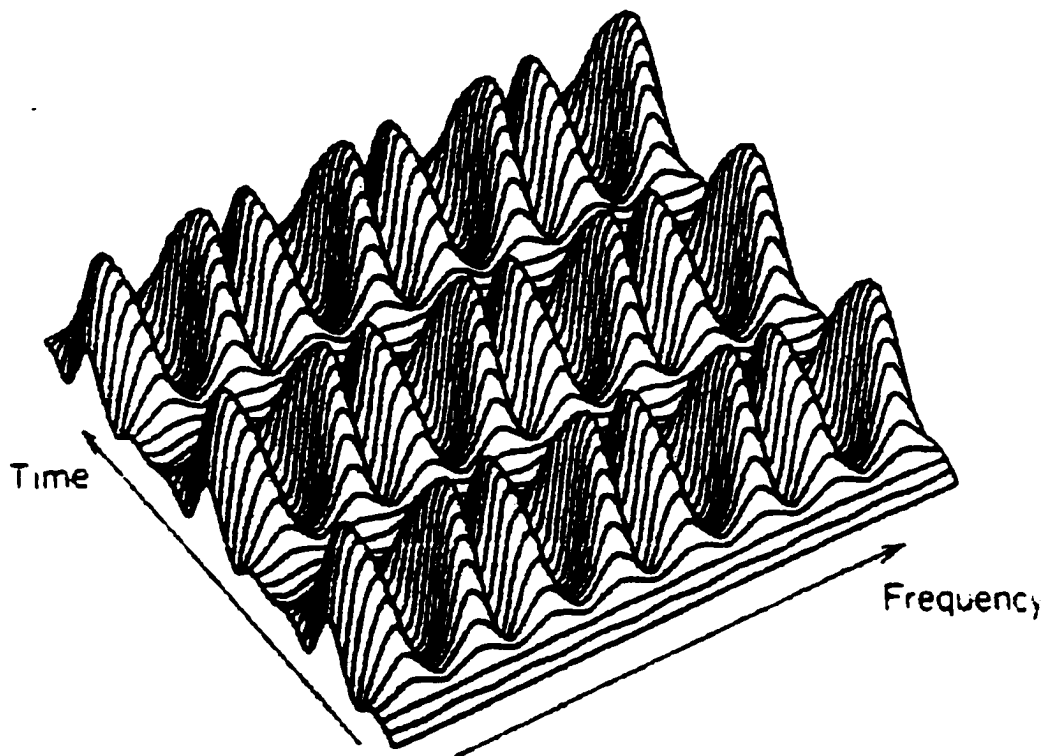


Figure 6.1 Spectrogram for a Force Impulse Applied to a Stretched String (Hodges et al., 1985)

One noteworthy characteristic of the spectrogram is that its “shape”, and consequently the information that can be gathered from its interpretation, is highly dependent upon the length of the time segments chosen for the frequency analysis. Since time and frequency are not truly independent variables, but are both temporal in nature, there is a “trade-off” of sorts in their resolution when a spectrogram is formed. Hodges et al. described the compromise by noting that

[s]onograms are subject to what is essentially Heisenberg’s Uncertainty Principle. It turns out that the change in the sonogram pictures as one varies the window length mirrors the transition from a ‘mode viewpoint’ (with a long window) to a ‘travelling wave viewpoint’ (with a short window) of how the string (or whatever other structure we are considering) behaves.

Figures 6.2 (a) through (d) (Hodges et al., 1985) show the progression of spectrogram shapes for the stretched string, starting with a time window that is long compared to the string’s natural period in (a), and progressing in (d) to a window having a time span short enough to allow identification of specific impulses in the time domain.

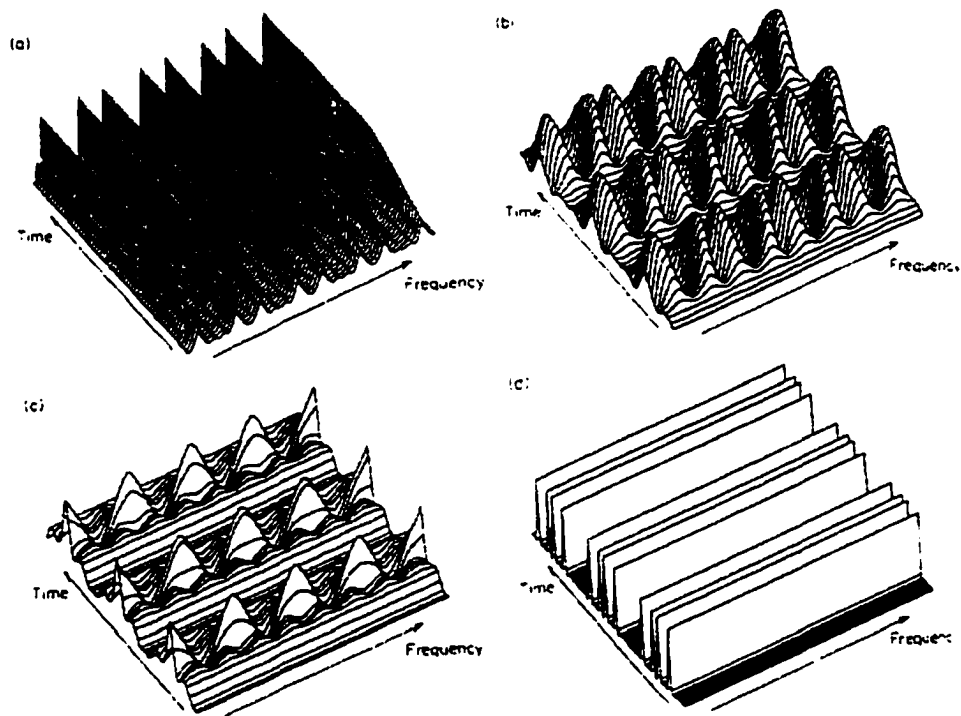


Figure 6.2 (a) – (d) Spectrograms for a Stretched String with Window Lengths Decreasing from (a) to (d) (Hodges et al., 1985)

As evidenced in the figures, if the time window over which the Fourier analysis is performed is decreased (producing a greater number of time segments with shorter lengths, thereby increasing the time resolution), the frequency resolution decreases accordingly. In Figure 6.2(a), there is essentially no variation in the spectrogram with time after the initial stage, in which the authors note that the very long time window makes the signal appear to start slowly. There is however, a clear modal picture corresponding to the shape of the signal's power spectrum. Figure 6.2(b) shows the case for which the time window is comparable to the natural period of the string, and it can be seen that the time variation has

become more distinct, while the frequency variation has lost some of its definition. Figures 6.2(c) and (d) follow the same trend; the time window for (d) is shorter than the separation of the individual impulses created by the force application, so that these impulses can be identified along the time axis; there is, however, no variation in the spectrogram with frequency. At this point, Hodges et al. state that a “travelling wave” picture has been formed which “mirrors the original time series exactly.”

Although spectrogram shapes vary with time window length, it is important to note that the information contained in each is identical. As the authors state, selection of the most appropriate window length is governed by the specific application for which the spectrogram is being created—different aspects of a structure’s behavior become apparent in different spectrograms. Hodges et al. suggest that it is often prudent to create a number of spectrograms with a range of window lengths to thoroughly identify a structure’s vibrational characteristics.

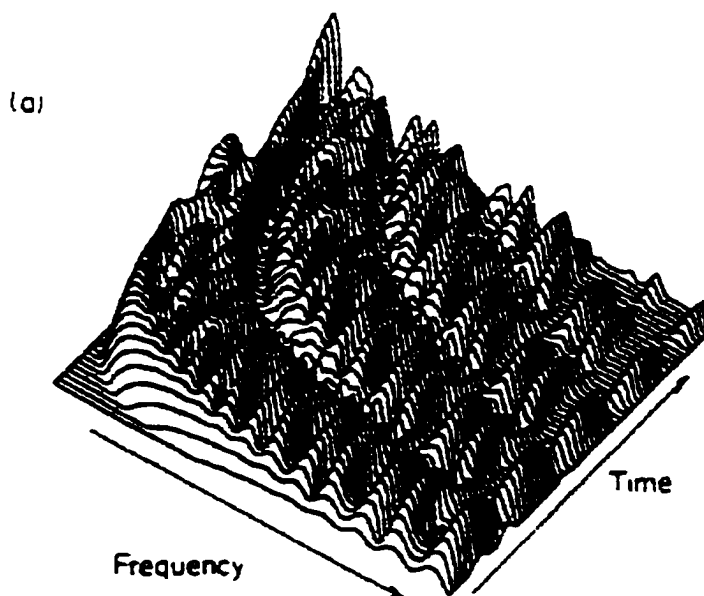
6.2 Dispersion in Spectrograms

Another property related to wave propagation that affects the appearance of a spectrogram is the presence of dispersion in the signal. If a structural system is excited in such a manner that the wave propagation velocity is a function of frequency, dispersion is said to occur. Such is the case for a beam that has been excited transversely to produce flexural waves. Hodges et al. describe the effect that dispersion has on a spectrogram’s shape in the following discussion of a beam subjected to a transverse impact:

Before looking in detail at the [spectrogram], one should decide what one expects to see. If one were to restrict attention to a particular narrow frequency range, one would see the evolution in time and frequency of a wave packet composed of that

range of frequencies. This will reflect back and forth along the beam at a speed equal to the group velocity of the beam at that frequency.... Thus in that narrow frequency range, one should see...packets [of impulses] passing the observing point in each round-trip period of the beam at that group velocity. The only difference from the string will be that different frequency bands will produce different group velocities: the group velocity for a bending beam is zero at zero frequency, and increases proportional to the square root of frequency. Thus, one expects to see a sequence of behaviour (sic) in the [spectrograms] generally similar to those (sic) for the string, except that the lines corresponding to a given arrival will no longer be straight, connoting synchronous arrival of all frequencies, but will be curved according to the inverse of the group velocity-frequency relation.

Figures 6.3 (a) through (c) (Hodges et al., 1985) show the spectrograms for a simply-supported beam impacted transversely at $3/10$ of its length for a signal recorded at $4/5$ of its length. Once again, the time window chosen for the spectrogram decreases progressively from (a) to (c); the curving of the spectrogram “bands” caused by the dispersion phenomenon is quite pronounced in each of the figures. Additionally, one can again identify the decrease in frequency resolution as the time-domain resolution increases.



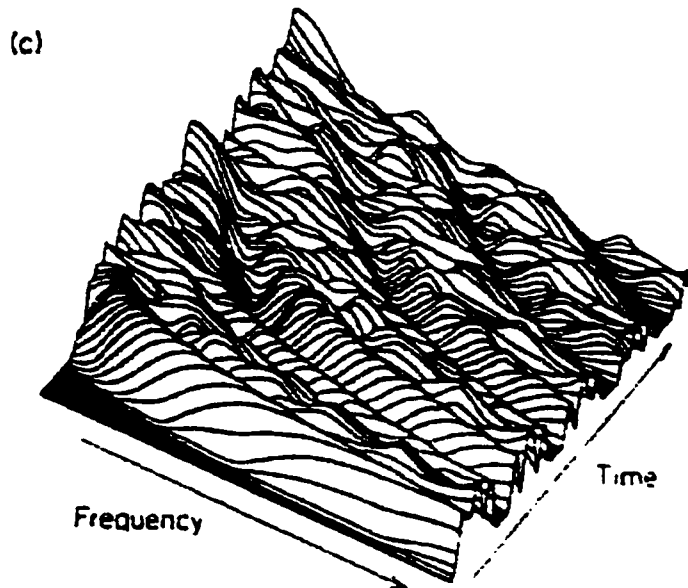
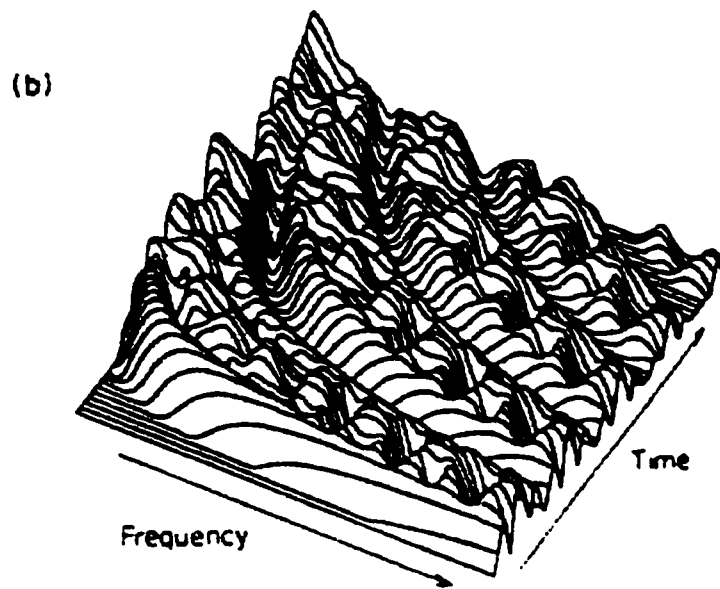


Figure 6.3 (a) – (c) Spectrograms for a Beam Impacted Transversely with Window Lengths Decreasing from (a) to (c)

6.3 Spectrograms for Steel Flat Stock

Tests were performed on a 20.2-foot long rectangular steel section having a 1.25" x .25" cross section. The freely-suspended beam was impacted on one of its 1.25-inch sides with the hammer described in Chapter II (fitted with its plastic tip) at a point corresponding to $3/10$ of its length; additional tests were performed with the impact applied at $8/10$ of the beam length. Acceleration was then measured in the same direction at various locations along its length. In the acceleration time history for the measurement point, one might expect to see "bursts" of waves that appear as the bending waves created by the impact travel past the measurement point the first time, then are reflected from the end of the beam and pass by once again, then pass again after reflection from the other end of the beam, etc. What one sees instead is an acceleration time history like that shown in Figure 6.4, in which no bursts of waves corresponding to specific wave passages are discernible.

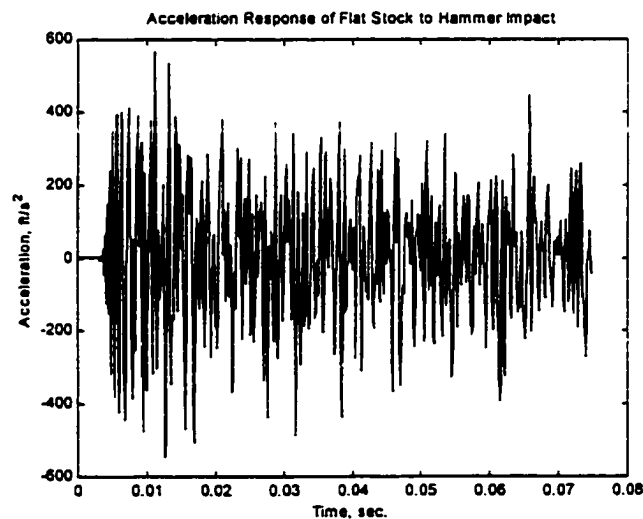


Figure 6.4 Acceleration Time History for Hammer Impact on Flat Stock, Impact Applied at $.3L$, Acceleration Measured at $.8L$

No clearly defined wave reflections are apparent in Figure 6.4 because dispersion of the bending waves has caused multiple reflections to pass the measurement point at every given time. Since, in a dispersive medium, waves of different frequencies travel at different velocities, waves of varying frequencies are almost continuously traveling through the reflection point and being reflected from the beam ends. In his treatment of the topic, Newland (Newland, 1996) notes that “[i]ulls between the arrival of reflected waves are not visible on the time history.”

As stated previously, acceleration data similar to that shown in Figure 6.4 was collected at several points along the beam, and spectrograms were produced for each case using overlapping time segments of varying lengths. In every case, the Hanning weighting function was used to window the overlapping segments, and results from five impacts were averaged for each spectrogram to minimize bias error. The results of two calculations (performed using MATLAB[®] mathematical software) are shown in Figure 6.5 below; in Figure 6.5(a), the time record was divided into 128-term blocks, with each block advanced eight points from the beginning of the last. In Figure 6.5(b), the segment size was reduced to 32 points, and each block was advanced only two points from the beginning of the preceding block. For convenience in plotting, a logarithmic scale was used for the vertical axes of the pictured spectrograms.

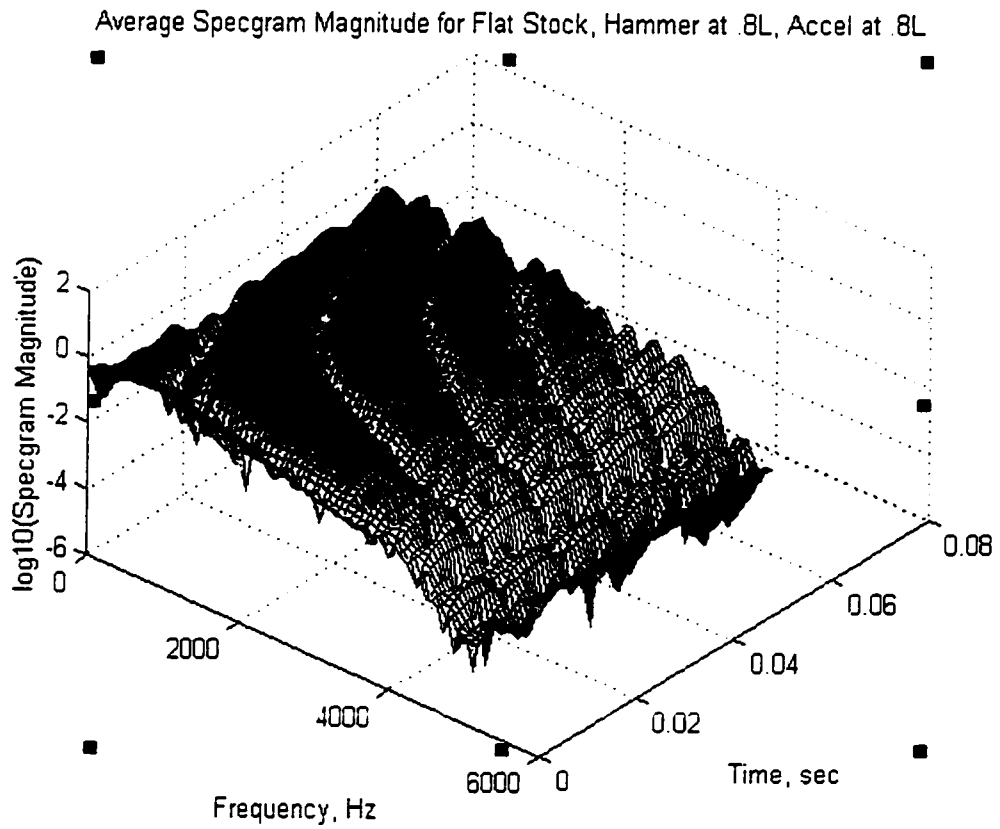


Figure 6.5(a) Spectrogram for Flat Stock Subjected to Transverse Impact (Window Length = 128)

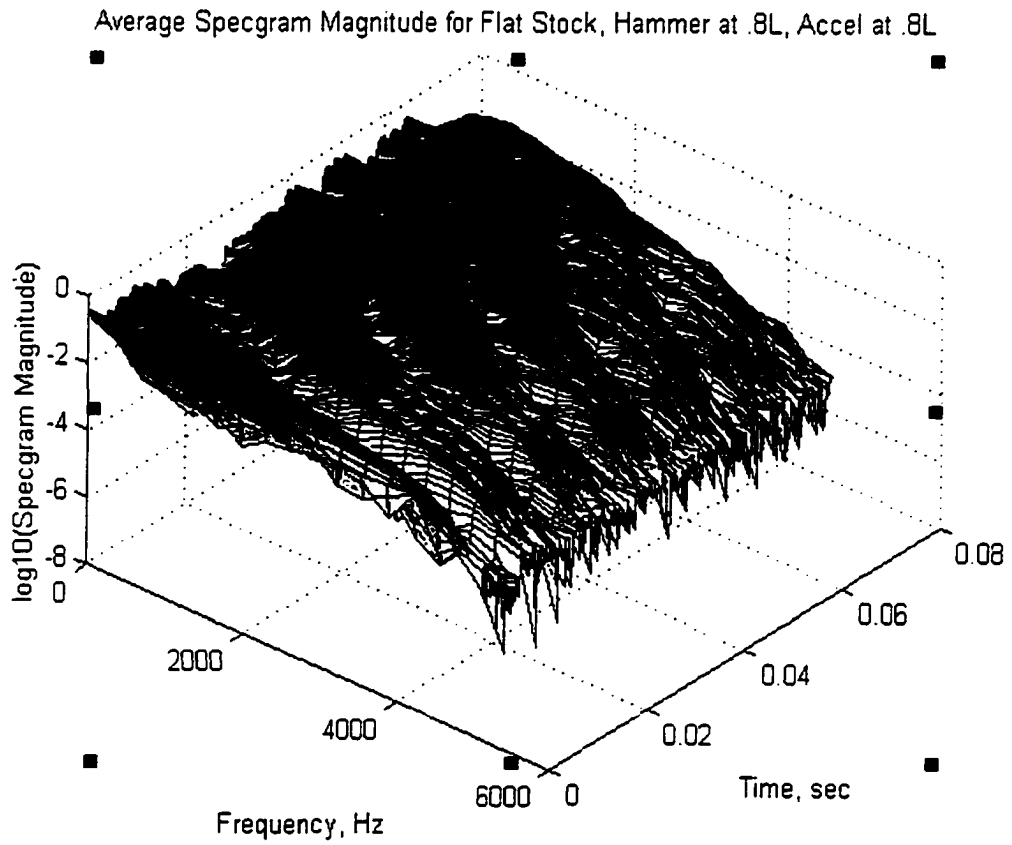


Figure 6.5(b) Spectrogram for Flat Stock Subjected to Transverse Impact
(Window Length = 32)

As in Figure 6.3, the curving bands indicative of waves traveling in a dispersive medium are clearly apparent. Also, one can yet again see the improvement in time resolution as the frequency resolution decreases from case (a) to case (b). In fact, in Figure 6.5(b), one can begin to distinguish the “packets” of waves passing the measurement point at constant successive time intervals. Such plots are experimental “confirmation” of the principles illustrated earlier by the analytically generated data of Figure 6.3

In his comparison of the spectrogram with the harmonic wavelet transform, Newland makes an important statement concerning a spectrogram’s (which Newland refers to as a short-time Fourier transform) usefulness:

At any chosen frequency..., it can be seen that the mean-square response rises and falls as waves arrive from successive reflections and then pass the measuring point. Knowing the dimensions of the beam and the position of the measuring point relative to the two ends, it is possible to estimate the group velocity of the waves and to determine its dependency on frequency from the time-frequency map.

Using this method and the spectrogram of Figure 6.5(b), a dispersion relationship for the flat stock was computed; the results are shown in Figure 6.6 below.

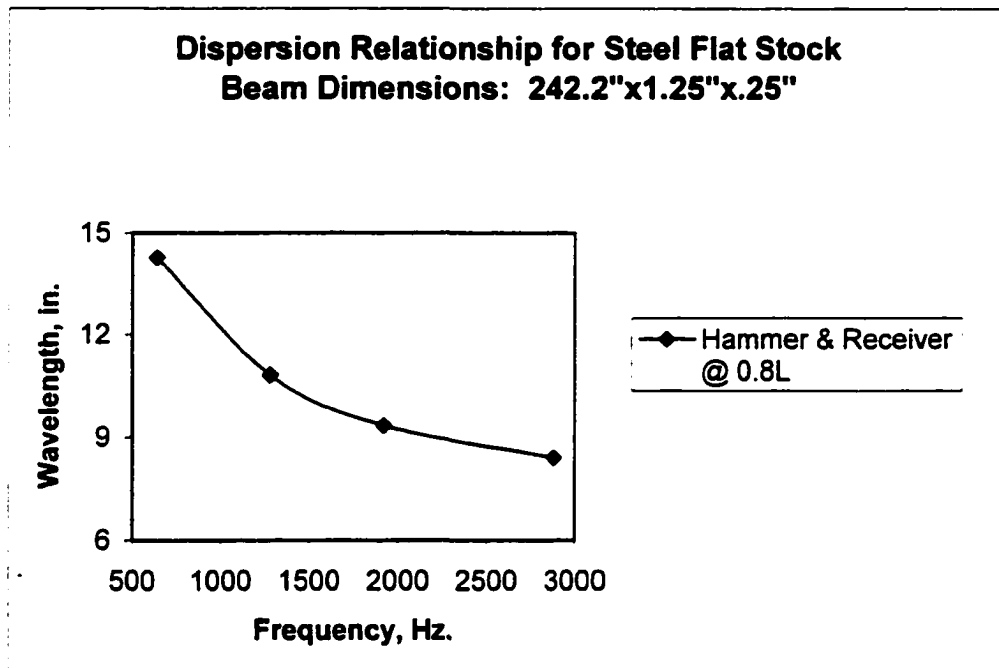


Figure 6.6 Dispersion Relationship for Steel Flat Stock

The curve pictured above agrees somewhat well with that corresponding to the generally accepted formula for estimating the dispersion relationship for flexural waves in a long, thin beam, given as follows (Cremer et al., 1993):

$$c_p = \sqrt{1.8hfc_l} \quad (6.1)$$

where

c_p = phase velocity for flexural waves in a long, thin beam,

h = thickness of the beam,

f = frequency, and

c_l = longitudinal wave speed in the beam material.

Though they are similar in form, there is some discrepancy in magnitude between the two curves, perhaps due to nature of the suspension apparatus employed to freely suspend the beam. A polynomial fit of the experimentally derived curve (such as that of Figure 6.6) can be computed, though, to produce a dispersion relation for each particular testing situation. Such a fit, then, can be used to determine the unknown length of a portion of a beam, if the exposed (known) length can be measured. For the most basic case, in which the beam is nonembedded, a method to determine the unknown length is as follows.

First, the receiver should be located at a position that is less than half the distance from the exposed end to the point where the beam is no longer exposed, and the impact applied at the same location. This placement will ensure (for the nonembedded case) that the first wave arrival at the measurement point will be that of the wave that has traveled from the impact point (also the measurement location) to the exposed beam end and back to the receiver location, a distance which is known. After creating a spectrogram of the measured data, plots of the spectrogram amplitude versus time can be generated for several frequency values. From these plots, the arrival time of the first wave can be determined and used, along with the known traveled distance, to calculate the group velocity of the flexural waves for each of the specific frequencies. From these values, the wavelengths at each frequency can be computed and plotted versus the frequency to produce a dispersion curve similar to

that shown in Figure 6.6. As stated previously, a polynomial curve fit of the measured curve can be produced so that wavelengths can be determined for any corresponding frequency.

At this stage, any frequency and its corresponding wavelength can be selected from the dispersion curve and multiplied to determine the phase velocity (and subsequently the group velocity) at that particular frequency. This value can then be multiplied by the time of arrival of the second peak of the spectrogram amplitude versus time plot for that frequency (which should correspond to the time it takes for the wave to travel from the receiver location to the nonexposed beam end and back to the measurement point). Knowing the phase velocity and the time it takes to travel the unknown distance, simple multiplication of those two parameters will yield the unknown distance. Of course, the calculated distance would then be divided by two to discover the actual distance between the receiver location and the nonexposed beam end.

The procedure described above is somewhat more elaborate than is actually necessary, but calculation of the dispersion curve allows for the investigation of any frequency of interest (within the range of the spectrogram calculation). All that is actually needed (for the simple case of a nonembedded beam) is to calculate the group velocity from one spectrogram amplitude versus time plot at a particular frequency. Then the time to the second peak of the same plot could be observed and multiplied by that group velocity (and divided by two) to determine the unknown length from the receiver to the nonexposed beam end. Since it is not much more computationally intensive, though, to repeat this process for several frequencies, it is a good idea to make multiple determinations of the unknown distance to ensure that they are essentially identical.

6.4 Spectrograms for S3x5.7 Model Pile Section

After confirming that the spectrogram could be successfully used to characterize the wave propagation behavior of the steel flat stock, acceleration measurements were collected for a transverse impact applied to the web of the S3x5.7 section used for the model piles. For the initial analysis, a 9-foot long section was freely suspended in a manner similar to that for the flat stock. As before, the plastic tip was fitted to the impact hammer, and the impact was applied at the same location (or very near) that the acceleration was measured; both were accomplished at a position 8/10 of its length from the end of the beam. Once again, spectrograms were produced using overlapping time segments of varying lengths, of which three are shown below. The Hanning window was used as a weighting function for the overlapping segments, and results from five impacts were averaged for each spectrogram to minimize bias error.

Three of the spectrograms calculated for the S3x5.7 section are shown below; for Figure 6.7(a), the windowed segments consisted of 128 terms each, with each segment advanced eight terms from the beginning of the last. In Figure 6.7(b), the segment size was reduced to 64 terms, and each block was advanced four points from the beginning of the preceding block. The segment size was again reduced in Figure 6.7(c) to 32 terms, with each block advanced two points from the beginning of the previous block. Once again, a logarithmic scale has been employed for the vertical axis, on which the spectrogram magnitude is plotted.

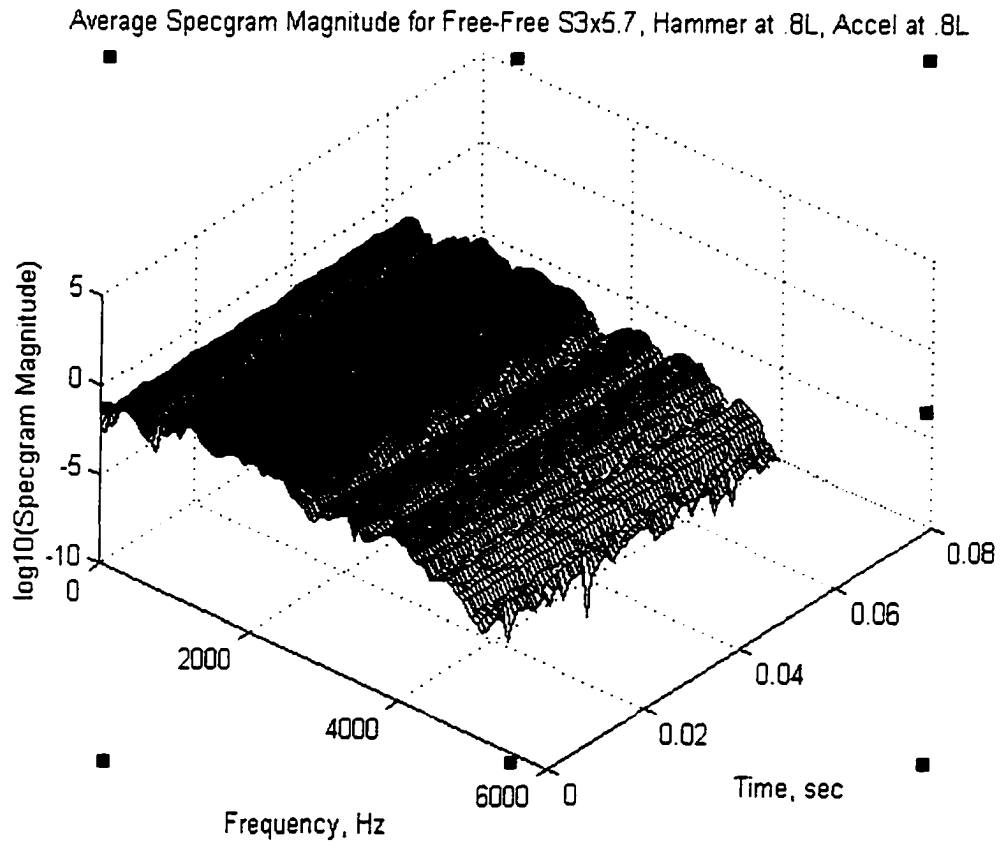


Figure 6.7(a) Spectrogram for S3x5.7 Section Subjected to Transverse Impact in Middle of Web (Window Length = 128)

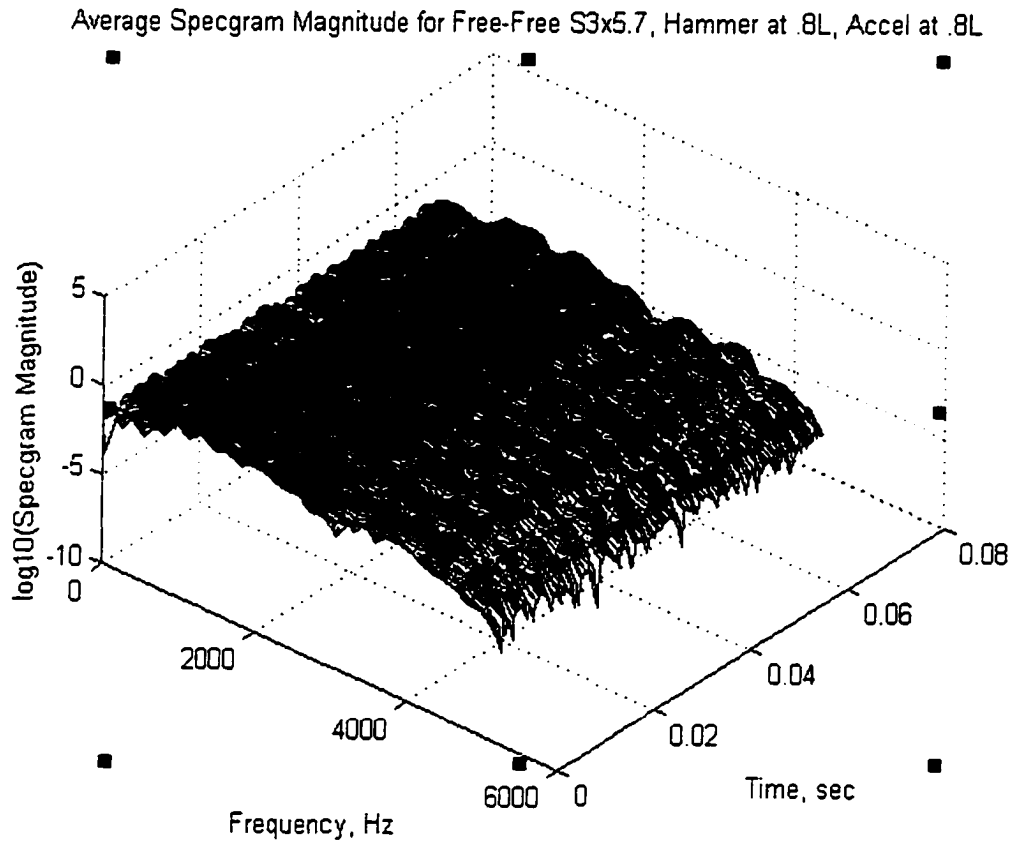


Figure 6.7(b) Spectrogram for S3x5.7 Section Subjected to Transverse Impact in Middle of Web (Window Length = 64)

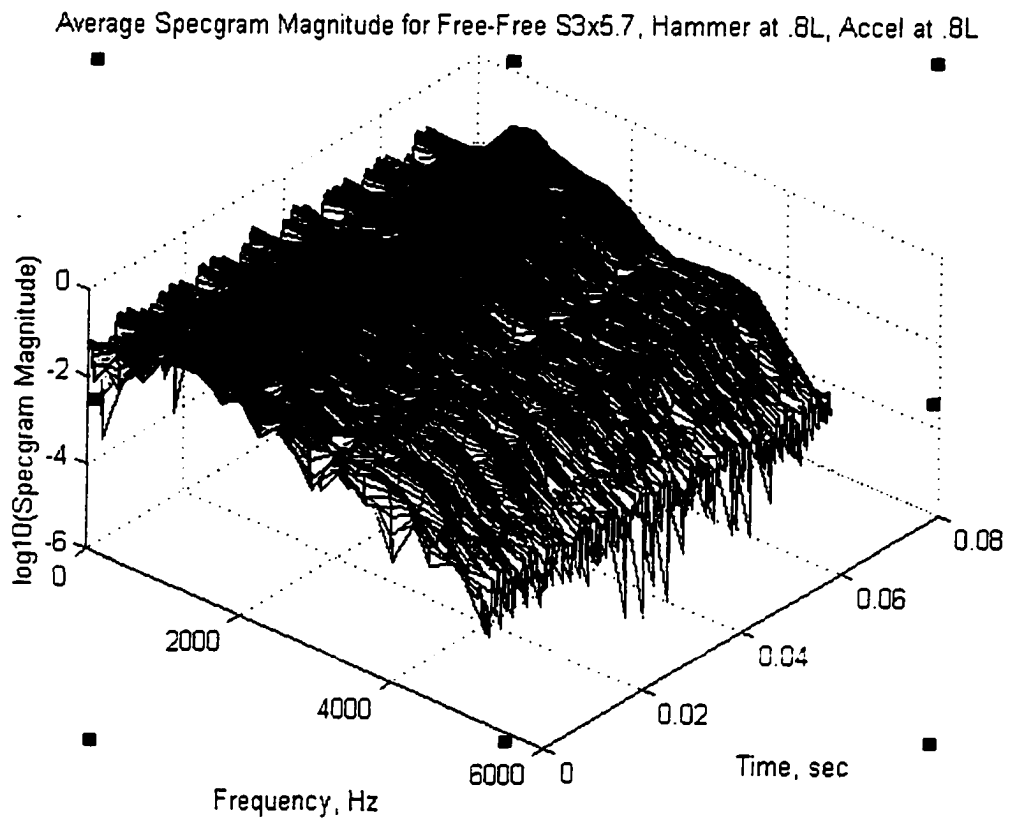


Figure 6.7(c) Spectrogram for S3x5.7 Section Subjected to Transverse Impact in Middle of Web (Window Length = 32)

Although an increase in time resolution can be discerned as the window length is decreased from (a) to (c), the curving bands that indicated dispersion in the flat stock section are not clearly apparent in the spectrograms above. Additionally, plots of spectrogram magnitude versus time for various frequencies do not exhibit any corresponding peaks that can be readily identified as the same wave arrival in each plot. (Tests were repeated on a beam fixed at one end and free at the other; similar results were obtained.) Much of the poor definition in the spectrograms for the S3x5.7 section may be due, as indicated earlier, to the presence of the several reflecting surfaces inherent in the shape of the cross section. It is not possible to say with certainty which reflection reaches the measurement point first, or second, etc. For these reasons, it is not practical to attempt to identify unknown lengths in this manner (as was done for the flat stock) for the S3x5.7 section, even for the nonembedded case. Since the inclusion of embedment soil would only serve to add a new reflective surface, increasing the complexity of the problem even further, it was concluded that the determination of unknown pile lengths for the S3x5.7 model pile sections through the characterization of their wave propagation behavior using a spectrogram is not a feasible task.

CHAPTER VII

CONCLUSIONS AND RECOMMENDATIONS

7.1 Conclusions

The determination of unknown pile embedment depths seemed a likely candidate for solution via modal analysis techniques, since all but one of the pile-soil system characteristics were known or could be measured. As was discussed in Section 3.3, it was expected that since the modal parameters were dependent on some combination of the quantities pictured in Figure 3.10 (shown on page 85), they would vary accordingly with a particular value of L_2 ; it was believed that this quantity could be backcalculated from an analysis of the measured frequency response function data. Another favorable aspect of the modal analysis technique that was considered is that it is well-suited to the examination of impact data, which is easily measured, recorded, and stored, even in the somewhat “less-than-laboratory” conditions found surrounding older bridge piles whose lengths are unknown. Also, since access to the top of most piles is not commonly available, a technique was needed that could utilize flexural impact data, created with a transverse impact to the side of a pile, rather than axial data, generated in response to a longitudinal impact applied to the exposed top of a pile. Finally, it was anticipated that this method of analysis would

eliminate the need for the subjective visual interpretation of graphical data trends, such as that necessary for many of the techniques previously employed to accomplish this task.

7.1.1 Modal Parameter Estimation of Experimental Frequency Response Function Data

Results of the comprehensive experimental study reported herein indicate that the physics of the pile-soil system preclude identification of embedment depth from its modal parameters in the frequency range considered valid for the modal parameter identification process. It is evident from the graphs of natural frequency versus mode number for the experimental data collected on the Group I piles (presented in Chapter IV) that for a given mode, the natural frequency values for each of the five piles are virtually identical (for tests along both the X and Y axes). Although the damping versus mode number plots show a greater variation with each pile for a given mode number, no clear trend is discernable that would allow a unique embedment length to be determined from backcalculation of the modal data.

As stated previously, it was believed that since only one property of the pile-soil system was unknown, a variation of that characteristic should produce a corresponding, unique change in the modal parameters associated with the system. What is more accurate, however, is that as the embedded length changes, the amount of soil included in the structural system changes as well; this additional soil influences the system's vibration response to a flexural impact by affecting its mass, as well as the level of restraint that is experienced. Thus, there are, in essence, three unknown system characteristics being varied, namely the pile length, system mass, and system stiffness. The interaction of these three

concurrently changing parameters produces an effect that is more complex in nature than that produced from a change in length alone. Results of the numerical analyses, discussed below, provide supporting evidence for this conclusion—they also furnish insight into the nature of the natural frequency trends for frequencies beyond those that are practical to measure experimentally.

Since the results of the analyses performed for the Group I piles proved that the modal analysis technique was not well-suited to the length determination of piles embedded in soil, further analysis of more intricate pile configurations (such as those encountered in the Group II piles) was deemed unwise. Additionally, no further efforts were made to fully characterize the fixity condition presented by the pile cap, or to account for the effect that other factors, such as the mass of the bridge deck or the presence of water, has on an embedded pile's natural frequency.

7.1.2 Numerical Analyses

Three types of numerical analyses were performed to simulate the frequency response function data gathered in the experimental study. As described in Chapter V, the first analysis consisted of the analytical generation (and subsequent modal parameter estimation), of frequency response functions corresponding to those of the Group I model piles; the MATLAB[®] programs used to produce the FRF's were written according to the theories presented in the papers by Novak, Nogami, and Aboul-Ella (Novak et al., 1978; Novak and Aboul-Ella, 1978a; Novak and Aboul-Ella, 1978b). For the second numerical analysis, finite element models were created for each of the Group I model piles; the effects of the

soil were included via a set of springs whose stiffness values corresponded to those computed in the first analysis. Similarly, these stiffness values were included in the third analysis, which was an adaptation of the solution presented by Weaver, Timoshenko, and Young for a beam resting on elastic supports.

Results of each of the three analyses were quite similar to those produced from the experimental study, and all indicated that in the 0-2000 Hz frequency range considered valid for the experimental parameter estimation, there is no identifiable difference in the natural frequency and damping values for a given mode. The finite element study did show, however, that above a certain “threshold” frequency value, the natural frequencies of the Group I piles branched into individual curves ordered in a progressive manner from Pile A to Pile E. These results, coupled with those from the theoretical solution for a beam resting on elastic supports, which indicated that all of the Group I piles exhibited natural frequency values much closer to those of a fixed-fixed beam than to a free-free beam, suggest the following pattern of behavior as the mode number is increased: the stiffness of the pile-soil system is great enough (even for Pile A, whose embedded length is only 17 percent of its total length) that for each pile in its embedded state, the natural frequencies of the first few modes (those whose frequency are below the threshold) are virtually identical. Once the threshold value is reached, though, the restraint provided by the soil becomes the dominant effect, and the natural frequency values are progressively lower as the percentage of embedment increases. As stated above, however, the threshold frequency appears to be above that which is practically attainable for the experimental modal parameter

identification process, so that the frequencies estimated from the experimental data appear to be nearly identical for all of the model piles.

The modal analysis process described herein, then, appears not to be the ideal method for identifying unknown pile embedment lengths. The information assembled does, however, provide valuable insight for future research into the nondestructive evaluation of pile tip elevations.

7.1.3 Wave Propagation Investigation

Results of the rudimentary wave propagation study described in Chapter 6 indicate that the many reflective boundaries inherent in the S3x5.7 model pile shape render it a poor candidate for pile embedment length identification via an investigation of its flexural wave propagation characteristics. Although this process would be beneficial for piles having very simple cross sections (i.e., circular or rectangular), the interacting wave reflections generated after impact in piles with more complex shapes might make it impractical for use in those cases. Also, the method as described in Chapter VI requires visual identification of graphical peaks, which makes it less attractive than a technique which relies on objective data itself rather than a subjective interpretation of the data.

7.2 Recommendations for Future Work

Although the modal analysis approach as described in this work did not prove to be a practical solution to the pile embedment length problem, there are several concepts that deserve consideration for future investigations of this topic. First, if a reliable technique

could be developed for obtaining data that was well-defined past the “threshold” frequency indicated by the finite element results, the principles presented in this study could presumably be applied to that experimental data, allowing modal parameter estimation in the higher frequency range, and subsequent backcalculation of embedded lengths. Similarly, if a method is developed by which reliable structural damping estimates can be obtained experimentally, this could perhaps be the modal parameter used to distinguish between piles of differing embedment lengths. Both of these options are attractive in that they make use of data collected as a result of a transverse, rather than a longitudinal impact, so that access to the top of the pile is not necessary. Also, they would both, in all likelihood, make use of objective interpretation of the measured data, rather than visual perceptions of the positions of graphical peaks.

As stated previously, pile lengths have been determined quite accurately in the past via the measurement of axial waves produced by longitudinal impacts (tests of this type are described in Chapter I). If the process developed by Pandey et al. for timber piles could be extended for use on piles of other materials, field determination of unknown pile embedment lengths would be a relatively simple, efficient, and inexpensive task. Recall that in their assessment of timber piles in Clallam County, Washington (Pandey et al., 1998) (detailed in Chapter I), the authors inserted lag bolts into each of the piles under investigation at an angle 45 degrees relative to their longitudinal axes. They then impacted the head of the bolt, inducing a wave with enough energy in the longitudinal direction to be considered an axial wave. The length determination was then completed by measuring the time required for the wave to travel to the base of the pile and reflect back along the pile

length. This time, coupled with the stress wave velocity, was used to calculate the length of the piles. A similar procedure could be applied to piles of other materials if a fixture was fashioned that could be attached to the piles, and that, if impacted, would induce longitudinal waves in the accompanying pile.

An investigation into the use of ground penetrating radar imaging may also prove useful for the length identification problem. This technique involves the transmission and subsequent reception of high frequency electromagnetic energy that is radiated into a particular medium. It has previously been employed to detect and identify the shapes of subsurface objects, provide soil profiles of a given area, and to determine the position of rebar in in-place concrete structures (Thomas, 1995). Perhaps with some modifications it could be used to determine unknown embedment lengths from tests performed at the soil surface.

After a valid method has been devised for determining the embedment lengths of piles of the type tested in Group I (which include only the piles themselves and the surrounding soil), the technique should be expanded to account for the effects of the various parameters encountered in the Group II piles, such as partial concrete encasement and end-bearing conditions. Tests should also be conducted on full-scale bridge piles of known length to ensure that the process developed produces similar results for large-scale test specimens as for the small-scale laboratory pile sections. As a final step in the procedure, then, a determination of the true fixity condition provided by a typical pile cap should be made, and an investigation of the effects of the attached deck mass and presence of water on a pile's modal parameters should be conducted.

7.3 Contributions

Several contributions to the current body of knowledge have been realized from the results of the study described herein. The modal analysis approach has been discounted as a practical, efficient method for identification of unknown pile embedment lengths. Not only has it been discounted, but the degree to which the method is inappropriate for the current application has been quantified through an analysis of the modal characteristics of piles with embedment lengths ranging from 17 to 50 percent of their total length. Additionally, the study's results revealed the previously unknown fact that quite a significant amount of restraint is provided to a pile by the surrounding soil, even for relatively small embedment length percentages. (Such findings seem to naturally suggest a related investigation of the restraint mechanism that occurs in piles having embedment lengths less than 17 percent of their total length.) Finally, a comprehensive, methodically-obtained, and well organized dataset has been collected that quantifies the frequency response characteristics of embedded piles having various lengths, section properties, casement attributes, and end-bearing conditions. (Tests similar to those described for the laboratory piles were also conducted on a limited number of full-scale bridge piles, though the results were not presented in this work.) This frequency response function dataset, along with the results of the experimental and numerical analyses contained herein, can serve as useful information for researchers in this field as they formulate future investigations into this, and related topics.

APPENDIX A

EXPERIMENTAL FREQUENCY RESPONSE FUNCTIONS

PILE C

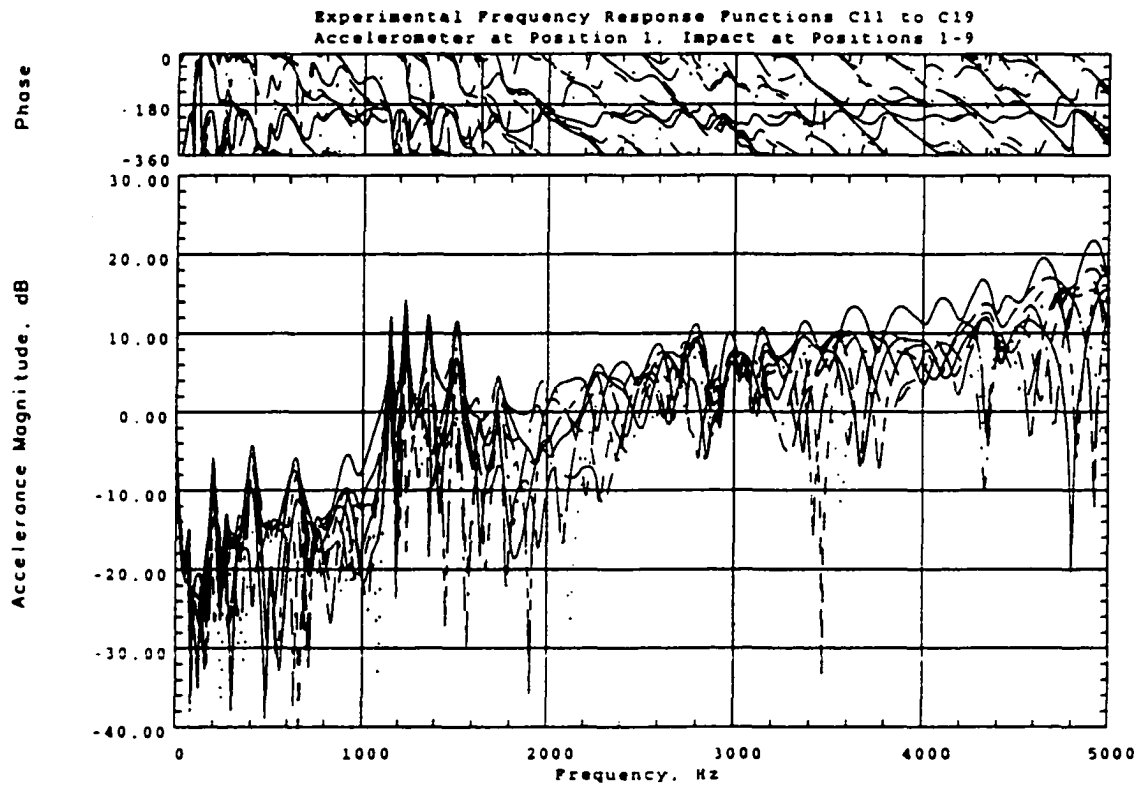


Figure A.1 Experimental Frequency Response Functions for Pile C, Tested Along X Axis, Accelerometer at Position 1, Impact at Positions 1-9

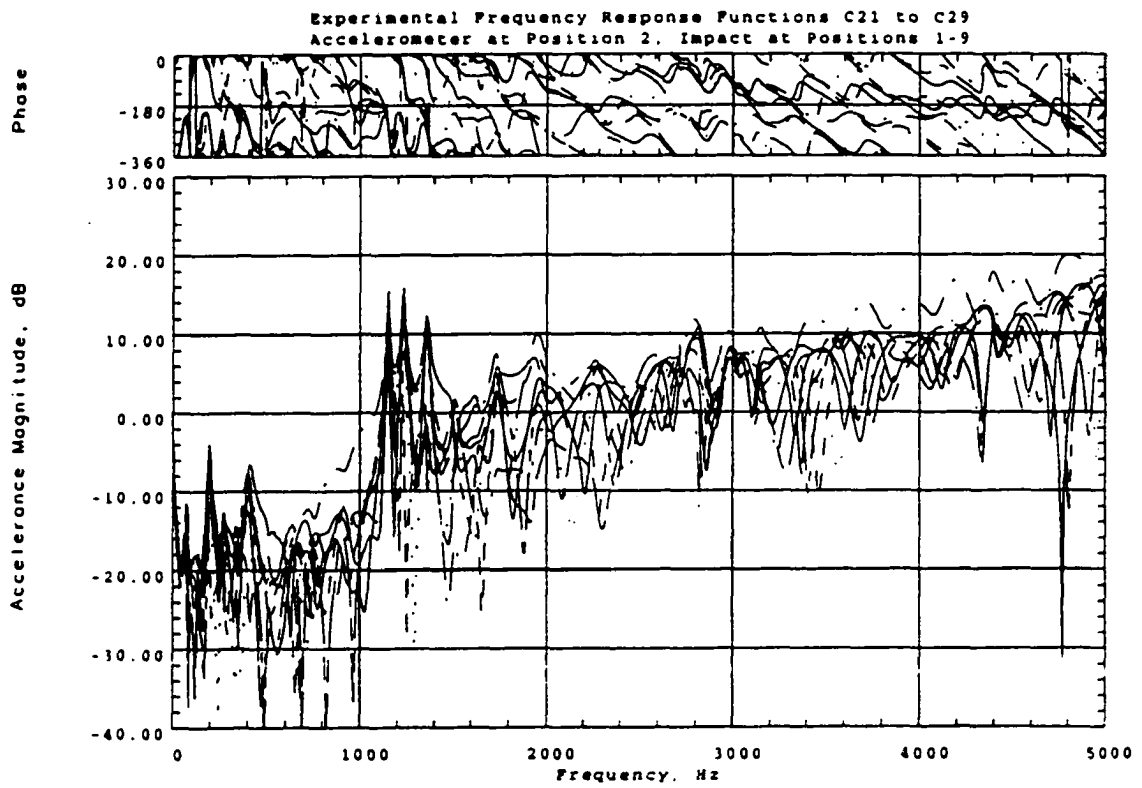
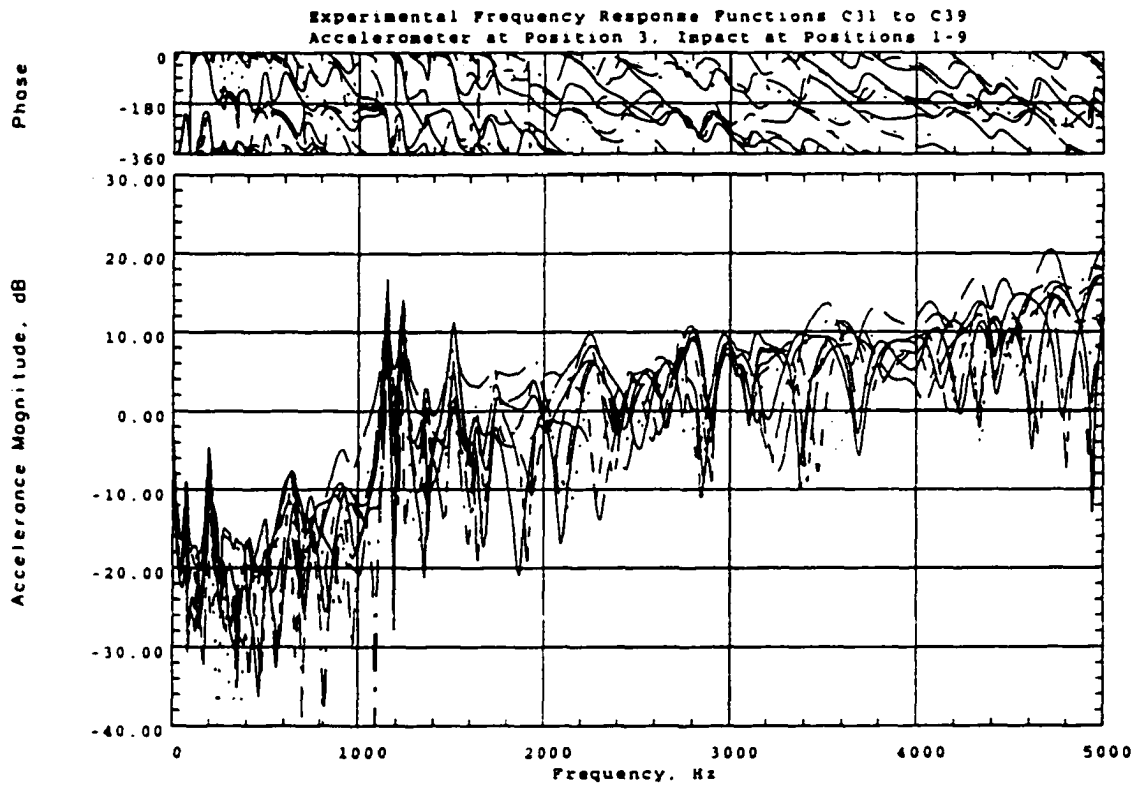
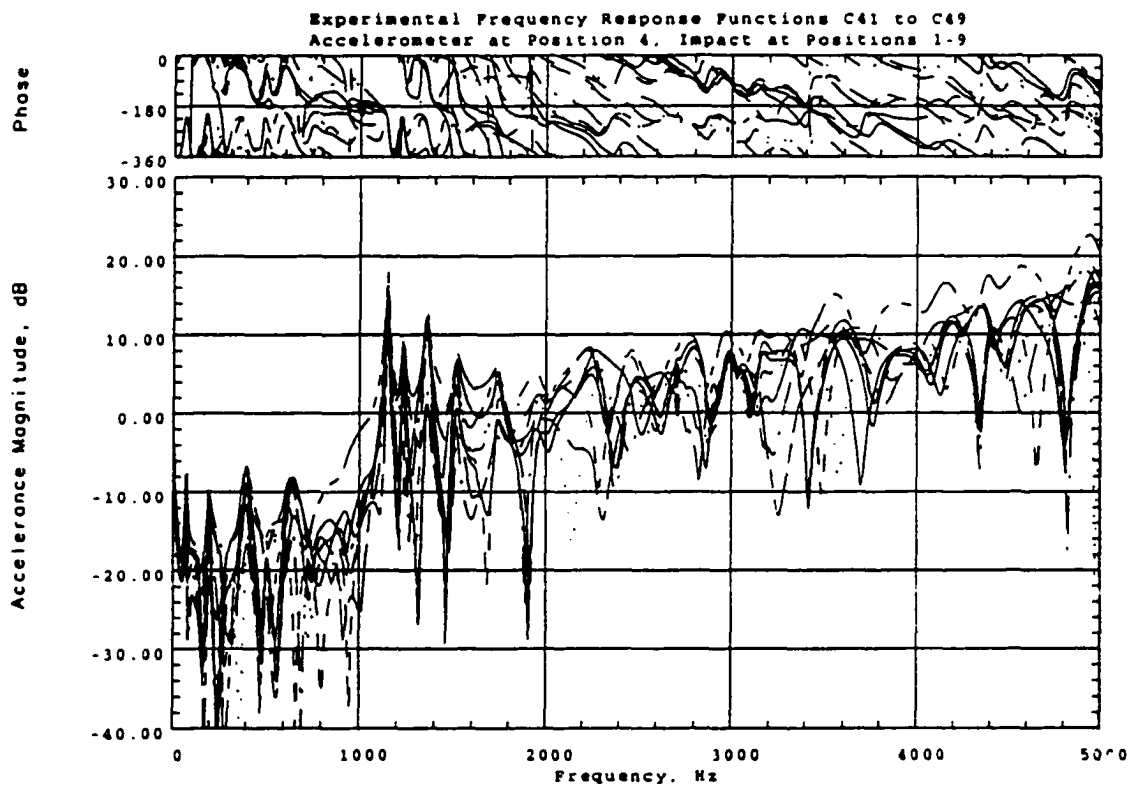


Figure A.2 Experimental Frequency Response Functions for Pile C, Tested Along X Axis, Accelerometer at Position 2, Impact at Positions 1-9



**Figure A.3 Experimental Frequency Response Functions for Pile C, Tested Along X Axis,
Accelerometer at Position 3, Impact at Positions 1-9**



**Figure A.4 Experimental Frequency Response Functions for Pile C, Tested Along X Axis,
Accelerometer at Position 4, Impact at Positions 1-9**

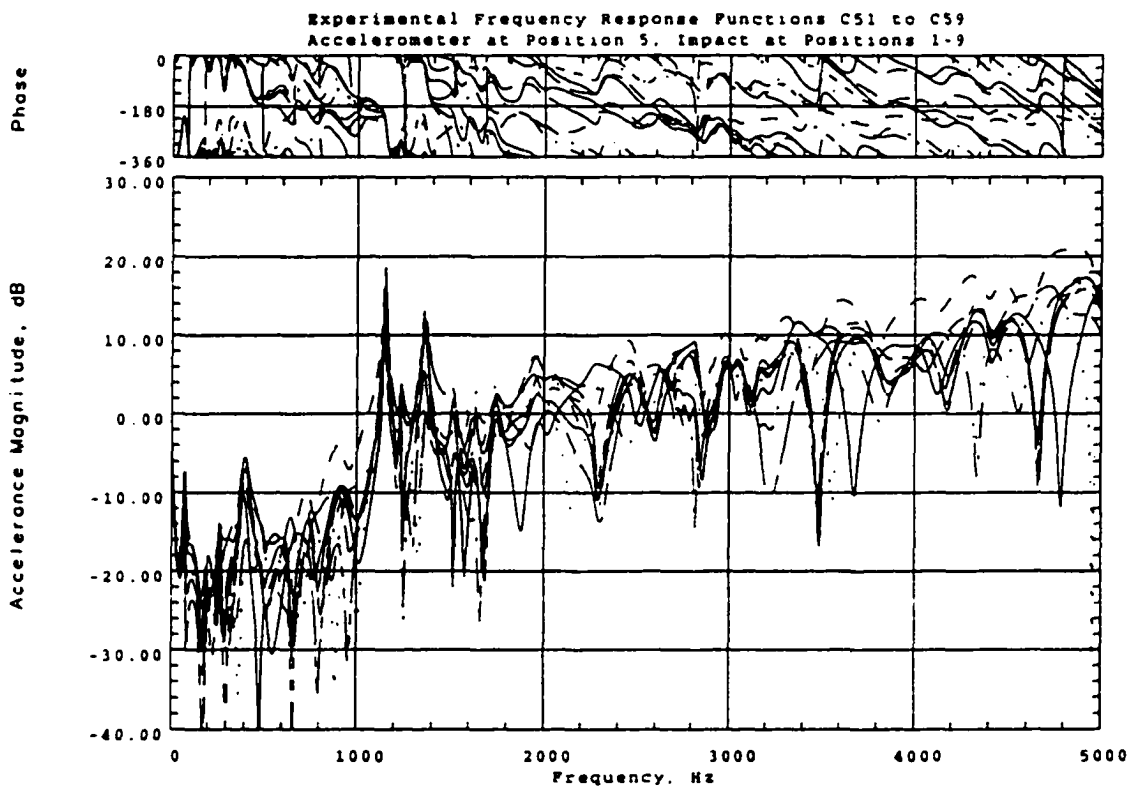


**Figure A.5 Experimental Frequency Response Functions for Pile C, Tested Along X Axis,
Accelerometer at Position 5, Impact at Positions 1-9**

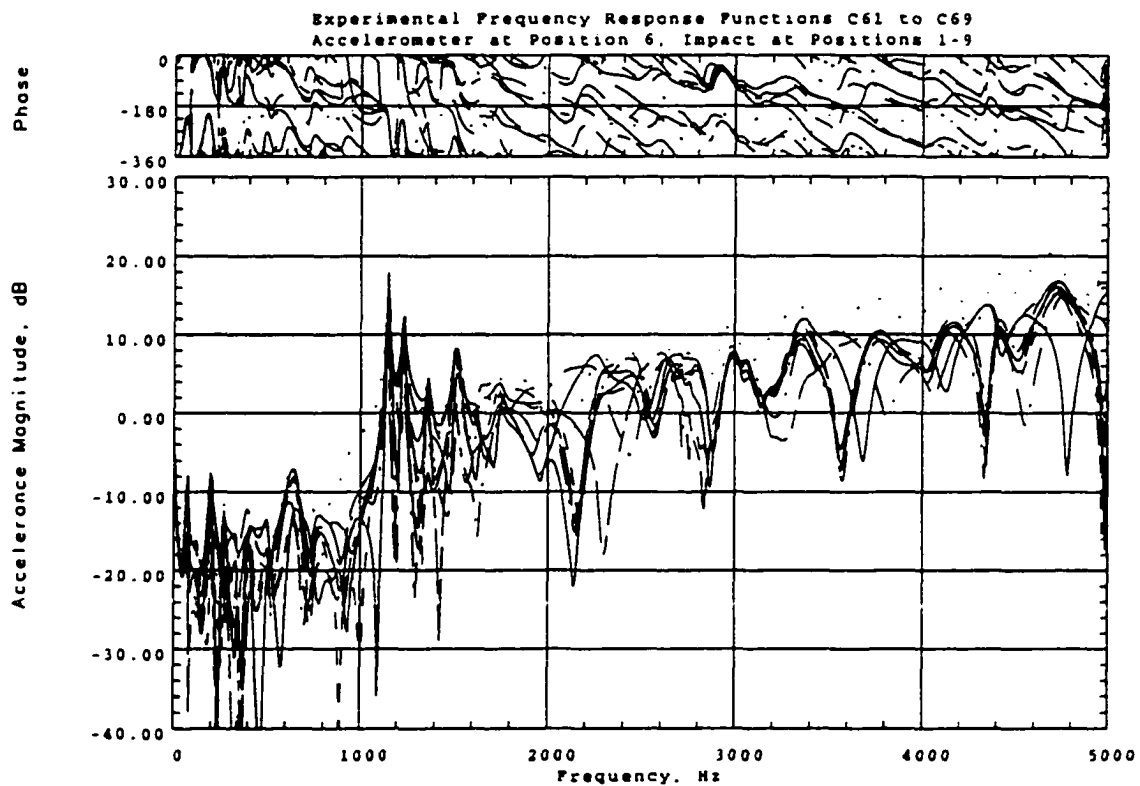


Figure A.6 Experimental Frequency Response Functions for Pile C, Tested Along X Axis, Accelerometer at Position 6, Impact at Positions 1-9

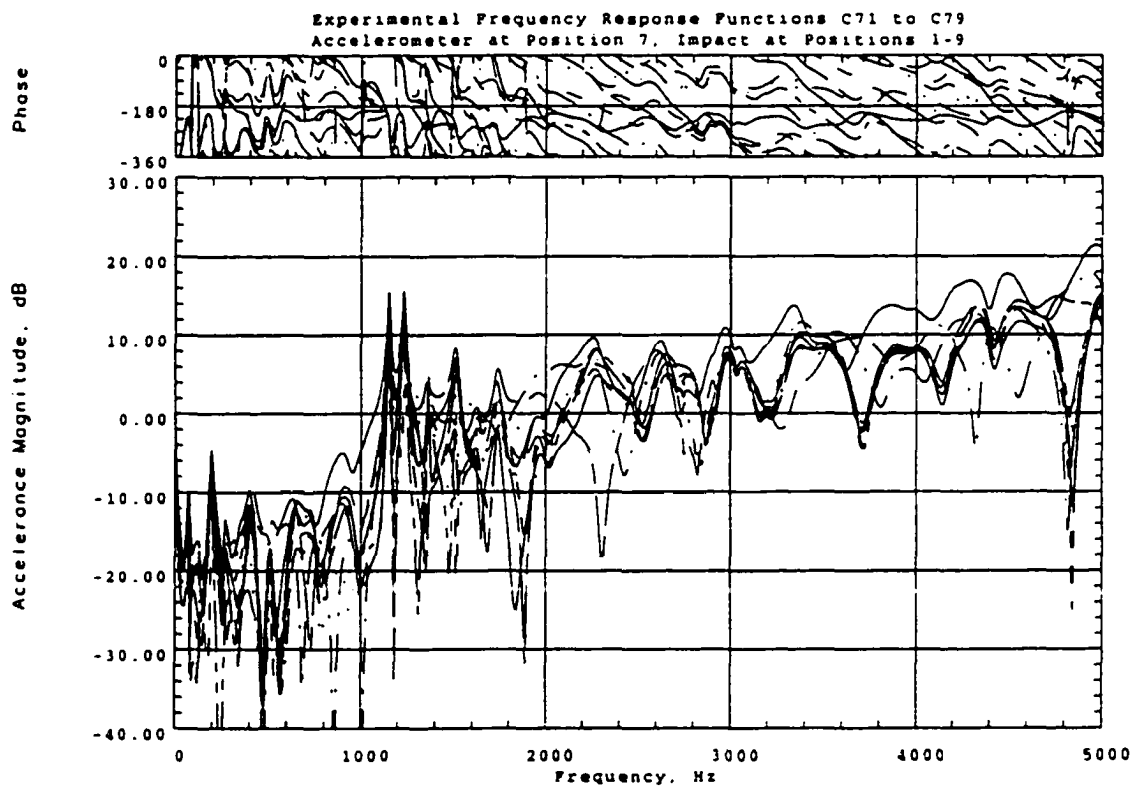


Figure A.7 Experimental Frequency Response Functions for Pile C, Tested Along X Axis, Accelerometer at Position 7, Impact at Positions 1-9

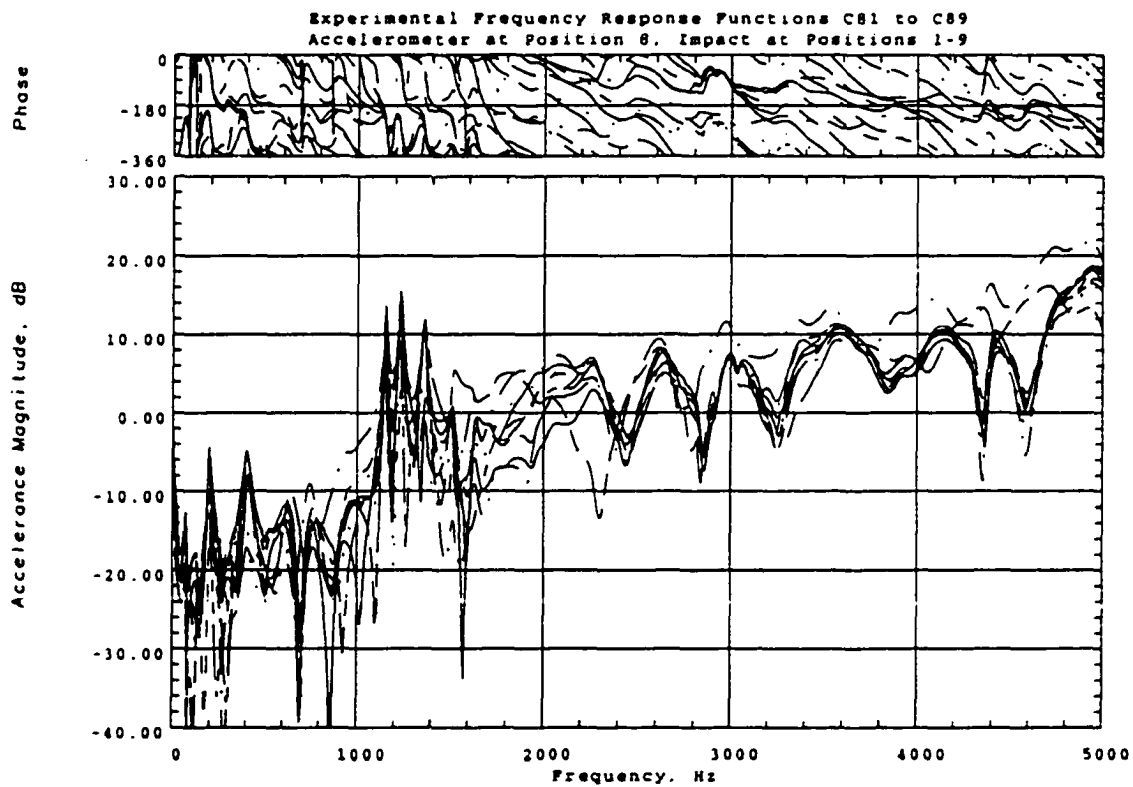


Figure A.8 Experimental Frequency Response Functions for Pile C, Tested Along X Axis, Accelerometer at Position 8, Impact at Positions 1-9

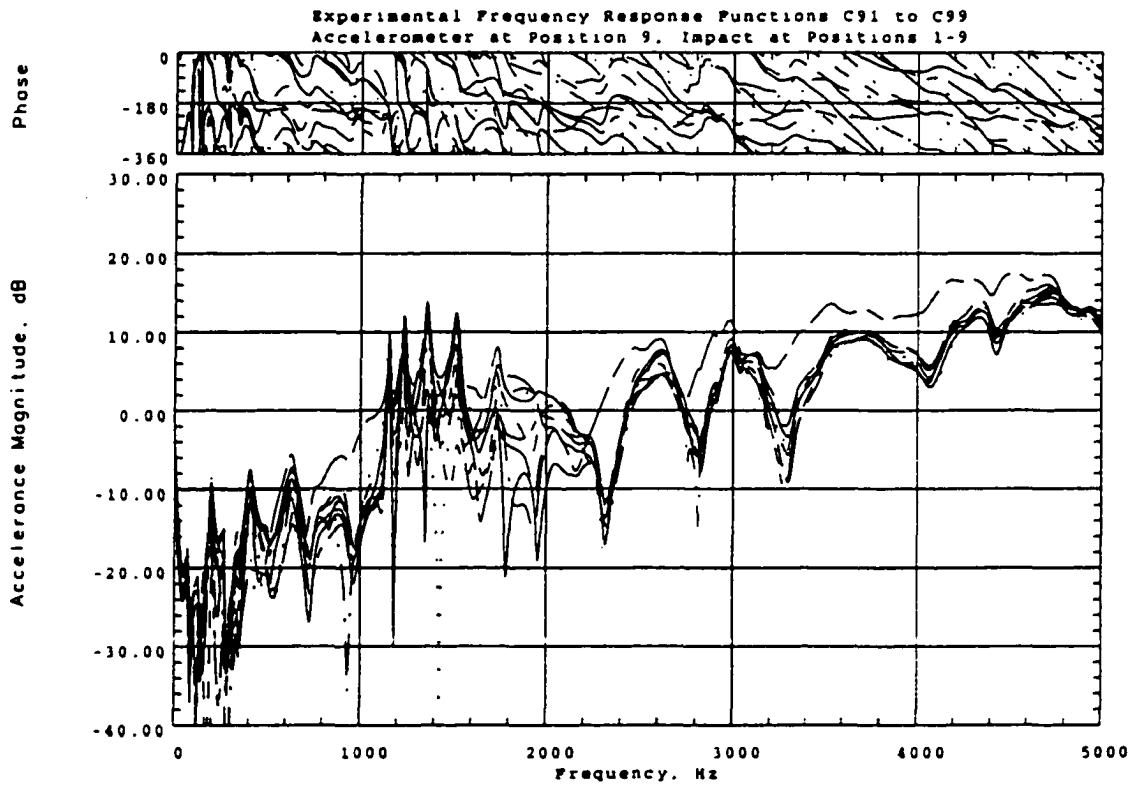


Figure A.9 Experimental Frequency Response Functions for Pile C, Tested Along X Axis, Accelerometer at Position 9, Impact at Positions 1-9

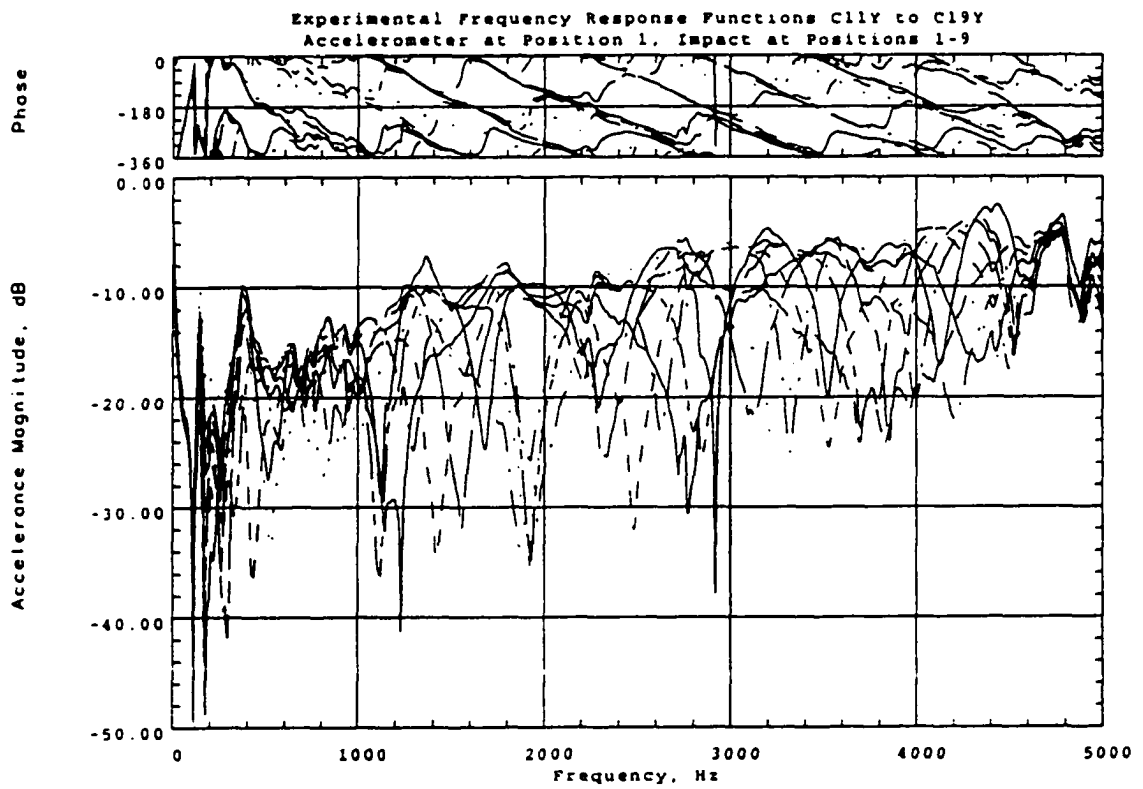


Figure A.10 Experimental Frequency Response Functions for Pile C, Tested Along Y Axis, Accelerometer at Position 1, Impact at Positions 1-9

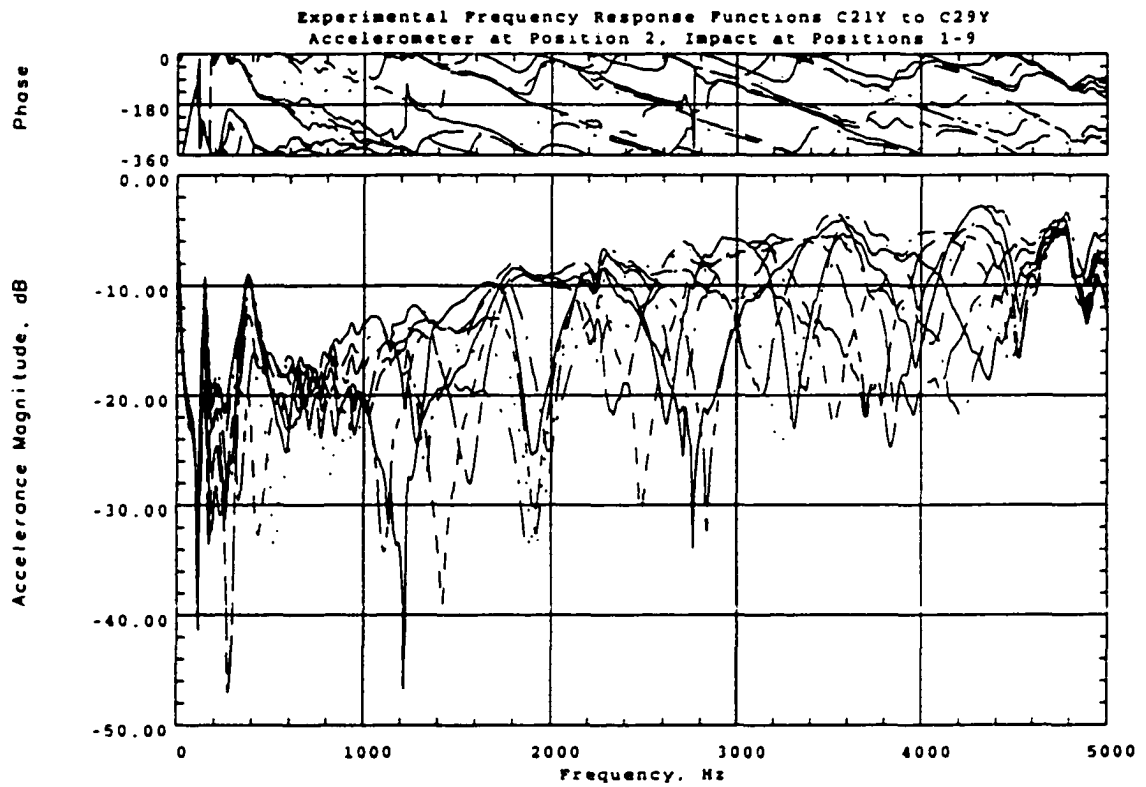


Figure A.11 Experimental Frequency Response Functions for Pile C, Tested Along Y Axis, Accelerometer at Position 2, Impact at Positions 1-9

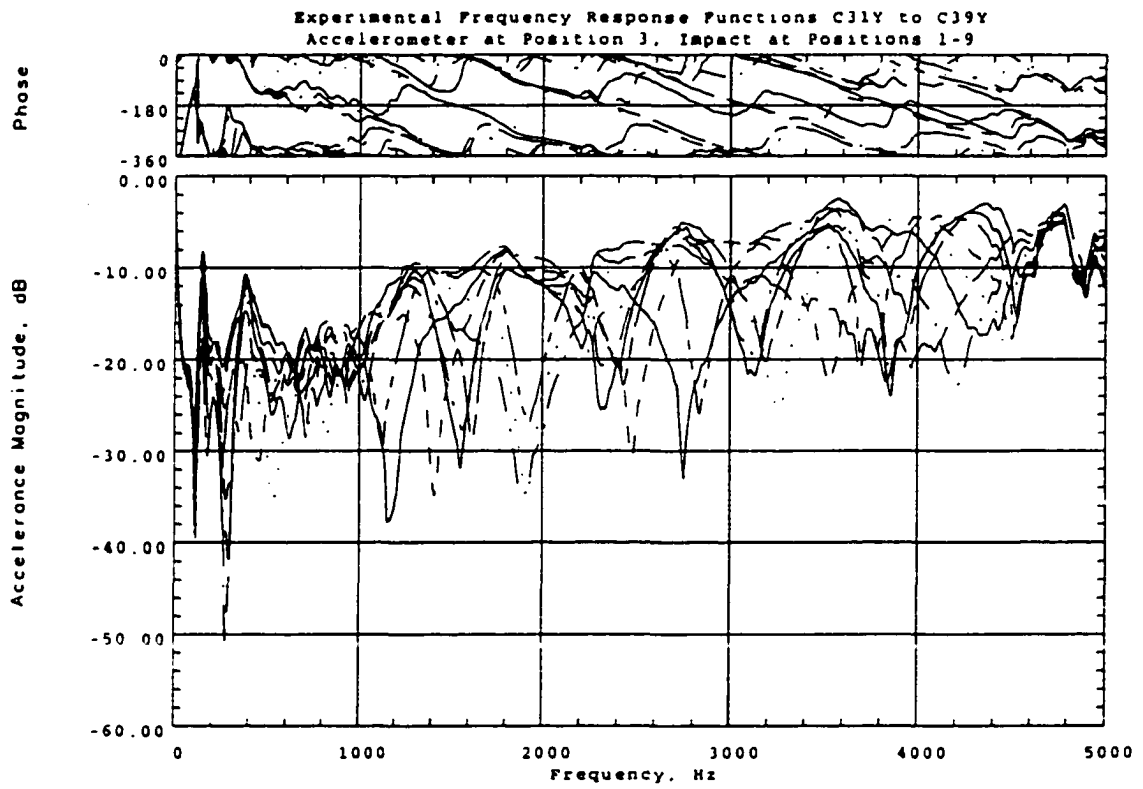


Figure A.12 Experimental Frequency Response Functions for Pile C, Tested Along Y Axis, Accelerometer at Position 3, Impact at Positions 1-9

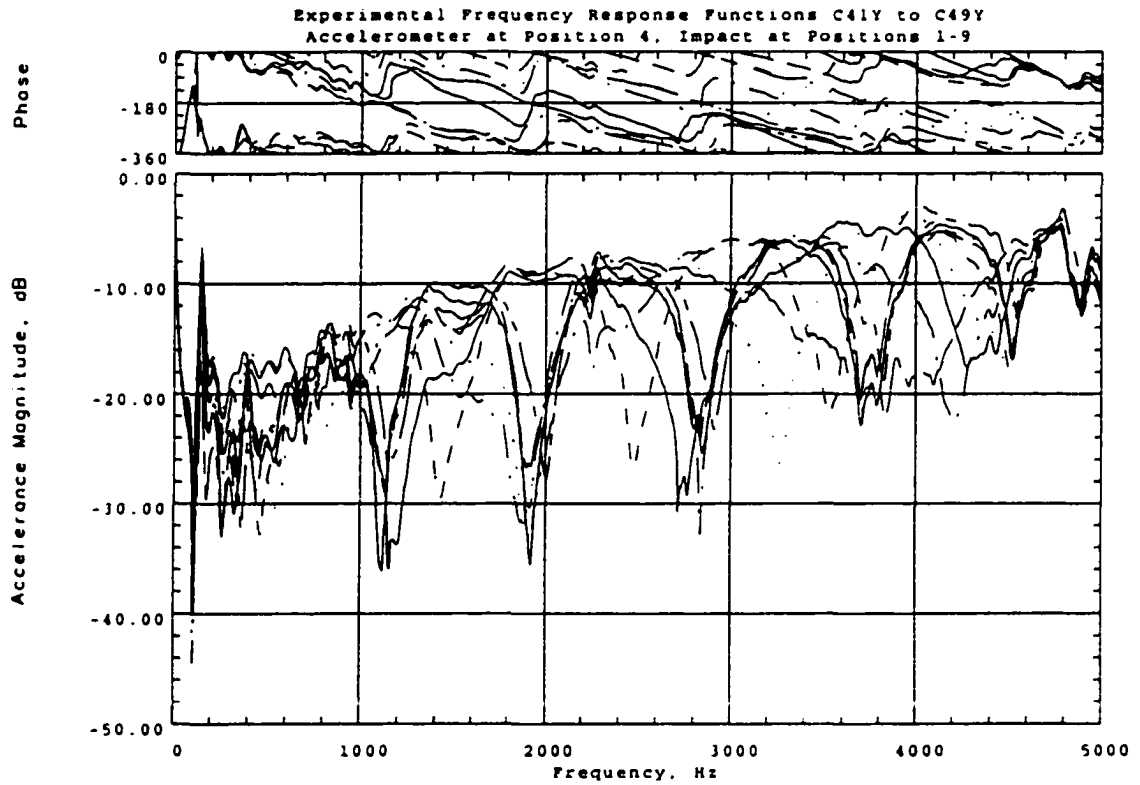


Figure A.13 Experimental Frequency Response Functions for Pile C, Tested Along Y Axis, Accelerometer at Position 4, Impact at Positions 1-9

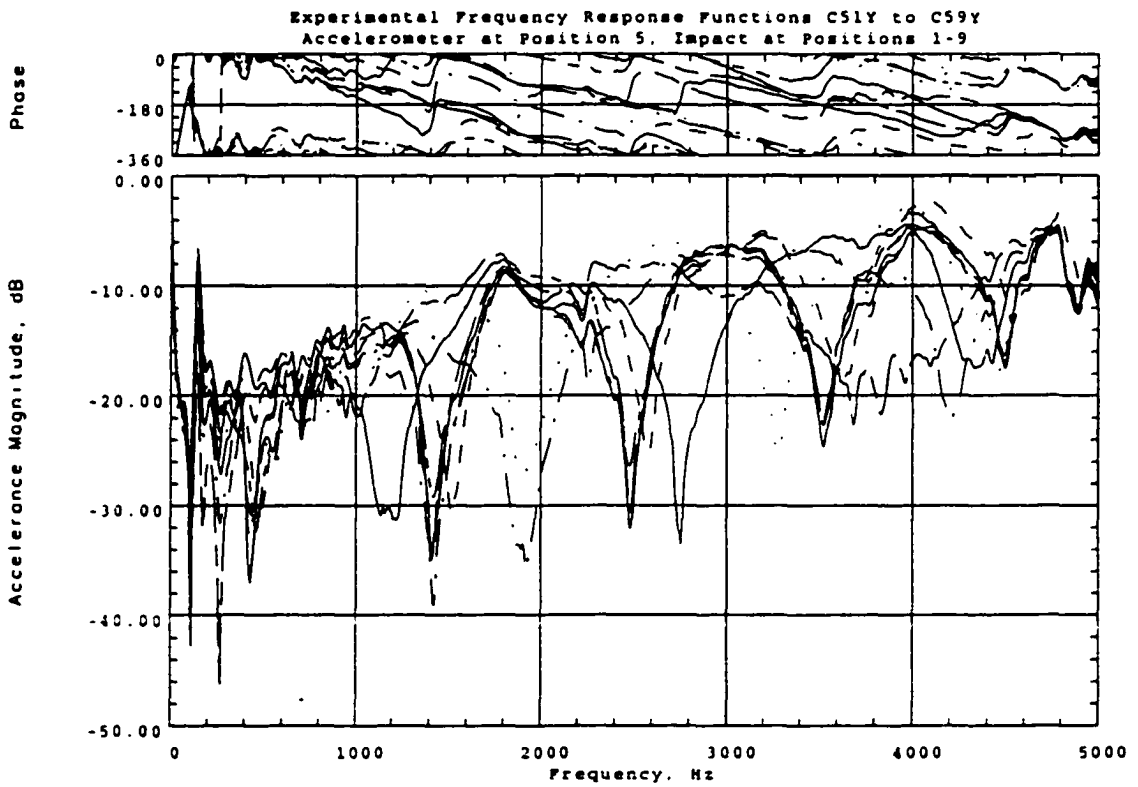


Figure A.14 Experimental Frequency Response Functions for Pile C, Tested Along Y Axis, Accelerometer at Position 5, Impact at Positions 1-9

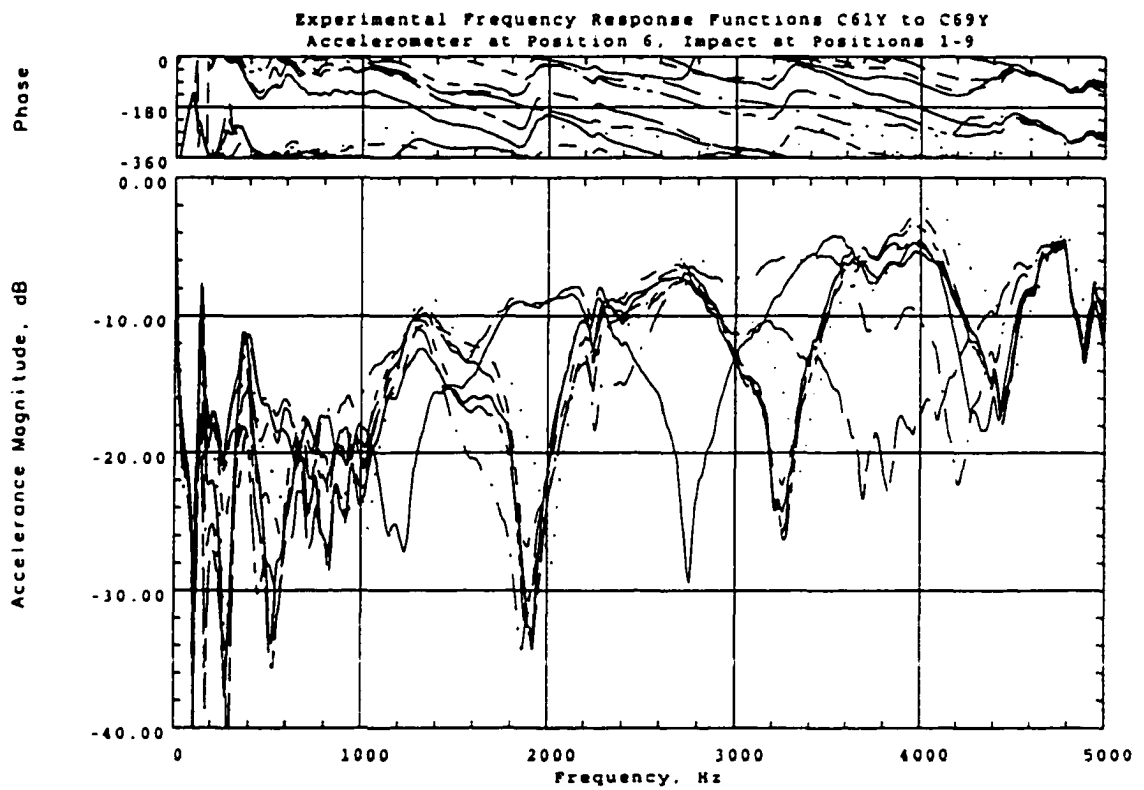
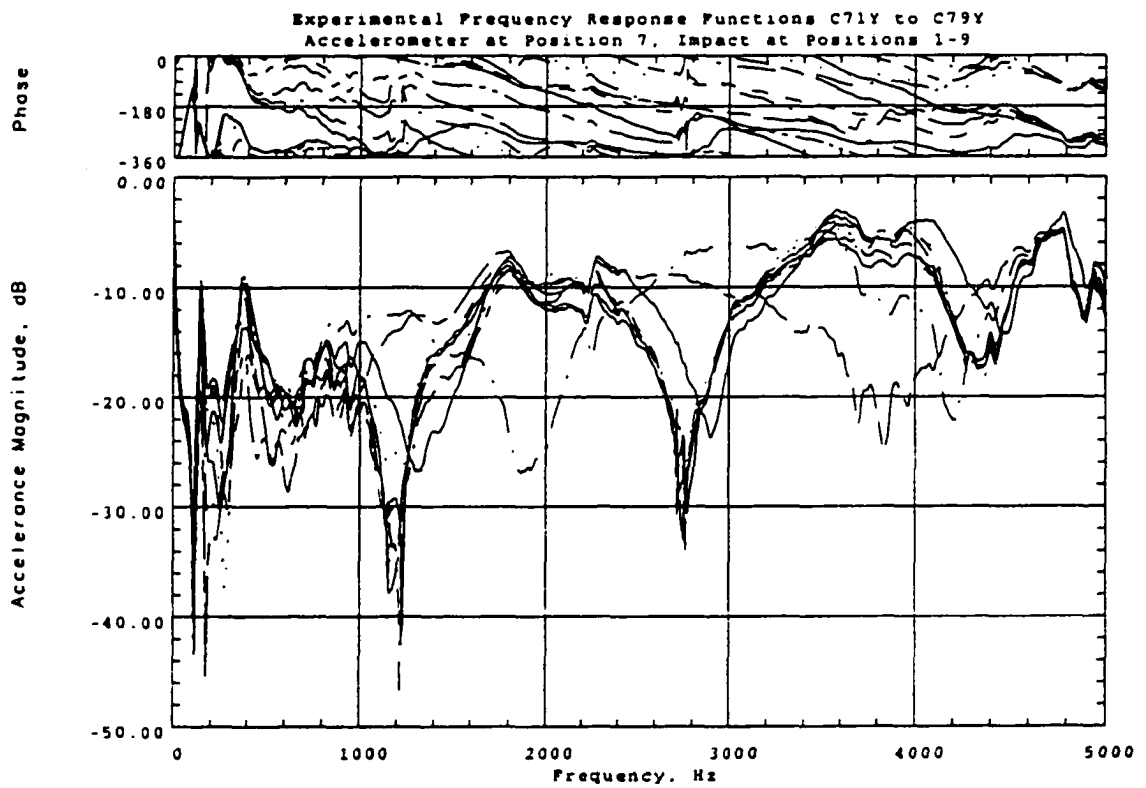


Figure A.15 Experimental Frequency Response Functions for Pile C, Tested Along Y Axis, Accelerometer at Position 6, Impact at Positions 1-9



**Figure A.16 Experimental Frequency Response Functions for Pile C, Tested Along Y Axis,
Accelerometer at Position 7, Impact at Positions 1-9**

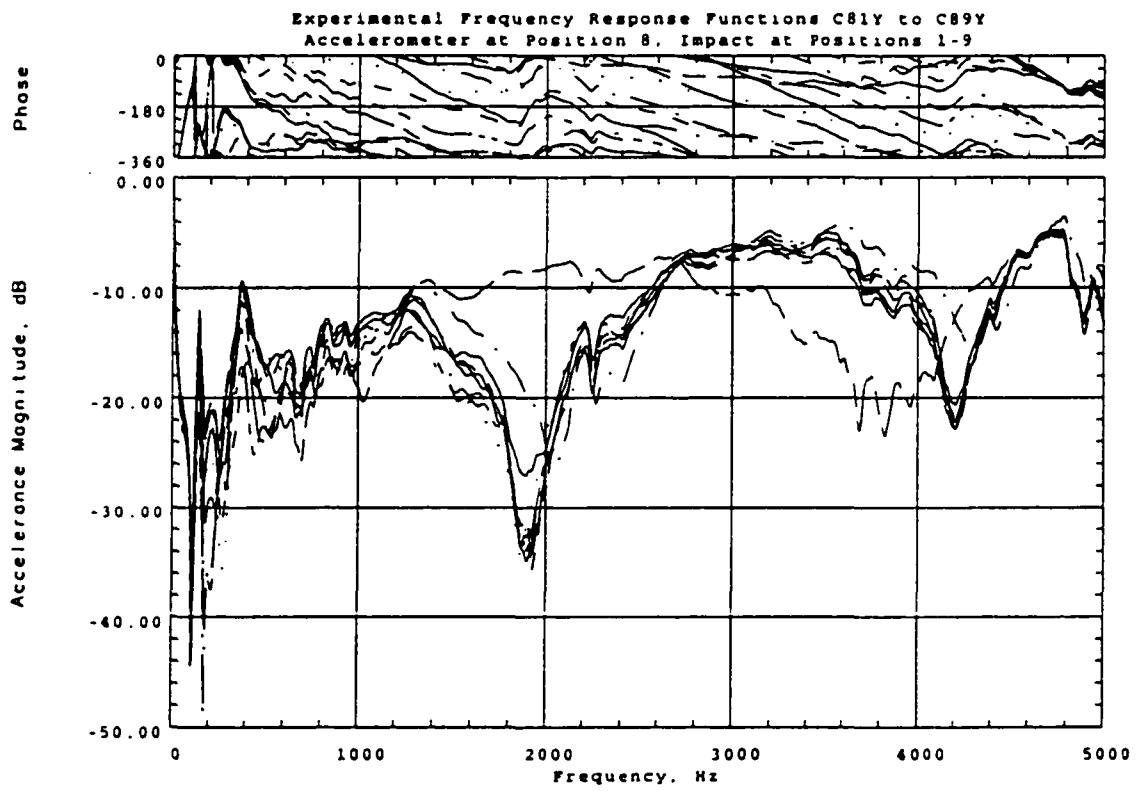
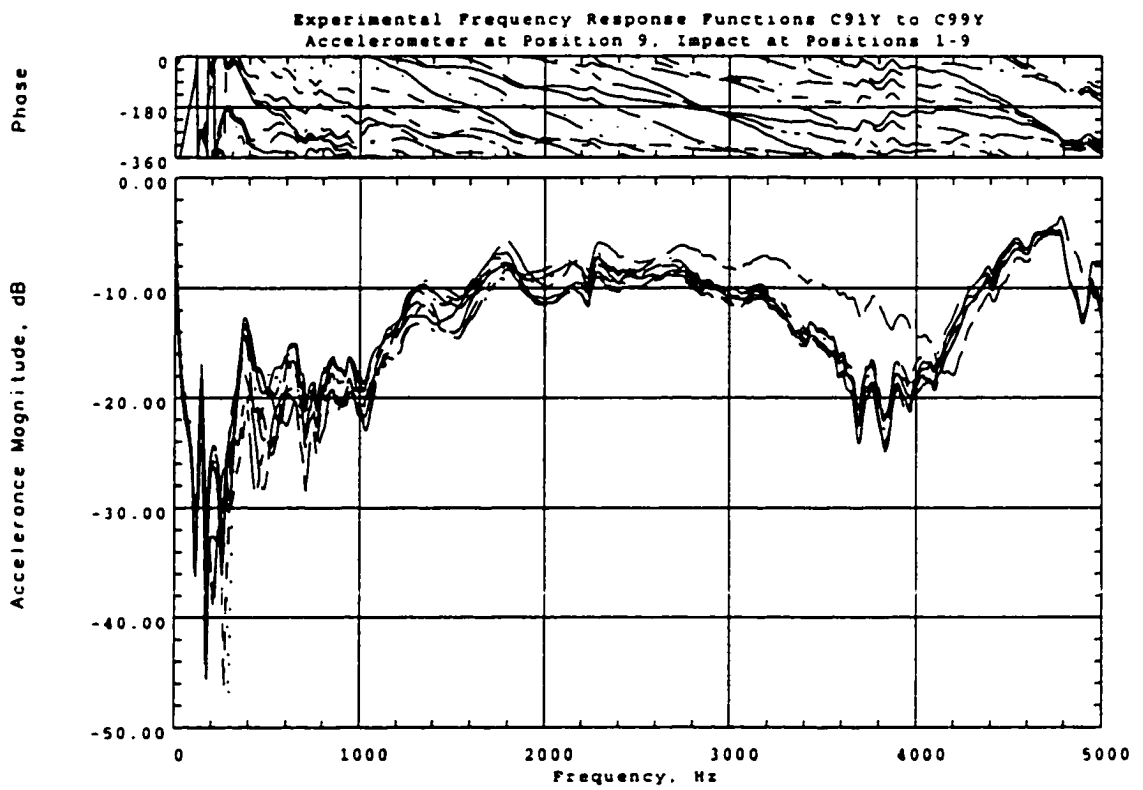


Figure A.17 Experimental Frequency Response Functions for Pile C, Tested Along Y Axis, Accelerometer at Position 8, Impact at Positions 1-9



**Figure A.18 Experimental Frequency Response Functions for Pile C, Tested Along Y Axis,
Accelerometer at Position 9, Impact at Positions 1-9**

APPENDIX B

PROGRAMS FOR ANALYTICAL GENERATION OF FREQUENCY RESPONSE

FUNCTION DATA

The programs presented in this appendix, written by Dr. Glenn Rix of the Georgia Institute of Technology, are those used to analytically derive frequency response function data for Group I Piles A through E, as described in Section 3.1. The main program was modified appropriately for each pile to account for its unique embedded length. The program used for Pile C is presented here to represent a typical case.

```
% Matlab m-file to calculate the frequency response function
% of a transversely vibrating pile

% Glenn J. Rix

% Establish the properties of the pile elements

h = [0.5 0.5 0.5 0.5 0.5 0.5 0.5 0.5 0.5 0.5 0.5 0.5 0.5 0.5 0.5
0.5]; % Element length

A = [0.0116 0.0116 0.0116 0.0116 0.0116 0.0116 0.0116 0.0116 0.0116 0.0116 0.0116
0.0116 0.0116 0.0116 0.0116 0.0116 0.0116 0.0116]; %Cross sectional
area

I = [2.194E-5 2.194E-5 2.194E-5 2.194E-5 2.194E-5 2.194E-5 2.194E-5 2.194E-5
2.194E-5 2.194E-5 2.194E-5 2.194E-5 2.194E-5 2.194E-5 2.194E-5
2.194E-5 2.194E-5]; % Area moment of inertia

EP = [4.2E9 4.2E9 4.2E9 4.2E9 4.2E9 4.2E9 4.2E9 4.2E9 4.2E9 4.2E9
4.2E9 4.2E9 4.2E9 4.2E9 4.2E9 4.2E9]; % Young's Modulus

DPile = [0.01 0.01 0.01 0.01 0.01 0.01 0.01 0.01 0.01 0.01 0.01 0.01 0.01 0.01
0.01 0.01 0.01 0.01]; % Pile damping ratio

RhoPile = [15.22 15.22 15.22 15.22 15.22 15.22 15.22 15.22 15.22 15.22
15.22 15.22 15.22 15.22 15.22 15.22 15.22]; % Mass density

NuPile = [0.27 0.27 0.27 0.27 0.27 0.27 0.27 0.27 0.27 0.27 0.27 0.27 0.27
0.27 0.27 0.27 0.27]; % Poisson's Ratio

Kappa = [1.0 1.0 1.0 1.0 1.0 1.0 1.0 1.0 1.0 1.0 1.0 1.0 1.0 1.0 1.0 1.0
1.0]; % Shape factor for shear

Nst = [0 0 0 0 0 0 0 0 0 0 0 0 0 0 0 0]; % Static axial load
```

```

width = [0.25 0.25 0.25 0.25 0.25 0.25 0.25 0.25 0.25 0.25 0.25 0.25 0.25
0.25 0.25 0.25 0.25];           % Width in the direction of loading

EPile = EP.*(1+2*i.*DPile);      % This is used to calculate a0 for
the soil reactions

r = sqrt(I./A);                  % Radius of gyration
MuPile = RhoPile.*A;             % Mass per unit length
GPile = EPile./(1+NuPile)./2;    % Shear modulus

% Establish the upper and lower boundary conditions
Top = 'fixed';                   % Fixed, free, or pinned
Bottom = 'free';                 % Fixed, free, or pinned

% Establish the soil properties

Vs = [0 0 0 0 0 0 0 0 0 0 550 550 550 550 550 550];
% Shear wave velocity

RhoSoil = [0 0 0 0 0 0 0 0 0 0 3.2 3.2 3.2 3.2 3.2 3.2];
% Mass density

NuSoil = [0 0 0 0 0 0 0 0 0 0 0.2 0.2 0.2 0.2 0.2 0.2];
% Poisson's ratio

D = [0 0 0 0 0 0 0 0 0 0 0 0 0 0 0 0];
% Damping ratio

Cs = Vs.*sqrt(1+2*i.*D);
% Complex shear wave velocity

GSoil = RhoSoil.*(Cs.^2);        % Complex shear modulus
LSoil = 2*GSoil.*NuSoil./(1-2*NuSoil); % Complex Lamé parameter

% Establish the load vector
P = eye(2*length(h)+2);

```

```

% Establish the range of frequencies
f = 6.25:6.25:5000;

% Establish the FRF vector
FRF = zeros(2*length(h)+2,2*length(h)+2,length(f));

waitHandle = waitbar(0,'Calculating...');

% Loop through all of the frequencies
for j = 1:length(f)

    waitbar(j/length(f));

    % Calculate the circular frequency
    Omega = 2*pi*f(j);

    % Preallocate and zero the global stiffness matrices
    KGlobal = zeros(2*length(h)+2,2*length(h)+2);

    % Calculate the soil reactions
    ku = Horizontal(GSoil,LSoil,NuSoil,Vs,D,(width/2),Omega);
    kr = Rocking(GSoil,Vs,D,(width/2),Omega);
    % ku = [0 0 0 0 0 0 0 0 0 0 0 0 0 0 0];
    % kr = [0 0 0 0 0 0 0 0 0 0 0 0 0 0 0];

    % Calculate the element stiffness matrices
    K = Element(Omega,ku,kr,h,r,MuPile,Kappa,EPile,GPile,I,A,Nst);

```

```

% Assemble the global stiffness matrix

for k = 1:length(h)

    KGlobal(2*k-1:2*k+2,2*k-1:2*k+2) = KGlobal(2*k-1:2*k+2,2*k-
1:2*k+2) + K(:, :, k);

end

% Apply the boundary conditions

switch lower(Top)

    case 'fixed'

        KGlobal(:,1) = 0;KGlobal(1,:) = 0;KGlobal(1,1) = 1;

        KGlobal(:,2) = 0;KGlobal(2,:) = 0;KGlobal(2,2) = 1;

    case 'pinned'

        KGlobal(:,1) = 0;KGlobal(1,:) = 0;KGlobal(1,1) = 1;

end

switch lower(Bottom)

    case 'fixed'

        KGlobal(:,2*length(h)+1) = 0;KGlobal(2*length(h)+1,:) =
0;KGlobal(2*length(h)+1,2*length(h)+1) = 1;

        KGlobal(:,2*length(h)+2) = 0;KGlobal(2*length(h)+2,:) =
0;KGlobal(2*length(h)+2,2*length(h)+2) = 1;

    case 'pinned'

        KGlobal(:,2*length(h)+1) = 0;KGlobal(2*length(h)+1,:) =
0;KGlobal(2*length(h)+1,2*length(h)+1) = 1;

end

% Solve the system of equations

U = KGlobal\P;

```

```

    % Calculate the inertance FRF
    FRF(:, :, j) = -(Omega^2)*U;

end

close(waitHandle);

% Eliminate the rows and columns corresponding to rotations
for k = 1:length(h)
    for n = 1:length(h)
        FRFMatrix(k,n,:) = FRF(2*k+1,2*n+1,:);
    end
end

save pilecsoil.mat FRFMatrix

-----

function k = Horizontal(G,L,Nu,Vs,D,r,Omega)
% Horizontal determines the complex horizontal stiffness per unit
% length of a cylinder using the approach described in Novak,
% Nogami, and Aboul-Ella (1978). The required input parameters are:

% G      Vector containing the shear modulus of each layer
% L      Vector containing the Lamé parameter of each layer
% Nu     Vector containing the Poisson's ratio of each layer
% Vs     Vector containing the shear wave velocity of each layer
% D      Vector containing the damping ratio of each layer

```

```

% r      Vector containing the radius of the pile element in each
layer

% Omega  Circular frequency (scalar)

% Preallocate and zero k
k = zeros(1,length(G));

% Determine the indices of the nonzero values of G
x = find(G);

a0 = Omega*r(x)./Vs(x);
a00 = i*a0./sqrt(1+2*i*D(x));
Dl = imag(L(x)+2*G(x))./real(L(x)+2*G(x));
n = sqrt(2*(1-Nu(x))./(1-2*Nu(x)));
b00 = i*a0./n./sqrt(1+i*Dl);
T = -(4*besselk(1,b00).*besselk(1,a00)+ ...
      a00.*besselk(1,b00).*besselk(0,a00)+...
      b00.*besselk(0,b00).*besselk(1,a00))./...
      (b00.*besselk(0,b00).*besselk(1,a00)+...
      a00.*besselk(1,b00).*besselk(0,a00)+...
      b00.*a00.*besselk(0,b00).*besselk(0,a00));
k(x) = pi*G(x).*(a0.^2).*T;

```

```

function k = Rocking(G,Vs,D,r,Omega)
% Rocking determines the complex rocking stiffness per unit
% length of a cylinder using the approach described in Novak,

```


Nogami, and Aboul-Ella (1978). The required input parameters are:

```
% G      Vector containing the shear modulus of each layer
% Vs     Vector containing the shear wave velocity of each layer
% D      Vector containing the damping ratio of each layer
% r      Vector containing the radius of the pile element in each
         layer
% Omega  Circular frequency (scalar)
```

```
% Preallocate and zero k
```

```
k = zeros(1,length(G));
```

```
% Determine the indices of the nonzero values of G
```

```
x = find(G);
```

```
a0 = Omega*r(x)./Vs(x);
```

```
a00 = i*a0./sqrt(1+2*i*D(x));
```

```
T = a00.*besselk(0,a00)./besselk(1,a00)+1;
```

```
k(x) = pi*G(x).*(r(x).^2).*T;
```

```
-----
function E =
Element(Omega,ku,kr,h,r,MuPile,Kappa,EPile,GPile,I,A,Nst)
```

```
% Element calculates the element stiffness matrix for each
```

```
% layer using the formulas in Novak and Aboul-Ella (1978).
```

```
% The results are stored in a 4x4xNLay matrix.
```

```
% Preallocate the element stiffness matrix
```

```

E = zeros(4,4,length(h));

% Calculate terms used in the element stiffness matrices
B1 = ((r.^2).*MuPile*Omega^2 - kr + ...
      Kappa.*EPile.*I.*(MuPile*Omega^2 - ku)./GPile./A + ...
      Nst.*(1+Kappa.*Nst./GPile./A))./EPile./I;

B2 = (MuPile*Omega^2 - ku).*(1-Kappa.*((r.^2).*MuPile*Omega^2 - ...
      kr - Nst)./GPile./A)./EPile./I;

a = h.*sqrt((B1 + sqrt(B1.^2 + 4*B2))/2);
b = h.*sqrt((-B1 + sqrt(B1.^2 + 4*B2))/2);
c = 1-Kappa.*((r.^2).*MuPile*Omega^2 - kr - Nst)./GPile./A;
abar = a.*(1-Kappa.*EPile.*I.*(b.^2)./GPile./A./(h.^2)./c)./...
      (1+Kappa.*Nst./GPile./A);
bbar = b.*(1+Kappa.*EPile.*I.*(a.^2)./GPile./A./(h.^2)./c)./...
      (1+Kappa.*Nst./GPile./A);

phi = 2*abar.*bbar.*(cosh(b).*cos(a)-1) + (abar.^2 -
bbar.^2).*sinh(b).*sin(a);

F1 = -(a.^2+b.^2).*(abar.*sinh(b) - bbar.*sin(a))./phi;
F2 = -(a.^2+b.^2).*(bbar.*cosh(b).*sin(a) -
abar.*sinh(b).*cos(a))./phi;
F3 = -abar.*bbar.*(a.^2+b.^2).*(cos(b) - cos(a))./phi;
F4 = (abar.*bbar.*(b.*bbar - a.*abar)).*(cosh(b).*cos(a)-1) + ...
      abar.*bbar.*(abar.*b + a.*bbar).*sinh(b).*sin(a))./phi;
F5 = abar.*bbar.*(a.^2+b.^2).*(bbar.*sinh(b) + abar.*sin(a))./phi;
F6 = -abar.*bbar.*(a.^2+b.^2).*(abar.*cosh(b).*sin(a) +
bbar.*sinh(b).*cos(a))./phi;

for j = 1:length(h)

```

```

    E(:, :, j) = EPile(j)*I(j)*[F6(j)/h(j)^3  F4(j)/h(j)^2
F5(j)/h(j)^3  -F3(j)/h(j)^2;
F3(j)/h(j)^2  F1(j)/h(j)  ;
F6(j)/h(j)^3  -F4(j)/h(j)^2;
F2(j)/h(j)];
    end

```

APPENDIX C

MODE SHAPES FOR PILE A IN EMBEDDED CONFIGURATION GENERATED BY FINITE ELEMENT MODEL

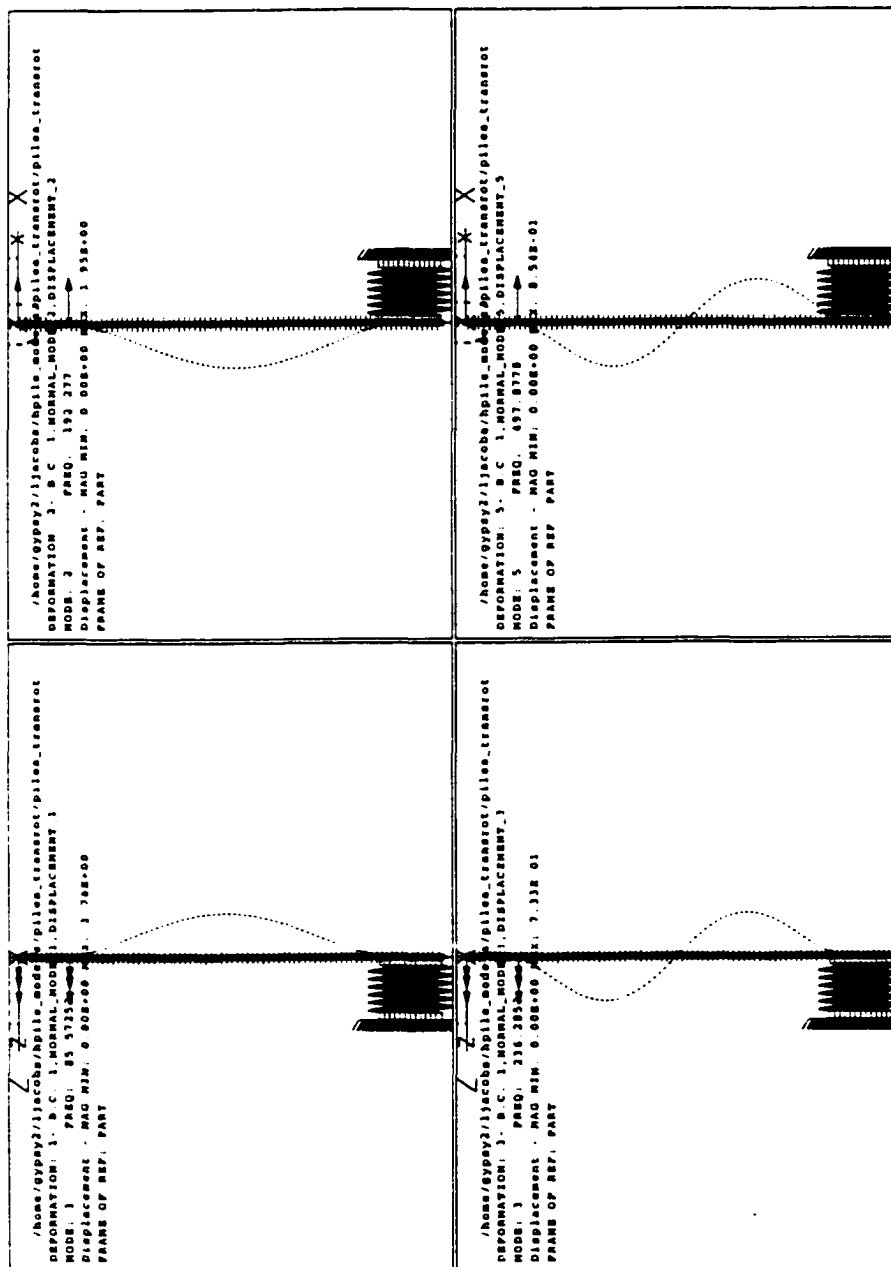


Figure C.1 Pile A, Embedded Configuration, Finite Element Mode Shapes 1,2,3,5

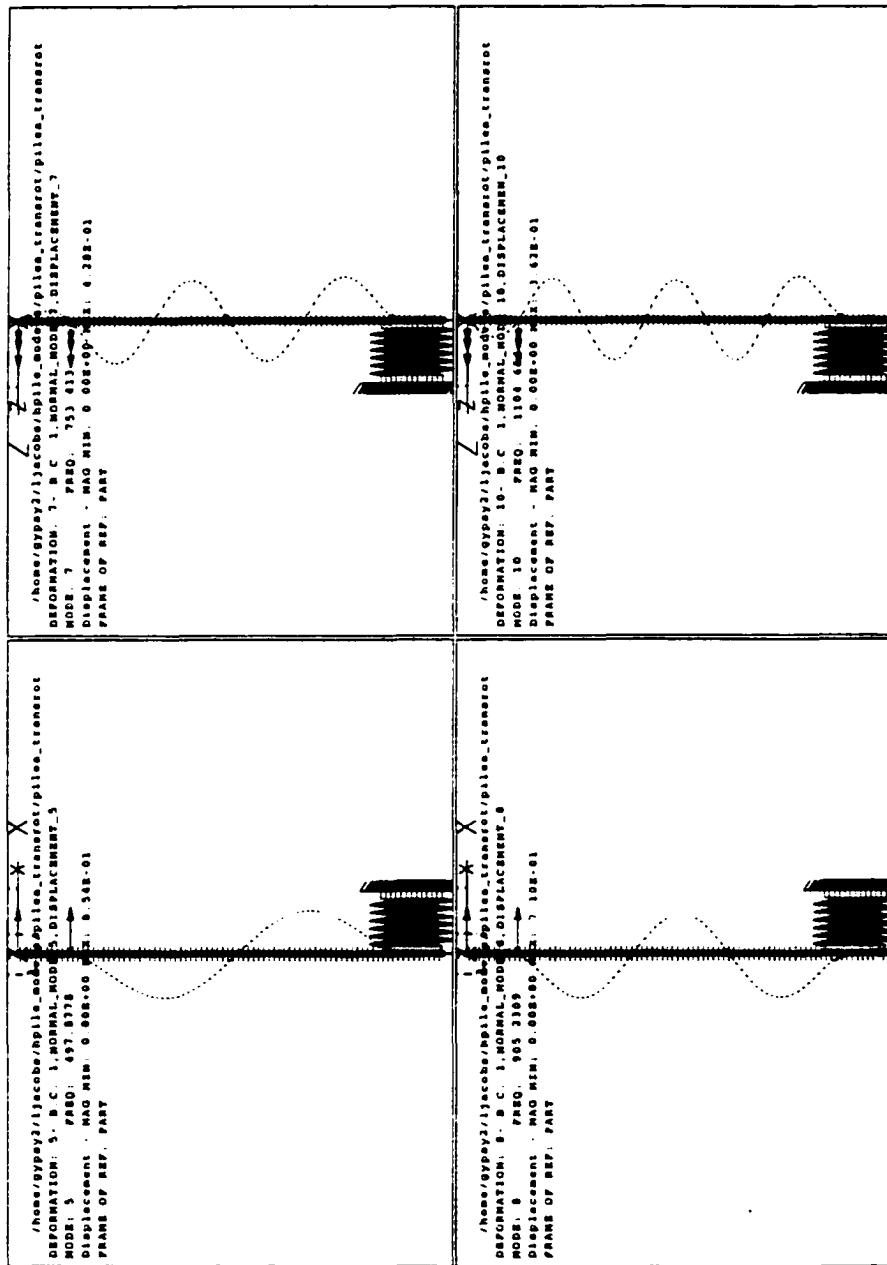


Figure C.2 Pile A, Embedded Configuration, Finite Element Mode Shapes 5,7,8,10

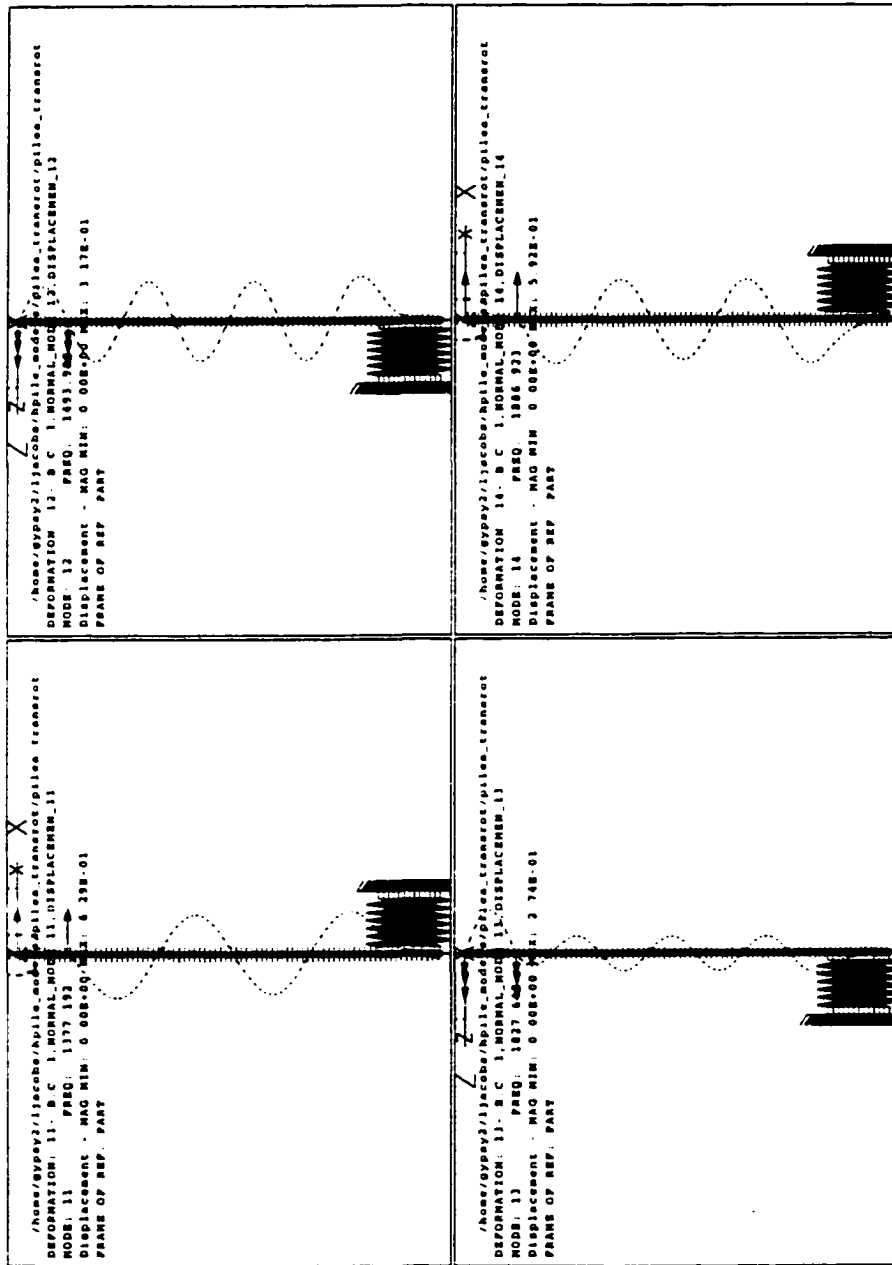


Figure C.3 Pile A, Embedded Configuration. Finite Element Mode Shapes 11,12,13,14

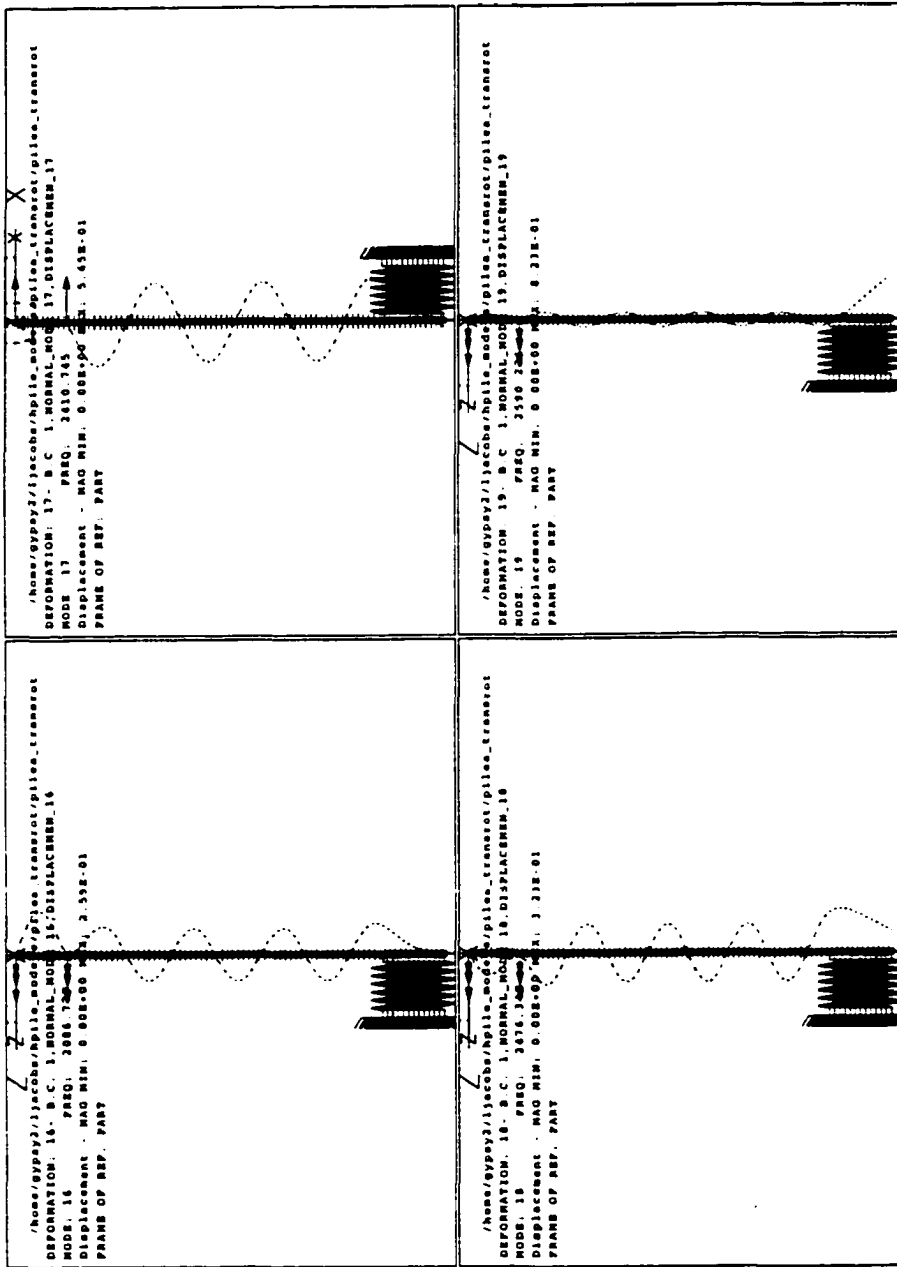


Figure C.4 Pile A, Embedded Configuration, Finite Element Mode Shapes 16,17,18,19

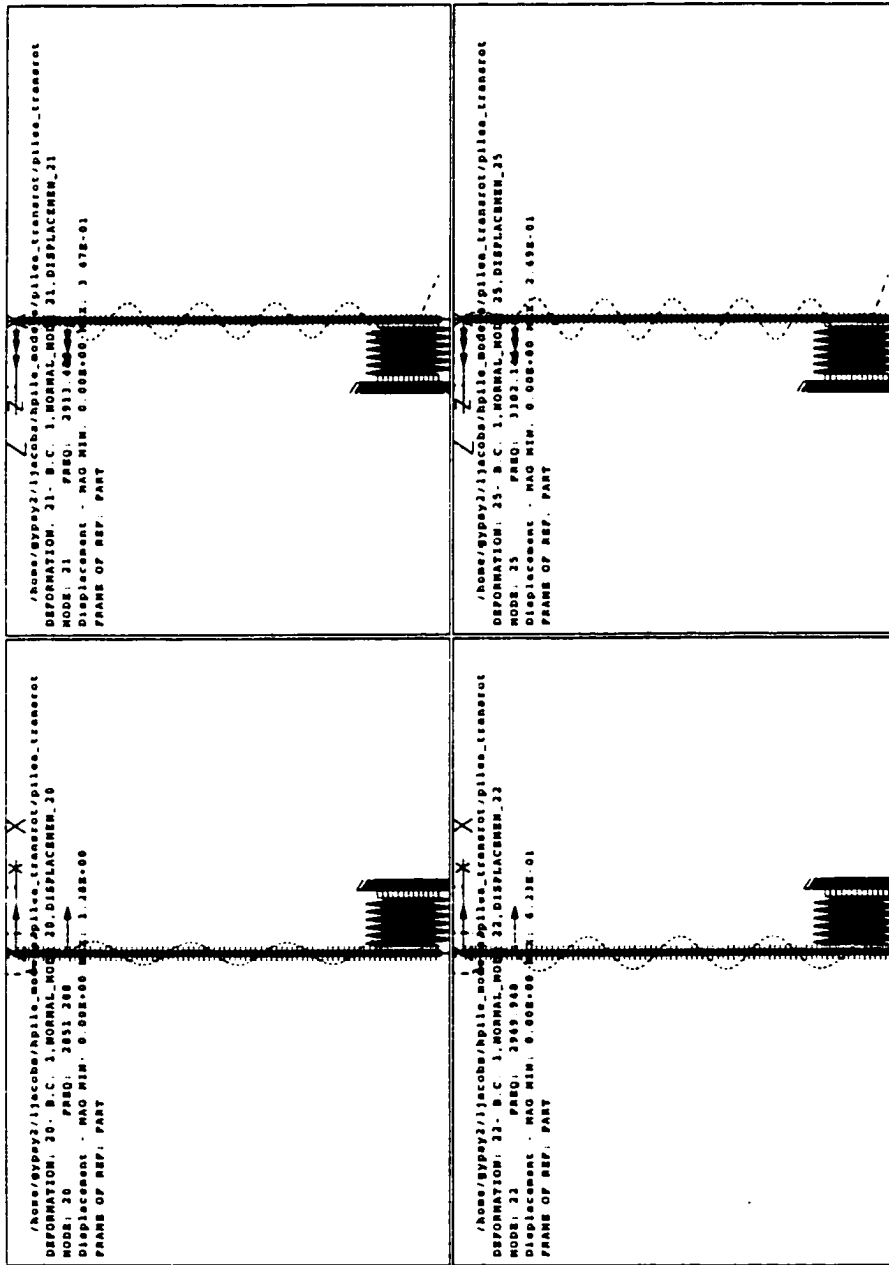


Figure C.5 Pile A, Embedded Configuration. Finite Element Mode Shapes 20,21,22,25

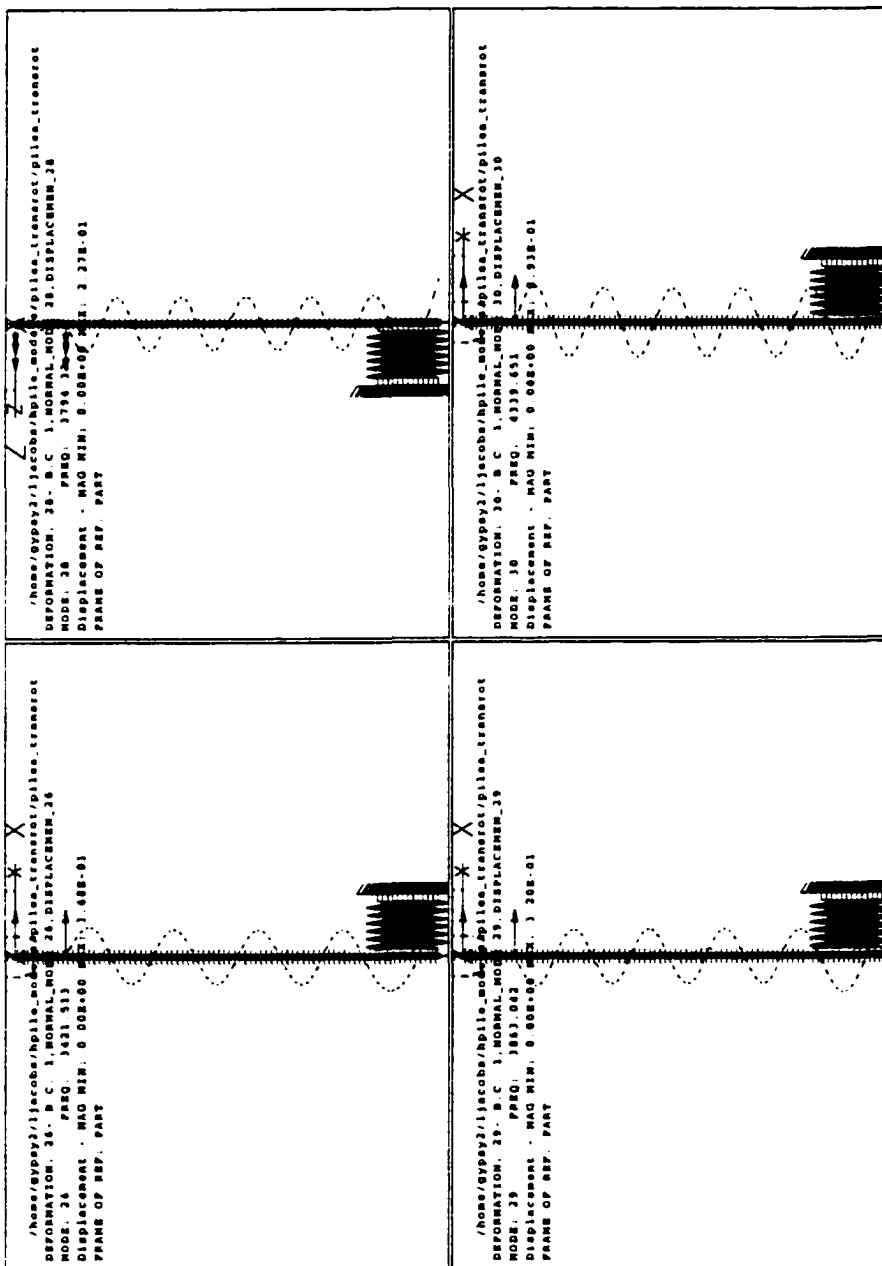


Figure C.6 Pile A, Embedded Configuration, Finite Element Mode Shapes 26,28,29,30

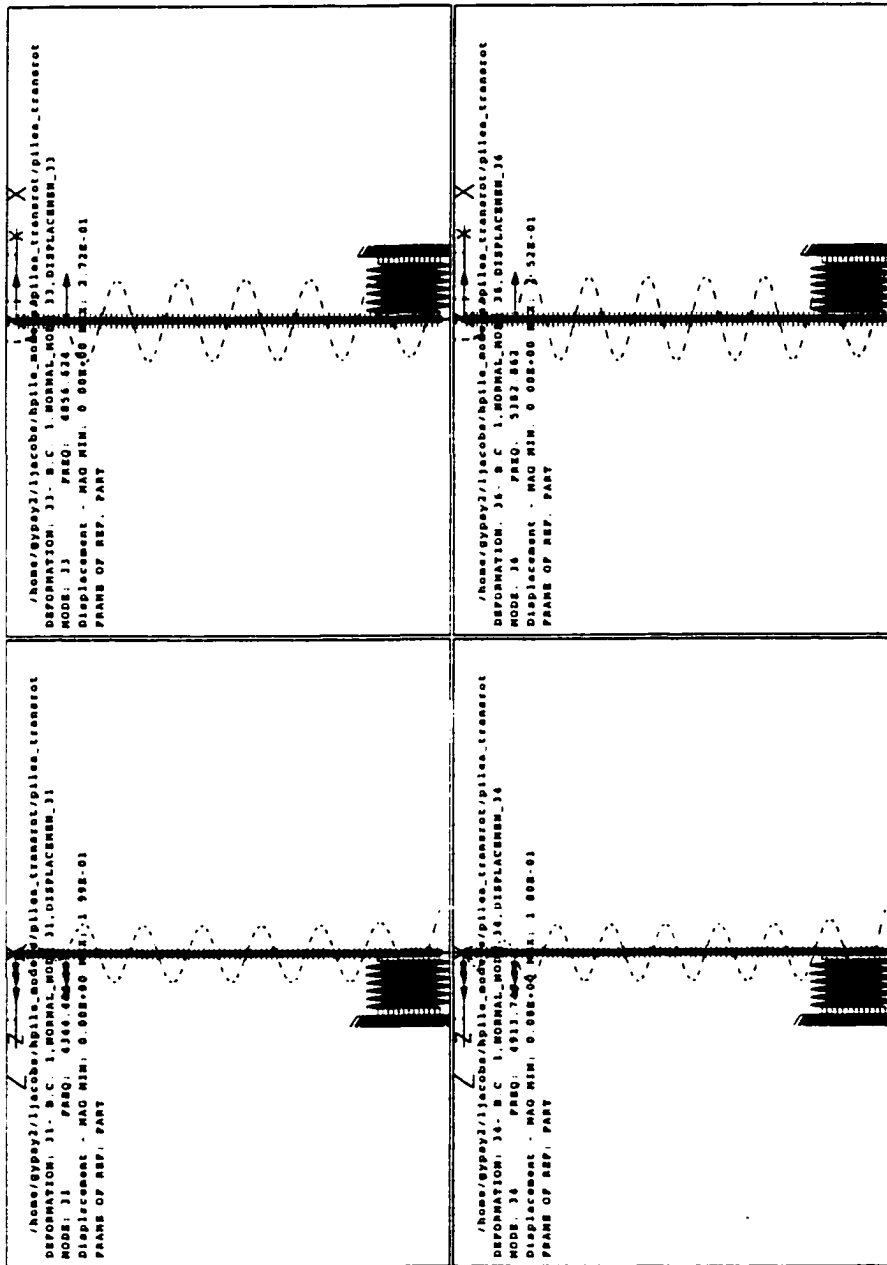


Figure C.7 Pile A, Embedded Configuration, Finite Element Mode Shapes 31,33,34,36

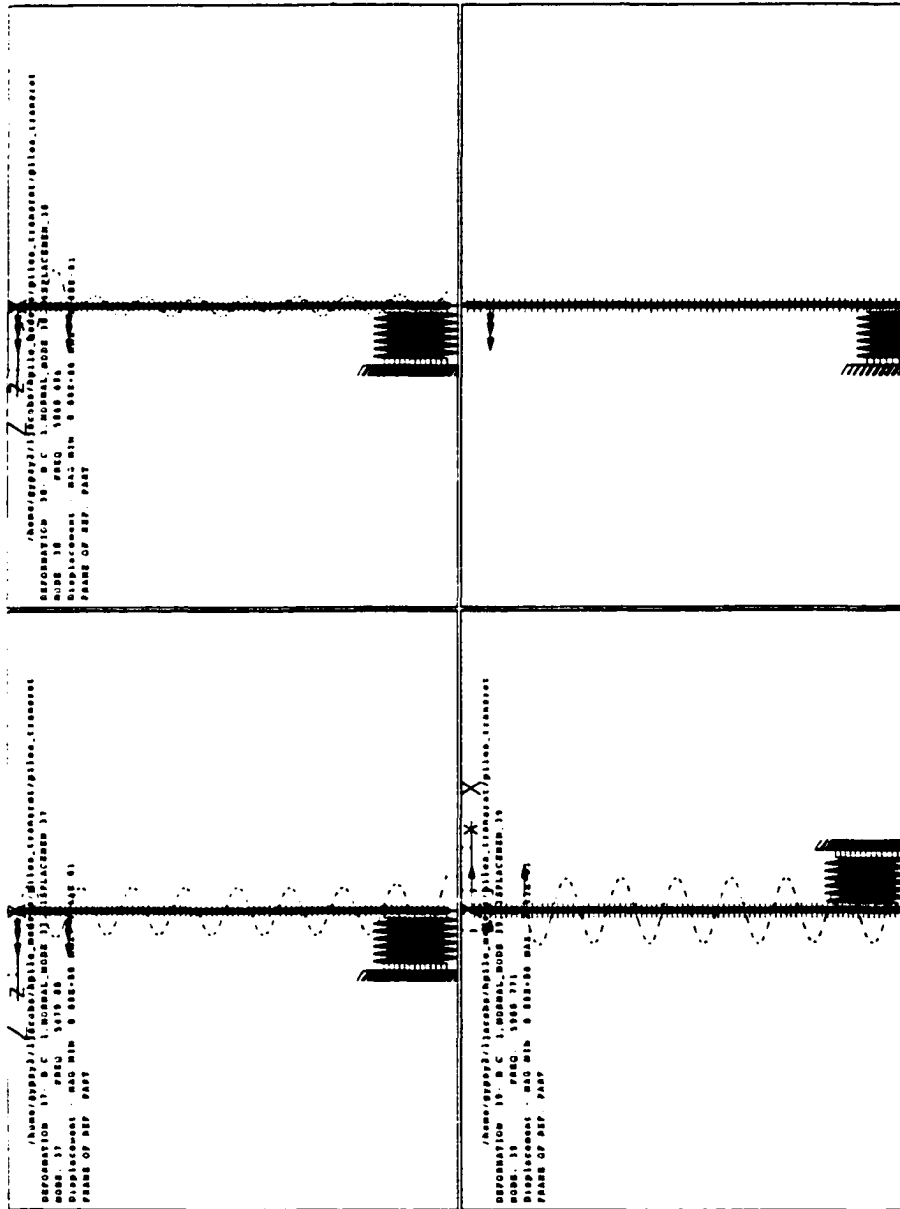


Figure C.8 Pile A, Embedded Configuration. Finite Element Mode Shapes 37,38,39

APPENDIX D

DERIVATION OF THEORETICAL SOLUTION

Beams on Elastic Supports or Elastic Foundations

The derivation shown below is developed in the text by Weaver et al. (1990), beginning on page 456. The authors state:

Support restraint conditions at the ends of a beam may be intermediate between the extremes of zero restraint and full restraint. If such restraints against either translations or rotations are linearly elastic, they may be idealized as springs, as shown in Figure [D.1]. Let the symbols k_1 and k_2 represent the stiffness constants for the translational and rotational springs at the left end; k_3 and k_4 are the stiffness constants for the translational and rotational springs at the right end. In this case the boundary conditions may be expressed as

$$V_{x=0} = EI(X''')_{x=0} = -k_1(X)_{x=0} \quad M_{x=0} = EI(X'')_{x=0} = k_2(X')_{x=0} \quad (D.1)$$

$$V_{x=L} = EI(X''')_{x=L} = k_3(X)_{x=L} \quad M_{x=L} = EI(X'')_{x=L} = -k_4(X')_{x=L} \quad (D.2)$$

where

V = shearing force,

x = position along the beam,

E = beam modulus of elasticity,

I = beam moment of inertia,

X = normal function for transverse vibration of a prismatic beam,

M = bending moment, and

L = beam length.

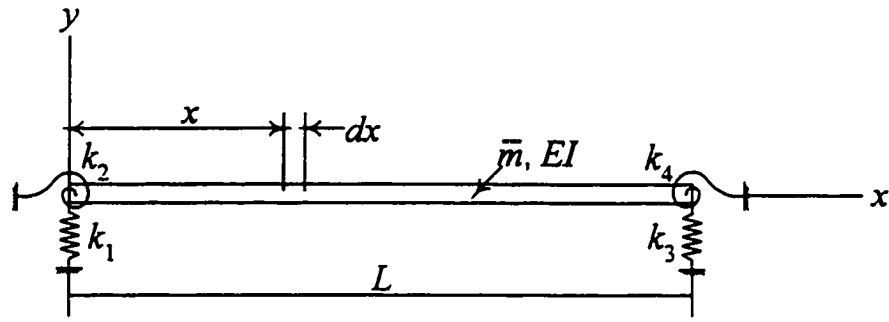


Figure D.1 Beam On Elastic Supports Idealized as Springs

For $k = \sqrt{\frac{\omega}{a}}$, where $a = \sqrt{\frac{EI}{\bar{m}}}$, the normal function X and its derivatives may be written as

(Weaver et al., 1990—see Equation (5.85), p. 418):

$$X = C_1 \sin kx + C_2 \cos kx + C_3 \sinh kx + C_4 \cosh kx \quad (D.3)$$

$$X' = k(C_1 \cos kx - C_2 \sin kx + C_3 \cosh kx + C_4 \sinh kx) \quad (D.4)$$

$$X'' = k^2(-C_1 \sin kx - C_2 \cos kx + C_3 \sinh kx + C_4 \cosh kx) \quad (D.5)$$

$$X''' = k^3(-C_1 \cos kx + C_2 \sin kx + C_3 \cosh kx + C_4 \sinh kx) \quad (D.6)$$

where C_1 through C_4 are constants that “must be determined in each particular case from the boundary conditions at the ends of the beam” (Weaver et al., 1990). Substituting

appropriately from Equations D.3 through D.6 into the boundary condition Equations D.1 and D.2 gives

$$EI k^3 C_1 - k_1 C_2 - EI k^3 C_3 - k_1 C_4 = 0 \Rightarrow -EI \frac{k^3}{k_1} C_1 + C_2 + EI \frac{k^3}{k_1} C_3 + C_4 = 0 \quad (D.7)$$

$$-k_2 C_1 - EI k C_2 - k_2 C_3 + EI k C_4 = 0 \Rightarrow C_1 + EI \frac{k}{k_2} C_2 + C_3 - EI \frac{k}{k_2} C_4 = 0 \quad (D.8)$$

$$\begin{aligned} &(-EI k^3 \cos kL - k_3 \sin kL) C_1 + (EI k^3 \sin kL - k_3 \cos kL) C_2 \\ &+ (EI k^3 \cosh kL - k_3 \sinh kL) C_3 + (EI k^3 \sinh kL - k_3 \cosh kL) C_4 = 0 \end{aligned} \quad (D.9)$$

$$\begin{aligned} &(-EI k \sin kL + k_4 \cos kL) C_1 + (-EI k \cos kL - k_4 \sin kL) C_2 \\ &+ (EI k \sinh kL + k_4 \cosh kL) C_3 + (EI k \cosh kL + k_4 \sinh kL) C_4 = 0. \end{aligned} \quad (D.10)$$

For a beam with one end fixed (say the left end), $k_1 = \infty$ and $k_2 = \infty$. Substituting these values into Equations D.7 through D.10, and setting the determinant of the coefficients of the constants C_1 through C_4 equal to zero (for a nontrivial solution) gives

$$\begin{vmatrix} 0 & 1 & 0 & 1 \\ 1 & 0 & 1 & 0 \\ -EI k^3 \cos kL & EI k^3 \sin kL & EI k^3 \cosh kL & EI k^3 \sinh kL \\ -EI k \sin kL & -EI k \cos kL & EI k \sinh kL & EI k \cosh kL \\ -k_3 \sin kL & -k_3 \cos kL & -k_3 \sinh kL & -k_3 \cosh kL \\ -k_4 \cos kL & -k_4 \sin kL & +k_4 \cosh kL & +k_4 \sinh kL \end{vmatrix} = 0. \quad (D.11)$$

Expanding the determinant produces the following:

$$\begin{aligned}
& k_3 k_4 \sinh^2(kL) - k_3 k_4 \cosh^2(kL) - (EI)^2 k^4 \cosh^2(kL) \\
& + (EI)^2 k^4 \sinh^2(kL) - k_3 k_4 \sin^2(kL) - k_3 k_4 \cos^2(kL) \\
& - 2EI k^3 k_4 \sin(kL) \cosh(kL) + 2EI k k_3 \cos(kL) \sinh(kL) \\
& + 2k_3 k_4 \cos(kL) \cosh(kL) - 2(EI)^2 k^4 \cos(kL) \cosh(kL) \\
& - 2EI k^3 k_4 \cos(kL) \sinh(kL) - (EI)^2 k^4 \cos^2(kL) \\
& - 2EI k k_3 \sin(kL) \cosh(kL) - (EI)^2 k^4 \sin^2(kL) = 0.
\end{aligned} \tag{D.12}$$

Simplifying produces

$$\begin{aligned}
& -[(EI)^2 k^4 + k_3 k_4] \sinh^2(kL) + [(EI)^2 k^4 + k_3 k_4] \cosh^2(kL) \\
& + [(EI)^2 k^4 + k_3 k_4] \sin^2(kL) + [(EI)^2 k^4 + k_3 k_4] \cos^2(kL) \\
& + [2EI(kk_3 + k^3 k_4)] \sin(kL) \cosh(kL) - [2EI(kk_3 - k^3 k_4)] \cos(kL) \sinh(kL) \\
& - [-2(EI)^2 k^4 + 2k_3 k_4] \cos(kL) \cosh(kL) = 0.
\end{aligned} \tag{D.13}$$

Further simplification gives

$$\begin{aligned}
& [(EI)^2 k^4 + k_3 k_4] [\cosh^2(kL) - \sinh^2(kL)] \\
& + [(EI)^2 k^4 + k_3 k_4] [\sin^2(kL) + \cos^2(kL)] \\
& + [2EI(kk_3 + k^3 k_4)] \sin(kL) \cosh(kL) \\
& - [2EI(kk_3 - k^3 k_4)] \cos(kL) \sinh(kL) \\
& + [2(EI)^2 k^4 - 2k_3 k_4] \cos(kL) \cosh(kL) = 0.
\end{aligned} \tag{D.14}$$

Noting that $\cosh^2(kL) - \sinh^2(kL) = 1$ and that $\sin^2(kL) + \cosh^2(kL) = 1$, equation D.14 further simplifies to

$$\begin{aligned} & 2[(EI)^2 k^4 + k_3 k_4] + 2[EI(kk_3 + k^3 k_4)] \sin(kL) \cosh(kL) \\ & - 2[EI(kk_3 - k^3 k_4)] \cos(kL) \sinh(kL) \\ & + 2[(EI)^2 k^4 - k_3 k_4] \cos(kL) \cosh(kL) = 0. \end{aligned} \quad (D.15)$$

Dividing each term by 2, and multiplying and dividing by appropriate powers of L gives

$$\begin{aligned} & \frac{1}{L^4} [(EI)^2 (kL)^4 + L^4 k_3 k_4] + \frac{1}{L^3} [EI(L^2 k_3 (kL) + (kL)^3 k_4)] \sin(kL) \cosh(kL) \\ & - \frac{1}{L^3} [EI(L^2 k_3 (kL) - (kL)^3 k_4)] \cos(kL) \sinh(kL) \\ & + \frac{1}{L^4} [(EI)^2 (kL)^4 - L^4 k_3 k_4] \cos(kL) \cosh(kL) = 0. \end{aligned} \quad (D.16)$$

Remembering that $k = \sqrt{\frac{\omega}{a}}$ and $a = \sqrt{\frac{EI}{m}}$, the following may be written:

$$k^2 = \frac{\omega}{a} \Rightarrow \omega_i = k_i^2 a = k_i^2 \sqrt{\frac{EI}{m}} = \frac{(kL)_i^2}{L^2} \sqrt{\frac{EI}{m}} \quad (D.17)$$

where i refers to the mode of interest. Remembering also the properties of the S3x5.7 section under investigation and combining them in the proper fashion produces the following useful quantities:

$$\left. \begin{aligned} E &= 4.2 \cdot 10^9 \text{ lb/ft}^2 \\ I_{y-y} &= 0.455 \text{ in}^2 = 2.194 \cdot 10^{-5} \text{ ft}^4 \\ L &= 5 \text{ ft} \end{aligned} \right\} EI = 92148 \text{ lb} \cdot \text{ft}^2$$

$$\bar{m} = \frac{5.7 \text{ lb/ft}}{32.18 \text{ ft/s}^2} = 0.177 \frac{\text{lb} \cdot \text{s}^2}{\text{ft}^2}$$

The following values of k_3 and k_4 for each pile were determined from the programs Horizontal.m and Rocking.m, which were used in the process of analytically generating frequency response functions as described in Section 5.1:

For Pile A:

$$k_3 = 5.7583 \cdot 10^7 \text{ (lb/ft)/ft} \cdot (1 \text{ ft}) = 5.7583 \cdot 10^7 \text{ lb/ft} \quad (\text{from Horizontal.m})$$

$$k_4 = 3.3769 \cdot 10^5 \text{ (ft} \cdot \text{lb/rad)/ft} \cdot (1 \text{ ft}) = 3.3769 \cdot 10^5 \text{ ft} \cdot \text{lb/rad} \quad (\text{from Rocking.m})$$

For Pile B:

$$k_3 = 5.7583 \cdot 10^7 \text{ (lb/ft)/ft} \cdot (2 \text{ ft}) = 1.15166 \cdot 10^8 \text{ lb/ft}$$

$$k_4 = 3.3769 \cdot 10^5 \text{ (ft} \cdot \text{lb/rad)/ft} \cdot (2 \text{ ft}) = 6.7538 \cdot 10^5 \text{ ft} \cdot \text{lb/rad}$$

For Pile C:

$$k_3 = 5.7583 \cdot 10^7 \text{ (lb/ft)/ft} \cdot (3 \text{ ft}) = 1.727 \cdot 10^8 \text{ lb/ft}$$

$$k_4 = 3.3769 \cdot 10^5 \text{ (ft} \cdot \text{lb/rad)/ft} \cdot (3 \text{ ft}) = 1.013 \cdot 10^6 \text{ ft} \cdot \text{lb/rad}$$

For Pile D:

$$k_3 = 5.7583 \cdot 10^7 \text{ (lb/ft)/ft} \cdot (4 \text{ ft}) = 2.303 \cdot 10^8 \text{ lb/ft}$$

$$k_4 = 3.3769 \cdot 10^5 \text{ (ft} \cdot \text{lb/rad)/ft} \cdot (4 \text{ ft}) = 1.351 \cdot 10^6 \text{ ft} \cdot \text{lb/rad}$$

For Pile E:

$$k_3 = 5.7583 \cdot 10^7 \text{ (lb/ft)/ft} \cdot (5 \text{ ft}) = 2.879 \cdot 10^8 \text{ lb/ft}$$

$$k_4 = 3.3769 \cdot 10^5 \text{ (ft}\cdot\text{lb/rad)/ft} \cdot (5 \text{ ft}) = 1.688 \cdot 10^6 \text{ ft}\cdot\text{lb/rad}$$

Substituting the section property values and the appropriate values of k_3 and k_4 for each pile into Equation D.16, and solving for the (kL) values that rendered the equation equal to zero produced the quantities that were then inserted into Equation D.17 to determine the theoretical natural frequency values for the Group I test pile systems. These values are reported in Section 5.3.1.

REFERENCES

- Aktan, A. E., Lee, K. L., Chuntavan, C., and T. Askel, "Modal Testing for Structural Identification and Condition Assessment of Constructed Facilities," Proceedings of the 12th International Modal Analysis Conference, 1994, pp. 462-468.
- Allemang, R. J., Brown, D. L., and William Fladung, "Modal Parameter Estimation: A Unified Matrix Polynomial Approach," Proceedings of the 12th International Modal Analysis Conference, 1994, pp. 501-514.
- Alexander, A. M., "Development of Procedures for Nondestructive Testing of Concrete Structures, Report 2: Feasibility of Sonic Pulse-Echo Technique," Structures Laboratory, U. S. Army Engineer Waterways Experiment Station Miscellaneous Paper C-77-11, April 1980, 25 pp.
- Alexander, A. M., "Development of Procedures for Nondestructive Testing of Concrete Structures, Report 3: Feasibility of Impact Technique for Making Resonant Frequency Measurements," U. S. Army Engineer Waterways Experiment Station Miscellaneous Paper C-77-11, November 1981, 31 pp.
- American Society of Testing Materials Standard ASTM D 4254-91, "Standard Test Method for Minimum Index Density and Unit Weight of Soils and Calculation of Relative Density," 1991.
- American Society of Testing Materials Standard ASTM D 4253-93, "Standard Test Methods for Maximum Index Density and Unit Weight of Soils Using a Vibratory Table," 1993.
- Askel, T., Lee, K., and A. E. Aktan, "Condition Assessment of Highway Bridges," Structures Congress XII, American Society of Civil Engineers, 1994, pp. 1124-1130.
- Balmès, E., "New Results on the Identification of Normal Modes from Experimental Complex Modes," Proceedings of the 12th International Modal Analysis Conference, 1994, pp. 1576-1582.
- Bendat, J. S. and Piersol, A. G., Random Data: Analysis and Measurement Procedures, 2nd Edition, John Wiley & Sons, New York, New York, 1986.

Bendat, J. S. and Piersol, A. G., Engineering Applications of Correlation and Spectral Analysis, John Wiley and Sons, Inc., New York, N. Y., 1980.

Catbas, F. N., Lenett, M., Brown, D. L., Doebling, S. W., Farrar, C. R., and A. Turer, "Modal Analysis of Multi-Reference Impact Test Data for Steel Stringer Bridges," *Proceedings of the 15th International Modal Analysis Conference*, 1997, pp. 381-391.

Chase, S. B. and Washer, G., "Nondestructive Evaluation for Bridge Management in the Next Century." *Public Roads*, Vol. 61, No. 1. 1997, pp. 16-25.

Cremer, L., Heckel, M., and Ungar, E. E., Structure-Borne Sound, Springer-Verlag, New York, 1973.

Davis, A. G., "Evaluation of Deep Foundations Beneath Buildings Damaged During the 1994 Northridge Earthquake", *Innovations in Nondestructive Testing of Concrete*, Stephen Pessiki and Larry Olson, editors, ACI SP-168, 1997, pp. 319-331.

Davis, A. G., and C. S. Dunn, "From Theory to Field Experience with the Non-destructive Vibration Testing of Piles," *Proceedings*, Institution of Civil Engineers, Part 2, Vol. 57, 1974, pp. 571-593.

Doebling, S. W. and C. R. Farrar, "Computation of Structural Flexibility for Bridge Health Monitoring Using Ambient Modal Data," *Proceedings of the 11th ASCE Engineering Mechanics Conference*, Ft. Lauderdale, Florida. 1996, pp. 1114-1117.

Doebling, S. W., Farrar, C. R., Prime, M. B., and Shevitz, D. W., "Damage Identification and Health Monitoring of Structural and Mechanical Systems From Changes in Their Vibration Characteristics: A Literature Review," Los Alamos National Laboratory Report LA-13070-MS, 1996.

Døssing, Ole, "The Hitchhiker's Guide to Modal Space," *Sound & Vibration*, January, 1995, pp. 14-24.

Døssing, Ole, Structural Testing, Part 1: Mechanical Mobility Measurements, Brüel & Kjær Publication, DK-2850 Nærum, Denmark, April 1988.

Døssing, Ole, Structural Testing, Part 2: Modal Analysis and Simulation, Brüel & Kjær Publication, DK-2850 Nærum, Denmark, March 1988.

Douglas, R. A., Eddy, J. L., and H. E. Wahls. "On Transforms and the Dispersion Computations Used for Evaluating Layer Properties," *Nondestructive Testing of Pavements and Back Calculation of Moduli*, A. J. Bush III and B. Y. Baladi, eds., ASTM STP 1026, 1989, ASTM, Philadelphia, Pa., pp. 612-627.

Douglas, R. A. and G. L. Eller, "Nondestructive Pavement Testing by Wave Propagation: Advanced Methods of Analysis and Parameter Management," *Pavement Response, Evaluation, and Data Collection*, Transportation Research Record 1070, Transportation Research Board, National Research Council, Washington, D. C., 1986, pp. 53-62.

Eddy, J. L., *A Laboratory Model of a Multi-Layer System for Nondestructive Testing*, M. S. Thesis, North Carolina State University, Raleigh, 1988.

Ewins, D. J., Modal Testing: Theory and Practice, Research Studies Press, Ltd., John Wiley & Sons, New York, NY, 1985.

Finno, Richard J., "Impulse Response Evaluation of Existing Foundations," *Proceedings of the 5th ITI Bridge NDE Users Group Conference*, <http://iti.acns.nwu.edu/clear/bridge/nde97/fin.html>, Sacramento, CA, 1997.

Gratton, Georgia Department of Transportation. personal communication with Dr. Glenn J. Rix, 1994.

Halvorsen, W. G. and Brown, D. L., "Impulse Technique for Structural Frequency Response Testing," *Sound and Vibration*, v. 11, November, 1977, pp. 8-21.

Hellier, C. J., "The Role of Nondestructive Evaluation in an Infrastructure," *Nondestructive Evaluation of Aging Structures and Dams*, Proceedings of SPIE-The International Society for Optical Engineering, Vol. 2457, 1995, pp. 28-33.

Hemez, F. M., "Practical Guide to High Accuracy Identification of Structural Damage in Complex Structures," Proceedings of the 13th International Modal Analysis Conference, 1995, pp. 1297-1304.

Hewlett-Packard Application Note 243-3, The Fundamentals of Modal Testing, 1986.

Hodges, C. H., Power, J., and Woodhouse, J., "The Use of the Sonogram in Structural Acoustics and an Application to the Vibrations of Cylindrical Shells," *Journal of Sound and Vibration*, Vol. 101, No. 2, 1985, pp. 203-218.

Holt, J. Darrin, Chen, S., and Douglas, R. A., "Determining Lengths of Installed Timber Piles by Dispersive Wave Propagation," *Soils, Geology, and Foundations*, Transportation Research Record 1447, Transportation Research Board, National Research Council, 1994, pp. 110-115.

I-DEAS Modal™, Master Series 5, Structural Dynamics Research Corporation, 1997.

I-DEAS™ Test Modal Analysis User's Guide, Structural Dynamics Research Corporation, 1995.

International Standard, "Vibration and Shock—Experimental Determination of Mechanical Mobility—Part 5: Measurements Using Impact Excitation with an Exciter Which is Not Attached to the Structure," ISO 7626-5:1994, p. 18.

Jones, R., Non-Destructive Testing of Concrete, Cambridge University Press, 1962.

Lenett, M., Catbas, N., Hunt, V., Aktan, A. E., Helmicki, A. and D. Brown, "Issues in Multi-Reference Impact Testing of Shell-Stringer Bridges," Proceedings of the 15th International Modal Analysis Conference, 1997, pp. 374-380.

MATLAB[®] Version 5.2, The Mathworks, Inc., 1998.

McConnell, Kenneth G., Vibration Testing: Theory and Practice, John Wiley & Sons, New York, New York, 1995.

Morgan, B. J. and R. G. Oesterle, "On-Site Modal Analysis—A New, Powerful Inspection Technique," Proceedings of the 2nd International Bridge Conference, Pittsburgh, Pennsylvania, 1985, pp. 108-114.

Newland, David E., "Wavelet Analysis of Vibration Signals, Part II: Wavelet Applications," *International Journal of Acoustics and Vibration*, Vol. 2, No. 1, 1997, pp. 21-27.

Novak, M., Nogami, T., and Aboul-Ella, F., "Dynamic Soil Reactions for Plane Strain Case," *Journal of the Engineering Mechanics Division*, Proceedings of the American Society of Civil Engineers, Vol. 104, No. EM4, August, 1978, pp. 953-959.

Novak, M. and Aboul-Ella, F., "Stiffness and Damping of Piles in Layered Media," *Proceedings, Earthquake Engineering and Soil Dynamics*, ASCE Special Conference, Pasadena, CA, June, 1978a, pp. 704-719.

Novak, M. and Aboul-Ella, F., "Impedance Functions of Piles in Layered Media," *Journal of the Engineering Mechanics Division*, Proceedings of the American Society of Civil Engineers, Vol. 104, No. EM6, June, 1978b, pp. 643-661.

Olson, L. D., and D. A. Sack, "Nondestructive Evaluation of Concrete Dams and Other Structures," *Nondestructive Evaluation of Aging Structures and Dams*, Proceedings of SPIE-The International Society for Optical Engineering, Vol. 2457, 1995, pp. 113-124.

Olson, L. D., Jalinoos, F., and M. F. Aouad, "Determination of Unknown Subsurface Bridge Foundations," Final Report, NCHRP Project E 21-5, National Cooperative Highway Research Program, Transportation Research Board, National Research Council, Washington, D.C., April, 1995, 264 pp.

- Olson, L. D., and Clifford C. Wright, "Nondestructive Testing of Deep Foundations with Sonic Methods," *Foundation Engineering, Current Principles and Practices*, Proceedings of the Congress, ASCE, Vol. 2, 1989, pp. 1173-1183.
- Pandey, A. K., R. Tyler, C. G. Arnette, and R. W. Anthony, "Assessment of Timber Piles in Clallam County, Washington," *Structural Materials Technology III, An NDT Conference*, Medlock, R. D. and D. C. Laffrey, eds., SPIE Vol. 3400, 1998, pp. 513-521.
- Richardson, M. H. and M. A. Mannan, "Correlating Minute Structural Faults with Changes in Modal Parameters," Proceedings of the 11th International Modal Analysis Conference, 1993, pp. 893-898.
- Rix, G. J., Jacobs, L. J., Raparelli, R. Q., and Rhodes, P. B., "Nondestructive Assessment of Pile Tip Elevation Using Flexural Waves," Symposium on the Application of Geophysics to Engineering and Environmental Problems, Keystone, CO, April, 1996, pp. 1-9.
- Rix, G. J., Jacobs, L. J., and C. D. Reichert. "Evaluation of Nondestructive Test Methods for Length, Diameter, and Stiffness Measurements on Drilled Shafts," *Field Performance of Structures and Nondestructive Evaluation of Subsurface Infrastructure*, Transportation Research Record 1415, Transportation Research Board, 1993, pp. 69-77.
- Salawu, O. S., "Non-destructive Evaluation of Constructed Facilities Using Vibration Testing," *Insight*, Vol. 36, No. 8, August, 1994. pp. 611-615.
- Samman, M. M. and M. Biswas, "Vibration Testing for Nondestructive Evaluation of Bridges. I: Theory," *Journal of Structural Engineering*, Vol. 120, No. 1, January, 1994a, pp. 269-289.
- Samman, M. M. and M. Biswas, "Vibration Testing for Nondestructive Evaluation of Bridges. II: Results," *Journal of Structural Engineering*, Vol. 120, No. 1, January, 1994b, pp. 290-306.
- Stain, R. T., "Integrity Testing," *Civil Engineering (London)*, April, 1982, pp. 54-59.
- Structural Dynamics Research Corporation. "Overview of Modal Analysis: Frequency Polyreference", I-DEASTTM SmartView. p. 9.
- Thomas, Graham, "Overview of Nondestructive Evaluation Technologies," *Nondestructive Evaluation of Aging Structures and Dams*. Proceedings of SPIE-The International Society for Optical Engineering, Vol. 2457, 1995, pp. 5-9.
- Washer, G. A., "Developments for the Nondestructive Evaluation of Highway Bridges in the USA," *NDT&E International*, Vol.31, No. 4, 1998, pp. 245-249.

Weaver, W., Jr., Timoshenko, S. P., and Young, D. H., Vibration Problems in Engineering, John Wiley & Sons, 1990, pp. 456-460.

Wojnarowski, M. E., S. G. Stiansen, and N. E. Reddy, "Structural Integrity Evaluation of a Fixed Platform Using Vibration Criteria," Proceedings of the 9th Annual Offshore Technology Conference, 1977, pp. 247-256.

VITA

Mary Leigh Hughes was born on August 1, 1964, in Fort Myers, Florida to Jack and Maggie Hughes; she has four brothers, John, Mike, Chris, and David. She graduated from Auburn High School in Auburn, Alabama, in 1982, and received a Bachelor's degree in Pre-Medicine from Auburn University in 1986. In 1990, she received an additional Bachelor's degree from Auburn University in Civil Engineering. At that time, she was selected for membership in the United States Air Force Palace Knight Program. As an employee of the Wright Laboratory Airbase Technology Branch, she then pursued a Master's degree in Civil Engineering from Auburn University, with an emphasis in the area of structural engineering.

In 1992, Ms. Hughes began working at Tyndall Air Force Base in Panama City, Florida, where she supervised and conducted research pertaining to the use of composite materials for civil engineering applications. In 1995, she returned to her studies, and entered the Georgia Institute of Technology in Atlanta, Georgia, to pursue a doctoral degree in Civil Engineering. After receiving her Ph.D. in Civil Engineering from Georgia Tech in 1999, with a major in structural engineering and a minor in engineering science and mechanics, Ms. Hughes began working at the Air Force Research Laboratory Munitions Directorate's Damage Mechanisms Branch, located at Eglin Air Force Base, Florida.